UNIVERSITE MATIERE BRETAGNE MOLECULES LOIRE ET MATERIAUX

UNIVERSITÉ DE NANTES

THESE DE DOCTORAT DE

L'UNIVERSITE DE NANTES
COMUE UNIVERSITE BRETAGNE LOIRE

ECOLE DOCTORALE N° 596
Matière, Molécules, Matériaux
Spécialité : Sciences des Matériaux

Par
Sacris Jeru TAMBIO

Evaluation of electrochemical performance of lithium-ion batteries and measurements of their transport properties by high-field NMR

Thèse présentée et soutenue à l'Université de Nantes, le 16 Décembre 2019
Unité de recherche : institut des Matériaux Jean Rouxel

Rapporteurs avant soutenance :

Fannie ALLOIN Directrice de Recherche, CNRS
Laure MONCONDUIT Directrice de Recherche, CNRS

Composition du Jury :

Présidente :	Laure MONCONDUIT	Directrice de Recherche, CNRS
Examinateurs :	Alejandro FRANCO	Professeur, Université Picardie Jules Verne
	Willy PORCHER	Docteur-Ingénieur de recherche, CEA-Liten
Dir. de thèse :	Bernard LESTRIEZ	Maître de Conférence HDR, Université de Nantes
Co-dir. de thèse :	Michaël DESCHAMPS	Professeur, Université d'Orléans

Invité(s)

	Nicolas BESNARD	Docteur-Ingénieur de recherche, RENAULT Technocentre

TABLE OF CONTENTS

CHAPTER 1: GENERAL INTRODUCTION

Electric vehicles have been eyed as a potential application for lithium-ion battery technology to aid in the search for greener alternatives to fossil fuels. This has led to numerous industrial companies to invest in lithium-ion battery research in order to unlock it as a potent energy source for automobiles. One of the biggest hurdles of using battery as an energy source is power performance. Electronic vehicles, to compete vs. fossil fuel based automobiles, should be able to both charge fast and exert enormous power on demand. Most researches aim to answer this by synthesizing new compounds but another aspect of battery development is also trying to seek answers through the aspect of “electrode engineering”.

Electrode engineering aims to optimize the formulation of the battery electrode in order to deliver both maximized energy and power densities. In the context of automobiles, increasing battery energy equates to greater mileage and increasing power leads to greater torque and in turn greater speeds. Energy on one hand can be easily solved by increasing the amount of active material present in the battery electrode. Power on the other hand, relies on the electrochemical kinetics associated with the micro-design of the electrode composite, specifically the diffusion of the lithium-ion in the porous matrix of the composite. Ironically, increasing the active material, which increases electrode capacity, has detrimental effects on the transport of the lithium-ion in the pore matrix. This is due to that the additional material increases both electrode thickness and tortuosity which in turn are both detrimental to lithium-ion transport within the pore matrix. This then translates to poor power performance and renders Li-ion battery technology less attractive for automobile applications.

In order to maximize power at increased energy, the relations between electrode composite architecture, ion diffusion and electrochemical performance must be further understood. In this study, this will be done through relating electrochemical performance with the different electrode mass loadings and then identifying key kinetic limitations such as electronic wiring, ionic wiring, charge transfer limitation and most importantly ionic transport. A simple model called the PD model (Penetration Depth) will then be developed and tested as a means to aid electrode design and formulation and in turn identify key limitations to power performance. This model will be a

derivative of existing models in literature but will be tuned to the results of this study in relating electrode morphology and ionic transport. To better understand ionic transport, a novel technique is employed via PFG-SE NMR (or commonly called as diffusion NMR). PFG-SE NMR is an attractive technique due to that it has been used to successfully measure diffusion in different media. From a battery design point of view, both the electrochemical results and the diffusion NMR findings will enable us to develop a model that could aid in the optimization of electrode design and in turn be able to achieve desired power performance in batteries.

OUTLINE:

CHAPTER 2: Review of Related Literature – Electrochemistry and Electrode Formulation

CHAPTER 3: Review of Related Literature – Nuclear Magnetic Resonance (NMR)

CHAPTER 4: NMR Methodology and Results

CHAPTER 5: Electrochemistry Methodology and Results

CHAPTER 6: Summary, Discussion and General Conclusion

CHAPTER 2: REVIEW OF RELATED LITERATURE – ELECTROCHEMISTRY AND ELECTRODE FORMULATION

2.1) Introduction

We would discuss first as to how battery electrodes perform especially those based from the chosen active material for this study: NMC. We will understand on how not the active material is the sole player in the electrode's electrochemical performance. Moreover, NMC can be synthesized with different transition metal stoichiometry which also dictates its electrochemistry. Focused discussion will be emphasized on how electrode formulation can be an improvement or detriment to the electrochemical performance if balance between the electrode parameters is not achieved. Most importantly, we will see how power performance greatly relies on Li^+ ion transport within the electrode pore matrix – the core interest of this study.

2.2) Electrode Battery Materials: NMC

Various compounds of different chemistries have been introduced as promising materials for Li-ion battery technology. Each compound aims to improve properties ranging from power and energy density to safety and cycle life. $LiCoO_2$ (LCO) is the progenitor of these materials which was developed by Goodenough for use in SONY Li-ion batteries in the 1990s [1]. The improved performance both in energy density and cyclability in comparison with NiCd and NiMH batteries propelled Li-ion to its ubiquitous status. Still, further research aims to improve further the capacity and cyclability of Li-ion technology by searching new materials that share the same intercalation chemistry as LCO but with better electrochemical performance. Two prominent cathode material families have been studied in recent years mainly the olivine LFP [2] and the LMO families [3].

LMO stands for $Li_xM_yO_z$ where x, y and z are the stoichiometric coefficients and M is a transition metal (LCO for example]. Recent advances in synthesis have produced several LMO chemistries with different M combinations which include but are not limited to: Ti, Ni, Cu, Mn, Al, Zn, Cr, etc. [4,5]. The richest of these chemistries might be the Ni-rich oxide family.

To understand the development of Nickel-rich cathode materials, we need to understand some of the chemistries linked with the LMO family namely $LiNiO_2$, $LiNi_{x-y}Mn_yO_2$, and $LiNi_{x-y}Co_yO_2$. $LiNiO_2$ has been described in literature with having very good gravimetric capacity (around 200-250 mAh/g). Difficulties with this compound come from its synthesis and its structural instability during cycling. The addition of manganese ($LiNi_{x-y}MnyO_2$), although decreased the deliverable capacity, increased the compound's thermal stability and cheapened the synthesis process. The addition of cobalt ($LiNi_{x-y}Co_yO_2$) increased rate capability and also decreased cation mixing between Li and Ni. A ternary compound was then synthesized mixing these three transition metals with the end result having the chemical formula: $LiNi_{x-y-z}Mn_yCo_zO_2$ or known in abbreviation as NMC. The mixing of the three transition metals balances the positive properties namely: capacity (Ni), safety (Mn) and rate capability (Co).

NMC typically is described with three numbers corresponding to the stoichiometric ratio between the transition metals. For example, NMC 532 corresponds to $LiNi_{0.5}Mn_{0.3}Co_{0.2}O_2$. The electrochemical redox couples are as follows: Ni^{2+}/Ni^{3+}, Ni^{3+}/Ni^{4+}, Co^{3+}/Co^{4+} where Ni redox is the more favored mechanism from low to moderate delithiation and Co redox is the favored mechanism during deep delithiation [6]. The aforementioned properties coming from Ni, Co and Mn make NMC a good prospect for batteries in EV applications [7]. Modifying the stoichiometric ratios between the transition metals also allow to tailor the properties of NMC [8,9]. The most favored technique is to maximize Ni ratio against both Mn and Co. Chemistries corresponding to this strategy include NMC 532, NMC 622, and NMC 811 among others. Increasing Ni content greatly increases the achievable capacity and the rate capability but suffers from reduced stability with the decreased Mn and Co contents [10]. Figure 2.1 illustrates the practical achievable capacities of varying compositions of NMC as elaborated by Noh et.al. and Figure 2.2 illustrates the relative stabilities of the NMC compositions as compiled by Kim et. al. From these chemistries, the most favored in terms of balanced capacity, stability and rate performance is NMC 532.

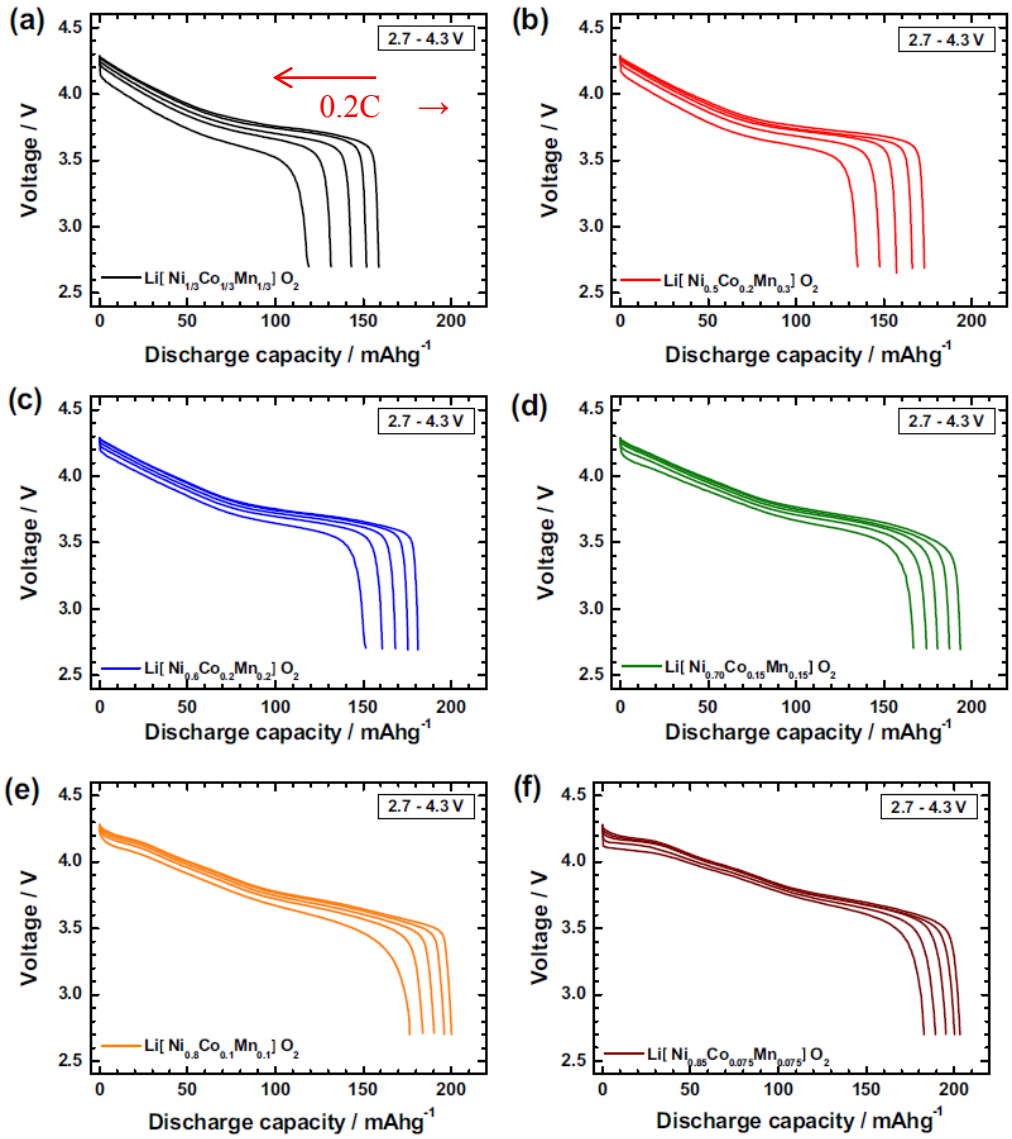

Figure 2.1 : Typical V vs. Capacity curves of different NMC stoichiometries (a) x = 1/3, (b) x = 0.5, (c) x = 0.6, (d) x = 0.7, (e) x = 0.8 and (f) x = 0.85 at different C-rates [10].

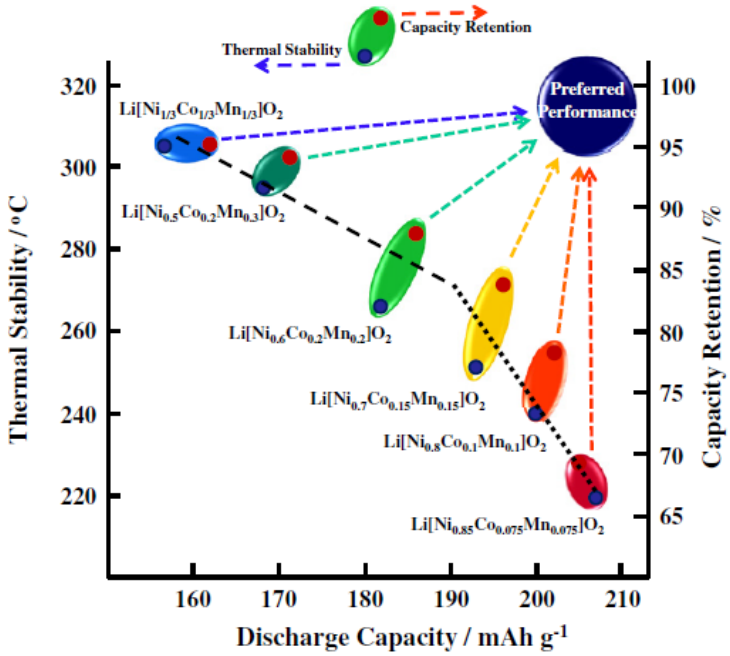

Figure 2.2: NMC composition map relating transition metal stoichiometry and performance [11]

NMC 532 ease of synthesis has also lead to the tailoring of its particle morphology in order to improve its electrochemical properties. Different calcination steps can produce NMC secondary particles having intra porosities to solid monocrystalline sphere [11,12,13]. The increased porosities produced from different calcination steps were hypothesized mostly to facilitate both ionic and solid state diffusion. It was observed that the intra particle-agglomerate porosities do help with energy performance at low C-rates but does not translate to power performance especially at high rates. It was also observed by using bulk density measurements that the volumetric capacity is inversely proportional to the amount of intra porosity in the AM (active material) which puts into question the practicality of porous AM particles.

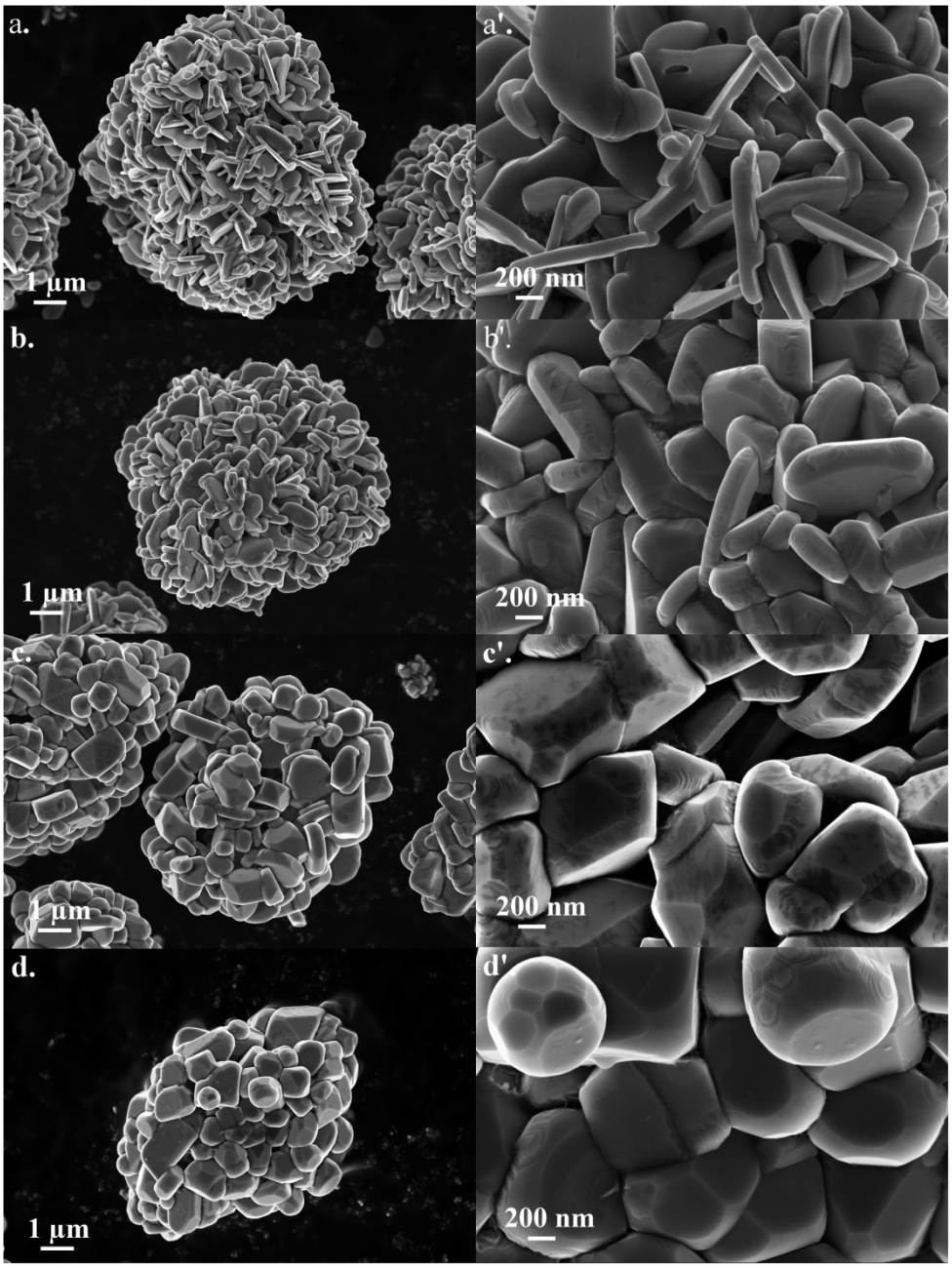

Figure 2.3: Various particle morphologies synthesized by Cabelguen et.al. [12]

The tailoring of the AM particles also tries to tackle the minimization of electronic and ionic resistive regions. The formation of the spinel phase in compounds of high Ni content blocks further ionic intercalation in the particle. Increased Ni content also increases reactive surface areas increasing SEI formation which also impedes ionic transport [14]. Increased particle cracking linked with heavy calendaring also decreases electronic wiring in the particles and

increases the probability of Li-ion detouring; both increases electronic and ionic resistances (Figure 2.4).

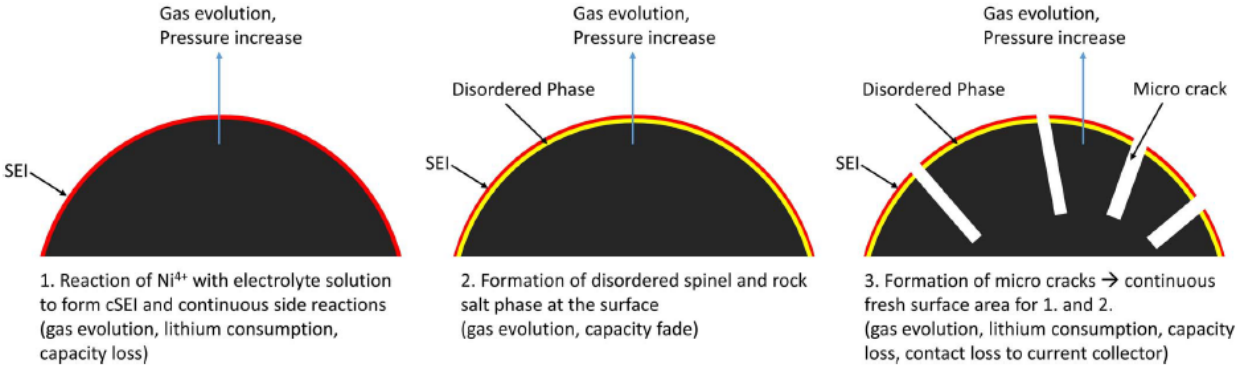

Figure 2.4: Eventual particle cracking and further surface exposure inducing further SEI formation [14]

2.2.1) General Aspects on Limitations Regarding Power Performance of NMC-Based Composite electrodes

The majority of battery electrodes are film composites deposited on a substrate surface (typically aluminum at the positive side and copper at the negative side) to practically facilitate the electrochemical reaction. The powdered nature and electronic conductivity of most active materials render them impractical for battery use on their own. Conductive additives and binders are mixed with the active material in a slurry and is then casted on the current collector to allow mechanical stability, and electronic conduction to allow the electrochemical reaction to proceed. The resulting electrode film after casting and drying is porous due to the nature of the composite, which is essential as it allows electrolyte impregnation which permits ions to travel to the surfaces of the NMC particles for the electrochemical reaction to proceed. The micrometric complexities of the electrode composite introduce parameters (size and geometrical distribution of the various constituents and of the porosity, their intra- and interconnectivity, and the tortuosity of the different networks involved in the transportation of charges), that can affect the electrochemical performance of the battery. Smart design of the electrode formulation is needed to optimize the electrochemical performance. This requires the understanding of the relationships between the binder, AM and carbon powders (bulk, surface) characteristics, the processing parameters, the morphology within the electrode, the properties (electrical, mechanical) of the

electrode, and finally the electrochemical performance. In the following, we will focus on the limitations to the power performance of NMC-based composite electrodes.

2.2.2)Several Possible Rate-Determining Steps That May Occur in a Typical State-of-the-Art Positive Electrode

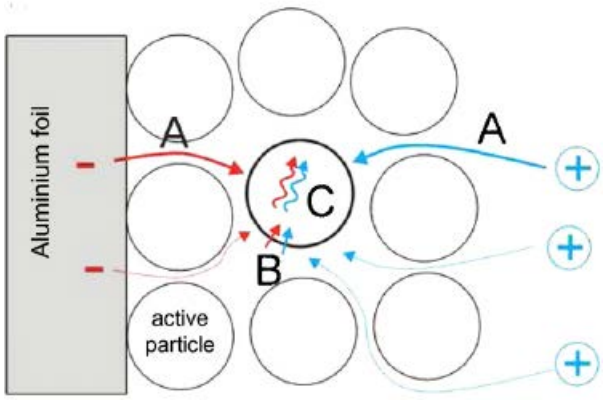

Figure 2.5:Schematic presentation of the division of overall electrode kinetics into three steps: A, B and C [15]

The overall electrode kinetics in a typical electrode composite can be divided into three steps (Figure 2.5): (A) the transport of electrons and ions from their "reservoirs" to the active matter (e.g. active particles), (B) the charge incorporation reaction which involves the transfer of both charged species from the outside into the interior of active particles and (C) the transport of lithium component inside the solid active particles.

Li intercalation compounds like NMC are semiconductors meaning that their electronic conductivity is not as high as metals. This is due to that a band gap exists between the conduction band and the valence band in semiconductors. This band gap should also not exceed at most 4eV because larger energy gaps are generally too large for electrons to hop on to the conduction band. This is mostly resolved by increasing the temperature (decreasing the band gap) and/or doping (adjusting the Fermi level). The intercalation reaction cannot initiate if the particle cannot conduct electrons leading to the underutilization of the particle hence a decrease in the nominal capacity of the electrode. The particle nature of the active material, as opposed to a uniform film or single crystal in common semiconductor technologies, demands another practical way to induce interparticle conductivity in the electrode. This is generally done through

the addition of conducting additives such as carbon black (CB) to increase electronic percolation in the electrode film. To further establish the percolation network, the components are then held together by a polymeric binder. The conductive additive-binder network acts as an electron tunnel aiding in the transfer of electrons from the current collector directly to the active material [16]. In most cases, the electrode is also calendered for further densification. This allows increased contact between the electrode components (in particular with the current collector) and to an extent, additional structural integrity. The major drawback of using binders and conducting additives is that both components do not participate in the intercalation of lithium further decreasing the gravimetric capacity (when the weight of the whole electrode is accounted for). Balance between the percent compositions of these components much be achieved in order to optimize the maximum capacity delivered and at the same time adequate electronic conductivity.

Another aspect that concerns the intercalation reaction of lithium in the electrode is diffusion. There are two diffusion phenomena that govern the whole intercalation reaction: ion diffusion in the electrolyte and ion diffusion within the active material particle. From an electrode architecture perspective, the geometric network generated from the electrode particles conform to a porous network. This porous network provides spatial access for the lithium ion to travel through the electrolyte solution to the surfaces of the active material surface. At the same time, the ease of transport in this porous network is highly dictated by the tortuosity of the pore geometry [17] thus determining the ion conductivity of the electrode. Increased tortuosity will augment the difficulty of the lithium ion to proceed with the intercalation reaction and will eventually halt the electrochemical reaction.

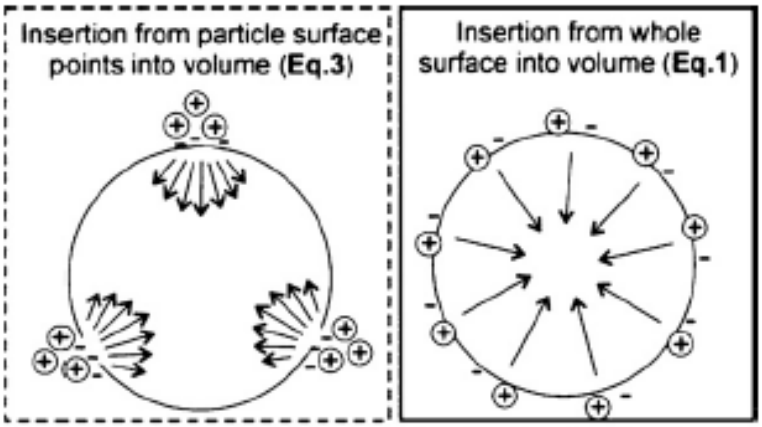

Figure 2.6: *Diagram of how the intercalation reaction proceeds with a poor (left) and adequate (right) ionic and electronic wiring of the active material particle [15]*

This intercalation of lithium is initiated by the charge transfer reaction or charge incorporation reaction which involves the transfer of both charged species (electron and ion) from the outside into the interior of active particles [14]. The electrochemical reaction occurs and lithium is then intercalated on the surface of the active material particle. Two cases that define the charge transfer reactions are then possibly generated. The first case happens in the electrolyte. The loss of lithium ion near the active material surface decreases ion concentration at the locality and in turn creates a concentration gradient from the electrolyte bulk to the depleted locality. In the deepest parts of the electrode pore matrix, this depletion cannot be replenished fast enough therefore putting the reaction into a halt and decreasing overall capacity. This is better mitigated by decreasing the C-rate to a value where the electrolyte pores can replenish its concentration fast enough as the rate of insertion reaction occurs (typically low rates). The second case is tied with the electronic percolation as previously stated. If the electronic conducting network is inadequate to transport electrons to the AM surface, the redox reaction cannot occur which then contributes also to underutilization and eventually ceasing the reaction (Figure 2.6).

Finally the diffusion of the ion in the active material, particularly in the vacancies of the crystal lattice completes the electrochemical intercalation reaction. The most accepted mechanism of diffusion is that as the lithium ion is inserted at the surface of the particle, a concentration gradient is created from the surface to the center of the particle due to the vacancies. The lithium ion then diffuses to these vacancies up until all the sites are filled and the reaction can no longer proceed. If the diffusion to these vacant sites is not as fast as the rate of insertion on the surface, all vacant sites on the surface will eventually be filled and a decrease in cell voltage will follow and consequentially halt the electrochemical reaction and the capacity obtained will also be lower than that of the nominal capacity.

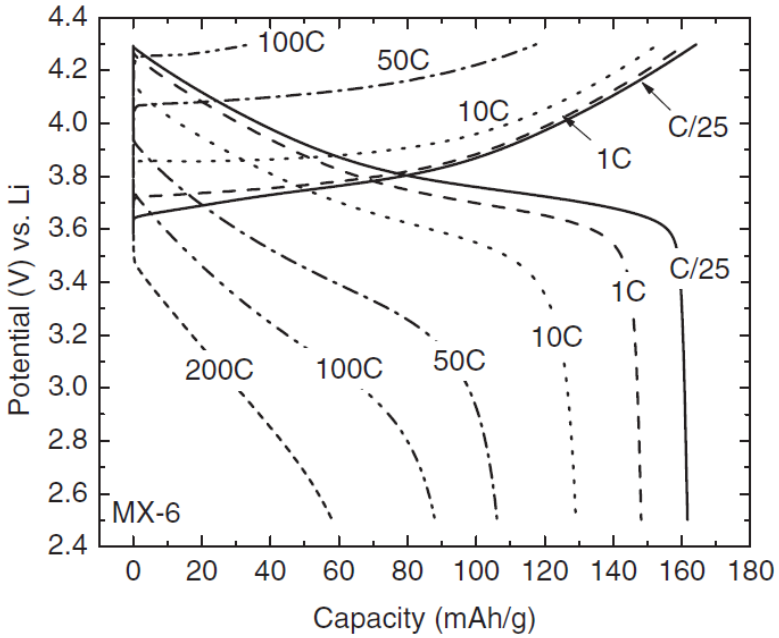

Figure 2.7:Experimental charge and discharge curves on thin NMC 333 electrodes at various rates. The thickness of the electrode is 11 µm, which corresponds to a monolayer of NMC clusters. The surface capacity 0.12 mAh/cm². The electrode composition is 71% NMC, 13% CB and 16% PVDF [18]

The problem of diffusion in the active material is tackled by the synthesis of new materials which have been shown capable of charging and discharging at high C-rates including the aforementioned NMC (Figure 2.8). For electronic tunneling and ionic diffusion, these are mostly affected by the formulation of the electrode. This includes many aspects starting from the preparation of the slurry itself, upto the calendaring step. More importantly, since ionic diffusion is limiting at high C-rates which is of interest for EV (electric vehicle) applications, pore architecture should be optimized to increase pore diffusion without sacrificing electronic conductivity. The interplay between the two and how electrode formulation affects the electrochemical performance of the electrode is further explained by the following literature review.

2.3) Influence of Electrode Formulation, Thickness and Density on Power Performance Limitations

2.3.1) Influence of Conductive Additives

We first tackle the subject of conducting additives. From a practical perspective, the additives should be homogenously distributed along the composite to ensure that most, if not all the active material will adequately receive electrons. Varzi et.al. attempted to use functionalized multiwalled carbon tubes to improve distribution of the additive in the electrode [19]. Carbon nanotubes were suggested to form a well conducting network if the fibers are well spread within the composite. Electrodes of NMC and LFP were fabricated from slurries containing functionalized and non-functionalized carbon nanotubes. Results showed that the electrodes with functionalized nanotubes had better dispersion within the electrode thanks to the carboxylic moiety but the electrodes with non-functionalized nanotubes showed better rate performance. Irreversible capacities and surface films were also seen in NMC + functionalized nanotube electrodes. They attributed this result to a chemical reaction between the highly nucleophilic character of the NCM's basic oxygens and the carboxylic moieties on the nanotubes surface

Another way to improve connectivity between the active material and the conductive additive is to exploit its surface area. Increased surface area was believed to assure surface availability and therefore a better conducting network. Su et.al. improved carbon black distribution and contact through increasing its surface area [20]. CBC (hard carbon black from Cabot^{TM}), has decreased particle size than standard carbon black but also exhibits a more crystalline surface. Better crystallinity improves electrochemical stability and decreases parasitic reactions with the electrolyte. SEM images showed better distribution of CBC resulting in better utilization of the carbon additive via improved electronic percolation (intraconnectivity) and better interconnectivity with the active mass. This also lead to better rate performances in well dispersed carbon electrodes. The improved conductivity was also linked with the observation of a saturation current reflecting the non-linear behavior of the conductivity. This saturation current was defined as the current threshold into which the resistance will start to increase drastically. Lower saturation currents were observed when the conductivity of the material is inadequate to hold the specified current. Electrodes of 1% carbon additive, one well dispersed and the other

inadequately dispersed, showed that the electrodes with inadequate dispersion of carbon had a lower saturation current than the well dispersed one (4.5 mA/cm^2 vs. $45mA/cm^2$). Interestingly, a significant capacity drop was observed when the charge/discharge current is increased above the saturation current. This work was conducted on 10 $mg.cm^{-2}$ electrodes.

Carbon fibers (CF) also sparked interest for use in battery composites. Like carbon nanotubes, they were also believed to create a well conducting network if they are well dispersed. Kang et.al. incorporated carbon nanofibers in their electrode formulations with NMC 622 [21]. The studied electrodes were adjusted upto ≈60% porosity, which is high compared to the state of the art. Improvements in rate capability were seen for electrodes containing CF. Impedance measurements showed that carbon fiber electrodes exhibited lower charge transfer resistances thanks to the conductive network created by the well dispersed CFs. The same observations were seen with Du et.al. but with electrodes prepared from an aqueous route and NMC 532 as the active material [22]. It was suggested that better dispersion can be achieved using a binder that can be well dispersed in solvent (carboxylmethyl cellulose (CMC + water). This was supported by SEM images showing adhesion of CF on the surface of the NMC particle (Figure 2.8). Both studies also observed lower polarizations in carbon fiber containing electrodes.

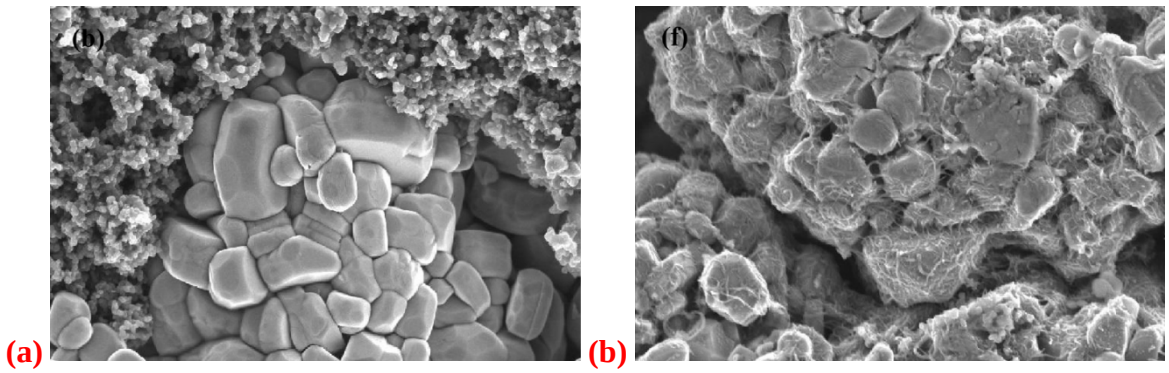

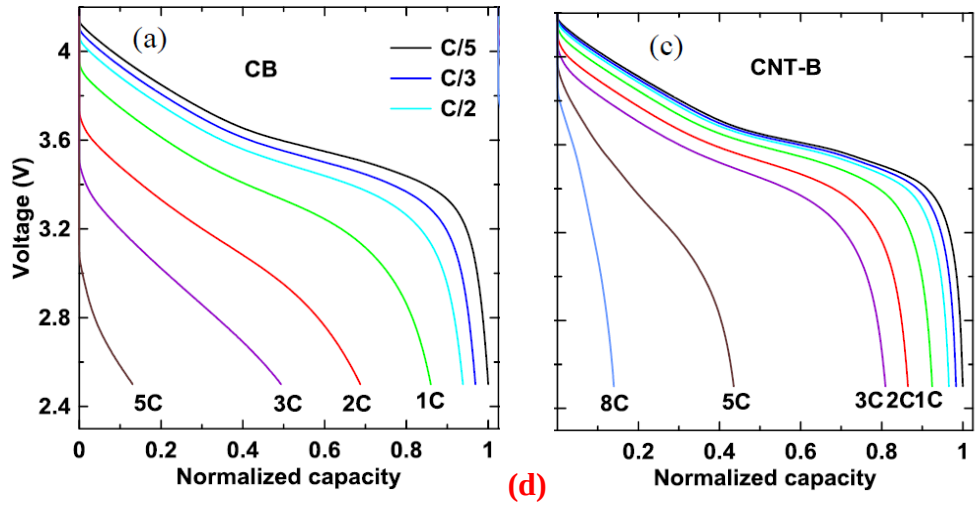

Figure 2.8: SEM images (a,b) and cell discharge voltage (c,d) of CB- (a,c) and CNT-based (b,d) NMC 532 electrodes [22].

The aforementioned studies discussed on how different types of carbon and how homogenous distribution affect electrochemical performance. Morelly et.al. also stressed the importance of the formulation aspect in making sure that the carbon additive is well utilized in creating a well ramified conductive network [23]. The study concentrated on how to assign a certain partition of "free carbon" (assigned as factor *f*) in the electrode composite. This was done via a premixing step wherein NMC 333 and a partition of CB (carbon black) were dried mixed separately before adding into the final slurry with all the other components and the rest of the remaining "free" CB. The slurries were characterized using rheology and the highest moduli were observed for slurries having a lot of free carbon, meaning that the free CB is responsible for the formation of a percolated 3D network. In other words, electrodes with a large fraction of free carbon have volume spanning networks of CB, while electrodes with a low fraction of free carbon have CB agglomerates connecting NMC particles. Electrodes with more free carbon also exhibited better conductivity than those with less free carbon. Rate performance evaluation showed that low free carbon ratio (f=0 and f=0.25 at 2.5wt% CB) had better rate performance than those of higher free carbon ratio. Changing electrode porosities also confirmed that the performance was not limited by ionic transport in the cases at hand. This meant that the performance was due to the fraction of "bound" carbon which makes up the "short-range contact" between the electrode components. The active mass loading of these electrodes was not given, but one may think that this one is low (typically a few to 10 $mg.cm^{-2}$) as the doctor blade gap used to coat the slurries onto the aluminum collector is low (100 µm).

All these works highlight the significant influence of the size, the shape and the distribution of the additive C on the transport of the electrons over long distances and on the distribution on shorter distances of these electrons to the AM clusters.

2.3.2) Influence of the Binder Type

Binder choice also affects the electrochemical performance of the electrode. Commercial electrodes presently use polyvinyledene fluoride (PVdF) as a binder for its well-established performance and stability. The preparation of electrodes with PVdF demands the use of N-methyl-pyrrolidone as its solvent which is both toxic and expensive. Carboxymethyl cellulose was proposed as a binder substitute due to its ease of preparation (water-based) and cost. Xu et al. compared the performance of NMC 333 electrodes with sodium carboxylmethyl cellulose (CMC), poly(vinylidene fluoride) (PVDF), and alginate as binder. The electrodes contained 5wt% of binder, 10 wt% of CB and had a loading of 6 mg/cm^2. The NMC electrode using CMC as binder had the highest rate capability, followed by those using alginate and PVDF binders, respectively. Electrochemical impedance spectroscopy test results showed that the electrode using CMC as the binder had lower charge transfer resistance and lower apparent activation energy than the electrodes using alginate and PVDF as the binders. However, the origin of such better kinetics (lower charge transfer resistance) was not elucidated [24]. For NMC 532, immersing the AM powder in water leads to both structural modification of the particles surface and the formation of lithium-based compounds over the surface (LiOH, Li_2CO_3). These surface compounds adversely affect the electrochemical performance and are notably responsible for the alkaline pH of the aqueous slurry, which causes corrosion of the aluminum collector during coating of the electrode [25].

2.3.3) Influence of the Ratio of the Components, the Porosity and the Thickness

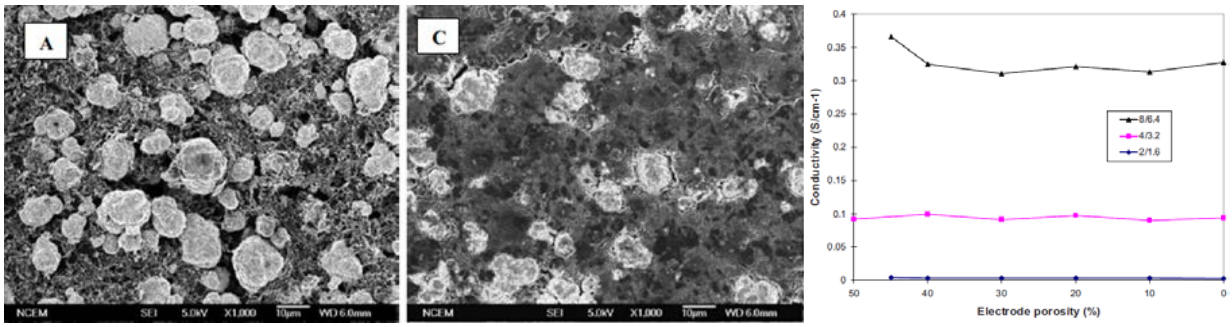

Figure 2.9: SEM images of the surface of the electrodes containing 8% PVDF and 6.4% acetylene black (AB) at different porosities, freestanding (50%), and nearly 0%. Electronic conductivities of the NCM electrode containing different levels of PVDF/AB inactive materials and at different porosities. These measurements were taken on films, initially cast on aluminum foil, gently removed from the aluminum, and then placed on a nonconducting glass substrate. [26]

The ratio of the components and the porosity of the electrode were also studied by Zheng et.al [26]. Electrodes of NMC 333 with varying additive content (the weight ratio of PVdF to CB was held constant at 5:4) and calendering were used here (with a loading of 30 mg/cm^2). It was observed that the electronic conductivity of the electrodes was highly dependent on the content of the additives and is weakly associated with the porosity (Figure 2.9). For electrodes with 3.2% or less of acetylene black, the best rate performances were observed at porosities at around 20% or less. Electrodes with higher carbon black content had better rate performances at higher porosities (Figure 2.10).

The observed trends suggested that there could be certain limitations at play depending on the relationship between materials ratio and the calendering of the electrode. The results from electrochemical impedance spectroscopy (EIS) showed different Nyquist plot behaviors between low carbon electrodes and high carbon electrodes at varying porosities. The three semicircles (Figure 2.11a) were assigned with three different resistances as suggested by their applied model namely: R_e (electronic particle-to-particle contact resistance), R_{CT} (Resistance of charge transfer), and R_d (diffusion within the active material or the electrolyte solution). The electrodes with lower carbon content tended to have higher R_e at increasing porosities (Figure 2.11b) and higher carbon electrodes tended to have higher R_{CT} and R_e at decreasing porosities (Figure 2.11c). This meant that increased calendaring compensates for the lack of particle interconnectivity within less carbon containing electrodes. In the case of the electrodes

containing higher amounts of carbon, the additives somehow act as hindrances along the porosity which somehow blocks ionic access on the surface on the active material. When combined with low porosities, these additives further close the ionic pathways therefore increasing charge transfer resistance. This is further supported by SEM images (Figure 2.9) which show how PVdF blocks the porosity at further electrode compression. Interestingly, the observed capacities between low and high carbon containing electrodes showed nearly the same values at their optimum (≈7mAh). With respect to the meaning of this result, one may however note that the power performance of these electrodes are modest compared to other studies (see later for example the work by N. Besnard) and thus maybe not fully representative.

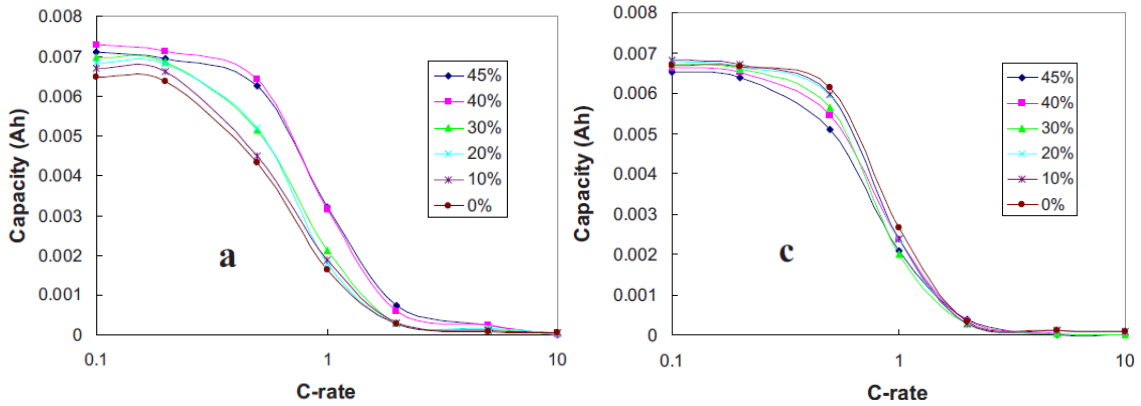

Figure 2.10: Rate capability of the NCM electrode as a function of the porosity with different amounts of inactive materials. PVDF and AB are (a) 8 and 6.4%, and (c) 2 and 1.6%, respectively. [26]

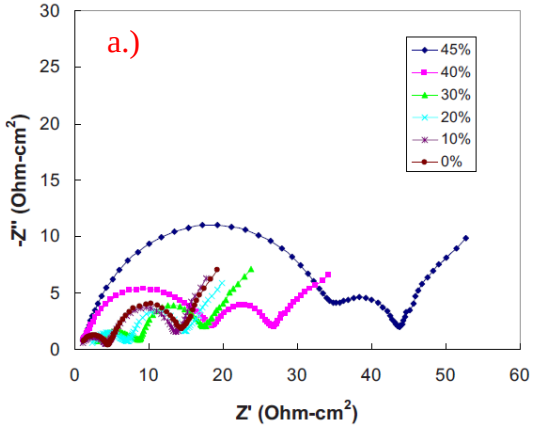

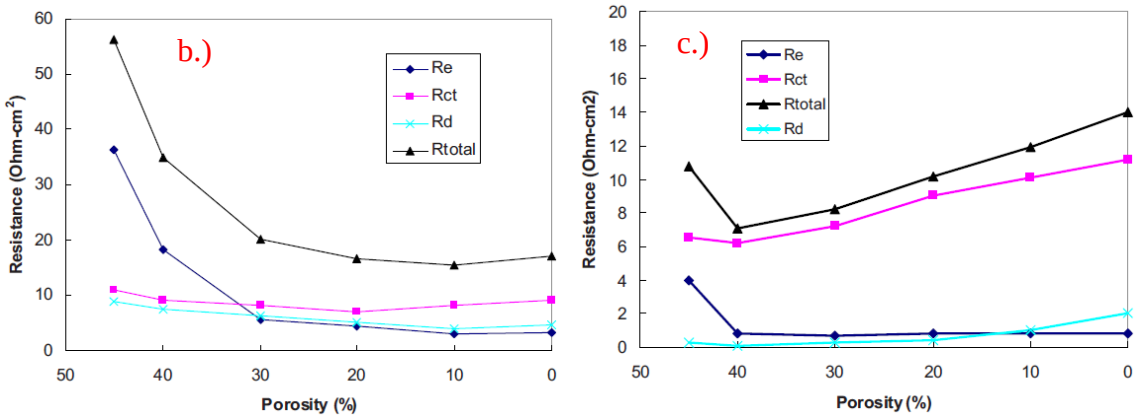

Figure 2.11: (a) Nyquist plots of the NMC 333 electrode of different porosities containing 2% PVDF and 1.6% carbon at 4.2 V after 10 formation cycles. (b) and (c) Variations in different EIS resistances of NCM electrodes containing 2% PVDF and 1.6% AB, and 8% PVDF and 6.4% AB, respectively, with electrode porosities. [26]

The effect of thickness on the electrochemical performance was also studied by the same group (Figure 2.12) [27]. They tested different electrodes of different thicknesses composed of LFP and NMC 333 as active material. Rate performances of the electrodes showed that all electrodes could deliver the same nominal capacities at a very low C-rate but at higher C-rates, thicker electrodes delivered lesser capacities than thinner ones. Up to a certain critical C rate, the descent of the discharge curve at increasing C rate is due to polarization induced by the internal resistance of the cell. When the discharge rate exceeds this certain critical value, a more brutal discharge capacity loss of the electrode is observed, which was mainly attributed by the Li ion diffusion into the electrode. As shown in Figure 2.12c, each capacity vs. discharge rate curve has an elbow. The point of inflection of the elbow occurs approximately at 70–80% of its full capacity. The discharge rate at the point of inflection, referred to as maximum working C rate (also called C* in other work and this manuscript), can be used to represent the curve and characterize the rate performance of the electrode. A power-law relation between the maximum working C rate and electrode loading is obtained, which independency with the active material kind (NMC or LFP) confirms that this maximum working rate is intrinsic to the active matter (Figure 2.12d).

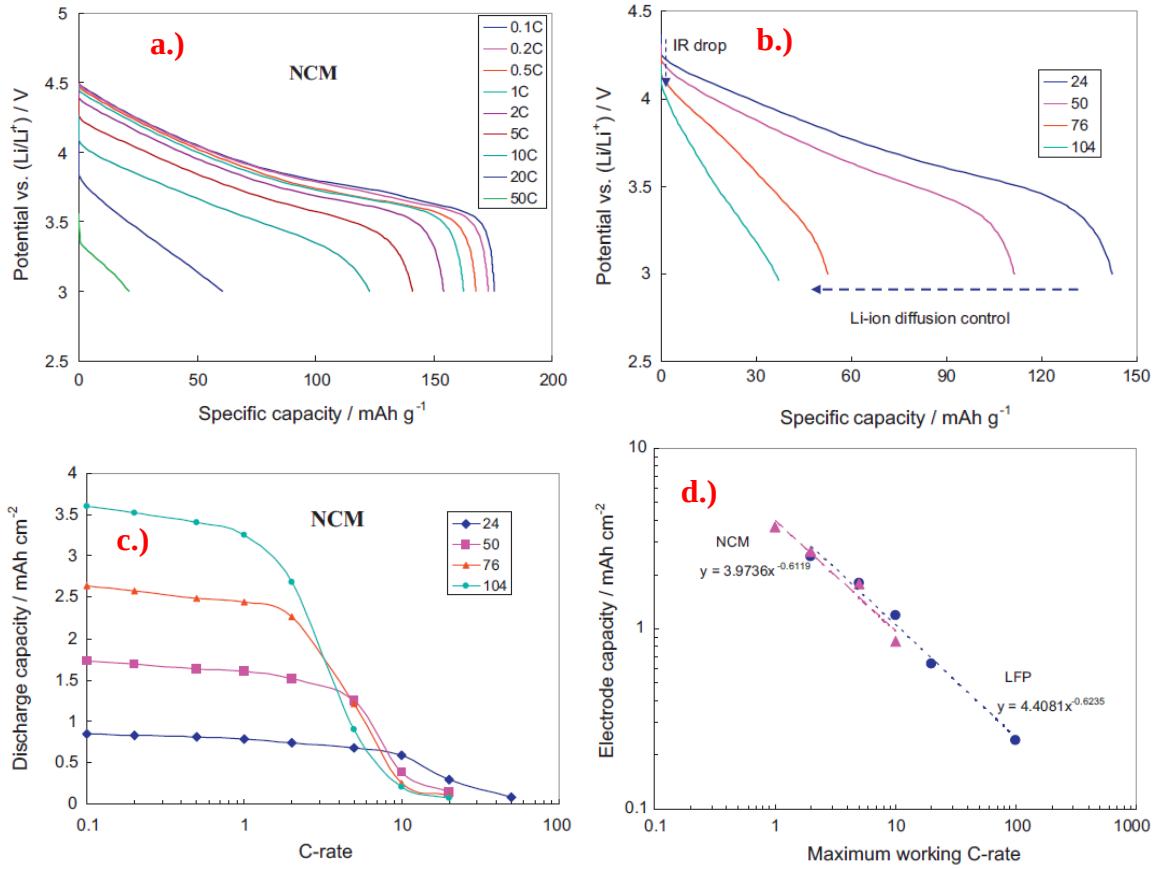

Figure 2.12: (a) Discharge profiles of the NCM electrodes at thickness of around 25 µm (exclusive of Al foil). (b) Comparison of discharge profiles for the NCM electrode for different thickness (in µm) at the same current density of 5C. (c) Discharge areal capacity as a function of C rate for the NCM electrodes at different thicknesses (in µm). (d) Log–log plots between the electrode areal capacity and the maximum working C rate for the NCM and LFP cathodes. [27]

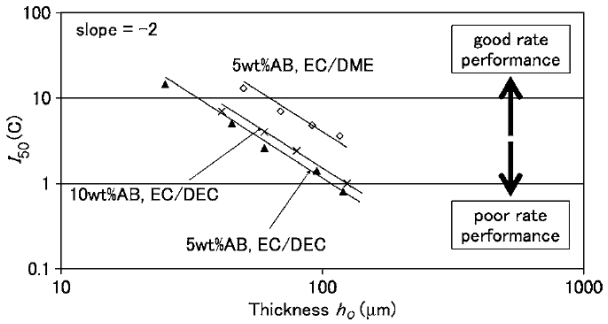

Figure 2.13: Dependence of the characteristic discharge rate (I50) on film thickness with different electrode configurations and electrolyte for LFP. [28]

An earlier work on LFP-based composite electrodes also observed such a behavior [28]. Indeed, a power law was found between the characteristic discharge rate (I50 = 50% of the maximum capacity) and electrodes thickness, h_0 (Figure 2.13). The data points show a linear dependence with a slope of −2. This indicates that $h_o^2 I_{50}$=constant, which is typical for a diffusion-related

system, in this case the movement of Li through the electrode, from dimensional analysis. Electrodes were tested with 1 M $LiPF_6$ in EC/DME that has a lower viscosity and higher ionic conductivity than EC/DEC solution. A large improvement in capacity is observed with EC/DME, confirming this interpretation.

Knowing that cycling at high rates is highly affected by electrode morphology (thickness, porosity, etc.) and their effects to lithium ion diffusion, probing how geometry of the porous matrix will be crucial in understanding how it facilitates or hampers ion transport to the active material. X-ray tomography was one of the techniques used by Ebner et.al. to generate useful images for the geometric evaluation of the pore matrix [29]. Kitada et.al characterized thick electrode reactivity by using in-situ energy-scanning confocal XRD to monitor the lithium concentration in the active material particles in the difference regions of the electrode [30]. This was done via the use of a calibration curve correlating the d-spacing of the NMC lattice with the degree of insertion of Li. Four sections were designated from top to bottom (positions a to d) and were studied individually during cycling (Figure 2.14). Cycling at low C-rates showed that the four areas exhibited the same lithiation behavior. At higher C-rates, especially during the initial cycle, the degree of lithiation was not homogenous from top to bottom ($x_a = 0.87$, $x_b = 0.81$, $x_c = 0.72$ and $x_d = 0.60$). The degree of lithiation between the electrode sections did not converge up until 30 mins. of resting suggesting that the ion diffusion in the pores of the electrode takes time before the local reservoirs are replenished for the reaction to proceed further, which leads to active material underutilization. This is further supported by the electrochemical performances at varying porosities wherein lower capacities were attained when the electrode porosity was at ≈18% which diminishes ion access to the deeper parts of the electrode.

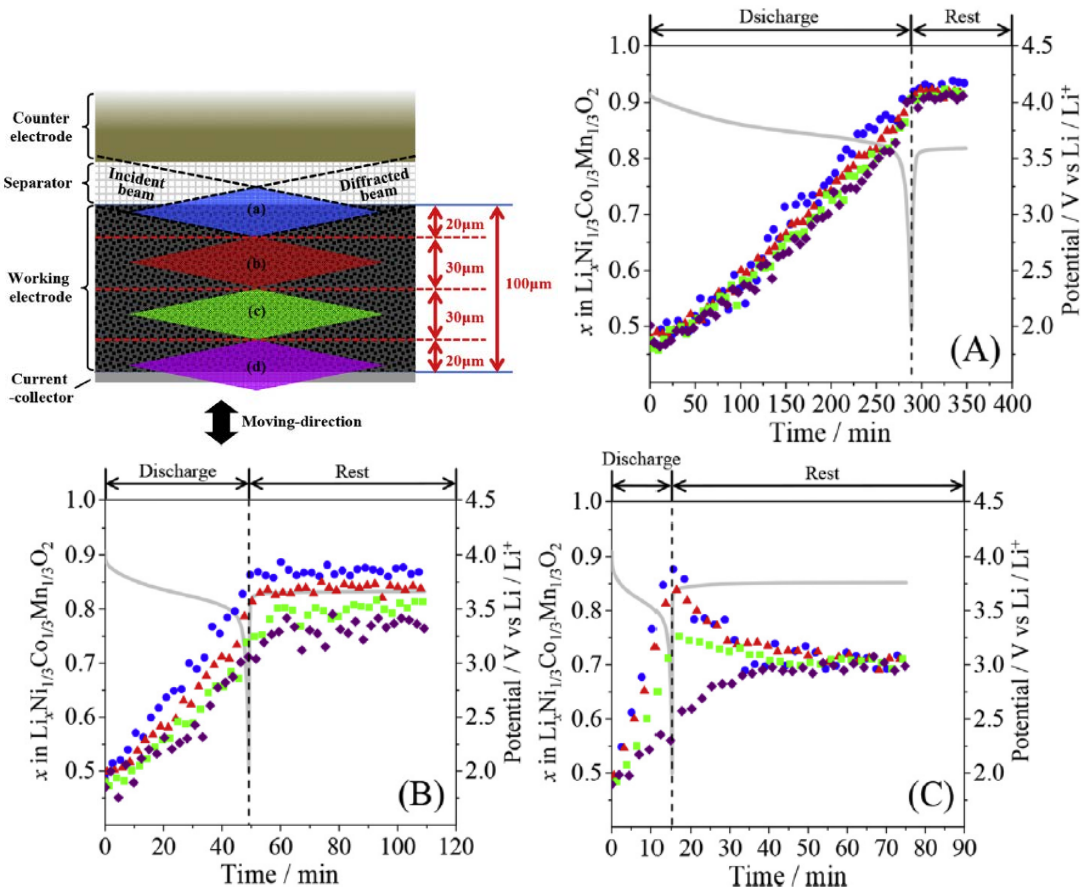

Figure 2.14: *Illustration of the confocal point, between the incident and diffracted beams, in the cross-section imaging generated by X-ray diffraction. Li^+ concentration of NCM in cells fabricated using 18% porosity electrodes and 1 M $LiPF_6$ in EC/EMC (3/7), where the cells were discharged at rates of (A) 0.1C, (B) 0.5C and (C) 1C. The symbols ●, ▲, ■ and ◆ correspond to positions (a), (b), (c) and (d), respectively, in the cross-section of the electrode. The gray plots correspond to the change in cell potential. The broken lines show the end of the cell discharge. [**Erreur ! Signet non défini.**]*

The interplay between the active material particles size and the design of the electrode formulation was studied by Besnard et.al. This group studied blends of NMC, LFP, CB and PVdF with varying electrode parameters. The electrode blends exhibited hybrid properties from both NMC based electrodes and LFP based electrodes [31]. NMC and LFP are two different cathode materials that generate two separate types of interconnectivity environments. NMC typically has larger particle size than LFP and therefore has less surface area. This gives NMC a significant advantage for particle interconnectivity which is supported by how NMC needs minimal CB to have it electronically percolated. On the contrary, LFP's higher surface area requires a larger amount of conductive additive to attain percolation hence it needed additional calendering and increased carbon black content to ensure electronic conductivity. In the case of

ionic conductivity, the particle size and surface area of LFP have the advantage due to that the resulting tortuosity of the electrode is way less than NMC based electrodes. This restriction to lithium diffusion across the electrode porosity was evaluated by quantifying the tortuosity of the porosity at the macro and the local scales, by X-Ray and FIB/SEM tomographies. 2D maps of the tortuosity factors at the electrode and local scales are shown in Figure 2.15. They were determined by calculating the length of trajectories starting from planes located near to the separator and oriented toward the current collector. These tortuosity factors were converted into Bruggeman coefficients to better compare the different microstructures (The Bruggeman law is reminded in a following section). The higher Bruggeman coefficients for NMC-based electrodes (= 1.54) indicated that the large NMC particles significantly elongate the diffusion distance than the small LFP particles (= 1.20). Furthermore, the addition of more CB-PVdF blocked both the NMC surfaces and the porous matrix of the electrode which hampered ionic diffusion. Interestingly, LFP electrodes did not perform well until additional calendering which was an indication of the difficulty of successfully percolating the LFP particles.

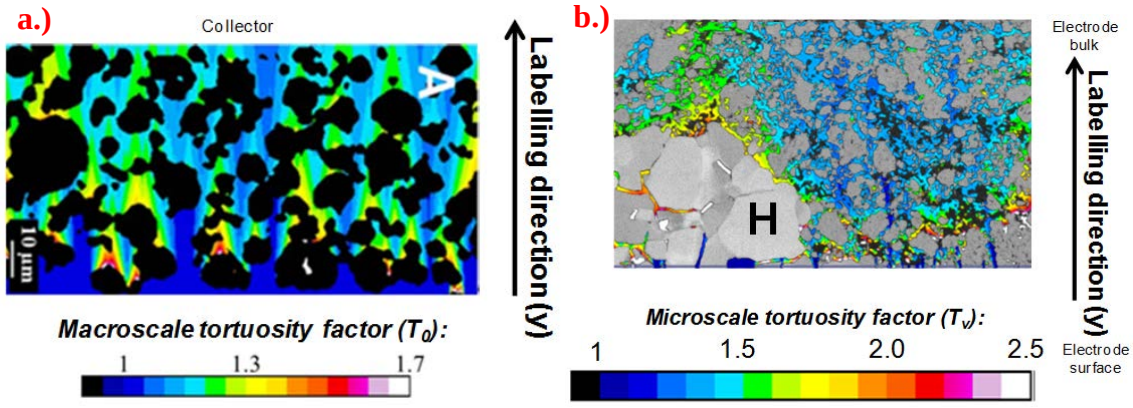

Figure 2.15: 2D maps for the tortuosity factor, at the different scales. (a) The first map shows the elongation of the macroscopic diffusion distance imposed by the presence of the NMC particles (in black) compared to the length of the thickness of the electrode. The second map shows the elongation of the diffusion distance imposed by the presence of LFP nanoparticles (in grey) and the CB + PVdF mixture (in black). [31]

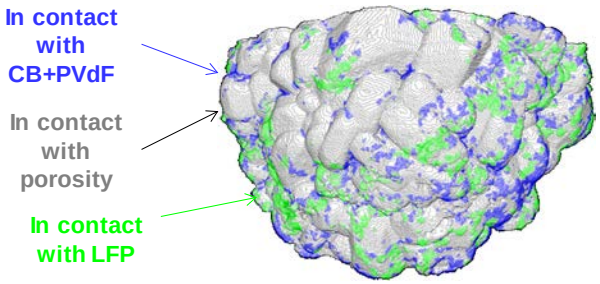

Figure 2.16: 3D FIB-SEM reconstructed views of the NMC particles with the NMC surface area in contact with LFP (green zone), CB + PVdF mixture (blue zone) and porosity (gray zone) for a blended NMC/LFP electrode with 3 wt% of CB. [31]

In an attempt to combine the advantages of NMC and LFP, the group turned to blend formulations which were electrodes comprised of both NMC and LFP as active materials and were mixed with both CB and PVdF. The electrodes had varying porosities, densities as well as ratios of electrode components. Electronic conductivity measurements showed that the blends have conductivities that are in between NMC and LFP values. Tomographic data also showed that the tortuosities were also in between pure NMC and pure LFP based electrodes. Contact surface area values for the blend electrode having 3% CB-PVdF content showed that while LFP is adequately electronically percolated in the electrode, at the same time NMC has not enough interconnectivity with the conductive additive. This was remedied by further addition of CB and densification which resulted in better performances.

The maximum working rate or critical regime C* was defined by relating a certain coefficient k(h) (capacity loss coefficient) with I (specific current) (Figure 2.17a). This was then correlated with the temperature to determine energies of activation (Figure 2.17b). Two coefficient sets namely k_1 and k_2 were taken from two regions: before C* and after C* respectively. The energies of activation from these two regions were different from each other wherein Ea_1 has values similar to that of the charge transfer process while Ea_2 has values similar to that of the diffusion process in the electrolyte. It was also seen that k_1 is independent of loading contrarily to k_2 (Figure 2.17c). From this, it could be concluded that the discharge capacity is mainly governed by the local scale of the electrode microstructure below the critical regime C* (and eventually, charge transfer). Above C*, the discharge capacity is mainly governed by the limitations opposed to lithium diffusion across the total electrode thickness by the pore tortuosity.

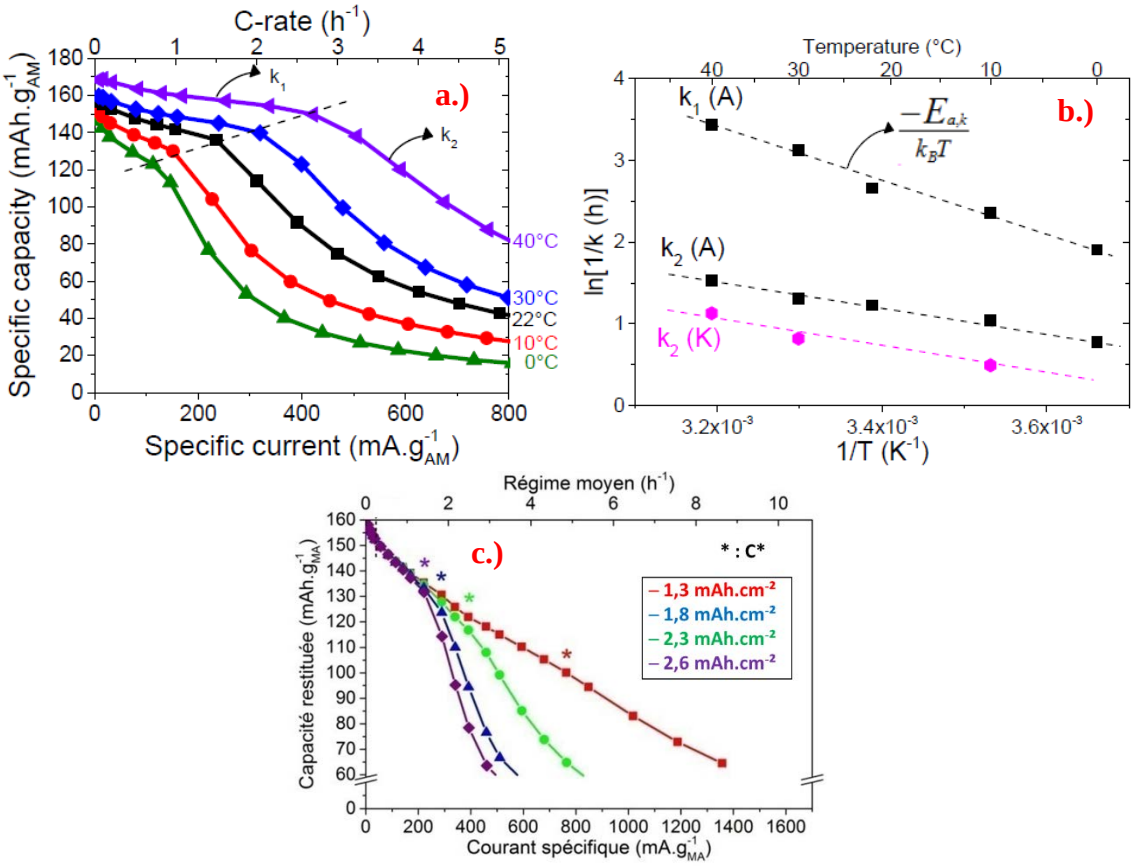

Figure 2.17: (a) Discharge capacity as a function of the C-rate for an NMC electrode of 2.6 mAh/cm² at different temperatures. (b) Temperature dependence of k1 and k2 for an NMC electrode (A), and of k2 for an LFP electrode (K). (c) Discharge capacity as a function of the C-rate at room temperature for NMC electrodes of various surface capacities. [31]

Heubner et al. focused on NMC 622 based electrodes to better demonstrate thickness effects on electrochemical performance [32]. The electrodes parameters are given in Table 2.1. Their group studied the impedance signatures of their electrodes via electrochemical impedance spectroscopy and the respective spectra are shown in Figure 2.18. The semicircles from high to low frequencies were assigned as respectively: 1.) particle contact and current collector contact resistance, 2.) charge transfer resistance, 3.) diffusion in the AM particle/electrolyte solution. Thicker electrodes were observed to have increased diffusion impedance and charge transfer resistance (Figure 2.18c). Densifying the electrode increased charge transfer resistance and diffusion resistance. This is due to that densifying the electrode increases contact points but also increases ion path tortuosity, and decreased exposure of the AM surface to the electrolyte (Figure 2.19).

Table 2.1: Electrode properties used in Heubner's work

Sample	m_{areal} [mg cm^{-2}]	Thickness L [µm]	Porosity ε [%]	Q_{areal} [mAh cm^{-2}]
S1	30.1	129	43	4.72
S2	32.9	126	36	5.17
S3	35.2	128	33	5.5
S4	39.1	172	45	6.07
S5	42.6	163	36	6.69
S6	45.2	166	34	7.03
S7	49.5	210	43	7.68
S8	54.8	215	38	8.55
S9	57.0	212	34	8.98

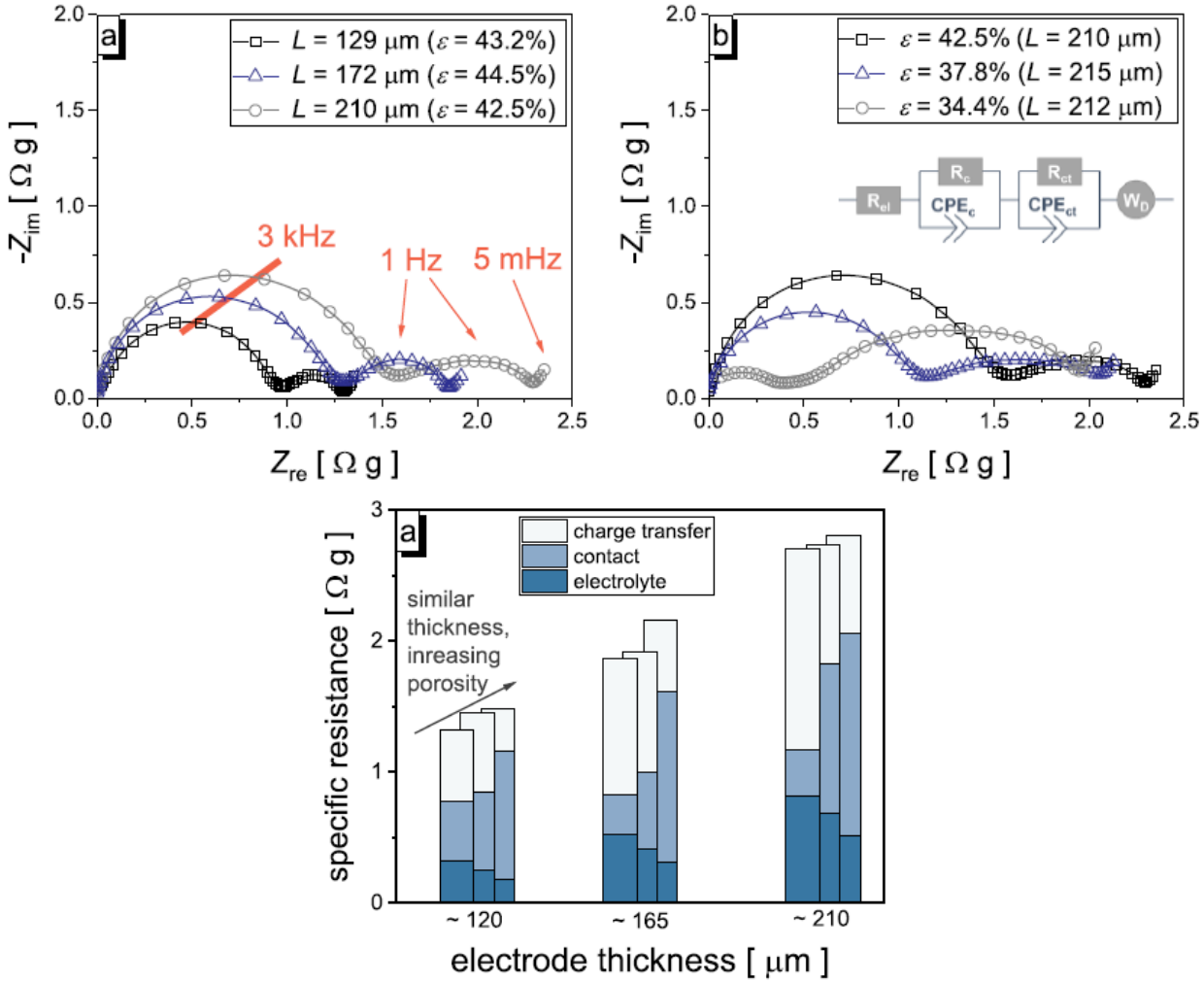

Figure 2.18: (a) Nyquist plots obtained for electrodes with varying a) thickness and b) porosity. a) additionally indicates typical frequencies of the occurring processes and (b) includes the equivalent circuit used to fit the measured impedance spectra. 3-electrode setup using T-type Swagelok® cells. Metallic lithium acted as the reference and counter electrodes. [32] Specific resistances obtained from fitting the impedance data to the equivalent circuit model. [32]

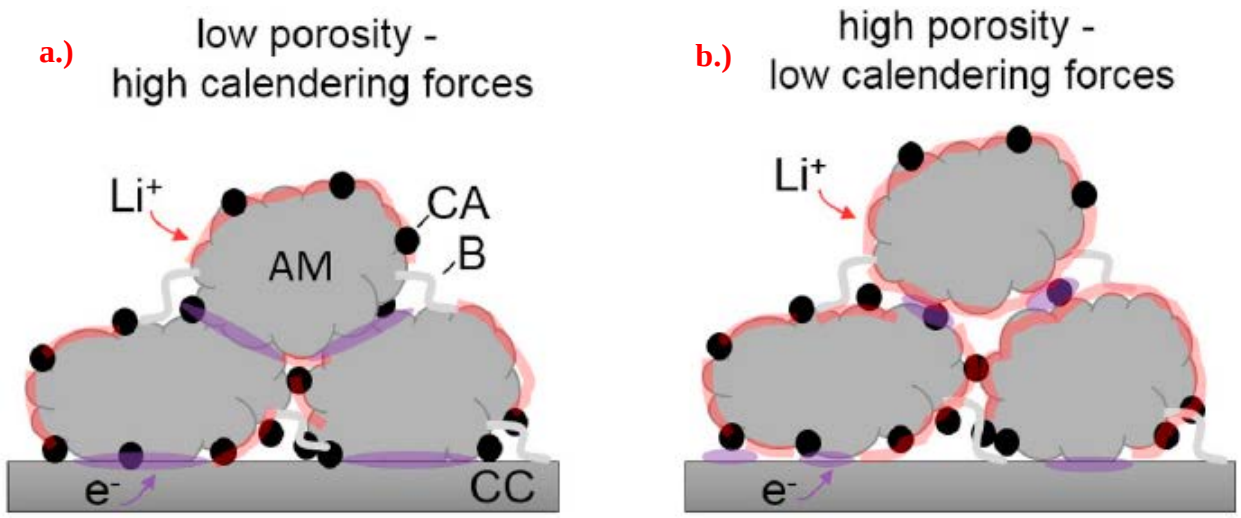

Figure 2.19: Schematic illustration of ionic and electronic pathways for high (left) and low (right) compression forces during calendering (AM: active material, CA: conductive additive, B: binder, CC: current collector). [32]

Rate capability tests show that capacities at low C-rates are unaffected by thickness and porosity variations. This supports the idea that performances at low C-rates are mostly governed by charge transfer and/or electronic conductivity. While at high C-rates capacities are detrimentally affected by an increase of the thickness and a decrease of the porosity (Figure 2.20).

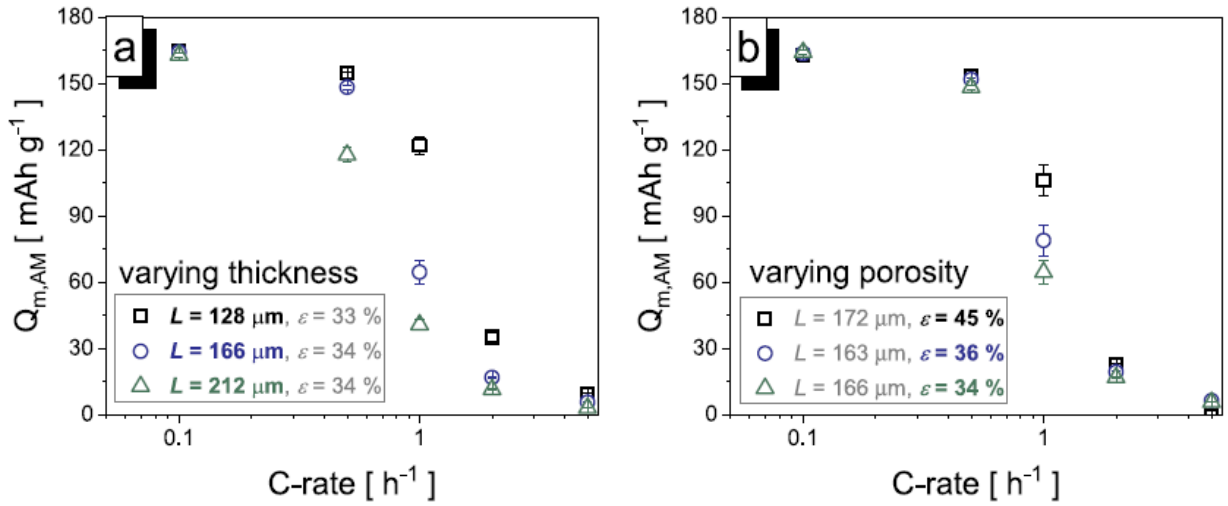

Figure 2.20: Results of rate capability tests of NCM-622 electrodes with different (a) thickness and (b) porosity. [32]

Thickness effects are not only limited to positive but also with negative electrodes. Full cells assembled from graphite and NMC 532, NMC 622 and NMC 811 were cycled at high C-rates by Mao et.al. [33]. Full cells typically involve negative electrode "overhang" which is additional negative electrode mass to avoid lithium plating phenomenon. In general, the mass ratio of negative vs. positive electrodes in full cells is 1.2 : 1 respectively. This is done by either increasing the electrode area of the negative side and or increasing the negative electrode mass loading (meaning thicker or denser electrode). Charge and discharge capacities for the full pouch cell at high rates, particularly at 6C showed minimal capacity retention/delivery which is expected due to diffusion limitations (Figure 2.21). Cycling both NMC half cells and graphite half cells and comparing them to the full cell showed that the graphite electrode suffered more capacity drop during lithiation especially at high rates than NMC. This was further highlighted by the rate performances of the symmetrical cells. Symmetrical cells of graphite showed worse rate performance than NMC at a rate of 6C. The poor performance was related to the poor ability of the lithium ions to successfully diffuse in the pore matrix of graphite which was due to its thickness and higher tortuosity. This results into facilitated lithium plating on the surface of the negative electrode as observed in post mortem analyses.

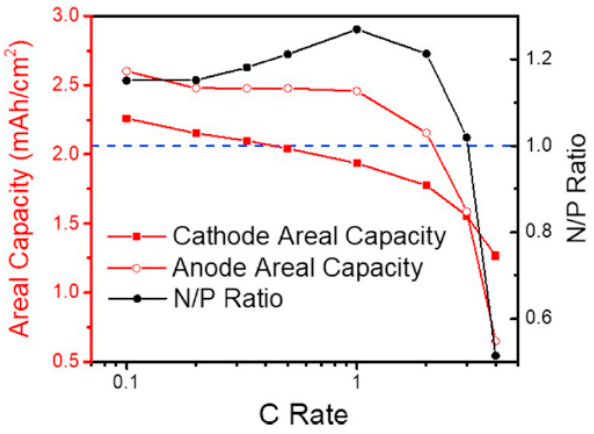

Figure 2.21: Areal capacity of the NMC 811 cathode and graphite anode at each rate and the resulting Negative to Positive electrodes capacity N/P ratio. [33]

2.3.4) Influence of the Electrode Slurry Processing

Finally, from a macroscopic point of view, the casting formulation also plays a role in electrochemical performance. The entire geometry of the film composite can also have a significant effect on the performance. Mohanty et.al. studied various electrode defects such as

particle agglomerates, metal impurities, pinholes and film non-uniformity in their electrodes [34]. In general, the presence of these defects had a detrimental effect on capacity delivery (agglomerates and pinholes), electrochemical stability (metal impurities), and long term cyclability (trenching/non-uniformity). All of the abovementioned observations and studies clearly defines the role of electrode engineering in allowing any electrochemically active material to perform optimally.

2.4) Analytical Modelling of Power Performance Limitations

Most of these studies found in literature correlate qualitatively how electrode parameters dictate electrochemical performance. Quantitative analysis is crucial from an engineering and design point of view not only to improve electrochemical performance but to also reduce cost in the development of such optimal designs. Modeling has been used in both science and engineering to help qualitatively assess phenomena and battery technology is not alien to such approaches which will be presented in the next section.

Modeling has been also used to describe electrode architecture effects on their electrochemical performance. In the field of materials that deal with pore matrices, the quantitative evaluation of pores is mostly done mathematically in conjunction with statistical analyses to accurately describe pore distribution, pore size etc. In the battery field, this is better aided by tomography as mentioned in the previous section.

Thickness effects for electrode composites have been such an extensive parameter due to that the tortuosity in the pore matrix becomes more complicated as the electrode thickness increases. Danner et.al. tried to decipher these effects using modeling [35]. They used a 3D micro-structure resolved model of a NMC-graphite Li-ion battery parametrized with data from the literature and dedicated experiments on thin electrodes to estimate the transport properties. The model simulated lithium ion concentration maps throughout the anode, separator and cathode during charge and discharge identifying mass transport limitations. For NMC lithiation, results showed that increasing the electrode thickness decreased the concentration of lithium ions deep in the electrode pore matrix particularly near the current collector. In the case of graphite delithiation,

the difficulty of the ions getting out of the graphite pore matrix created areas of depletion near the separator-positive electrode interface. Both phenomena lead to an increase in cell potential ending the electrochemical process. This can be further amplified by the distribution of the carbon additive in the composite showing that local inhomogeneity has a significant impact in the underutilization of the active material which further decreased the maximum practical capacity.

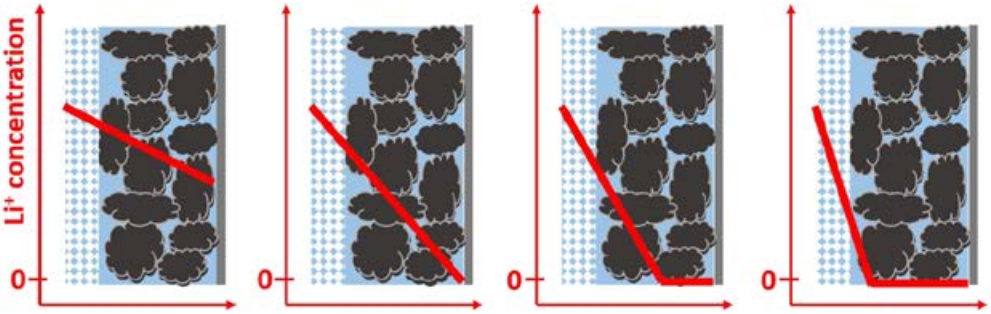

Figure 2.22: Illustration of Li-ion diffusion limitations in the electrolyte during discharging of the cell. The Li-ion concentration in the electrolyte decreases inside the porous cathode. A concentration gradient forms throughout the cell, depending on the applied current and the effective transport properties of the porous structures. Enhancing the current from the left to the right increases the concentration gradient. For a particular current, the Li-ion concentration close to the cathode current collector decreases to zero. [32]

To describe ion depletion in the pore locality, a mathematical expression was formed by Gallagher et. al. to relate electrode thickness, porosity, tortuosity and electrochemical performance based on concentrated solution theory (neglecting convection and changes in solvent concentration) [36]. As illustrated in Figure 2.22, concentration gradients form within the electrodes of the cell as current is passed in a single direction (i.e. charge or discharge). As a result of the salt depletion near the current collector electrode boundary the current distribution within the electrode may shift. The penetration depth for electrolyte transport in the electrode, L_d, at the steady-state is expressed as

$$L_d = \frac{\epsilon}{T}\frac{D_0 C_0 F}{(1-t_+)I} \qquad \text{(eq. 2.1)}$$

where ε is the electrode porosity, T is the tortuosity factor, D_0 is the salt diffusion coefficient in electrolyte, C_0 is the electrolyte salt concentration, t_+ is the cation transference number and I is the current density. For cases where solid state diffusion of lithium in the active material is not limiting, the electrolyte transport in the electrode is limiting the capacity if the penetration depth

is less than the electrode thickness. We used a derivation of the Gallagher's expression to fit our electrochemical data. This will be developed into more details in the experimental section.

Another interesting approach was done by Heubner et.al. through semi-empirical modeling [37]. The model involves a time constant which is correlated with the rate limiting process. In general, two rate limiting process that involve relaxation can be described by this time constant which are lithium ion diffusion in the active material and the diffusion of the lithium ion in the porous matrix of the electrode. The practical capacity can be related with the relaxation time constant and stated as follows:

$$Q(t) = Q_0 - Q_0 exp\left[-\left(\frac{t}{\lambda}\right)^{\beta}\right] \qquad \textit{(eq. 2.2)}$$

where λ is the characteristic time constant of the rate limiting process and t is the discharge time. β is an empirical value to stretch the exponential function. This exponent would capture some kind of cooperative interactions leading to delayed ($\beta < 1$) or accelerated ($\beta > 1$) non-exponential relaxation, or traduce a distribution of relaxation times (the non-exponential relaxation being then a superposition of exponentially relaxing processes). For $t \gg \lambda$, the second term on the right hand side tends to zero and the capacity is close to the nominal capacity. For $t \ll \lambda$, the relaxation of the system is not sufficient and the capacity is significantly smaller compared to the nominal capacity. The time constants that will be taken from this equation will be then comparted to two other time constants namely λ_s and λ_E. The time constants of lithium diffusion in the solid intercalation host is stated as

$$\lambda_S = \frac{L_S^2}{D_S} \qquad \textit{(eq. 2.3)}$$

where the radius of the particles is assumed to be equal to the characteristic diffusion length, L_S, and D_S is the lithium diffusion coefficient in the solid intercalation host. The time constants of lithium diffusion in the liquid electrolyte is stated as

$$\lambda_E = \frac{L_E^2}{\epsilon^{\alpha} D_{el}} \qquad \textit{(eq. 2.4)}$$

where L_E is the electrode thickness, D_{el} is the lithium diffusion coefficient in the electrolyte, ε is the porosity of the electrode (volume fraction of the electrolyte) and α is the Bruggeman coefficient. The Bruggeman coefficient is a coefficient that helps describe tortuosity in porous media, as described in the following section. The rate limiting step is then determined by comparing which value of τ_s and τ_E is closest to τ. Electrochemical cycling was done with various electrodes of various active materials which include but are not limited to NMC, LFP, and LTO with varying electrode specifications (porosity, thickness, AM particle size etc.). Most of the electrodes, especially the thick ones exhibited matching τ and τ_E showing that the diffusion within the pores is the limiting step. The contrary is observed for LCO and LTO electrodes (Figure 2.23).

Sample	Active material	Particle size $L_{s,50}$ [µm]	Electrode thickness L_e [µm]	Porosity ε [%]
LTO-G1	$Li_4Ti_5O_{12}$	1.1	28	28
LTO-G2	$Li_4Ti_5O_{12}$	1.1	67	28
LTO-G3	$Li_4Ti_5O_{12}$	1.1	100	26
LTO-G4	$Li_4Ti_5O_{12}$	1.1	145	28
LTO-H1	$Li_4Ti_5O_{12}$	0.7	29	30
LTO-H2	$Li_4Ti_5O_{12}$	0.7	76	31
LTO-H3	$Li_4Ti_5O_{12}$	0.7	117	31
LTO-H4	$Li_4Ti_5O_{12}$	0.7	149	31
NCM-1	$LiNi_{1/3}Co_{1/3}Mn_{1/3}O_2$	0.8	119	39
NCM-2	$LiNi_{1/3}Co_{1/3}Mn_{1/3}O_2$	0.8	120	33
NCM-3	$LiNi_{1/3}Co_{1/3}Mn_{1/3}O_2$	0.8	129	32
NCM-4	$LiNi_{1/3}Co_{1/3}Mn_{1/3}O_2$	0.8	164	41
NCM-5	$LiNi_{1/3}Co_{1/3}Mn_{1/3}O_2$	0.8	163	35
NCM-6	$LiNi_{1/3}Co_{1/3}Mn_{1/3}O_2$	0.8	166	29
NCM-7	$LiNi_{1/3}Co_{1/3}Mn_{1/3}O_2$	0.8	206	42
NCM-8	$LiNi_{1/3}Co_{1/3}Mn_{1/3}O_2$	0.8	208	36
NCM-9	$LiNi_{1/3}Co_{1/3}Mn_{1/3}O_2$	0.8	216	31
MTI-LCO	$LiCoO_2$	2.9	94	34
MTI-LFP	$LiFePO_4$	0.4	116	37
MTI-LMO	$LiMn_2O_4$	0.7	85	36

a.)

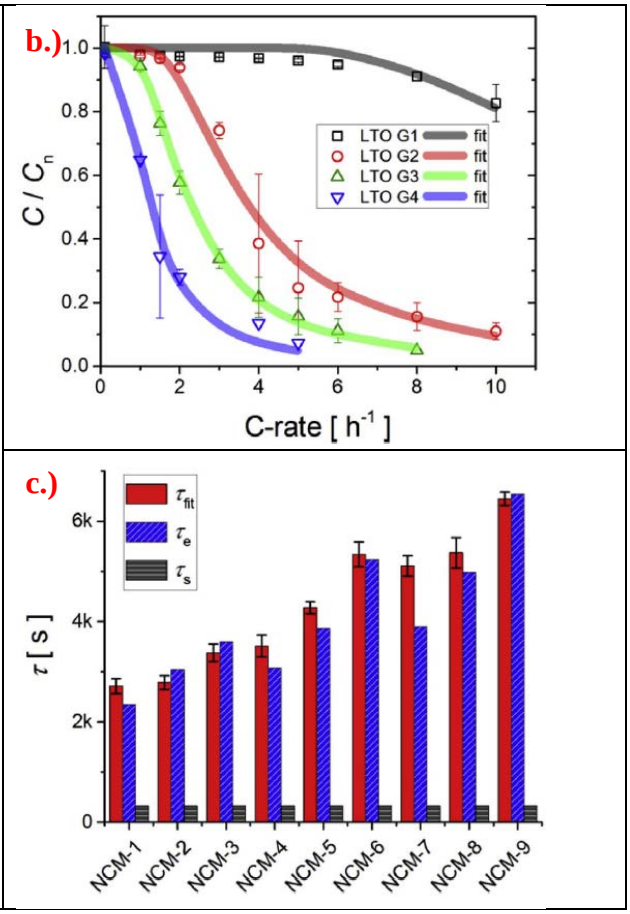

Figure 2.23: (a) Electrodes designs. (b) Rate capability of LTO-based electrodes and lines of the best fit to the proposed rate capability model. (c) Comparison of time constants of NCM electrodes obtained from the fit and time constants of lithium diffusion in the liquid electrolyte and the solid intercalation host calculated from Eqs. 2.3 and 2.4 [37].

It must be noted that the model assumes that the charge transfer process is not a limiting step in the performance of the electrode. However, if charge transfer limitations are significant, e.g. limited electron transport via the active material/conductive additives or limited contact surface area at the active material/electrolyte interface, this renders electrodes with large ohmic limitations and exhibit a large ohmic potential drop (IR-drop) lowering the operating voltage. Consequently, the cut-off voltage may be reached before the nominal capacity is achieved even without significant diffusion limitations. Therefore, the model is not capable to describe the behavior of such an electrode and the rate capability would be overestimated. The proposed master curve will only be valid for an optimized electrode with low charge transfer resistance and minimal ohmic losses.

2.5) Tortuosity and Bruggeman Law

As it can be seen with the Gallagher's expression, the tortuosity of the electrolyte transport paths through microstructure pores is important as it limits battery maximum charge/discharge rate. Pore tortuosity,τ, is defined as the ratio between the actual path length to the straight distance. For a porous medium with L_{pore} as the effective actual path length through pores from point A to point B, and $L_{straight}$ as the straight (Euclidian) distance, the strict geometrical definition of its tortuosity is:

$$\tau = \frac{L_{pore}}{L_{straight}} \qquad \textit{(eq. 2.5)}$$

It naturally influences the liquid phase transport of electrolyte species, and the following relationship between the intrinsic diffusion coefficient D_0 in a non-tortuous path and the effective one D_{eff} is generally considered in battery papers. [38,39,40,41,42]

$$D_{eff} = D_0 \frac{\varepsilon}{\tau^2} = D_0 \frac{\varepsilon}{T} \qquad \textit{(eq. 2.6)}$$

ε is the porosity. T, which is often confused to τ in the literature, is called the tortuosity factor. The same equations can be used to relate effective ionic conductivity σ_{eff} with the ionic conductivity of the bulk σ_0. Bruggeman theory provides a theoretical relation between porosity and geometric tortuosity for ideal geometries [38-42]:

$$T = \tau^2 = \gamma \varepsilon^{1-\alpha} \qquad \textit{(eq. 2.7)}$$

where α (Bruggeman coefficient) and γ are constants. It was initially assumed that γ=1 and α=1.5 in battery models. However, α=1.5 corresponds to an ideal electrode packed with identically sized non-overlapping spheres. In practical electrodes, and different γ and/or α values have been obtained from experimental and simulation methods. Zacharias et al. [39] established through polarization-interrupt (restricted-diffusion) experiments modified Bruggeman-type functions for $LiFePO_4$- and $LiCoO_2$-based electrodes (Figure 2.24). For example, the electrode that was fabricated by SAFT with 94 wt% $LiCoO_2$, 2 wt% carbon), and 3 wt% PVDF obeys a Bruggeman-type function with γ = 2.5 and α = 1.27. The polarization-interrupt method measures electrode-film tortuosity in terms of effective diffusivity. This is accomplished by building up a concentration gradient of ions in the film using a DC current and then interrupting the current and determining diffusivity using the slope of the relaxation curve.

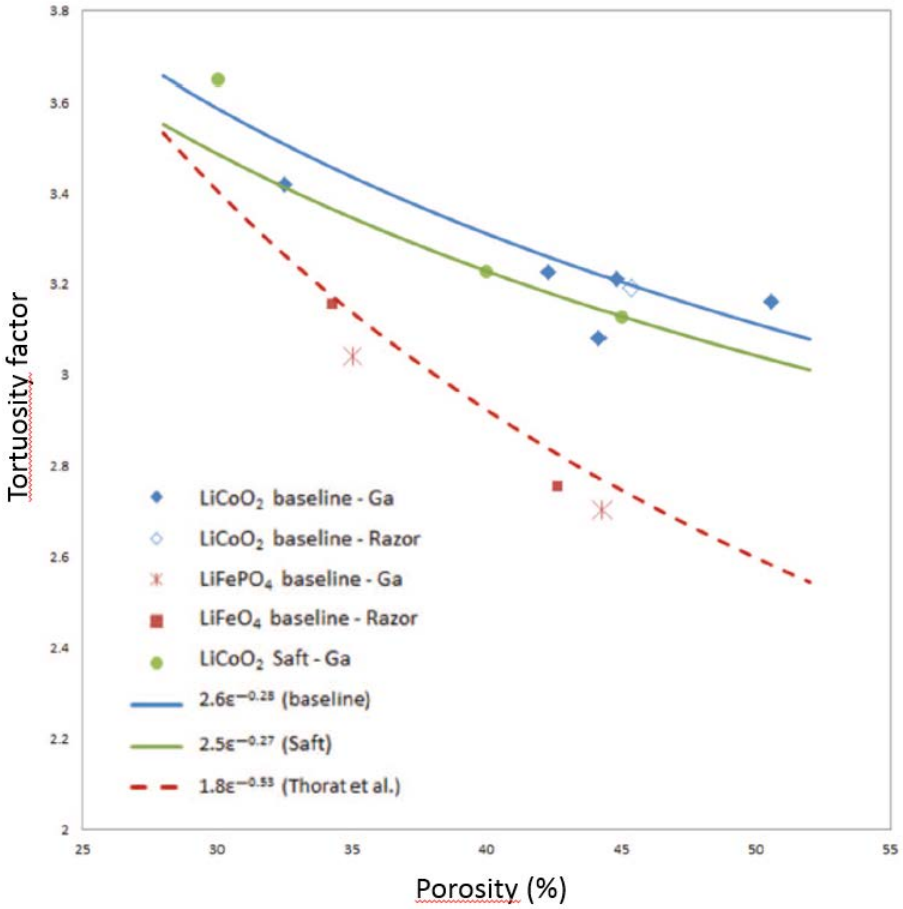

Figure 2.24: Bruggeman-type functions determined by Zacharias et al. [39] with polarization-interrupt (restricted-diffusion) experiments for $LiFePO_4$- and $LiCoO_2$-based electrodes. The electrodes compositions in AM/CB/Gr/PVdF are 84.4:3.9:3.9:7.8 for $LiCoO_2$ baseline, 84.4:3.9:3.9:7.8 for $LiFePO_4$ baseline, and 94.5:2.0:3.5 for Saft.

A more recent study by Usseglio-Viretta et al. [43] have applied three independent approaches to quantify the tortuosity factor of NMC532 lithium-ion battery electrodes with loadings ranging from 2.29 to 8.27 $mAh.cm^{-2}$ and with porosities and thickness ranging from 34% to 52% and 34 to160µm, respectively. Cathodes were fabricated using 90 wt% NMC532, 5 wt% carbon black (C45), and 5 wt% polyvinylidene fluoride (PVDF). Graphite lithium-ion battery electrodes were also studied.

The first approach is a microstructure model based on three-dimensional geometries from X-ray computed tomography (CT) and stochastic reconstructions enhanced with computationally generated carbon/binder domain, as CT is often unable to resolve these ones. The effective diffusivity of the microstructure is simulated and then the tortuosity factor is computed. The

steady state diffusion equation (i.e., the Laplace equation) is solved within the connected pore network. The effective diffusion coefficient is deduced from the analysis of the calculated concentration field using the Fick's first law as detailed in [43]. The tortuosity factor was then calculated from Eq. 2.6. This approach assumes lithium ions do not accumulate locally in the microstructure, for instance due to local defects, and does not consider the nonuniform electrochemical reaction that occurs during battery operation across the active material/electrolyte interface.

The second approach used a previously reported macro-homogeneous electrochemical model [44] to fit electrochemical data at several rates. The model uses the pseudo-2D formulation originally proposed by Newman and coworkers [45]. The macro-homogeneous model prediction is based on matching to experimentally measured electrochemical data at the highest achievable rate, here this was lithiation at 1C. The tortuosity range was selected to approximately match the final capacity and to a lesser extent match the voltage profile of those experimentally measured.
The third approach experimentally measures tortuosity factor by collecting electrochemical impedance spectroscopy data for a symmetric cell infiltrated with a non intercalating or blocking electrolyte (20 mM tetrabutylammonium hexafluorophosphate in a 1:1 (w:w) mixture of ethylene carbonate (EC) and dimethyl carbonate), according to a method described by Landesfeind et al. [46]. The resulting Nyquist spectrum was then fitted to a transmission line model to obtain effective ionic conductivity of each porous electrode film, which could be directly translated to, knowing the porosity of the sample and the bulk electrolyte conductivity, to a tortuosity factor. Tortuosity values obtained through the blocking-electrolyte method are generally in agreement with those obtained through the polarization interrupt method [47].

The results from the three approaches are reproduced below (Figure 2.25). Tortuosity factors for positive electrodes have been found to be fairly similar among the three methods. Lower and upper bound Bruggeman type functions are observed with $\gamma = 1.3$ and $\alpha = 1.59$ for lower bound and $\gamma = 1.3$ and $\alpha = 1.99$ for upper bound.

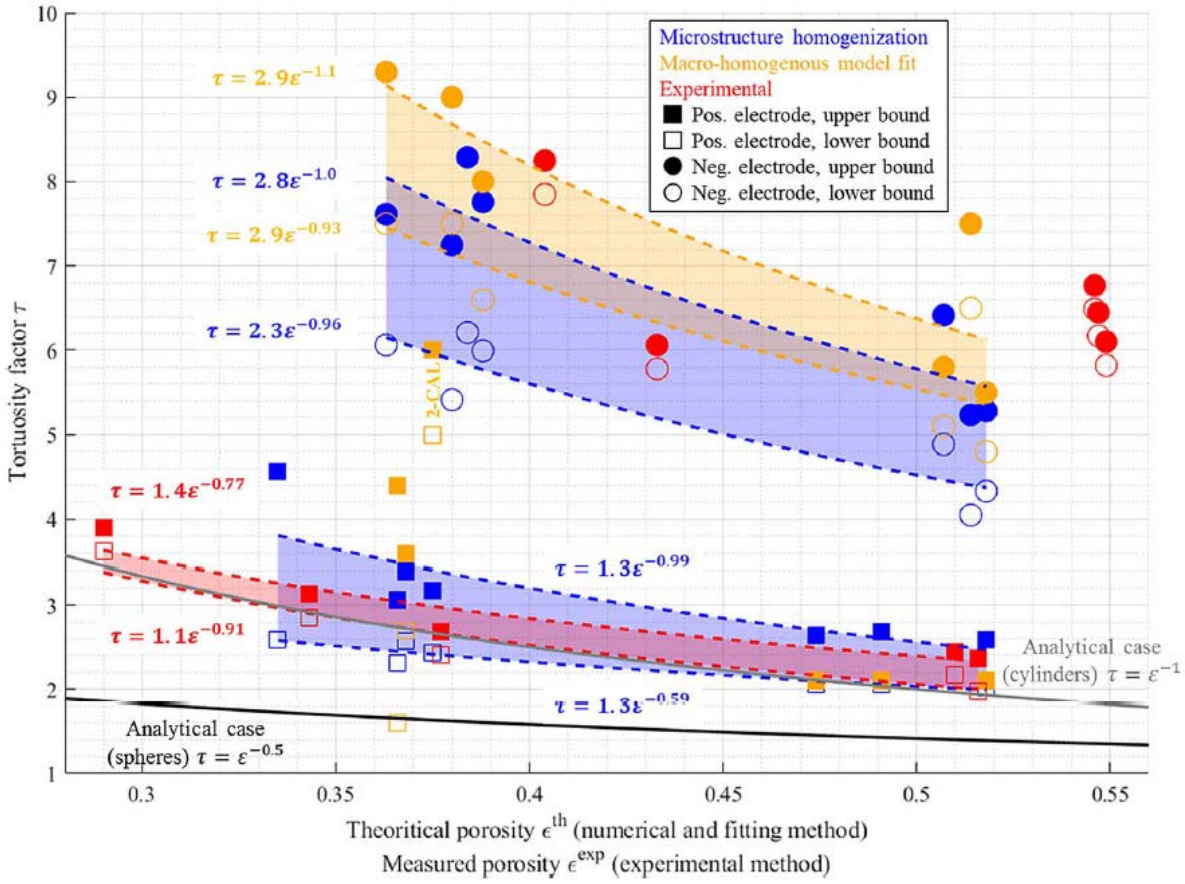

Figure 2.25: Through-plane tortuosity values comparison for three methods of determination (see the text). Lower and upper bounds of the tortuosity are deduced from the error analysis, and colored *areas correspond to the region between these two bounds. Squares correspond to NMC532 positive electrode with 5 wt% carbon black (C45) and 5 wt% polyvinylidene fluoride (PVDF). Circles correspond to graphite negative electrodes with 2 wt% carbon black (C45), 6 wt% polyvinylidene fluoride (PVDF) and 0.2 wt% oxalic acid. [43]*

2.6) Electrochemical models

Electrochemical Models have been developed for more than 40 years to predict the electrical behavior of lithium-ion batteries [48,49]. Through a rigorous theoretical approach including solid and liquid phase transport as well as lithium intercalation, they aim to rigorously describe the phenomena occurring in a cell. In such models, the variables of interest include:

- In the solid phase: the current density i_1, the potential Φ_1 and the Li concentration C_s,
- In the liquid phase: the current density i_2, the potential Φ_2 and the electrolyte concentration c,

- At the interface: the pore wall flux j_n that takes into account Li insertion and de-insertion phenomena.

Inside the solid phase, the active material is considered as a juxtaposition of spherical particles and the concentration profile is solved in spherical coordinates. The liquid and solid concentration profile is also solved in the porous media along the thickness of the electrode, and allows the model to be pseudo-2-dimensional (P2D). The model is composed of a system of partial differential equations, which includes diffusion and Ohm's law in solid phase, material balance and potential relation in liquid phase, Butler-Volmer kinetics and pore wall flux relation at the interface (Figure 2.26).

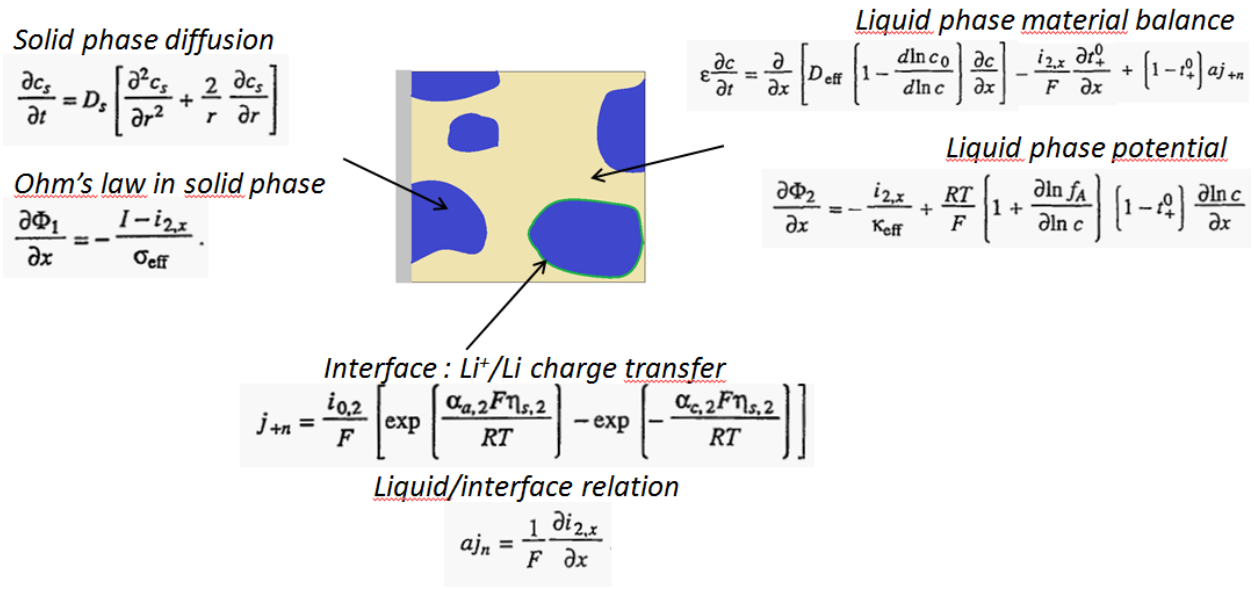

Figure 2.26: Porous electrode model description

This model needs numerous input parameters to run properly, and they must be robust enough to ensure a good accuracy of the simulation. Input parameters can be divided in two categories: cell design parameters and physical properties. On one hand, the first category is quite easy to inform when the cell design is well known (Table 2.2). On the other hand, the second category is composed of physical properties, mainly transport and kinetic ones, which are more difficult to evaluate, because of the imprecise measurements or the difficulty to set up a suitable experimental technique (Table 2.2). The model also needs the implementation of the open circuit potential of the active materials *vs.* stoichiometry, which can be assessed by electrochemical measurements on half cells like low-rate CCCV or PITT.

Table 2.2: *Porous model design parameters and physical properties*

Cell design parameters		**Physical properties**	
x_e, x_c, x_s,	thickness of electrode, current collector, separator (m)	y	initial stoichiometry in active material
v_{ps}, ε_s	volume fraction of polymer, electrolyte in separator	D_s	Li diffusion coef. in solid phase (m^2/s)
v_p, v_i, ε,	volume fraction of polymer (binder), inert filler (carbon), electrolyte in the electrode	r_i	radius of particles (m)
ρ_c, ρ_s, ρ_e, ρ_i, ρ_p, ρ_a,	density of current collector, inert separator material, electrolyte, inert filler (Carbon), of polymer material (binder), active material (kg/m^3)	σ_m	Electronic conductivity of the matrix (S/m)
c_i	Initial salt concentration (mol/m^3)	k_0	rate constant for Li insertion
Q_a	capacity of active material (mAh/g)	R_C	Electrode/collector contact resistance ($ohm.m^2$)
		τ	tortuosity
		t_{Li+}	transference number of Li^+
		D_0	Li diffusion coef. in electrolyte (m^2/s)
		λ	conductivity of the salt (S/m)
		f_a	Activity factor for salt

Handling such models is therefore the *business* of specialists and their use is not easy to generalize. One difficulty lies in the many parameters to be filled in, the exact values of which are not easy to determine, in particular those of the transport properties. Thus, it is common to read in the articles that one of the parameters has been adjusted to allow a good fit of electrochemical performance. It is often tortuosity.

For our part, and this is what we have tried to do in this thesis, we are looking for equations that are both simple and based on physical parameters representative of the microstructure of the electrodes, as well as transport properties, which allow the electrochemical performances to be predicted quite correctly, and thus be tools for diagnosing and optimizing the efficiency of the composition and the microstructure of an electrode.

2.7) Conclusion

Battery systems that rely on composite based electrodes for capacity delivery can attribute their electrochemical performance on a number of factors concerning the formulation of the electrode film composite. Effective delivery of the electrochemical capacity not only relies solely on the active material but also with the balance between charge transfer, electronic wiring, ionic wiring, and ionic diffusion. As this study concentrates on power performance which greatly relies on the replenishment of Li^+ reservoirs in the pore matrix via ion diffusion, we aim to not only link how electrode parameters affect power performance but also to be able to develop a method in optimizing these parameters to improve electrode design and achieve the best power capability. Another aspect we would like to explore is the effect of reduced binder and conducing additive contents relative to the compositions explored in various literatures. In theory, this increases practical areal capacities and should aid in increasing power performance.

Table 2.3: Summary of different electrode compositions presented in the included literatures in this chapter.

NMC type	Binder (wt%)	Conductor (wt%)	Capacity (mAh/cm²) *Loading (mg/cm²)*	Cell & electrolyte (solvent ratio in wt%)	Porosity (%)	% Q at 2C-3C	Reference
532	CMC (5.0)	CB (5.0)	1.8 *11.2*	Full cell (pouch) 1.2M $LiPF_6$ in EC/EMC 30:70	30-35	50	[21]
	CMC (2.5)	CB (0.3) + CNT (1.2)				80	
333	PVdF (4)	Super P (4)	0.8 mAh/cm²	2032 half-cell, 1 M $LiPF_6$ in EC/DMC1:1	0-50	75	[12,13]
333	PVdF (16)	Acetylene Black (12.8)	160 mAh/g	2032 half-cell, 1 M $LiPF_6$ in EC/DMC 1:1	-	90	[7]
333	PVdF (8)	CB (2)	160 mAh/g	Three electrode half-cell Swagelok, 1 M $LiPF_6$ in	-	19	[19]
		MWCNT (2)				56	
		MWCNT-				≈1	

		COOH (2)		EC/DMC 1:1			
532	PVdF (5)	CB (5)	190 mAh/g	Half-cell coin cell, 1.2 M $LiPF_6$ in EC/ EMC 30:70	30	79	[20]
		CBC (5)				82	
		CB (1)				77	
		CBC (1)				82	
622	PVdF (8)	CF: interwoven CF (5:3)	180 mAh/g, (4-11 mg/cm^2)	Half-cell 2016 coin cell, 1M $LiPF_6$ in EC/EMC 30:70	20-60	≈70	[21]
532	CMC (5)	CB (5)	1.8mAh/cm^2	Full cell (pouch) 1.2M $LiPF_6$ in EC/EMC 30:70	30-35	50	[22]
	CMC (5)	CB-CNT (0.7:1.8)				70	
	CMC (2.5)	CB-CNT (0.3:1.2)				80	
333	PVdF (8)	AB (6.4)	5.5 mAh/cm^2	Coin cell half-cell, 1 M $LiPF_6$ in EC/DEC mixture 1:1	10-50	7	[26]
	PVdF (4)	AB (3.2)				7	
	PVdF (2)	AB (1.6)				7	
333	PVdF (8)	AB (7)	5.56 mAh/cm^2	2325 Coin cell full-cell, 1 M $LiPF_6$ in EC/DEC mixture 1:1	35	87.5	[27]
			11.48 mAh/cm^2			82	
			17.52 mAh/cm^2			69	
			24.01 mAh/cm^2			50	
622	PVdF (4.1)	Carbon (4.4)	195 mAh/g, 12.5 mAh/cm^2	Full cell pouch cell, 1M $LiPF_6$ in EC/EMC 30:70	35	ONLY CYCLED UPTO 1C	[36]
			195 mAh/g, 19mAh/cm^2				
			195 mAh/g, 25.1 mAh/cm^2				
			195 mAh/g, 31.2 mAh/cm^2				
			195 mAh/g, 37.6 mAh/cm^2				
333	PVdF (5)	C65 (3)	158 mAh/g 2.6 mAh/cm^2	Swagelok half-cell, 1M $LiPF_6$ in EC/DMC mixture 1:1	34	95	[31]
	PVdF (7.5)	C65 (4.5)	155 mAh/g 2.6 mAh/cm^2		30	80	
532	PVdF (1.8)	C65 (2.2)	2.5-4.2 mAh/cm²	Coin cell half-cell, 1M $LiPF_6$ in EC/DMC mixture 1:1	21 - 28	This work	
	PVdF (3.6)	C65 (3.2)	2.5-6.7 mAh/cm²		19 - 26		

** PVdF – Polyvinylidene Fluoride, EC – ethylene carbonate, DMC – dimethyl carbonate, DEC – diethyl carbonate, EMC – ethyl methyl carbonate, CB – Carbon Black, CF – Carbon fibers, CNT – Carbon Nanotubes, MWCNT – multiwalled carbon nanotubes*

[1] Mizushima, K., Jones, P. C., Wiseman, P. J. & Goodenough, J. B. Li_xCoO_2 ($0<x\leq1$): A new cathode material for batteries of high energy density. *Solid State Ionics* **3–4**, 171–174 (1981).
[2] Padhi, A. K., Nanjundaswamy, K. S. & Goodenough, J. B. Phospho-olivines as positive-electrode materials for rechargeable lithium batteries. *J. Electrochem. Soc.* **144**, 1188–1194 (1997).
[3] Scrosati, B., Sapienza, L. & Moro, P. A. Recent advances in lithium ion battery materials. **45,** 2461–2466 (2000).
[4] Manthiram, A., Song, B. & Li, W. A perspective on nickel-rich layered oxide cathodes for lithium-ion batteries. *Energy Storage Mater.* **6,** 125–139 (2017).
[5] Schipper, F. *et al.* Review — Recent Advances and Remaining Challenges for Lithium I. Nickel-Rich , $LiNi_xCo_yMn_zO_2$. **164,** 6220–6228 (2017).
[6] Hwang, B. J., Tsai, Y. W., Carlier, D. & Ceder, G. A combined computational/experimental study on $LiNi_{1/3}Co_{1/3}Mn_{1/3}O_2$. *Chem. Mater.* **15**, 3676–3682 (2003).
[7] Wu, S. *et al.* High Rate Capability of $Li(Ni_{1/3}Mn_{1/3}Co_{1/3})O_2$ Electrode for Li-Ion Batteries. **159,** 438–444 (2012).
[8] Manthiram, A., Song, B. & Li, W. A perspective on nickel-rich layered oxide cathodes for lithium-ion batteries. *Energy Storage Mater.* **6,** 125–139 (2017).
[9] Kim, J., Lee, H., Cha, H., Yoon, M. & Park, M. Prospect and Reality of Ni-Rich Cathode for Commercialization. **1702028,** 1–25 (2018).
[10] Noh, H., Youn, S., Seung, C. & Sun, Y. Comparison of the structural and electrochemical properties cathode material for lithium-ion batteries. **233,** 2–11 (2013).
[11] Kim, J., Lee, H., Cha, H., Yoon, M. & Park, M. Prospect and Reality of Ni-Rich Cathode for Commercialization. **1702028,** 1–25 (2018).
[12] Cabelguen, P. *et al.* Rational Analysis of Layered Oxide Power Performance Limitations in a Lithium Battery Application. **1700078,** 1–12 (2017).
[13] Cabelguen, P., Peralta, D., Cugnet, M. & Maillet, P. Impact of morphological changes of $LiNi_{1/3}Mn_{1/3}Co_{1/3}O_2$ on lithium-ion cathode performances. *J. Power Sources* **346,** 13–23 (2017).
[14] Schipper, F. *et al.* Review — Recent Advances and Remaining Challenges for Lithium I. Nickel-Rich, $LiNi_xCo_yMn_zO_2$. **164,** 6220–6228 (2017).
[15] Gaberscek, M. Towards optimized preparation of cathode materials: How can modeling and concepts be used in practice. *J. Power Sources* **189**, 22–27 (2009).
[16] Guy, D., Lestriez, B., Bouchet, R. & Guyomard, D. Critical Role of Polymeric Binders on the Electronic Transport Properties of Composites Electrode. *J. Electrochem. Soc.* **153,** A679 (2006).
[17] Inoue, G. & Kawase, M. Numerical and experimental evaluation of the relationship between porous electrode structure and effective conductivity of ions and electrons in lithium-ion batteries. *J. Power Sources* **342**, 476–488 (2017).
[18] Wu, S. *et al.* High Rate Capability of $Li(Ni_{1/3}\ Mn_{1/3}Co_{1/3})O_2$ Electrode for Li-Ion Batteries. **159,** 438–444 (2012).
[19] Varzi, A., Täubert, C. & Wohlfahrt-Mehrens, M. The effects of pristine and carboxylated multi-walled carbon nanotubes as conductive additives on the performance of $LiNi_{0.33}Co_{0.33}Mn_{0.33}O_2$ and $LiFePO_4$ positive electrodes. *Electrochim. Acta* **78,** 17–26 (2012).
[20] Su, X. *et al.* Nonlinear Conductivities and Electrochemical Performances of $LiNi_{0.5}Co_{0.2}Mn_{0.3}O_2$ Electrodes. *J. Electrochem. Soc.* **163,** A2720–A2724 (2016).

[21] Kang, J., Pham, H. Q., Kang, D. H., Park, H. Y. & Song, S. W. Improved rate capability of highly loaded carbon fiber-interwoven $LiNi_{0.6}Co_{0.2}Mn_{0.2}O_2$ cathode material for high-power Li-ion batteries. *J. Alloys Compd.* **657,** 464–471 (2016).
[22] Du, Z. *et al.* Three-dimensional conductive network formed by carbon nanotubes in aqueous processed NMC electrode. *Electrochim. Acta* **270,** 54–61 (2018).
[23] Morelly, S. L., Alvarez, N. J. & Tang, M. H. Short-range contacts govern the performance of industry-relevant battery cathodes. *J. Power Sources* **387,** 49–56 (2018).
[24] Xu, J., Chou, S. L., Gu, Q. F., Liu, H. K. & Dou, S. X. The effect of different binders on electrochemical properties of $LiNi_{1/3}Mn_{1/3}Co_{1/3}O_2$ cathode material in lithium ion batteries. *J. Power Sources* **225,** 172–178 (2013).
[25] Bichon, M. *et al.* Study of Immersion of $LiNi_{0.5}Mn_{0.3}Co_{0.2}O_2$ Material in Water for Aqueous Processing of Positive Electrode for Li-Ion Batteries. *ACS Appl. Mater. Interfaces* **11**, 18331–18341 (2019).
[26] Zheng, H. *et al.* Cathode Performance as a Function of Inactive Material and Void Fractions. *J. Electrochem. Soc.* **157,** A1060 (2010).
[27] Zheng, H., Li, J., Song, X., Liu, G. & Battaglia, V. S. A comprehensive understanding of electrode thickness effects on the electrochemical performances of Li-ion battery cathodes. *Electrochim. Acta* **71,** 258–265 (2012).
[28] Yu, D. Y. W., Donoue, K., Inoue, T., Fujimoto, M. & Fujitani, S. Effect of electrode parameters on LiFePO4 cathodes. *J. Electrochem. Soc.* **153**, (2006).
[29] Ebner, M., Geldmacher, F., Marone, F., Stampanoni, M. & Wood, V. X-Ray Tomography of Porous, Transition Metal Oxide Based Lithium Ion Battery Electrodes. *Adv. Energy Mater.* **3,** 845–850 (2013).
[30] Kitada, K. *et al.* Factors determining the packing-limitation of active materials in the composite electrode of lithium-ion batteries. *J. Power Sources* **301,** 11–17 (2016).
[31] Besnard, N. *et al.* Multiscale Morphological and Electrical Characterization of Charge Transport Limitations to the Power Performance of Positive Electrode Blends for Lithium-Ion Batteries. *Adv. Energy Mater.* **7**, (2017).
[32] Heubner, C. *et al.* Understanding thickness and porosity effects on the electrochemical performance of $LiNi_{0.6}Co_{0.2}Mn_{0.2}O_2$ -based cathodes for high energy Li-ion batteries. *J. Power Sources* **419,** 119–126 (2019).
[33] Mao, C., Ruther, R. E., Li, J., Du, Z. & Belharouak, I. Identifying the limiting electrode in lithium ion batteries for extreme fast charging. *Electrochem. commun.* **97,** 37–41 (2018).
[34] Mohanty, D. *et al.* Effect of electrode manufacturing defects on electrochemical performance of lithium-ion batteries: Cognizance of the battery failure sources. *J. Power Sources* **312,** 70–79 (2016).
[35] Danner, T. *et al.* Thick electrodes for Li-ion batteries: A model based analysis. *J. Power Sources* **334,** 191–201 (2016).
[36] Gallagher, K. G. *et al.* Optimizing Areal Capacities through Understanding the Limitations of Lithium-Ion Electrodes. *J. Electrochem. Soc.* **163,** A138–A149 (2015).
[37] Heubner, C. *et al.* Semi-empirical master curve concept describing the rate capability of lithium insertion electrodes. *J. Power Sources* **380,** 83–91 (2018).
[38] DuBeshter, T., Sinha, P. K., Sakars, A., Fly, G. W. & Jorne, J. Measurement of Tortuosity and Porosity of Porous Battery Electrodes. *J. Electrochem. Soc.* **161**, A599–A605 (2014).

[39] N.A. Zacharias, D.R. Nevers, C. Skelton, K. Knackstedt, D.E., Stephenson, D.R. Wheeler, *J. Electrochem. Soc*., **2013**, *160*, A306.
[40] I.V. Thorat, D.E. Stephenson, N.A. Zacharias, K. Zaghib, J.N. Harb, D.R. Wheeler, *J. Power Sources*, **2009**, *188*, 592
[41] M. Ebner, D.-W. Chung, R. E. García, and V. Wood, *Adv Energy Mater.* **2014**, *4*, 1301278
[42] D. Kehrwald, P.R. Shearing, N.P. Brandon, P.K. Sinha, S.J. Harris, *J. Electrochem. Soc*., **2011**, *158*, A1393
[43] Usseglio-Viretta, F. L. E. *et al.* Resolving the discrepancy in tortuosity factor estimation for li-ion battery electrodes through micro-macro modeling and experiment. *J. Electrochem. Soc.* **165**, A3403–A3426 (2018).
[44] Kim, G. H., Smith, K., Lawrence-Simon, J. & Yang, C. Efficient and extensible quasi-explicit modular nonlinear multiscale battery model: GH-MSMD. *J. Electrochem. Soc.* **164**, A1076–A1088 (2017).
[45] Doyle, M., Fuller, T. & Newman, J. Modeling of galvanostatic charge and discharge of the lithium/ polymer/insertion cell. *J. Electrochem. Soc.* **140**, 1526–1533 (1993).
[46] Landesfeind, J., Hattendorff, J., Ehrl, A., Wall, W. A. & Gasteiger, H. A. Tortuosity determination of battery electrodes and separators by impedance spectroscopy. *J. Electrochem. Soc.* **163**, A1373–A1387 (2016).
[47] Pouraghajan, F. *et al.* Quantifying tortuosity of porous Li-Ion battery electrodes: Comparing polarization-interrupt and blocking-electrolyte methods. *J. Electrochem. Soc.* **165**, A2644–A2653 (2018).
[48] Srinivasan, V. & Newman, J. Discharge model for the lithium iron-phosphate electrode. *J. Electrochem. Soc.* **151**, A1517 (2004).
[49] Santhanagopalan, S., Guo, Q., Ramadass, P. & White, R. E. Review of models for predicting the cycling performance of lithium ion batteries. *J. Power Sources* **156**, 620–628 (2006).

CHAPTER 3: REVIEW OF RELATED LITERATURE – NUCLEAR MAGNETIC RESONANCE (NMR)

3.1) Introduction

As aforementioned the diffusion of lithium in the electrode pores dictates the power performance at high C-rates. The majority of existing literatures have described this phenomenon by either correlating observed experimental results and/or through the use of modeling. As far as our knowledge is concerned, there is no existing experiment that has directly measured the diffusion of lithium ion species in the electrode matrix. This is essential because successfully measuring the lithium ion diffusion within the pore matrix can give electrode designers an idea into which electrode geometry yields optimal transport of the lithium ion and hence optimized electrochemical performance. The literatures discussed earlier have shown that the complexity of the electrode pore matrix is dictated by several factors including particle size, material component ratios, electrode thickness etc. This is shown through the microscopy and tomography images generated from real electrodes. The porous nature of the electrode poses a diffusion obstacle for the lithium ions in the electrolyte to reach the inner areas of the electrode and complete the ion insertion reaction in the active material. This porous nature is no different from the majority of naturally and synthetic systems and composites such as cement, soil, sponges, ceramics etc. Fortunately, there exists a spectroscopic technique capable of measuring diffusion in pore systems namely Pulsed Field Gradient Spin Echo Nuclear Magnetic Resonance Spectroscopy (PFG-SE NMR). This study will employ this technique in an attempt to measure the ion diffusion in the electrode pore matrix.

3.2) Diffusion and Mobility

Diffusion is a phenomenon that is very prominent in nature. This process is central to many biological systems and industrial process (mass transport) and of course in battery systems. Diffusion, in its simplest form, is the movement of particles due to differences in chemical potential. This means that the driving force for this to occur is to minimize free energy. Mostly in nature, the driving force to equilibrate this chemical potential is the concentration gradient. In the absence of the concentration gradient, the internal kinetic energy of the particle drives the

"random motion" process of diffusion [1]. Diffusion in the absence of a concentration gradient is called "self-diffusion". In systems involving chemical potential gradients, the "ansatz" of these processes can be described mathematically as [2]:

$$\dot{F} \propto \nabla C \qquad \textit{(eq. 3.1)}$$

where $\dot{F}$ is the flux and ∇C is the gradient of potential. In processes that involve mass transfer, ∇C is a concentration gradient classically described via Fick's law:

$$J = -D\frac{dC}{dx} \qquad \textit{(eq. 3.2)}$$

where C is the concentration of the specie, J is the flux, D is the diffusion coefficient and *x* is the distance traveled by the specie. This movement has been defined to be a phenomenon of "random walk" in which can be mathematically described by their "both mean square displacement" *s* and diffusion *D*. Considering the diagram:

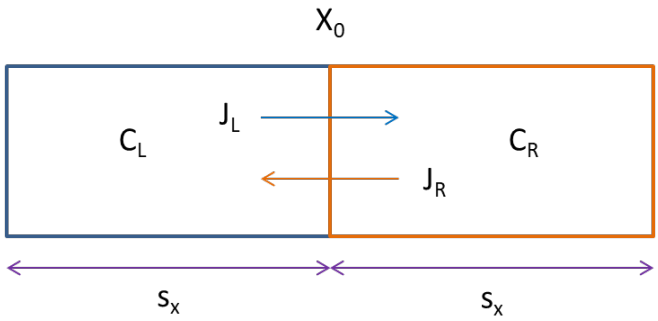

Figure 3.1: Simple diagram for displacement via concentration gradient.

We suppose at a certain time *t*, the particle has moved a distance of s_x along the direction of diffusion. In random motion, half of the particles from the right region move left and half of the particles from the left region move right. The total flux of movement can be described as $J_L \times t$. If C_L is the average concentration of the species in the left region, then we can describe the total flux per unit area as:

$$J_L t = \frac{s_x C_L}{2} \qquad \textit{(eq. 3.3)}$$

assuming that only half of the particles diffuses. The same equation can also be said with the species on the right still assuming that only half of them diffuse. The net flow inside the region X_0 can be summarily described as:

$$J = J_L - J_R = \frac{s_x(C_L - C_R)}{2t} \quad \textit{(eq. 3.4)}$$

defining (C_L-C_R) in terms of concentration gradient d_c/d_x we get:

$$-\frac{d_c}{d_x} = -\frac{(C_R - C_L)}{s_x} = \frac{(C_L - C_R)}{s_x} \quad \textit{(eq. 3.5)}$$

Combining both eq 3.4 and 3.5, we get:

$$J = \frac{s_x(C_L - C_R)}{2t} = -\frac{s_x^2}{2t}\frac{dc}{dx} \quad \textit{(eq. 3.6)}$$

Relating equation 3.6 with the simple Fick's law (equation 3.1) we get the relation:

$$D = \frac{s_x^2}{2t} \; or \; s_x^2 = 2Dt \quad \textit{(eq. 3.7)}$$

Equation 3.7 is only valid for 1D diffusion. For diffusion in 3D, we can express both the mean free path and the diffusion as:

$$s^2 = s_x^2 + s_y^2 + s_z^2 = 3s_x^2 : D = \frac{s^2}{6t} \quad \textit{(eq. 3.8), (eq. 3.9)}$$

Generalizing we get:

$$D = \frac{s^2}{2dt} \quad \textit{(eq. 3.10)}$$

where *d* is the dimensionality of the system. This simple relation derived by Einstein can simply describe diffusion in a relatively unobstructed environment. In lithium-ion batteries, as already

aforementioned in the electrochemical part of the literature review, the ion diffusion in the pore matrix is obstructed by both the pore tortuosity and pore size and flux is affected by the concentration gradient (diffusion) and electric fields, for example when a voltage difference is applied between the two electrodes (migration). Knowing that there are almost few to none electrochemical techniques that directly measure diffusion of the ions in the electrode pore matrix, we turn to a non-electrochemical based technique to help us describe diffusion in electrode pore matrices which is called PFG-SE NMR (Pulsed Field Gradient-Spin Echo Nuclear Magnetic Resonance).

3.3) Nuclear Magnetic Resonance

The spin is one of the properties of subatomic particles whose physical interpretation is abstract but is best described mathematically by quantum mechanics. It is in this property that the NMR technique is based upon. Spin is considered to have both angular and magnetic moment (as if charge rotation results in magnetic moment which is more conceptual and does not hold physically). Spin is also considered as a vector [3] and the direction of the vector is called the spin polarization axis. This axis tends to precess along the direction of an external magnetic field whenever present. The frequency of this precession along the spin polarization axis is called the Larmor Frequency which is stated as:

$$\omega = -\gamma B^0 \qquad \textit{(eq. 3.11)}$$

where γ is the gyromagnetic ratio and B^0 is the external magnetic field. In the laboratory frame, B^0 is oriented along the *z*-axis which is also the same axis along which the spin polarization orients itself. The macroscopic magnetization reaches zero at equilibrium because of symmetry reasons but the weak interaction of the spins on the external magnetic field leads to a small excess of spins with precession axes closer to *z* resulting in a small magnetization proportional to the Boltzmann factor: $\gamma B^0/kT$. The gyromagnetic ratio is an intrinsic property of the nucleus and is a proportionality constant.

In a typical NMR experiment, when the magnetization has built up during a certain time (with a characteristic relaxation time T_1), a RF-coil (radiofrequency) tuned to the Larmor frequency of

the studied nucleus generates a RF pulse. This pulse tilts the magnetization of the nucleus from the B^0 (*z*-axis) direction to the *y*-axis by 90° forcing the precession to continue along the transvers plane (*x*-*y* plane). Therefore, all nuclei under the influence of the RF pulse will simultaneously have their net magnetic moments in the transverse plane as seen below:

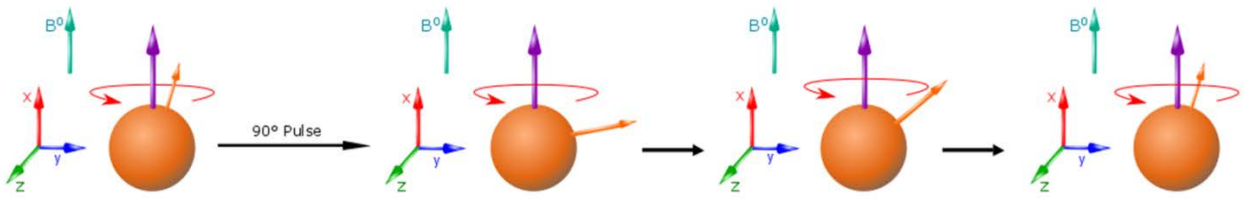

Figure 3.2: Diagram showing the effect of RF pulse on the precession vector (orange arrow) when shifting the magnetization to the transverse plane.

The precession of the spins acts like a small dynamo sending an electrical signal to the RF coil. This signal is detected and presented as the free induction decay (FID). The signal amplitude diminishes over a characteristic time T_2* as the bulk precession is unable to stay synchronized along the transverse plane, because of local field inhomogeneities and relaxation phenomena (T_2). In the case of composites, the multiple components present in the sample increases local field inhomogeneity further broadening the signal. The FID signal is a function of the Larmor frequency and can be correlated with the magnetization components: M_y^{nuc}, M_x^{nuc} in the y and *x* directions of the transverse plane respectively at time *t* through the relation (eq. 3.12):

$$M_y^{nuc} = -M_{eq}^{nuc}\, cos(\omega^0 t)\, exp\left\{-\frac{t}{T_2^*}\right\} \qquad \textit{(eq. 3.12)}$$

$$M_x^{nuc} = M_{eq}^{nuc}\, sin(\omega^0 t)\, exp\left\{-\frac{t}{T_2^*}\right\} \qquad \textit{(eq. 3.13)}$$

$$S(\omega) = \frac{\lambda}{\lambda^2 + (\omega - \omega^0)} \qquad \textit{(eq. 3.14)}$$

and $M_{eq}^{nuc}$is the magnetization component of the nucleus at equilibrium. T_2^* is the signal decay time constant and ω^0 is the Larmor frequency. Fourier transform is then applied to the FID which converts it to a Lorentzian absorption curve resulting into an absorption spectrum of S plotted against the Larmor frequency ω^0. In equation 12, ω denotes the angular frequency axis and λ is

the coherent decay constant given by ($1/T_2$*). This meant that a unique spectrum (S) is generated per nuclei due to their different Larmor frequency. Moreover, the different chemical environments experienced by each nucleus will also contribute to the experienced magnetic field (B_0) around the nucleus generating chemical shifts in the spectra and in the case of solids, chemical shift anisotropy. This can be illustrated by Figure 3.3. Herzfeld and Berger demonstrated how chemical shift anisotropy arises in solid state samples due to magnetic field anisotropies experienced by the ^{1}H nuclei [4]. The different, almost static spatial positions of each nucleus in the solid state allows them to experience the different inhomogeneities of the magnetic field which accounts for different Larmor frequencies depending on spatial orientation. Resolution of the solid state spectra can be improved via the use of Magic Angle Spinning which will be discussed later in section 3.6). We would like to stress for now that the ability to identify whether a sample is in either solid or liquid state can be qualitatively determined through NMR and this is essential in studying the diffusion behavior of the electrolyte species. Any observed broadening of the electrolyte spectra as it enters the pore matrix will be an indication of the degree of how the diffusing species experience obstructions along the tortuous pore matrix. The more obstructed the path is, the slower or more static is the movement of the diffusing specie and hence comes closer to mimicking solid state spectra.

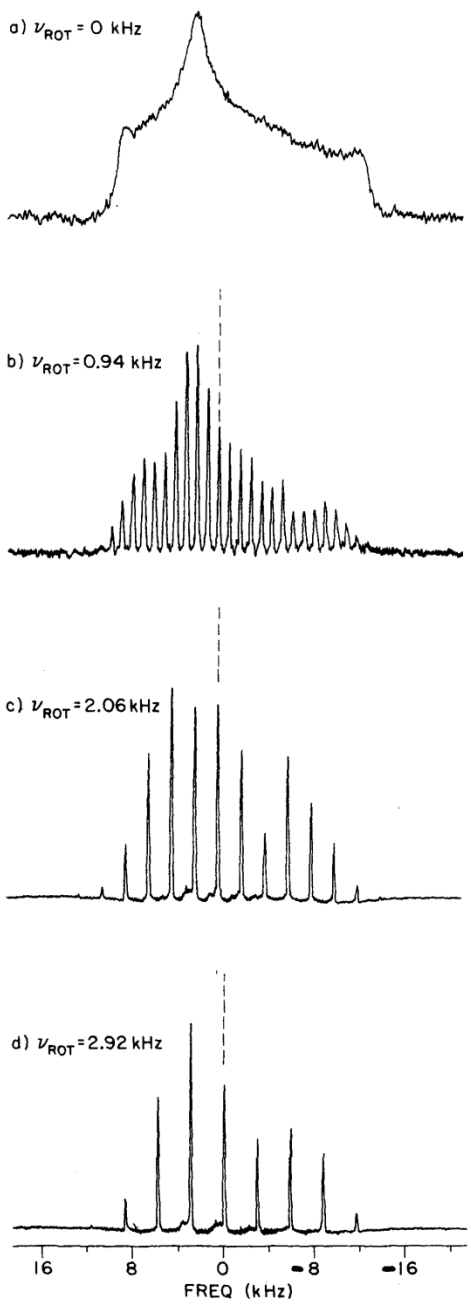

Figure 3.3: Static solid state spectra (a) of barium diethyl phosphate spun at increasing magic angle frequencies (b-d) clearly revealing anisotropy with spinning sidebands [4].

3.4) Pulsed Field Gradient Spin Echo and Magnetic Gradients

Diffusion NMR experiments require pulsed magnetic field gradients allowing spatial determination of spins. This is done through the use of gradient coils along the three axes (*x*, *y* and *z*) in addition to the external field B^0. This creates a small linear variation of the field

strength $B^0_z(x,y,z)$ along any of the three directions. This is illustrated in Figure 3.4. This results in areas where the spin precession can be either faster or slower. This is crucial in NMR diffusion experiments due to that the diffusion coefficient can be determined from the gradient strength and the loss of magnetization alignment of the signal.

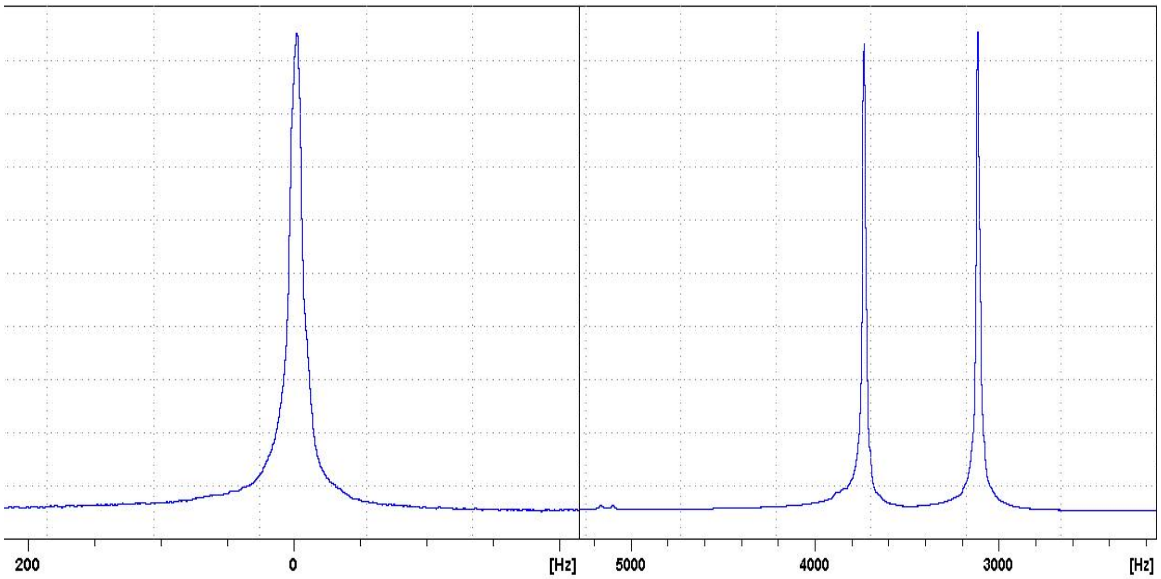

Figure 3.4: Simple NMR spectra of lithium (left) and hydrogen (right) taken from a solution of LP30 + 5% FEC

Pulsed field gradient spin echo (PFG-SE) is a popular NMR technique in studying diffusion. This includes a set of pulse sequences that exploit the spin echo (also known as the Hahn echo) phenomenon [5,6,7]. As aforementioned, a NMR signal is generated right after the 90° transverse magnetization which gradually fades due to spin de-phasing. However, at a certain time τ, a 180° pulse can be applied inverting the handedness of the precession. This results into a re-phasing of the spins and synchronization is again achieved at time 2τ. A signal can thus be observed again and is called the spin echo which was first observed by Hahn in 1950 [10]. This property is the exploited in most PFG-SE NMR experiments.

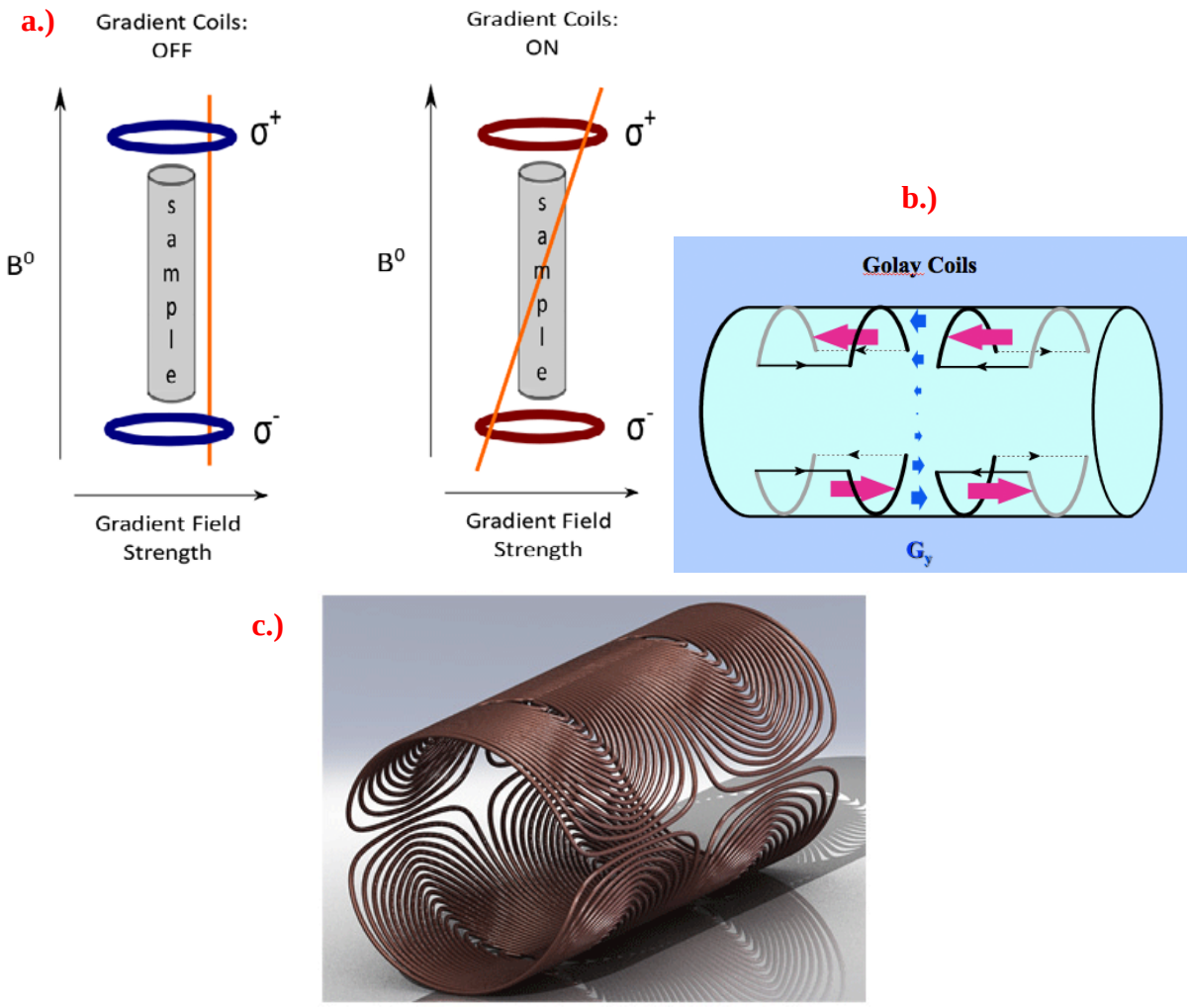

Figure 3.5: Magnetic gradient effect on field uniformity along the z-direction (a). The gradient coils are anti-Helmholtz pairs (opposite current flows) to allow magnetic field gradient generation (b). Golay pairs are used for B_0 gradients along x and y (b). (© 2019 AD Elster, ELSTER LLC http://mriquestions.com/x--and-y--gradients.html)

Figure 3.6 shows a typical PFG-SE sequence. A simple NMR signal is generated via the application of a 90° RF pulse and a gradient pulse of δ is then applied immediately to allow phase shift accumulation of the spins depending on their positions along the gradient axis. A 180° RF pulse is then applied at a certain time τ reversing the phase shifts of the spins along the transverse plane. Another gradient pulse also applied at time Δ (diffusion delay) cancelling the phase shifts after the first gradient pulse (as long as the spins did not move during Δ). A refocus of the magnetization occurs at time 2τ resulting in an observed signal. For a diffusing specie, the movement of the spins result in an incomplete refocusing of the magnetization at time 2τ generating an attenuated signal. Fortunately, the variation of signal attenuation at different

gradient strengths can be correlated to describe the self-diffusion coefficient as described by the Stejskal-Tanner equation given by:

$$\frac{S(2\tau)}{S(2\tau)_{g=0}} = exp(-D\, q^2 \left(\Delta - \frac{\delta}{3}\right)) \qquad \textit{(eq. 3.15)}$$

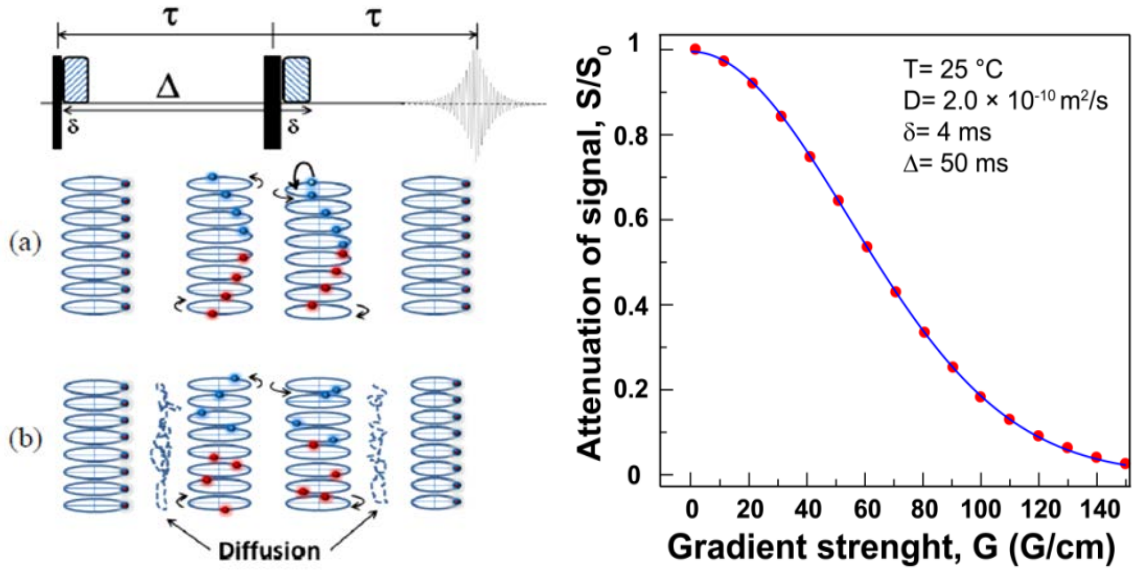

Figure 3.6: *Simple PFG sequence (top left) and the spin behaviors as they de-phase and re-phase during the PFG-SE experiment without diffusion (a) and with diffusion (b). A typical attenuation graph as a function of the gradient strength is presented on the right [5]*

Petrochemical rock sampling pioneered the development of the PFG-SE technique. More efficient oil extraction can be done by exploiting the diffusion behavior of oil in porous rocks [8,9]. This surveillance of oil permeability in rocks via diffusion NMR is called NMR logging [10,11,12]. Surveying optimal regions that contain oil-permeating rocks could prove difficult if surveillance was done through a trial and error drilling basis. By using small low frequency magnets with detectors that can perform PFG-SE measurements, oil drillers can determine regions that contain better oil effective diffusion and determine better drill placement for their extractors. The basis of the measurement diffusing species in restricted environments was done by Woessner in the 1960s. His experiments included water-sandstone systems and benzene-rubber systems determining their effective diffusion [13].

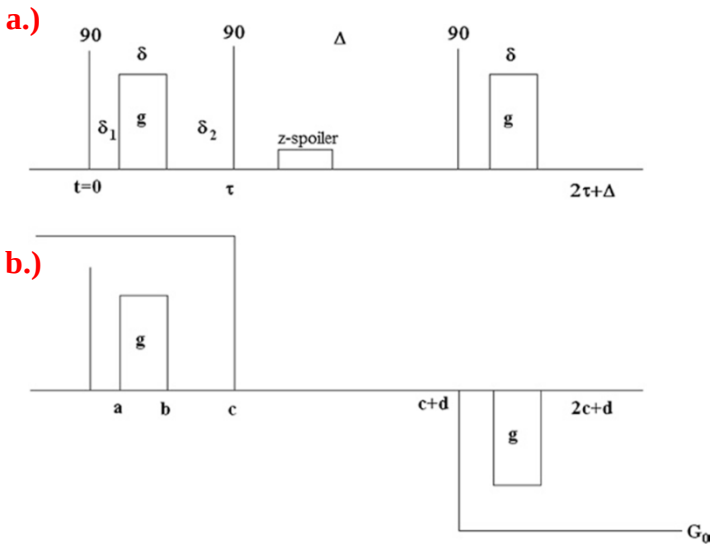

Figure 3.7: The pulsed field gradient stimulated echo (PFGSTE) sequence (a) with real (upper sequence) and effective (lower sequence) gradients (b). A short spoiler gradient pulse is applied in the z-storage interval to remove unwanted transverse magnetization coherences. This is known as a spoiler technique and means that during the z-storage delay any transverse magnetization is subjected to a dephasing gradient pulse. [14]

The PFG-SE pulse sequences can be tailored to generate the best possible attenuation for a given specie in a given system. As will be discussed in later sections, studying diffusion in pore systems can generate multiple T_2 losses through fast desynchronization of the spins. Stimulated echoes can be used to minimize these losses. Stimulated echo generally has this backbone sequence shown in Figure 3.7. Instead of a 180° inversion pulse applied at time 2τ. This ensures that at time τ, the transverse phase coherence is maximized therefore minimizing instantaneous T_2 losses on the initial spectra [14].

The derivation of the Stejskal-Tanner equation was done for species diffusing in an infinite reservoir. The Einstein relation $\langle(\Delta x)^2\rangle_{av} = 2D\Delta$ is valid when x is equal to the displacement at time $2\Delta^{(1/2)}$. It is stated that a specie that experiences physical barriers while diffusing will have an average displacement less than that of an infinite reservoir in specified time interval τ. However, the average displacement is the same as in the infinite reservoir when the limit of τ approaches zero (i.e. the diffusing species do not meet the physical barrier). This is due to that the distance between the specie and the boundary is comparatively large vs $(2D\Delta)^{1/2}$ in an infinite reservoir. For this to make sense in the Stejskal-Tanner equation, the self-diffusion coefficient D will be replaced with the spin echo determined coefficient D'.

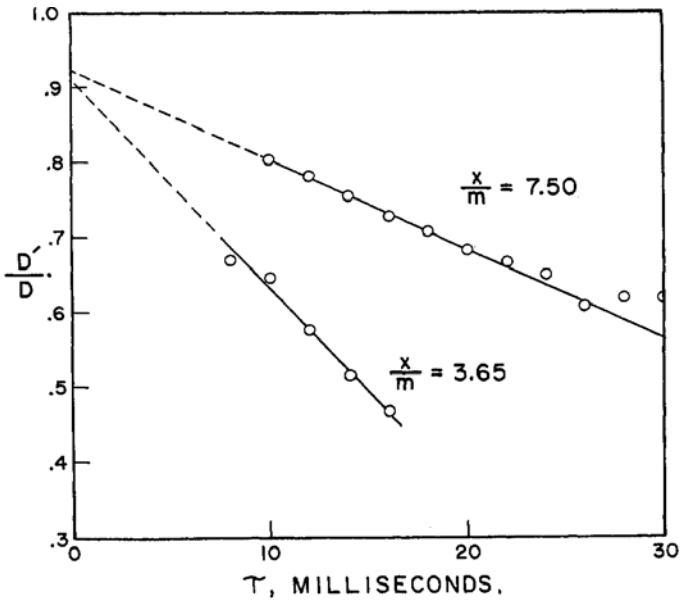

Figure 3.8: D'/D vs. τ for two different water-silica suspension rations as measured by Woessner [13]

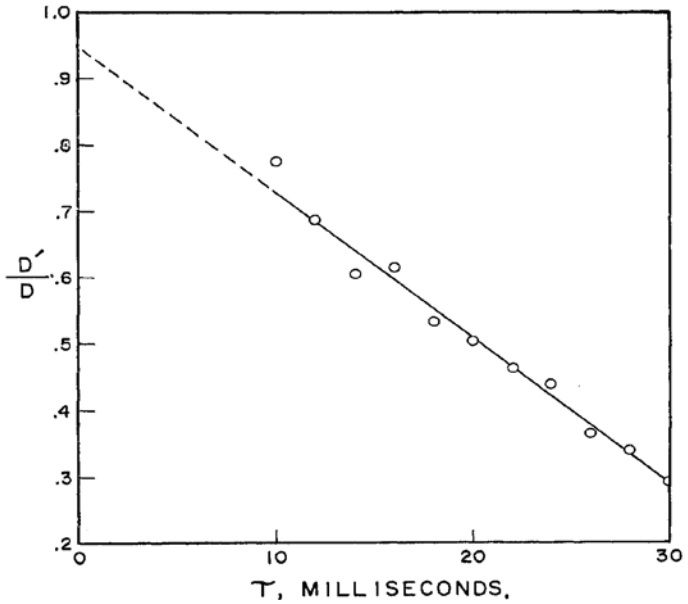

Figure 3.9: D'/D vs. τ for water in saturated sandstone of 33% porosity (22-28μm pore size) as measured by Woessner [13]

D' is the diffusion coefficient of the restricted specie as a function of the ratio between the displacement at time 2τ and the specie/s distance from the finite barrier. This coefficient decreases as the ratio of displacement to barrier distance increases and also when τ increases. D' is also independent of τ when τ is long enough to allow the displacement to be greater than the barrier distance. The same is true when τ=0 and when D=D'. These observations were verified by Woessner as seen in Figure 3.8 where X/m is the mass ratio between water and silica. At a X/m

ratio of 3.65, the D' value is shown to be smaller. This means that the wall distance between water and silica is smaller compared to that of X/m = 7.50. This is in accordance with the assumption that increased silica content decreases the distance between water and silica walls and highlighting the effect of pore restrictions (Figure 3.8). Also at increasing τ, water is experiencing decreased D' which is attributed with its decreasing distance with the pore walls. Interestingly, the distance of water to walls is at 3.7μm at τ = 10 ms at an average pore size of 25 μm. In comparison, the diffusion distance in the bulk is at 9.7 μm. The same trend line is also observed with sandstone suspensions. These observations demonstrate how PFG-SE NMR is adequate for studying restricted diffusion.

The application of diffusion NMR is not limited in the petroleum industry. Throughout the years, fluid diffusion in soil and cements were also surveyed by this technique. In the field of batteries, lithium diffusivities in active materials [15,16] and electrolyte solutions [17] have been determined through diffusion NMR. Diffusion coefficients of bulk electrolytes were also determined by diffusion NMR in supercapacitors [18] and polymeric membranes [19,20].

Richardson et.al. studied directly the self-diffusion of $LiBF_4$ salt species impregnated in PVdF based gel electrolytes [19]. ^{7}Li NMR and ^{1}H NMR spectral decays show 2 components while ^{19}F NMR spectral decays only show 1 component. These components were identified via fitting, differentiating spectra resulting from one environment (dotted lines, Figure 3.10) versus spectra resulting from two environments (smooth lines, Figure 3.10). The faster species dominates the intensity of the signal suggesting a higher concentration of mobile species in their gel system. This distinction is even more obvious with higher amounts of PVdF. The identification of a second, slower component is attributed to the restricted environment posed by the solvated amorphous phase in the gel. The lack of a two component identification for ^{19}F is due to the lack of interaction between the solvent and the polymer membrane which somehow renders both trapped and free BF_4^- to have similar viscosities and therefore almost similar spectral decays.

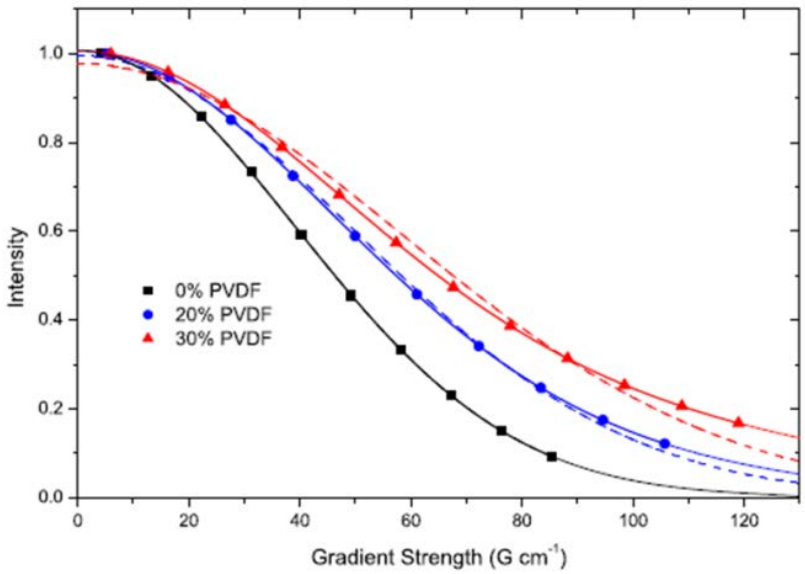

Figure 3.10: Intensity decay profile for ^{7}Li self-diffusion in solvent and in different PVdF environments. Dotted lines show 2 component fits [19].

Table 3.1: Table of ^{7}Li self-diffusion values determined by Richardson et.al. at different PVdF content and electrolyte salt concentrations [19].

Temp(K)	Diffusion ($\times 10^{-10}$ m^2 s^{-1})				
	0.3 M				
	Liquid	20%, slow	20%, fast	30%, slow	30%, fast
283	1.22	–	–	0.25	1.00
293	1.64	–	–	0.35	1.33
303	2.17	0.69	1.94	0.48	1.82
313	2.75	0.97	2.45	0.56	2.06
323	3.35	1.18	3.13	0.72	2.42
333	4.06	1.52	3.65	0.89	2.96
343	5.63	1.75	4.14	1.06	3.23

Temp(K)					
	1.0 M				
	Liquid	20%, slow	20%, fast	30%, slow	30%, fast
283	0.61	0.24	0.55	0.11	0.46
293	0.86	0.29	0.63	0.23	0.91
303	1.19	0.41	0.88	0.27	0.94
313	1.56	0.53	1.13	0.29	1.02
323	1.97	0.59	1.35	0.35	1.25
333	2.44	0.81	1.64	0.55	1.74
343	2.96	0.93	1.92	0.65	2.03

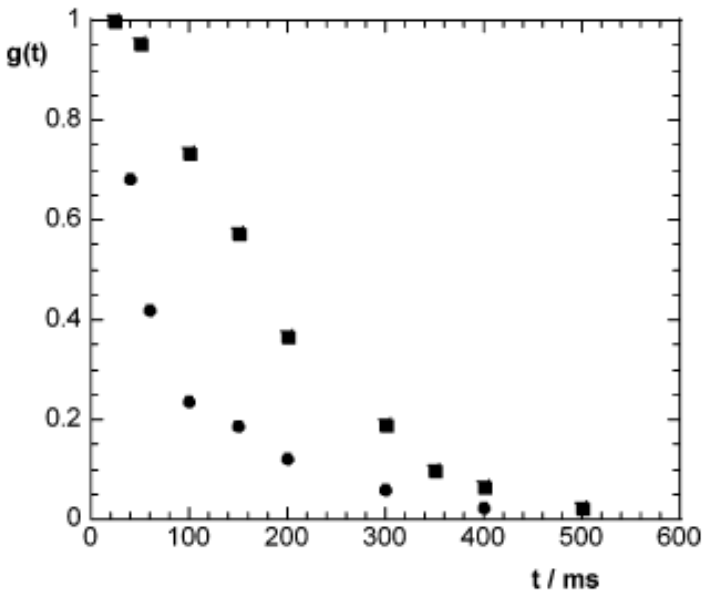

Figure 3.11: T_2 evolution vs. time for ^1H showing differences between hydrogen species in the bulk electrolyte (squares) and in the porous membrane (circles) at 300 K [20].

The restrictive nature of the swollen environment can also be seen in Saunier's work [20]. The presence of PVdF significantly decreased the self-diffusion coefficient of ^1H and also its transverse relaxation time T_2. Transverse relaxation describes how the NMR signal decays in relation to the dephasing of the spins. Faster T_2 means faster dephasing which can be accounted to the environments that pose any interaction with the spin and Larmor frequency modifications i.e. dipolar interactions, magnetic field etc. These decrease in ^1H T_2, observed in denser PVdF films are attributed to the changes in viscosity along the pore matrix which supports the idea of containment in the amorphous regions and in turn and mobility restrictions (a decrease factor of ≈2.1). Supporting also this idea are their ionic conductivity of the electrolyte species. They concluded that the decrease in ionic conductivity in the porous PVdF membrane was due to the viscosity changes brought about by the affinity of the solvents with the amorphous regions of PVdF.

This concept of relating T_2 values with the various states and environments of nuclei is a very handy tool for qualitative assessment for evaluating environments in systems. Figure 3.12 illustrates a simple graphic relating molecular size and physical states with the observed T_2 values. The larger and the more immobile the specie is, the shorter its T_2 value becomes. This resultant stems from the fact that T_2 can be greatly affected by both molecular tumbling (i.e.

diffusion) and dipole-dipole interactions (intermolecular reactions such as H-bonding). In the context of restricted diffusion, any interactions between the pore walls and the diffusing specie will introduce dipole-dipole interactions consequently dephasing the spins resulting in very fast T_2. In the case of Saunier et.al., this correlation explains greatly the observed decrease in T_2 values of 1H impregnated in the PVdF membrane.

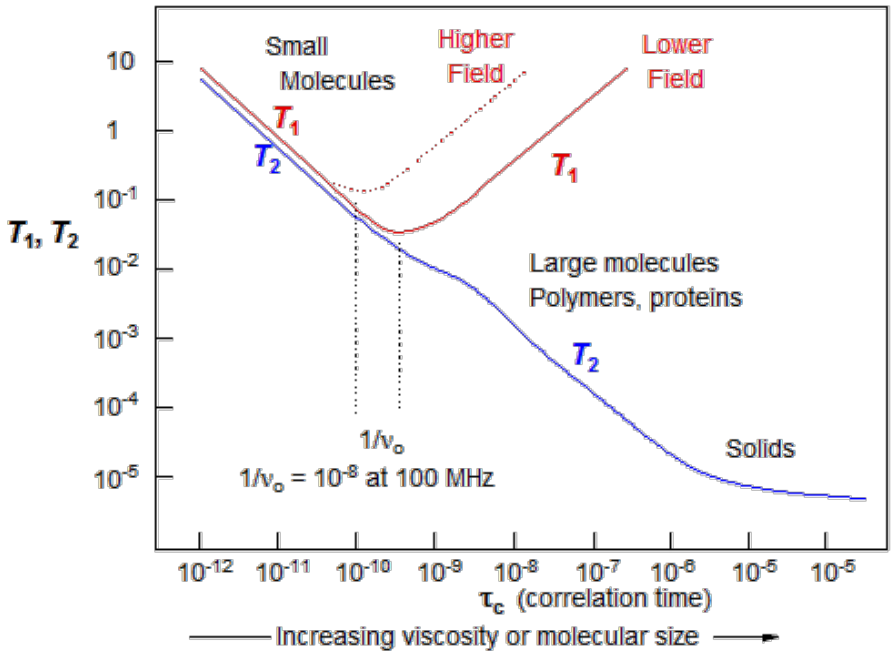

Figure 3.12: Relation of T_1 and T_2 values with various states of matter and atomic size [adapted from 21].

Another very notable work comes from Saito et.al. where diffusion kinetics of electrolytes in PVdF based membranes were determined through PFG-SE NMR [22]. D' vs. D ratios are seen to be less than 1 highlighting the effect of restricted diffusion in the membrane pores. Lithium and fluorine diffusivity ratios are also seen to be lower than that of hydrogen in both pure polypropylene (PP) and pure polyethylene (PE) membranes. It is hypothesized that the Coulombic interactions between ion pairs contribute to the decrease in diffusivity in ions. Also, the coefficient ratio for ^{7}Li is larger than that of ^{19}F suggesting selective interaction between the functional groups of the PVdF-based membrane and the ions. This work appears in contradiction with the work of Saunier et al., as the former concluded to stronger interactions between the ions and the PVdF, while the latter concluded to stronger interactions with the solvent molecules. It is however possible that different PVdF types were used in both studies.

Figure 3.13 shows the line broadening features of the fluorine ion impregnated in various membranes. Line broadening is a spectral feature of nuclei experiencing structural rigidity. The observation of this feature confirms the presence of electrolyte in the membrane pores. Looking closely, different broadening widths and spectral signatures which aid not only in determining different environments but also the extent of interactions that fluorine is experiencing (i.e. broader spectra means more interactions, more peaks mean distinct interaction environments etc.)

Table 3.2: Diffusion coefficients of electrolyte species in membrane systems as reported by Saito. Figures in parenthesis include ratios of the measured D' against D of each electrolyte system [22]

Sample	D_{Li}	σ_{Li}	D_F	σ_F	D_H	σ_H	$D_{Li}/(D_{Li}+D_F)$	porosity
Electrolyte solution	1.43E-10		2.85E-10		2.93E-10		0.33	-
PP	8.56E-11	4.2E-11	1.57E-10	4.7E-11	2.39E-10	4.5E-11	0.35	34
PE	7.53E-11 **(0.54)**	5.0E-11	1.51E-10 **(0.65)**	6.9E-11	2.45E-10 **(0.81)**	6.5E-11	0.33	31
PVDF coated PE	1.00E-10 **(0.69)**	3.8E-11	1.66E-10 **(0.58)** 1.30E-10 **(0.46)**	1.5E-11 8.1E-11	2.06E-10 **(0.70)**	3.1E-11	0.37 0.43	37
PVDF	1.20E-10 **(0.86)**	5.1E-11	1.42E-10 **(0.61)** 1.25E-10 **(0.54)**	5.1E-11 4.6E-11	2.55E-10 **(0.85)**	6.1E-11	0.46 0.49	7

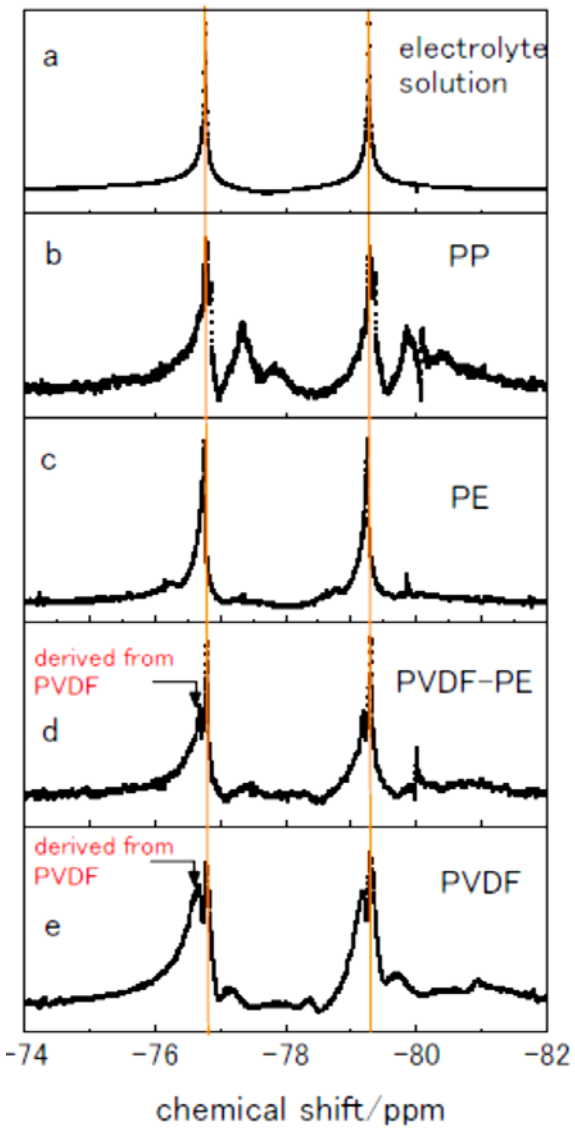

Figure 3.13: Fluorine spectrum for different electrolyte-membrane systems as observed by Saito [22]

The ability of PFG-SE NMR in studying diffusion in electrolyte systems and porous media makes it attractive to be a novel technique for our goal in studying pore diffusion. However, one final obstacle must be tackled in order to reinforce the idea of the use of this technique which is will be discussed in the next section.

3.5) Magnetic Susceptibility and Internal Gradients

Magnetic susceptibility is the intrinsic property of matter to be influenced by/influence an external magnetic field. This is tied to how the material is diamagnetic or paramagnetic for NMR studies. This is dictated by the parities of the spins in the nucleus. Diamagnetic substances have negative magnetic susceptibilities and are small in magnitude whereas paramagnetic substances bear a positive change with larger magnitude values [23]. Ferro/ferri-magnetic substances generate their own magnetic fields (i.e. iron magnet) resulting into large magnitudes of positive magnetic susceptibilities rendering them irrelevant in most NMR studies (interference of substance's own magnetic field in the NMR experiment and worse the substance permanently sticks on the magnet threatening a shutdown to remove it). In a physical sense, diamagnetic materials weaken the applied magnetic field whereas paramagnetic substances amplify the field.

Internal magnetic field gradients in porous materials are generated when both the liquid and solid phases have large differences in magnetic susceptibilities. In most cases, the solid and liquid phases have different magnetic susceptibilities. The shape of the internal field gradient can also be influenced by the size of the pores [24]. This can be simulated as highlighted by Zhang et.al. [25].

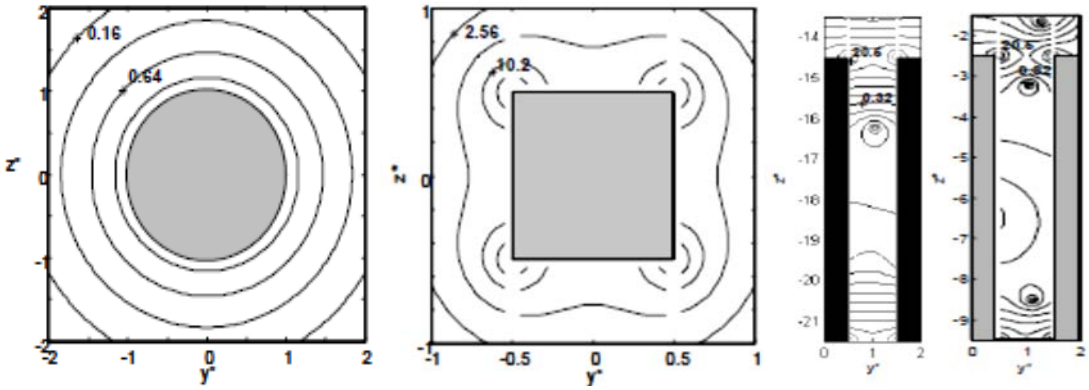

Figure 3.14: Generated gradient field lines as an effect of susceptibility differences and how the shapes are affected by particle shape (left) and pore morphology (right) [25].

The presence on internal field gradients in the porous sample affects the generated spectra in diffusion NMR experiments. This internal field gradient forces signal attenuation independent of the uniform external gradient sequenced by the diffusion experiment. This results into phase

shifts that cannot be refocused via spin echo and in the worst case the signal cannot be recorded even if G=0. Bipolar gradient pulses (i.e. (+G/2) - 180°- (-G/2) instead of a G gradient pulse reduce the internal gradient effects, but requires longer T_2's to be applied [26].

It has been observed that the majority of electrode active materials are highly paramagnetic. These values vary between 1 x 10^6 emu/mol for (LFP) $LiFePO_4$ [27] and 1 x 10^{-2} emu/mol for Li-NMC (Nickel Manganese Cobalt) [28] at room temperature. This is a big challenge for NMR diffusion as seen from porous rock-water samples. Alumina and silica are conceptualized as substitute materials for this study as they have magnetic susceptibilities close to LP30 which will be shown later in the methodology part. The use of a solid porous matrix poses another problem called line broadening due to anisotropic spin interactions (susceptibility, dipolar, etc…). Magic Angle Spinning will be employed to counter this effect.

3.6) Magic Angle Spinning

Localized spins can also interact as seen in nature. Electrons moving along the external magnetic field will generate their local fields due to their spin called secondary fields. This secondary field tends to oppose the external magnetic field [29] inducing a "shielding effect" or so-called "chemical shifts". These chemical shifts are greatly studied in organic compounds: each different functional groups give unique chemical shifts, and this information is used to elucidate their structures. Moreover, the interaction between electron orbitals and the magnetic field may not be isotropic, (depending upon energy levels), resulting in a chemical shift anisotropy which is manifested in a powder-like spectrum, as each orientation of the crystallites will give rise to a shifted peak, and solid-state spectra are usually broad. Magnetic susceptibility can also be anisotropic, and therefore, it will also generate a powder-like spectrum.

Dipolar interactions are also another important type of interaction that is very important for solid-state NMR. As aforementioned, secondary fields exist in particles that have spins, which being close with each other, will interact in an analogous manner to two bar magnets. This shift in energy is described by the Hamiltonian:

$$\widehat{H}_{dd} = -\left(\frac{\mu_0}{4\pi}\right)\gamma_I\gamma_S\hbar\left[\frac{I\cdot S}{r^3} - 3\frac{(I\cdot r)(S\cdot r)}{r^5}\right] \quad \textit{(eq. 3.16)}$$

where r is the distance between two different spins I and S. This can be express in the tensor form:

$$\widehat{H}_{dd} = -2\cdot\hat{I}\cdot D\cdot\hat{S} \quad \textit{(eq. 3.17)}$$

where D is the dipolar coupling tensor. The dipolar coupling tensor describes that the dipolar interaction between I and S is orientation dependent.

Since both dipolar coupling and chemical shifts are orientation dependent, in solid state powders, anisotropic interactions dominate the lineshapes and broad spectra are observed. In the liquid state, the rapid motion of the atoms/molecules results in an averaging of the tensors of the spin interactions giving the illusion of isotropy.

Magic Angle Spinning is used in solid-state NMR to minimize line broadening in solid-state spectra. MAS emulates the random motion of by spinning the solid sample at a "magic angle" of 54.7° [30]. It is called "magic angle" due to that any other angles would not produce the desired effect. Mathematically, rotating at this angle interchanges all *x*, *y* and *z* axes in the laboratory frame. Andrew et.al. demonstrated the spinning effect in his experiments as shown in Figure 3.15. The evolution of the spectra of ^{23}Na at varying rotation speeds and angles is observed. Line broadening is attenuated only if the sample is rotated at the magic angle. Moreover, increased spinning speeds better emulate liquid environments resulting into better spectral resolution. The isotropic spectrum is obtained by MAS when the spinning speed in Hz is much larger than the strength (in Hz) of the broadening interaction. Spinning at lower speeds results in the observation of spinning sidebands which are separated by multiples of the rotation rate.

In heterogeneous systems (such as soaked powders), when the liquid settles in porous media, the environment of molecules can become anisotropic. This results into an environment that is similar to solids. MAS will there help average these interactions and counteract line broadening.

For this study, it will be essential that MAS be applied to increase spectral resolution and obtain accurate measurements.

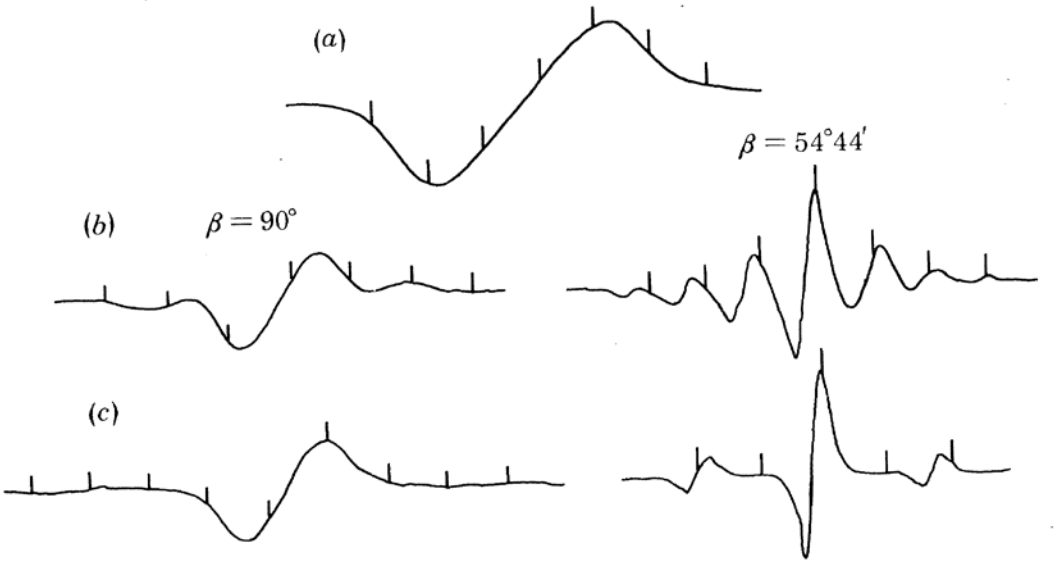

Figure 3.15: NMR spectra of ^{23}Na at static conditions (a), spun at a 90° angle (b, left), spun at the magic angle (b, right), spun at 800 Hz (c, left) and spun at 1600 Hz (c, right) as observed by Andrew [30]

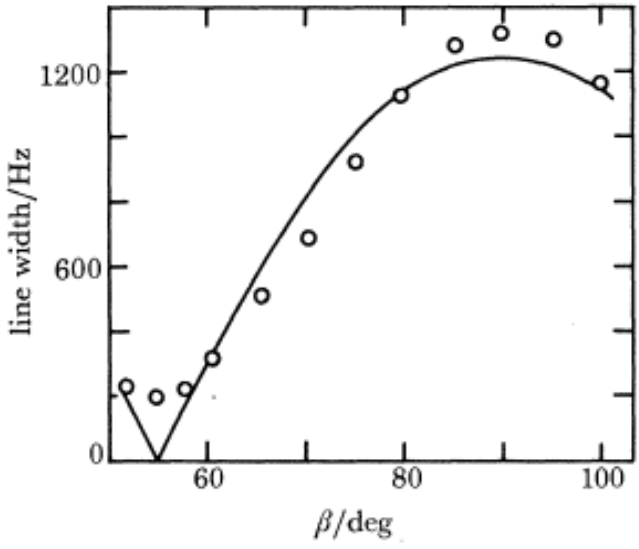

Figure 3.16: Line width of the isotropic peak as a function of the angle between B_0 and the spinning axis as observed by Andrew [30]

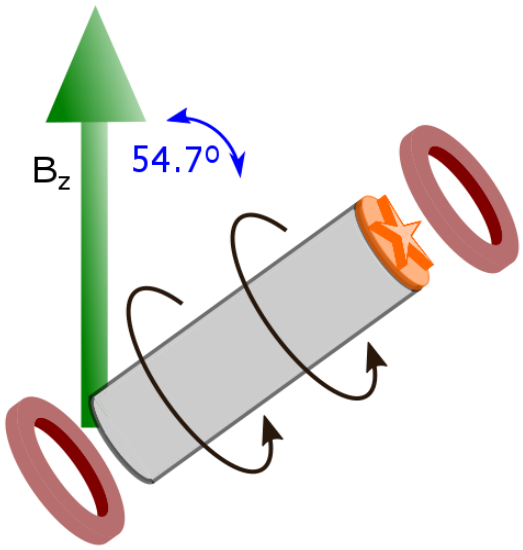

Figure 3.17: Illustration of a sample undergoing MAS in the laboratory frame

3.7) Conclusion

PFG-SE NMR has proven itself to be a useful tool in measuring diffusion of fluids in various porous media. Thanks to our previous study, which will be further discussed in the following experimental section, we have almost optimized a viable experimental protocol to be able to measure the diffusion coefficient of the lithium ion in an environment similar to real battery electrodes while minimizing internal gradients generated from magnetic susceptibility differences. Furthermore, the diffusion coefficients that we will measure from diffusion NMR will be essential benchmark values to compare and base our model upon.

---

[1] Grandjeana, J. Nuclear magnetic resonance spectroscopy of molecules and ions at clay surfaces. in *Interface Science and Technology* **1**, 216–246 (2004).
[2] Tjaden, B., Cooper, S. J., Brett, D. J., Kramer, D. & Shearing, P. R. On the origin and application of the Bruggeman correlation for analysing transport phenomena in electrochemical systems. *Curr. Opin. Chem. Eng.* **12**, 44–51 (2016).
[3] Levitt, M. H. *Spin dynamics: basics of nuclear magnetic resonance*. *Energy* (2010).
[4] Herzfeld, J. & Berger, A. E. Sideband intensities in NMR spectra of samples spinning at the magic angle. *J. Chem. Phys.* **73**, 6021–6030 (1980).
[5] Heisel, K. A., Goto, J. J. & Krishnan, V. V. NMR chromatography: molecular diffusion in the presence of pulsed field gradients in analytical chemistry applications. *Am. J. Anal. Chem.* **03,** 401–409 (2012).
[6] Callaghan, P.T. *Translational dynamics & magnetic resonance. Oxford* (2011)
[7] Hahn E. L. *Physical Review*. **80**(4), 580-594 (1950)

[8] Xiao, L. *et al.* Development of an NMR system for down-hole porous rocks. *Microporous Mesoporous Mater.* **205,** 16–20 (2015).
[9] Balzarini, M., Brancolini, A. & Gossenberg, P. Permeability estimation from NMR diffusion measurements in reservoir rocks. *Magnetic Resonance Imaging* **16,** 601–603 (1998).
[10] Brown, R. J. S. & Chandler, R. Part 1: Earth's-field nuclear magnetic logging. *Concepts Magn. Reson.* **13,** 344–367 (2001).
[11] Kleinberg, R. L. NMR well logging at Schlumberger. *Concepts Magn. Reson.* **13,** 396–403 (2001).
[12] Woessner, D. E. The early days of NMR in the Southwest. *Concepts Magn. Reson.* **13,** 77–102 (2001).
[13] Woessner, D. E. NMR Spin-echo self-diffusion measurements on fluids undergoing restricted diffusion. *J. Phys. Chem.* **67,** 1365–1367 (1963).
[14] G.H. Sørland, *Dynamic Pulsed-Field-Gradient NMR*, Springer Series in Chemical Physics 110
[15] Schmidt, W. & Wilkening, M. Diffusion-induced 7Li NMR spin-lattice relaxation of fully lithiated, mixed-conducting $Li_7Ti_5O_{12}$. *Solid State Ionics* **287,** 77–82 (2016).
[16] Tang, S. B., Lai, M. O. & Lu, L. Li-ion diffusion in highly (003) oriented $LiCoO_2$ thin film cathode prepared by pulsed laser deposition. *J. Alloys Compd.* **449,** 300–303 (2008).
[17] Noda, A., Hayamizu, K. & Watanabe, M. Pulsed-gradient spin-echo 1H and 19F NMR ionic diffusion coefficient, viscosity, and ionic conductivity of non-chloroaluminate room-temperature ionic liquids. *J. Phys. Chem. B* **105,** 4603–4610 (2001).
[18] Deschamps, M. *et al.* Exploring electrolyte organization in supercapacitor electrodes with solid-state NMR. *Nat. Mater.* **12,** 351–8 (2013).
[19] Richardson, P. M., Voice, A. M. & Ward, I. M. NMR self-diffusion and relaxation time measurements for poly (vinylidene fluoride) (PVDF) based polymer gel electrolytes containing LiBF4 and propylene carbonate. *Polymer (Guildf).* **97,** 69–79 (2016).
[20] Saunier, J., Gorecki, W., Alloin, F. & Sanchez, J. Y. NMR study of cation, anion, and solvent mobilities in macroporous poly(vinylidene fluoride). *J. Phys. Chem. B* **109,** 2487–2492 (2005).
[21] Bloembergen, N., Purcell, E. M. & Pound, R. V. Relaxation effects in nuclear magnetic resonance absorption. *Phys. Rev.* **73**, 679–712 (1948).
[22]. Saito, Y., Morimura, W., Kuratani, R. & Nishikawa, S. Ion transport in separator membranes of lithium secondary batteries. *J. Phys. Chem. C* **119,** 4702–4708 (2015).
[23] Zhang, G., Hirasaki, G. & House, W. Diffusion in internal field gradients. … *Symp. Soc. Core* … (1998).
[24] Hürlimann, M. D. Effective gradients in porous media due to susceptibility differences. *J. Magn. Reson.* **131,** 232–40 (1998).
[25] Zhang, G. Q., Hirasaki, G. J. & House, W. V. internal field gradients in porous media. *Petrophysics* **44,** 422–434 (2003).
[26] Kingsley, P. B. Peter b. kingsley. *Concepts Magn. Reson.* 155–179 (2007).
[27] Creer, J. G. & Troup, G. J. The magnetic susceptibility of $LiFePO_4$ and $LiCoPO_4$. **32,** 439–440 (1970).
[28] Mohanty, D. *et al.* Neutron diffraction and magnetic susceptibility Studies on a High-Voltage $Li_{1.2}Mn_{0.55}Ni_{0.15}Co_{0.10}O_2$ Lithium Ion Battery Cathode: Insight into the Crystal Structure. *Chem. Mater.* **25,** 4064–4070 (2013).

[29] Duer, J. *Introduction to Solid-State NMR Spectroscopy*. (2004).
[30] Andrew E.R. Magic angle spinning in N.M.R. Spectroscopy. Phil. Trans. R . Soc. Lond. A **299**, 505-520 (1981)

CHAPTER 4: NMR METHODOLOGY AND RESULTS

4.1) Introduction

We would like to begin our exploration of electrode pore tortuosity effects on diffusion by measuring bulk diffusion (D_0) and effective diffusion (D_{eff}) coefficients through the use of NMR spectroscopy. Our experimental backbone will be greatly based from our ongoing NMR measurements that our group had established since 2016 [1]. It is imperative to stress to the reader that the diffusion coefficients that we will measure are self-diffusion coefficients meaning diffusion without other external factors such as migration and convection. This is due to that the design of a rotor that can spin at MAS speeds while being passed with electric current to simulate migration will somehow be a whole research topic and is not the scope of this study. Nevertheless, we would greatly assume that the self-diffusion coefficients will be a good reflection of the extent of the effects of pore tortuosity as has been done in literatures regarding electrolyte ion transport.

4.2) Materials, Reagents and Electrode Preparation

Commercial electrode active materials have high magnetic susceptibility due to paramagnetic elements in their chemistry which makes it difficult for NMR studies. An idea was proposed to use a model material with minimal susceptibility. This study will be concentrating on micro sized alumina particles with nano alumina based pellets as comparison. Alumina was chosen due to the magnetic susceptibility reasons established both in the literature review and in our article [1]. Table 4.1 shows the magnetic susceptibility values of different substances. As aforementioned in the literature section, the best spin echo spectra generated by a liquid in a porous environment can only be attained if both the material of the pore walls and of the liquid has almost the same magnetic susceptibilities. Both alumina and LP30 are diamagnetic and have the same magnitude of susceptibility which makes it an ideal model material.

Table 4.1:Magnetic susceptibilities of different substances

Substance	Magnetic susceptibility ($cm^3.mol^{-1}$)
LP30	-42.6×10^{-6}
Carbon Black	$\approx -23.3 \times 10^{-6}$ [2,3]
Al_2O_3	-37.0×10^{-6} [4]
SiO_2	-29.0×10^{-6} [4]
$LiFePO_4$	$\approx +1.90 \times 10^{6}$ [5]
NMC	$\approx +4 \times 10^{-2}$ [6,7]
$LiCoO_2$	$\approx +5 \times 10^{-3}$ [8,9]

The following compounds and reagents were used to prepare model slurries Al_2O_3 (99.97% metal weight purity, 0.250 micron particle size, $8m^2/g$ surface area, Alfa Aesar), C65 Carbon Black (TIMCAL), Vapour Grown Carbon Fiber-S (house grown), PVdF-HFP (Poly-vinylidene Fluoride Hexa Fluoro Propylene, KynarFlex), PVdF (Poly-vinylidene Fluoride , Sigma Aldrich), CMC (Carboxymethylcellulose, MW-250000, Sigma Aldrich), Acetone (AR grade), NMP (N-methyl pyrrolidone, Carlo Erba, AR grade), LP30 ($LiPF_6$ in 1:1 Ethylene Carbonate:Dimethylcarbonate, Solvonic). All reagents and compounds were utilized without further purification. The model mixtures were prepared using different weight percentages of Alumina, conductive additive and binder. The detailed compositions for the nanoalumina-based samples are shown in Table 4.2 and for the macroalumina- ones in Table 4.3.

Table 4.2 Table of nanoalumina sample model compositions [1]

Sample	Nanoalumina wt%	Carbon Black wt%	PVDF-HFP wt%	Porosity
2	90	0	10	29
3	87	3	10	36
4	85	5	10	39
5.6 CB	83.5	6.5	10	38
5	83	7	10	38
7.9 CB	81.5	8.5	10	38
6	80	10	10	48

Table 4.3: Table of microalumina based sample model compositions used in the diffusion experiments. Porosity is equal to 30-35% in all cases.

Sample	Microalumina wt%	Carbon Black wt%	Carbon Fiber	PVdF wt%	CMC wt%	PVdF-HFP wt%
LP30	-	-	-	-	-	-
MacA-PVdFHFP7	95	-	-	-	-	5
MacA-CB3-PVdFHFP7	90	3	-	-	-	7
MacA-CB5-PVdFHFP7	88	5	-	-	-	7
MacA-CB7-PVdFHFP7	86	7	-	-	-	7
MacA-CF3-PVdFHFP7	90	-	3	-	-	7
MacA-CF5-PVdFHFP7	88	-	5	-	-	7
MacA-CF7-PVdFHFP7	86	-	7	-	-	7
MacA-CF5-PVdFHFP4	91	-	5	-	-	4
MacA-CF5-CMC2	93	-	5	-	2	-
MacA-CF5-CMC4	91	-	5	-	4	-
MacA-CF5-PVdF2	93	-	5	2	-	-
MacA-CF5-PVdF4	91	-	5	4	-	-

Figure 4.1: Pellet press (a), pellets (b), oversoaking scheme(c), and in rotor soaking scheme (d).

The basis weight for the slurry mixtures was at 400 mg. All slurries were prepared in IMN Nantes. The chosen binder was pre-dissolved in a plastic vial with 3-4 mL of solvent (NMP for PVdF, acetone for PVdF-HFP and water for CMC) for 1h. The rest of the components were then added with an additional 3-4 mL of solvent and were stirred in a DT-20 Turrax tube attached to an IKA® Ultra Turrax® Tube-Dispenser at a rate of ≈ 3000 rpm for 2 h. Carbon fiber containing mixtures were stopped after 1h and sonicated for 5 minutes before resuming to stir for another 1 h. Bulk of the solvent was dried under the hood and the remaining solvent was dried under a vacuum oven at 90°C. Dried powders were then homogenized using a mortar and pestle and were pelletized using a KBr Quick Press (International Crystal Laboratories) with a 2 mm die and were pressed twice at difference pressure settings. Thickness of the resulting pellets was measured using an IP65 Mitutoyo® micrometer and were regulated between 0.320 and 0.450 mm depending on pellet density resulting into 30-35% porosity. Pellet porosity and densities were determined using the equations:

$$Porosity = \frac{Experimental\ Volume - Theoretical\ Volume}{Experimental\ Volume} \quad \textit{(eq. 4.1)}$$

$$Theoretical\ Volume = \frac{1}{Bulk\ Density} \quad \textit{(eq. 4.2)}$$

$$Bulk\ Density = \frac{Carbon\ wt\%}{100 \times Density_{Carbon}} + \frac{PVdF\ wt\%}{100 \times Density_{PVdF}} + \frac{100 - Carbon\ wt\% - PVdF\ wt\%}{100 \times Density_{Alumina}} \quad \textit{(eq. 4.3)}$$

$$Experimental\ Volume = \frac{1}{Sample\ Density} \quad \textit{(eq. 4.4)}$$

$$Sample\ Density = \frac{Pellet\ mass\ (g)}{Pellet\ volume\ (ml)} \quad \textit{(eq. 4.5)}$$

4.3) NMR Measurements

Pulsed Field Gradient -Stimulated Echo NMR (PFG-STE) was the experimental mode for the determination of self-diffusion coefficients of the electrolyte salt in this study. The aforementioned pellets were soaked in electrolyte in two soaking schemes: oversoaking and precision soaking. Oversoaking involves the soaking of at least 5 pellets with around 0.5 mL of LP30 in an Eppendorf tube in a glove box overnight. Oversoaked pellets were drained of excess electrolyte via tissue before placing in a 3.2 mm rotor for NMR experimentation. Precision soaking (in-rotor soaking or IRS) involved the addition of the theoretical amount of electrolyte needed to occupy the porosity of the pellets (around 30% porosity). Both pellets and electrolyte were added simultaneously in the 3.2 mm rotor and was left to soak overnight. All rotors were centrifuged to ensure electrolyte settled around the pellets. The rotor was then placed in a 3.2 mm standard probehead with magic angle orientation. The probehead was then installed in a Bruker 750 MHz Ultrastabilized™ superconducting magnet (CNRS-CEMHTI Orléans). Magic Angle Spinning at an average speed of 3000 Hz was also employed to achieve optimal spectral narrowing. Spinning faster lead to no further improvement and minimal rotation induced perturbations were considered desirable.

Diffusion experiments were done for the electrolyte species including: Li^+ with ^7Li, PF_6^- with ^{19}F, EC, and DMC with ^1H. The standard stimulated echo sequence with bipolar gradient pulses

was used and spectra acquisition lasted for a maximum of 1-2 days for optimal signal collection. Measurements at different temperatures were done for the pure LP30 electrolyte to help determine the activation energy. Self-diffusion values were then determined by taking the slope of the line of the logarithm of the signal attenuation vs. the gradient strength (Stejskal-Tanner equation).

4.4) SEM Imaging of Alumina Model Composites

Figure 4.2 shows the images of the alumina composites used in the PFG-SE NMR measurements. The macrometric alumina samples composites have larger pores than that of the nanometric alumina composites and have less alumina agglomeration. Carbon fiber containing composites tend to have carbon fiber bundling in some areas. Carbon black appears to be uniformly distributed across the pellet. The particle sizes of the macroalumina pellets also mimic that of LFP in battery electrodes.

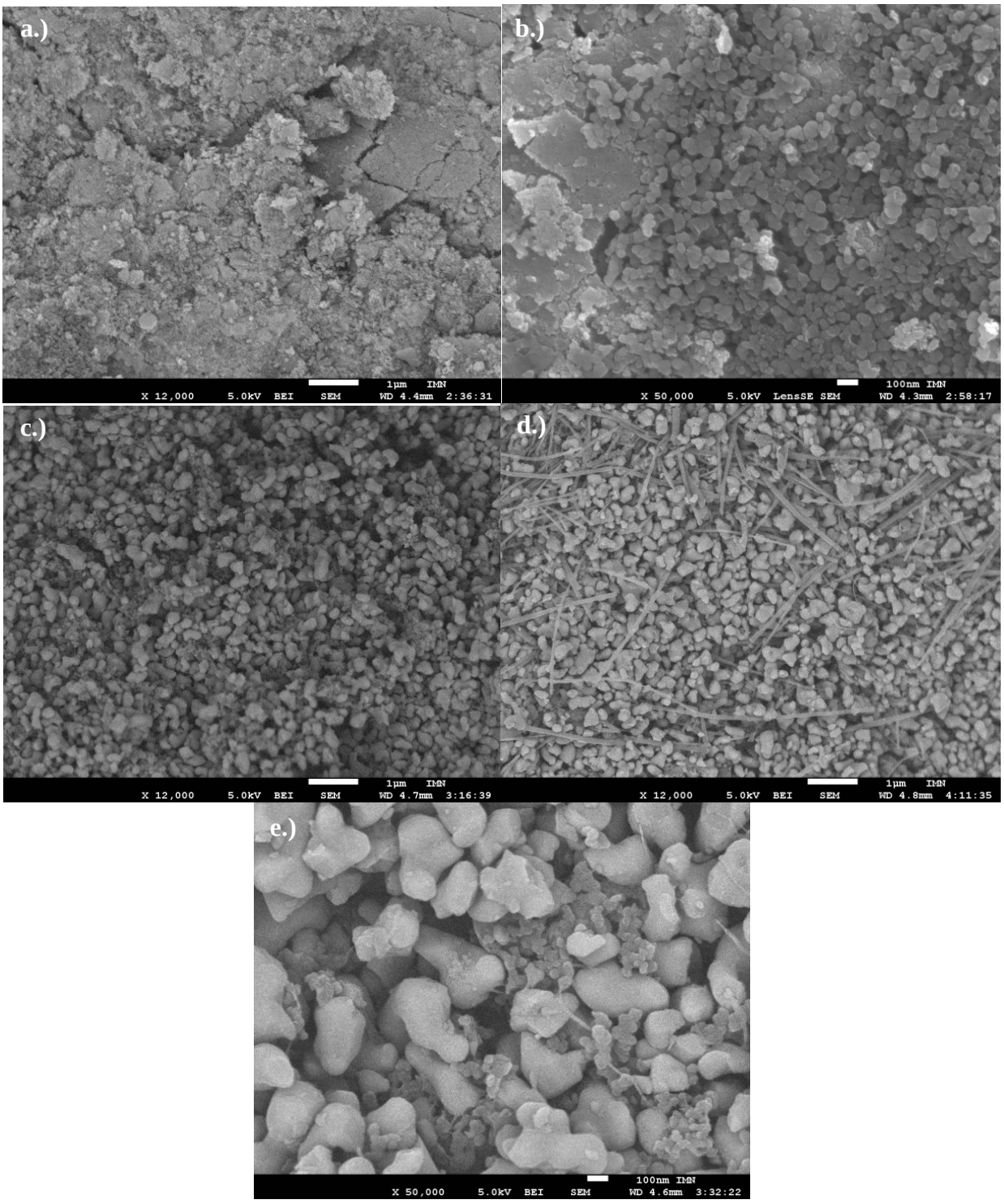

Figure 4.2: SEM images of model pellet surface for nanoalumina pellets based from the previous study at 12,000 (a) and 50,000 (b) magnifications [1], microalumina pellets with CB (c) and CF (d) at 12,000 magnification and at 50,000 magnification with CB (e)

4.5) Electrolyte Impregnation Equilibrium

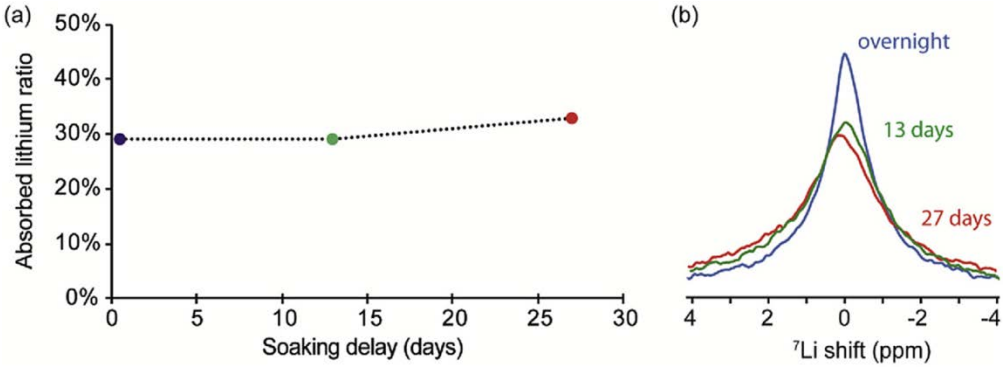

Figure 4.3: Impregnated amount of Li^+ in the nano-alumina pellet pores as a function of soaking time (a). ^7Li spectra at different soaking times (b) [1].

Soaking equilibration time was checked by monitoring the amount of Li impregnated in the nano-alumina based pellets at certain duration (days). This was done by oversoaking nano-alumina pellets with LP30 from 16 hrs. to a maximum of 27 days. Figure 4.3 shows both the ^7Li spectral evolution and the amount of impregnated electrolyte as a function of soaking time. We can clearly see that at all soaking times, we have the desired impregnation of 30% corresponding to the total theoretical porosity of the pellets and also of classic battery electrode composites. These values were determined quantitatively by taking the ratio of the impregnated ^7Li vs. a pure solution of LP30 having the same total volume of the pellets. The spectral shape between overnight soaking and the 27 day soaking regime reveals further broadening suggesting a highly restricted state (gelation) and/or more structural disorder (pellet swelling) at greater soaking times. Both observations tell us that overnight soaking is adequate to allow the electrolyte to impregnate in the pore matrix of the alumina based pellets.

4.6) Self-Diffusion of Bulk Electrolyte Species and Transference Numbers

It is essential to establish, first, the value of the bulk diffusion coefficient of the electrolyte species at different temperatures. Figure 4.4 shows the 1D and 2D spectra of ^7Li, ^{19}F and ^1H in bulk LP30 at 22°C. Knowing that LP30 has four diffusing species: Li^+, PF_6^-, EC (ethylene carbonate) and DMC (dimethyl carbonate), we can then assign the respective nuclei spectra with the four species. EC in the ^1H spectra is associated with the peak around ≈ 4.5 ppm and DMC is associated with the peak around ≈ 3.5 ppm. The 1D spectra of the dissolved species are very

narrow (0.15-0.02 ppm) confirming a liquid environment. 2D contour maps show smooth signal attenuation during the diffusion experiment. Figure 4.5 shows the graph of the diffusion coefficient of different species at increasing temperature. It is seen that the self-diffusion coefficient of the species increases by ≈1.2 at each temperature increment. This is expected due to the decrease in viscosity in the solution. Energies of activation were determined using the Arrhenius equation:

$$\frac{D}{D_0} = exp\left(\frac{-E_a}{RT}\right) \qquad \textit{(eq. 4.6)}$$

which is valid in the liquid state. Lower temperature values might require others fitting functions. From both the table of values and the diffusion coefficient graphs, it can be seen that DMC is the most mobile specie in LP30 is DMC and the slowest is lithium. This is mostly due to both the ion pair and the more preferable solvation affinities of EC with lithium salts [10,11,12]. This meant that DMC is the most labile in this solvent system. This is best seen at 40°C where DMC experiences a steeper increase in self-diffusion coefficient.

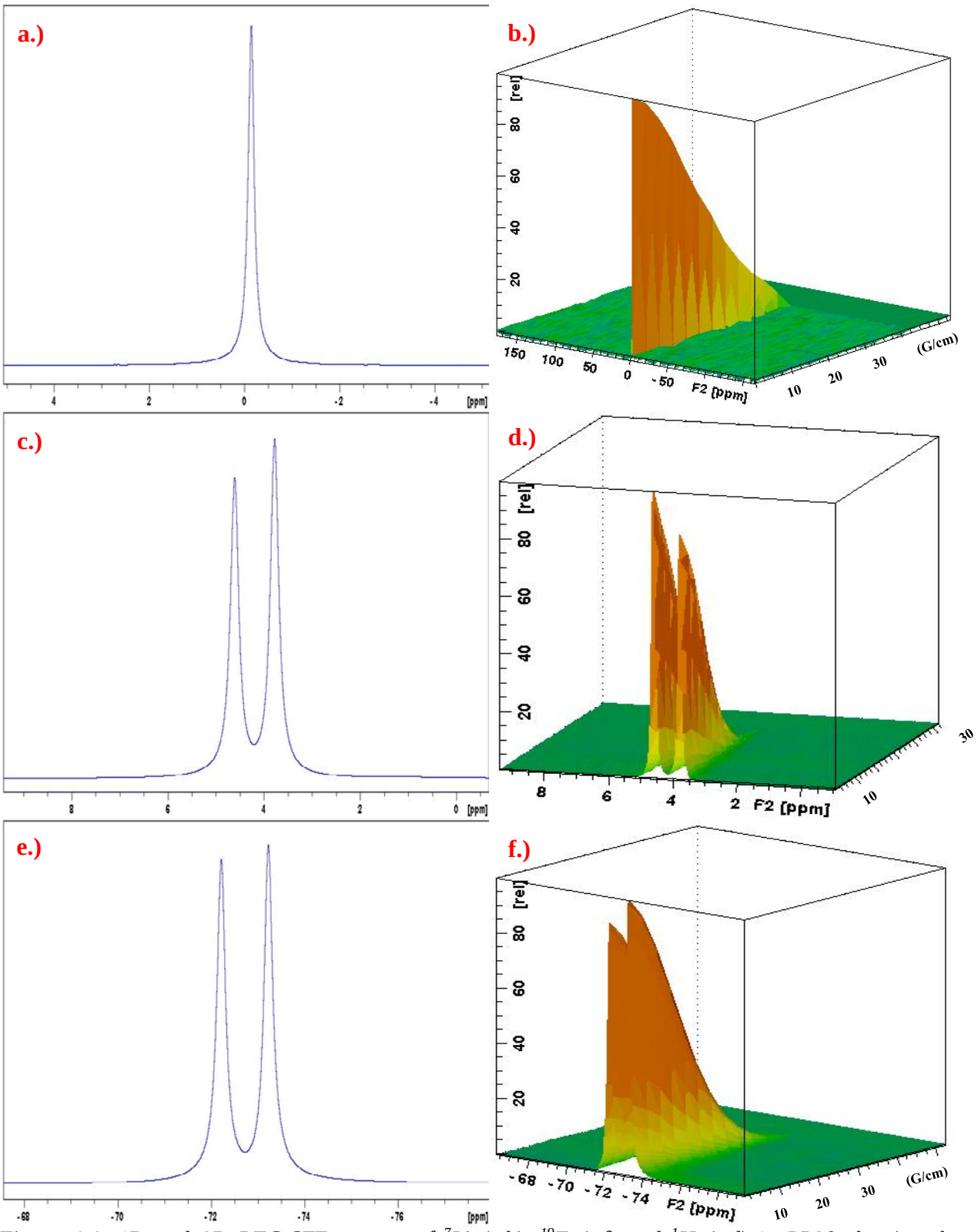

Figure 4.4: 1D and 2D PFG-STE spectra of ^{7}Li (a,b), ^{19}F (e,f) and ^{1}H (c,d) in LP30 showing the attenuation at different gradient strengths.

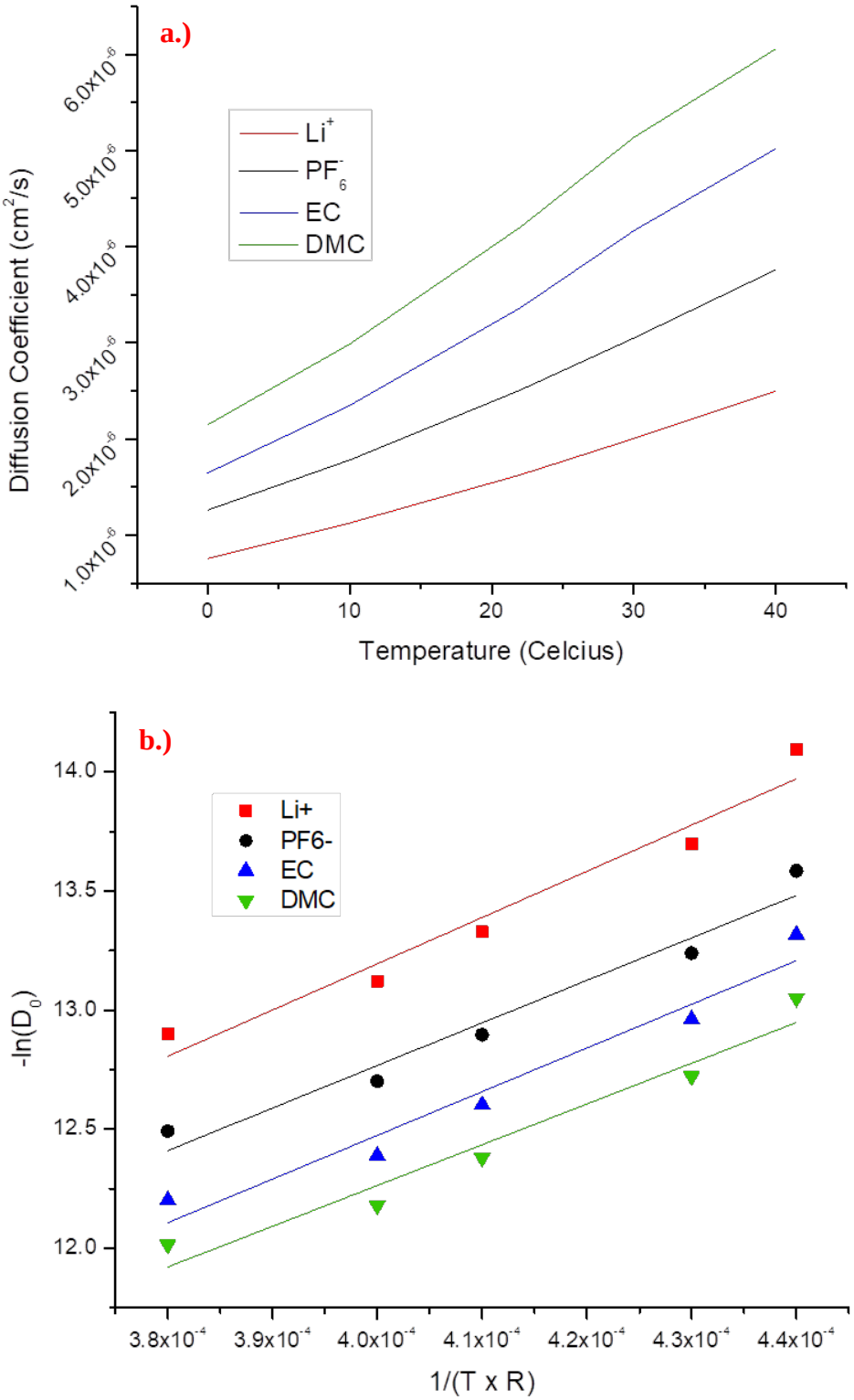

Figure 4.5: Self-diffusion coefficient values of each nuclei at varying temperatures (a), negative logarithm of the self-diffusion coefficients versus inverse temperature – R with linear fit (b).

Table 4.4: Energy of activation values of the different nuclei in LP30

Nucleus	**Li^+**	**PF_6^-**	**EC**	**DMC**
E_a (kJ/mol)	21.2	19.5	20	18.7
E_a (eV)	0.22	0.20	0.21	0.19

We can determine the transference numbers from the aforementioned diffusion coefficients. Various literatures have extrapolated these transference numbers solely from the self-diffusion coefficients of the electrolyte salt. In the case of $LiPF_6$, we can use the equation:

$$t_{Li^+} = \frac{D_{Li^+}}{\left(D_{Li^+} + D_{PF_6^-}\right)} \qquad \textit{(eq. 4.7)}$$

where D_x is the diffusion coefficient of the respective ions. Table 4.5 shows the corresponding transference numbers per temperature. These transference numbers not only show that the increase in charge carrying capacity of Li^+ at higher temperature but are also essential later for the computations concerned with the Penetration Depth Model developed in this thesis.

Table 4.5: Transference numbers of Li^+ at difference temperatures

Temperature (C°)	Li^+ Transference Number
0	0.375
10	0.387
22	0.393
30	0.397
40	0.399

4.7) Self-Diffusion of LP30 Electrolyte Species in Macro-alumina composites

4.7.1) Oversoaked Nanoalumina Pellets

Experiment optimization was done with nano-alumina pellets which were done during the preceding master of this PhD. Optimal diffusion delays were determined by monitoring the decrease in self-diffusion coefficient of the PF_6^- ion at varying diffusion delays. In the PFG-SE sequence as illustrated in Figure 3.6, Δ represents the diffusion delay which is the allowed time for the nuclei species to undergo diffusion before applying the 180° pulse (standard echo sequence) or the 3rd 90° pulse (stimulated echo) and start recording attenuation data. In the

context of a restricted environment, a short diffusion delay may not be enough time for the specie to travel from its local space up to the pore walls. The result is that the measured attenuation will be similar as to what you would expect when measuring diffusion in poor solution/liquid. Therefore the optimal diffusion time must be determined in order to accurately measure diffusion in restricted environments. We were able to observe that the diffusion of the PF_6^- reaches a plateau at a diffusion delay of ≈ 200 ms, suggesting that diffusion delays lower than this value will generate self-diffusion coefficients more similar to what would be observed in the liquid environment. This allowed us to optimize our diffusion time from a minimum of 200 ms. The diffusion coefficients of PF_6^- and Li^+ were then determined using this diffusion time and the D_{eff}/D_0 values are presented in Figure 4.6b. A large decrease in the self-diffusion coefficients of both ions suggests that they are experiencing a restrictive environment in the pellet pore matrix. Moreover, a decreasing trend in self-diffusion coefficient at increasing CB content is also seen suggesting the presence of interactions between CB and Li^+. This is supported by zeta measurements reported in literature [13,14]. Table 4.6 shows the estimated D_{eff}/D_0 values determined via FIB-SEM tomography. These values correspond to estimated D_{eff}/D_0 values of any specie traveling within the pore matrix of our nano-alumina samples at any direction when only geometrical restrictions are considered. Our values determined via PFG-SE NMR are lower than these estimated values further supporting our hypothesis that certain interactions exist between the electrolyte species and the carbon black.

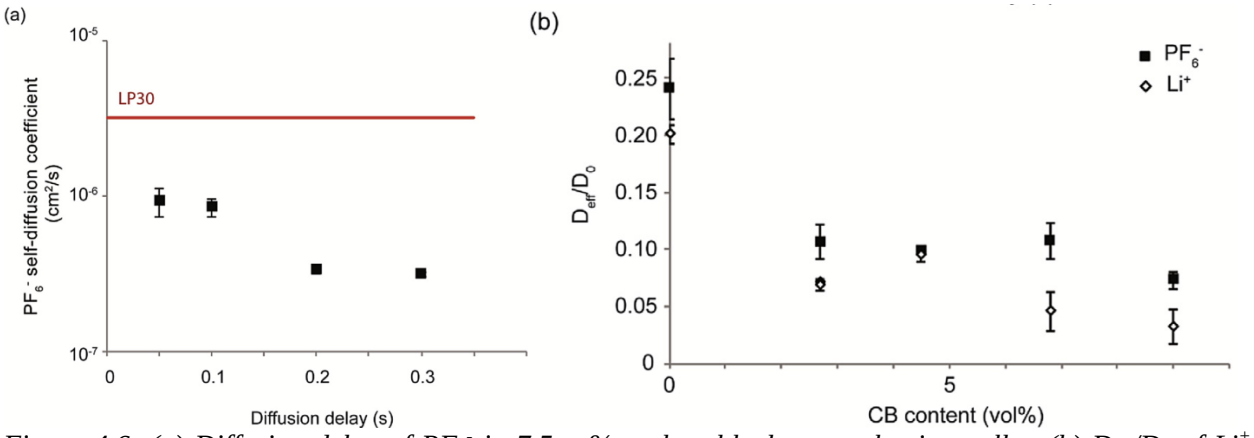

Figure 4.6: (a) Diffusion delay of PF_6^- in 7.5wt.% carbon black nano-alumina pellet. (b) D_{eff}/D_0 of Li^+ and PF_6^- in the nano-alumina pellets at varying carbon black content.[1]

Table 4.6: Table of D_{eff}/D_0 values determined via FIB-SEM tomography [1].

Sample	Tortuosity			D_{eff}/D_0		
	τ_x	τ_z	τ_y	x	z	y
S7	1.23	1.39	1.23	0.66	0.52	0.66
S4	1.21	1.36	1.24	0.68	0.54	0.65

4.7.2) Oversoaked Microalumina Pellets

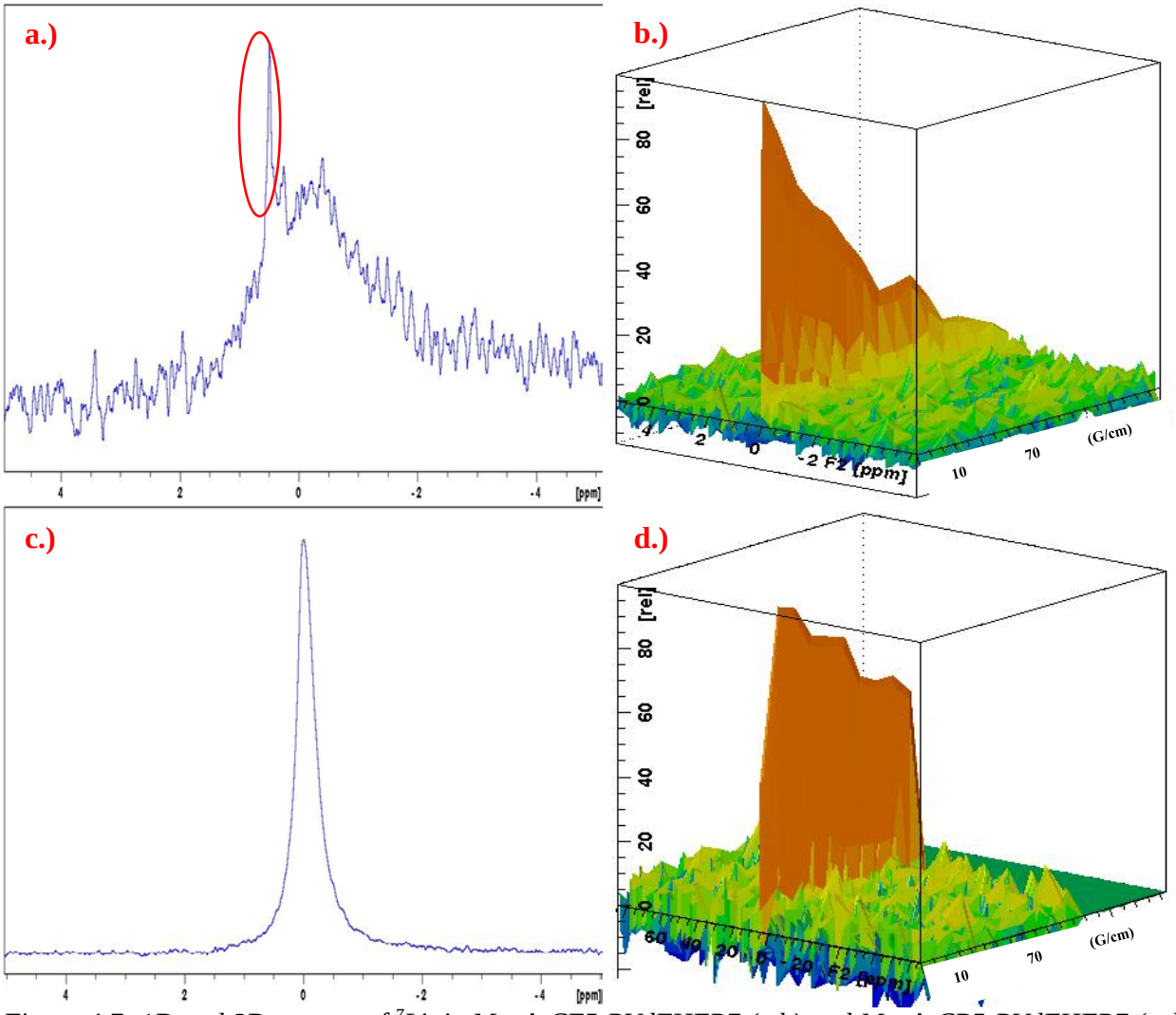

Figure 4.7: 1D and 2D spectra of ^{7}Li, in MacA-CF5-PVdFHFP7 (a,b) and MacA-CB5-PVdFHFP7 (c,d) pellets showing the attenuation at different gradient strengths.

Figure 4.7 shows both 1D and 2D spectra of ^{7}Li, in the oversoaked pellets. 1D spectral widths are 1.55 ppm and 0.3 ppm for the CF and CB containing pellets respectively. The increased

linewidths are indicators of an environment with more restricted dynamics than in liquids. Moreover, the ^{7}Li 1D spectra of MacA-CF5-PVdFHFP7 (Figure 4.7a) showed both broad and narrow peaks indicating two components. The diffusion spectra of MacA-CF5-PVdFHFP7 (Figure 4.7b) only showed the narrow peak suggesting that T_2 of the broader component is too fast for the signal to survive the pulsed gradient delays. The ^{7}Li 1D spectra of MacA-CB5-PVdFHFP7 (Figure 4.7c) only showed a single peak but still have a broader spectrum than the bulk electrolyte. Therefore, the resulting signal is quite low after the PFG-STE sequence, and the attenuation curve is affected by its low signal-to-noise ratio.

Figure 4.8a shows the diffusion coefficients of Li^+ and PF_6^- species in the oversoaked pellets containing either carbon fiber (CF) or carbon black (CB). The curved lines correspond to the superimposed diffusion curve determined from an earlier experiment with nano-metric alumina model composites [1]. The measured diffusion coefficients are almost in the same magnitude as the ones in the nanometric alumina pellet samples at carbon volume percentages of around 6-8%. At lower carbon additive contents, the electrolyte species in nanometric alumina composites have higher diffusion values than that in micrometric alumina composites. Moreover, both CF and CB containing micrometric alumina composites have an almost constant trend of diffusion coefficient at varying carbon additive content for both Li^+ and PF_6^-. This suggests that carbon additive does not play a role in dictating diffusion within these composites. This observation contradicts the results from nano-alumina based pellets wherein carbon black interacts with Li^+ especially at increased CB content. Judging from the SEM images provided in the previous section, the larger pore diameters of the micrometric alumina should allow faster diffusion than in the pores of the nanometric alumina composites. It was then determined during sample preparation and *post mortem* analysis that the composites, when oversoaked, expand and formed a gel-like pellet which was not observed in nanometric alumina pellets. It was then speculated that the PVdF-HFP binder is responsible for the gel formation and gel-like behavior. PVdF based films have been known to interact with common organic electrolyte solvents and form gels [15,16,17,18]. Another hypothesis is that the narrower line widths during the NMR experiment relative to the 1D MAS spectra is due to the T_2 differences between the more mobile species in the larger pores and the restricted species in the narrower pores or in the gel and therefore we

only see the average contribution between the species in the excess electrolyte and the ions in the gel in which the spectra is dominated by the former.

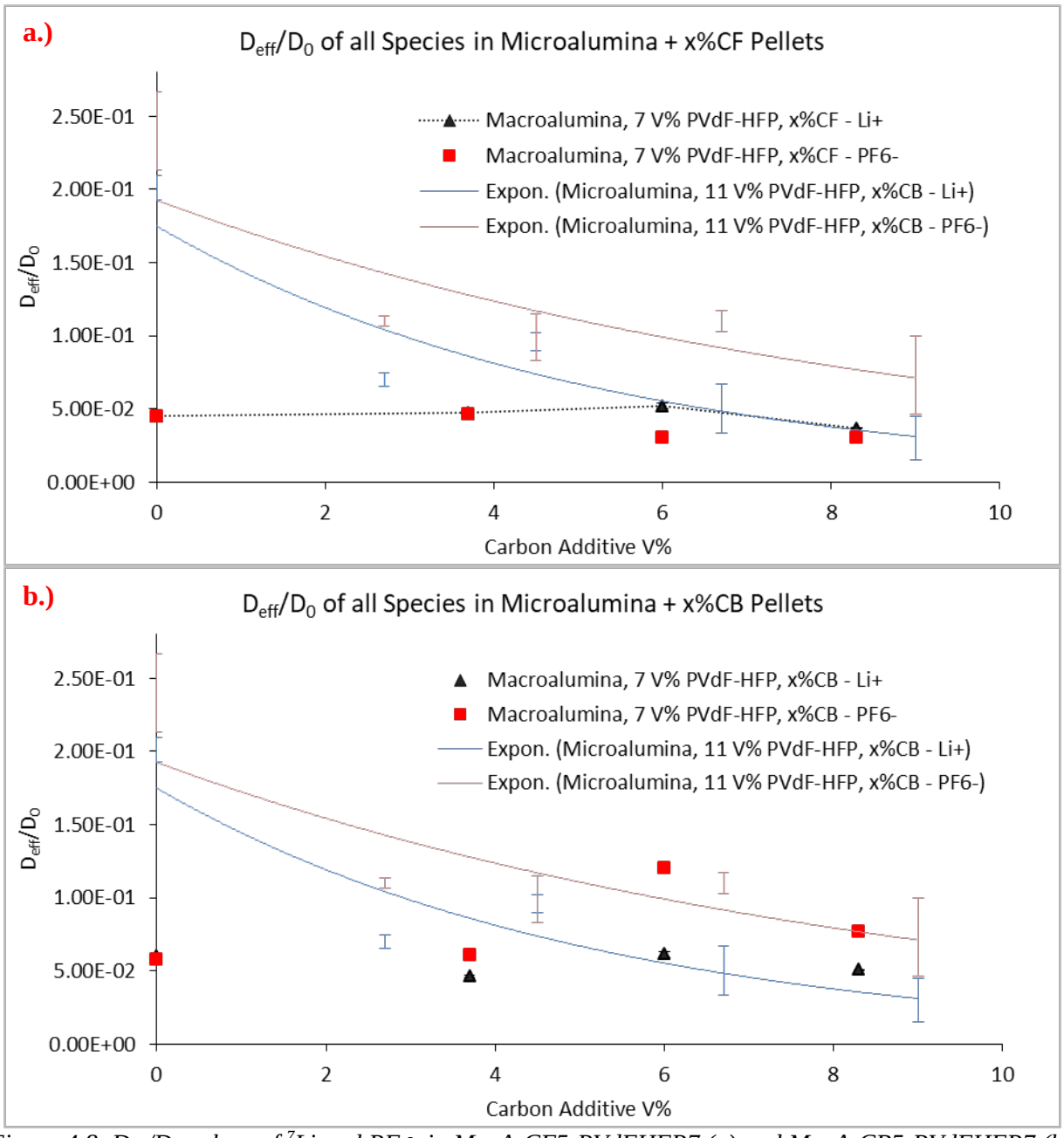

Figure 4.8: *D_{eff}/D_0 values of ^7Li and PF_6^-, in MacA-CF5-PVdFHFP7 (a) and MacA-CB5-PVdFHFP7 (b). Superimposed lines correspond to the D_{eff}/D_0 values that determined from an earlier study [1].*

Another concern is the electrolyte concentration present in the pellet composites. Preliminary analysis of the ^1H spectra of the MacA-CF5-PVdFHFP7 oversoaked pellets showed that the intensity of the DMC peak is lower than that of the bulk electrolyte (Figure 4.9a). This indicates

that there is less DMC content in the oversoaked pellets which could have been a result of the pellet transfer procedure and selective volatilization of DMC that is much more volatile than EC. The evaporation speed of a DMC drop was estimated to be as high as 150 μg/mm^2/s by Saunier et al. [19]. To determine the effects of decreased DMC concentration in the pellet, a comparison was made versus pellets under controlled soaking. This controlled soaking regime requires the introduction of the pellets directly inside the rotor and adding the corresponding amount of electrolyte that would theoretically fill the pellet porosity (30%). This was done with MacA-CF5-PVdFHFP7 pellet composites by adding 1.75 μl of LP30 directly in the pellets in the 3.2 mm rotor. 1D NMR spectra of ^{1}H (Figure 4.9c) reveal two possible components due to the presence of a sharp peak (≈ 0.2 ppm width) and a broad peak (≈ 2.5 ppm width) indicating both the presence of the solvent species and restrictive environments. The retention of the DMC peak intensity at ≈ 1 vs. EC indicates that there was almost no loss of DMC using the new soaking method. Interestingly, the diffusion spectra of the rotor soaked MacA-CF5-PVdFHFP7 pellet composites reveal an attenuated intensity of the DMC peak. This indicates that DMC has a T_2 that is different than that of EC inside the pellet samples. The phenomenon is not observed during diffusion measurements with the bulk electrolyte suggesting that there could be a selective interaction with DMC and with either the pore walls or the functional groups in PVdF-HFP. Moreover, any trapped DMC in the polymeric binder/pore matrix decreases the concentration in the bulk solution thus increasing viscosity and lowering bulk diffusion [20]. The new soaking procedure was then established and the binder was changed to see how the binder affects the NMR spectra of the electrolyte species.

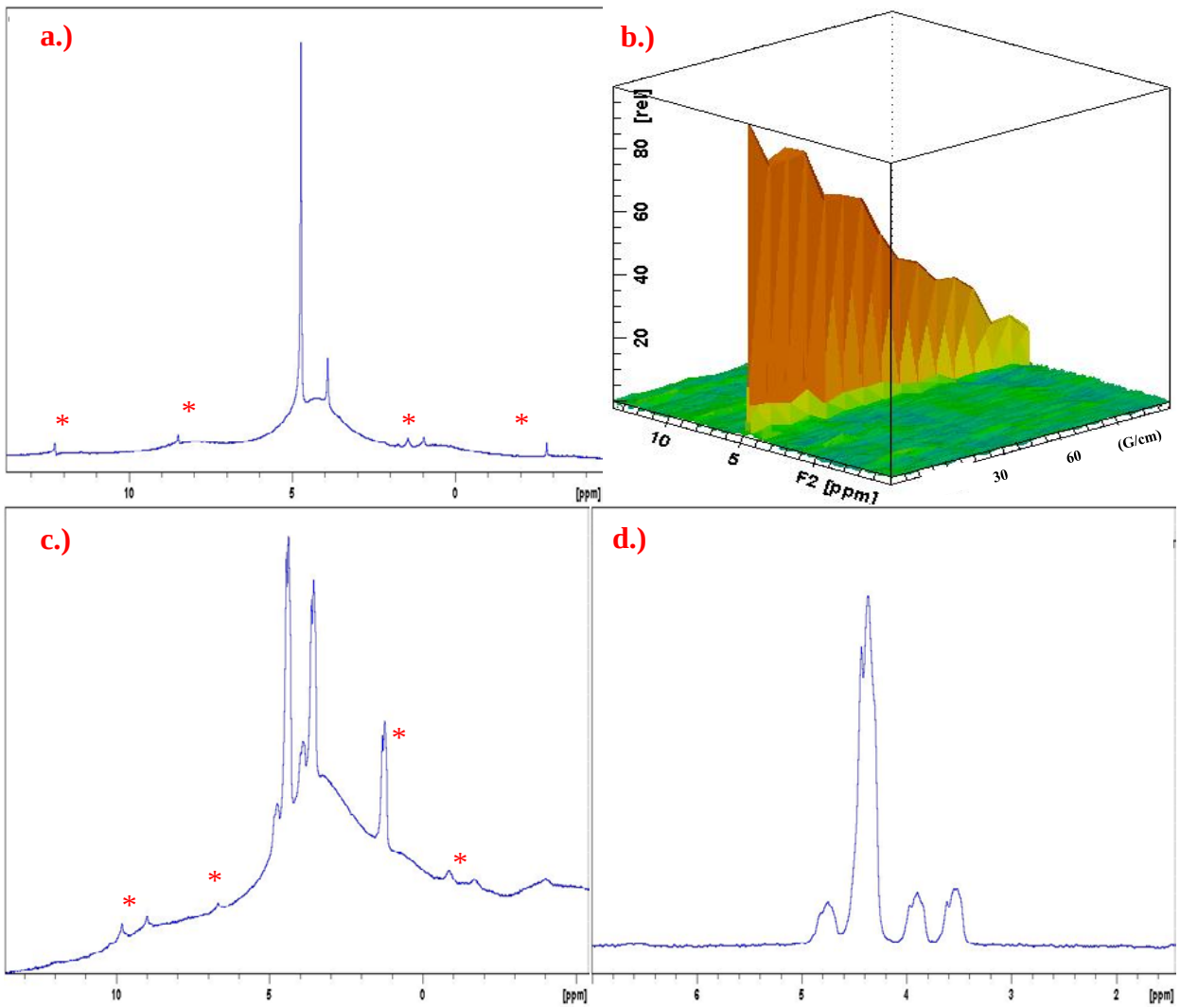

Figure 4.9: 1D and 2D spectra of ^{7}Li, in MacA-CF5-PVdFHFP7 (a) and MacA-CF5-PVdFHFP7 rotor soaked (c) pellets showing the attenuation at different gradient strengths (b). Stars represent spinning sidebands. The large signal attenuation of DMC at the beginning of the PFG-SE Experiment is also seen (d).

4.7.3) Rotor Soaked Pellets

Pellets containing CMC and PVdF were then prepared to examine any differences in diffusion coefficient vs. the previous experiments with PVdF-HFP. Soaking in these pellets were done using the new in-rotor soaking scheme (IRS) to prevent excess liquid and to prevent solvent loss. Figure 4.10 shows the spectra of Li^{+} in pellets containing CMC and PVdF binders. Spectral widths for Li^{+} in MacA-CF5-CMC2 and MacA-CF5-CMC4 pellet composites are ≈ 2.45 and ≈ 3.5 ppm respectively indicating the presence of a restrictive environment. The spectral widths of MacA-CF5-PVdF2 and MacA-CF5-PVdF4 are ≈ 2.6 ppm and ≈ 2.3 ppm also indicating

spectral broadening and restrictive environments. Unfortunately, diffusion experiments were unsuccessful in determining the self-diffusion coefficient of all the electrolyte species in the four sample pellets. Table 4.7 shows the T_2 values of the various species in the sample composites. T_2 is called transverse relaxation and describes the time it takes for the bulk magnetization of the spins to precess in desynchronization with each other. The same precession synchronization phenomenon that dictates the PFG-SE experiment is also the same precession phenomenon that dictates T_2. This means that dipolar interactions, internal gradients, etc. can affect transverse relaxation.

Table 4.7: T2 values of each nuclei in varied binder pellet samples

Sample	**T_2 Li^+ (ms)**	**T_2 PF_6^- (ms)**	**T_2 EC (ms)**	**T_2 DMC (ms)**
LP30	993	979	389	424
MacA-CB7-PVdFHFP7 (Oversoaked)	2.5	1	13.4	10
MacA-CF5-CMC2	44	0.002	7.5	-
MacA-CF5-CMC4	0.5	0.17	0.31	0.36
MacA-CF5-PVdF2	55	0.16	0.40	-
MacA-CF5-PVdF4	0.57	0.16	0.32 (both peaks overlapped)	

The T_2 values for Li^+ were observed to be 2 orders of magnitude lower than that of the bulk electrolyte. These very fast T_2 value highlight one of the big limitations of the PFG-SE technique. The gradient pulse should be applied in an adequate amount of time to allows the spins to properly precess according to the applied gradient strength. A gradient pulse that is too short will result in insufficient defocusing but a very long gradient pulse will result in too much defocusing of the spins. Since that T_2 is too fast compared to the minimum allowable gradient pulse (≈ 2 ms), it meant that the signal has already decayed long before the gradient pulse has ended. A crude attempt by combining the minimal gradient pulse with the strongest gradient field strength also did not yield any result. However, the difference in T_2 between the bulk electrolyte, the oversoaked pellets and in the rotor soaked pellets greatly suggest a highly restrictive behavior in the pellet pores. These fast T_2 relaxations indicate the presence of heavy interactions between the electrolyte species and the walls of the pores or functional groups of the binder.

In comparison with the NMR spectra of solid state substances (crystalline/powders), which typically have line widths in the range of hundreds to thousands of Hz, the spectral widths in the pellet samples are still too narrow to be considered to be in full solid state. Both observations suggest that this highly restrictive environment is close to a “gel state” in which a liquid is encased in a porous solid matrix, both held by interactions between the functional groups in both in the liquid and solid, in a similar manner to what is observed in polymer electrolytes [21]. Moreover, it is likely that the surviving narrow signal corresponds to electrolyte in larger pores.

One detail that came into our attention was the initial processing of the CMC binder in these samples. CMC in theory poorly interacts with the organic solvents of LP30 which in turn should not generate a gel environment. The T_2 values say otherwise. *Post mortem* analysis also showed that both the PVdF containing pellets and the CMC containing pellets become “mushy” similar to the oversoaked pellets. Indeed, the composite samples are obtained, after mixing of the various constituents, by removing the solvent for processing and scraping the dry material. The resulting powder is then pressed to form a pellet. But in this one, there are no mechanical links between the different particles because the polymer bridges were broken during the scraping of the material to recover it in powder form. It was then recognized that the CMC pellets needed post-pelletization treatment which meant exposure to water to reactivate the CMC hydroxyl hydrogen bonds improving the structural integrity of the pellets. A new post-treatment scheme was then formulated to increase binder-binder interaction and eventually decrease the possibility of gelation and eventually increase T_2 and possibly determine the diffusion coefficient of the electrolyte species.

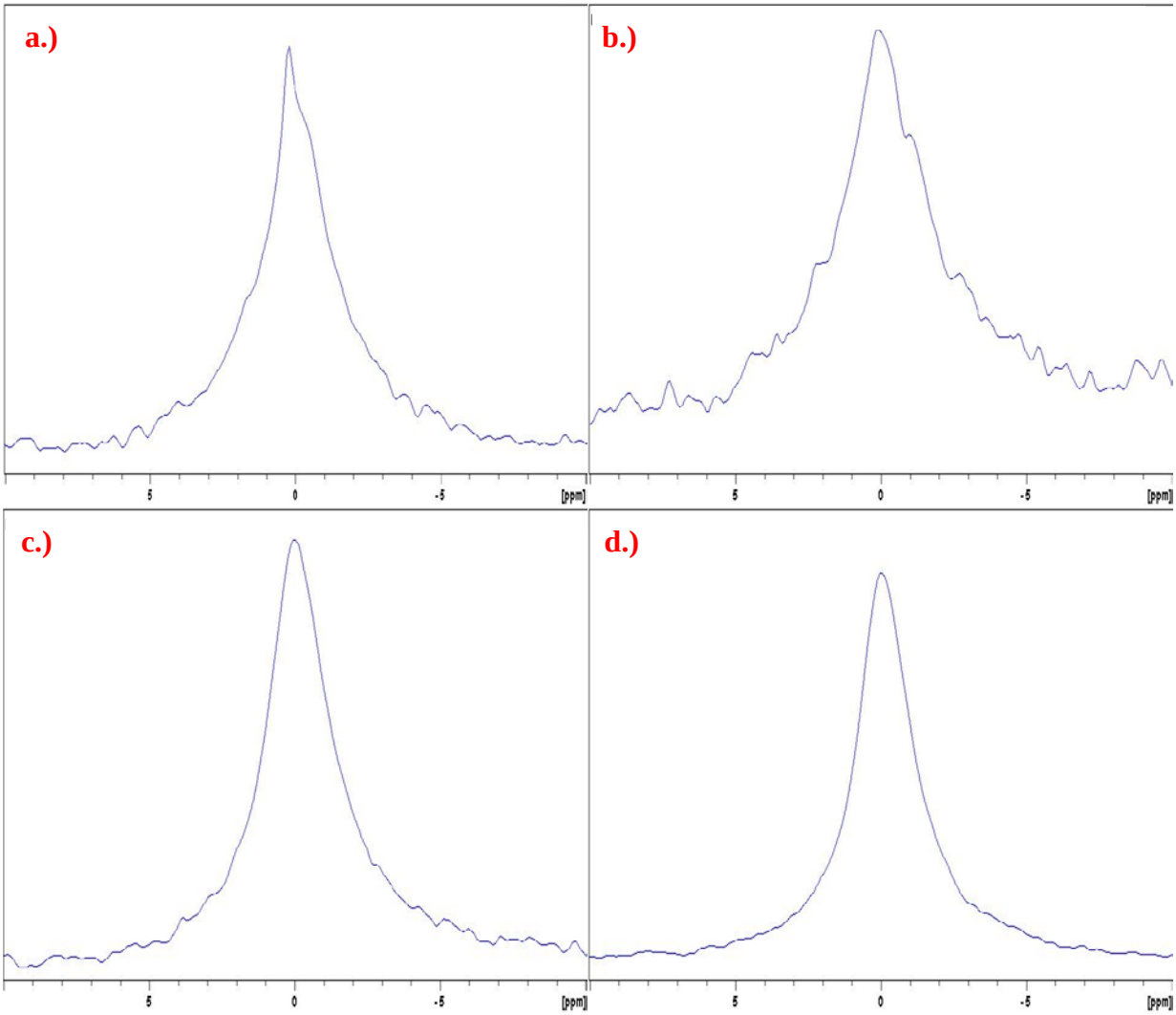

Figure 4.10: 1D spectra of ^{7}Li in MacA-CF5-CMC2 (a), MacA-CF5-CMC2 (b), MacA-CF5-PVdF2 (c), MacA-CF5-PVdF2 (d), untreated pellets showing no change in line width at increased electrolyte amounts.

4.8) Rotor Soaked Pellets After Solvent Treatment

Post-pelletization treatment was done through exposure of the pellets through solvent vapor. Pellets containing PVdF were exposed to NMP vapors and pellets containing CMC were exposed to water vapor. The vapor chamber setup is shown in Figure 4.11. The pellets were exposed to the vapors of their respective solvents at a temperature of 60°C overnight and were then dried in a vacuum oven at 90°C overnight. The treated pellets, especially CMC macroscopically exhibited better resistance to pulverization and cracking. These pellets were then soaked with electrolyte using IRS and were then eventually ran with PFG-SE experiments

in a 3.2 mm rotor. The electrolyte amount was increased twice with an increment of 5% volume to monitor effects of slight increments of electrolyte on the diffusion coefficients.

Figure 4.11: Solvent chamber setup for binder activation treatment

Table 4.8: Li^+ T_2 values in the IRS pellets while gradually increasing the electrolyte content.

Sample	**T_2 Li^+ (ns)**
LP30	993 (ms)
MacA-CF5-CMC4 (30% IRS)	0.258
MacA-CF5-CMC4 (35% IRS)	0.232
MacA-CF5-CMC4 (40% IRS)	0.381
MacA-CF5-PVdF4 (30% IRS)	0.532
MacA-CF5-PVdF4 (35% IRS)	0.393
MacA-CF5-PVdF4 (40% IRS)	0.517

The Li^+ spectra of LP30 in MacA-CF5-CMC4 and MacA-CF5-PVdF4 pellets at different electrolyte amounts are shown in Figure 4.12. The spectra at each electrolyte increment for all pellet samples seem to have the same spectral width indicating minimal to no evolution of the restrictive environment in the pore matrix. This is supported by the T_2 values of Li^+ in all the samples indicated in Table 4.8. The magnitudes of the values are at the sub-microsecond scale

even at increasing electrolyte content suggesting the possibility of inadequately surpassing the full gel state, or having strong Li^+-OH-CMC interactions.

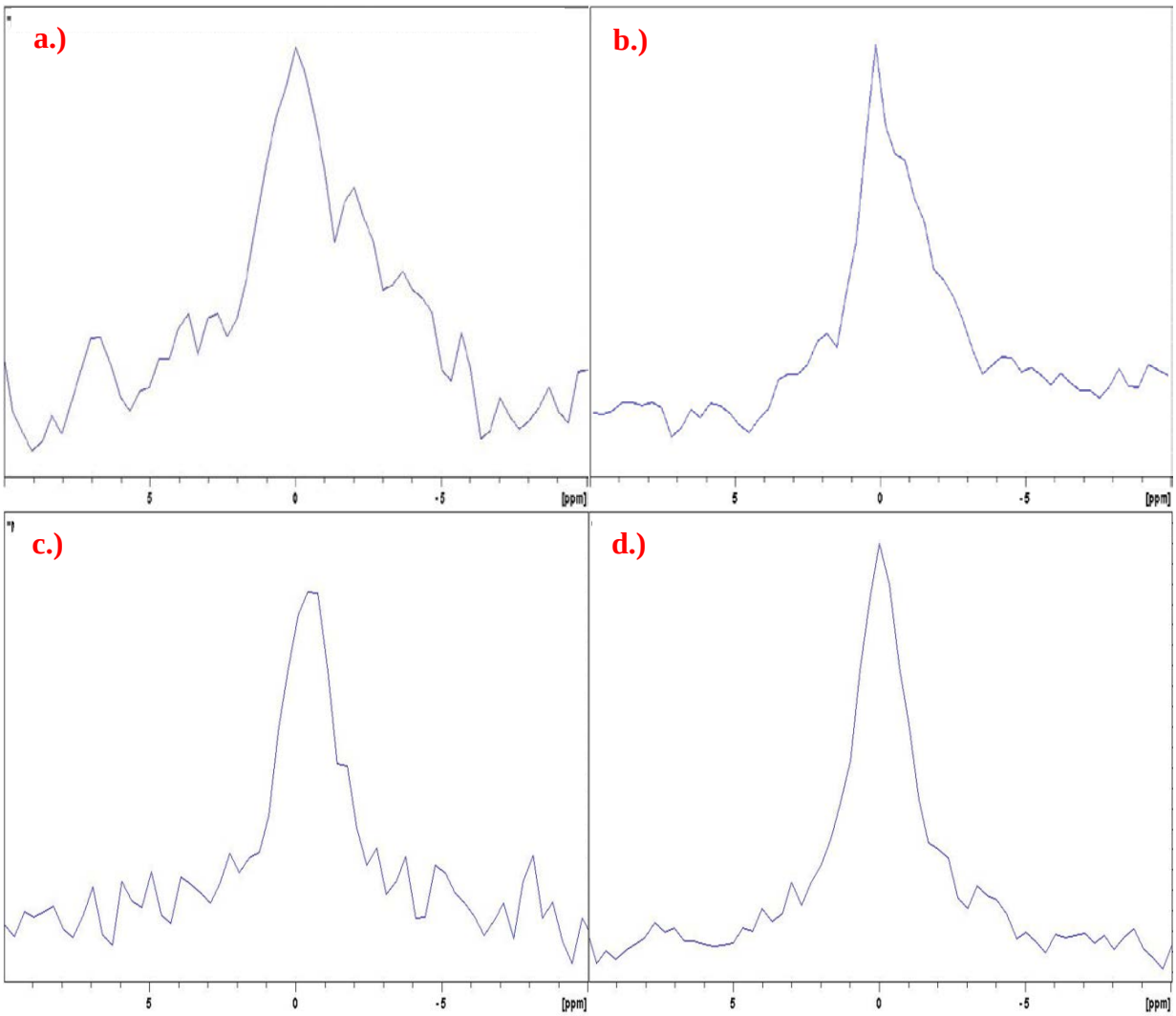

Figure 4.12: 1D spectra of ^7Li in MacA-CF5-CMC4 soaked in 30% (a) and 40%(b) electrolyte amount. MacA-CF5-PVdF4 soaked in 30% (c) and 40% (d) electrolyte amount. Both treated pellets showed no change in T_2 despite spectral narrowing at increased electrolyte amounts.

4.9) Equilibrium Time Gelation Study

To better understand the diffusion kinetics of lithium ions in a gel-like system, diffusion NMR experiments were performed at different temperatures with a binder-electrolyte system. The system was comprised of a mass ratio of 16% of polymer impregnated in 84% of electrolyte. This corresponds to 3,9 mg of PVDF film impregnated with 15,9 µL of LP30. A diffusion delay of 300 ms were used for both $\Delta(^7Li)$ and $\Delta(^{19}F)$. Temperature increments were made every 5°C

between 25°C and 50°C. At the end of this thermal cycle, the measurement was repeated at 25°C to determine the reversibility of the system. All experiments were performed by Benjamin Porcheron of CEMHTI Orleans.

Figure 4.13a describes the evolution of the diffusion coefficients of Li^+ and PF_6^- in the polymer-electrolyte system at varying temperatures. As expected, the diffusion coefficients increase at increasing temperatures due to viscosity changes. Two components for PF_6^- are seen for this system, one of which is faster than Li^+ and the other is slower than Li^+. Interestingly, the diffusion coefficients of Li^+ and the restricted PF_6^- in this system are lower than in the bulk but the diffusion coefficients of the more labile PF_6^- is almost the same as the bulk diffusion coefficient of Li^+. This observation suggests that there exists an interaction of both Li^+ and PF_6^- with PVdF. More interestingly, it appears that the majority of the Li^+ ions were slowed down but PF_6^- has two identifiable components. This suggests that PVDF has a major selectivity of interaction with Li^+ due to that almost all of the species are slowed down and only a fraction of PF_6^- is slowed down due to that two components were distinguished with one being slower than Li^+. We would like to remind the reader that NMR is a bulk technique wherein the generated spectra are dependent on the average of the sum of the environments that a nucleus is experiencing. Also, lithium is three times less sensitive to the gradient (small gyromagnetic ratio) and in combination with its interaction with the polymer, could have made it almost impossible to detect the end of the decay tail (very fast T_2) and in turn extract the slow Li^+ component.

The E_a diffusion values of the species determined from the fits of the data with equation 4.6 in in Figure 4.13b are also presented in Table 4.9. It is remarkable that the E_a values are lower than those found in the bulk diffusion values highly suggesting different environments between the two. These values correspond closely to those that are found in literature [16]. The activation energies of diffusion in the presence of a porous membrane may be lower than that of what is found in the electrolyte bulk but looking closely, the slope of the line for the diffusion in the membrane is due to the minimal increment in diffusion relative to what is found in the bulk. Hence, the E_a may be lower but it describes the restricted environment in comparison to a more mobile environment.

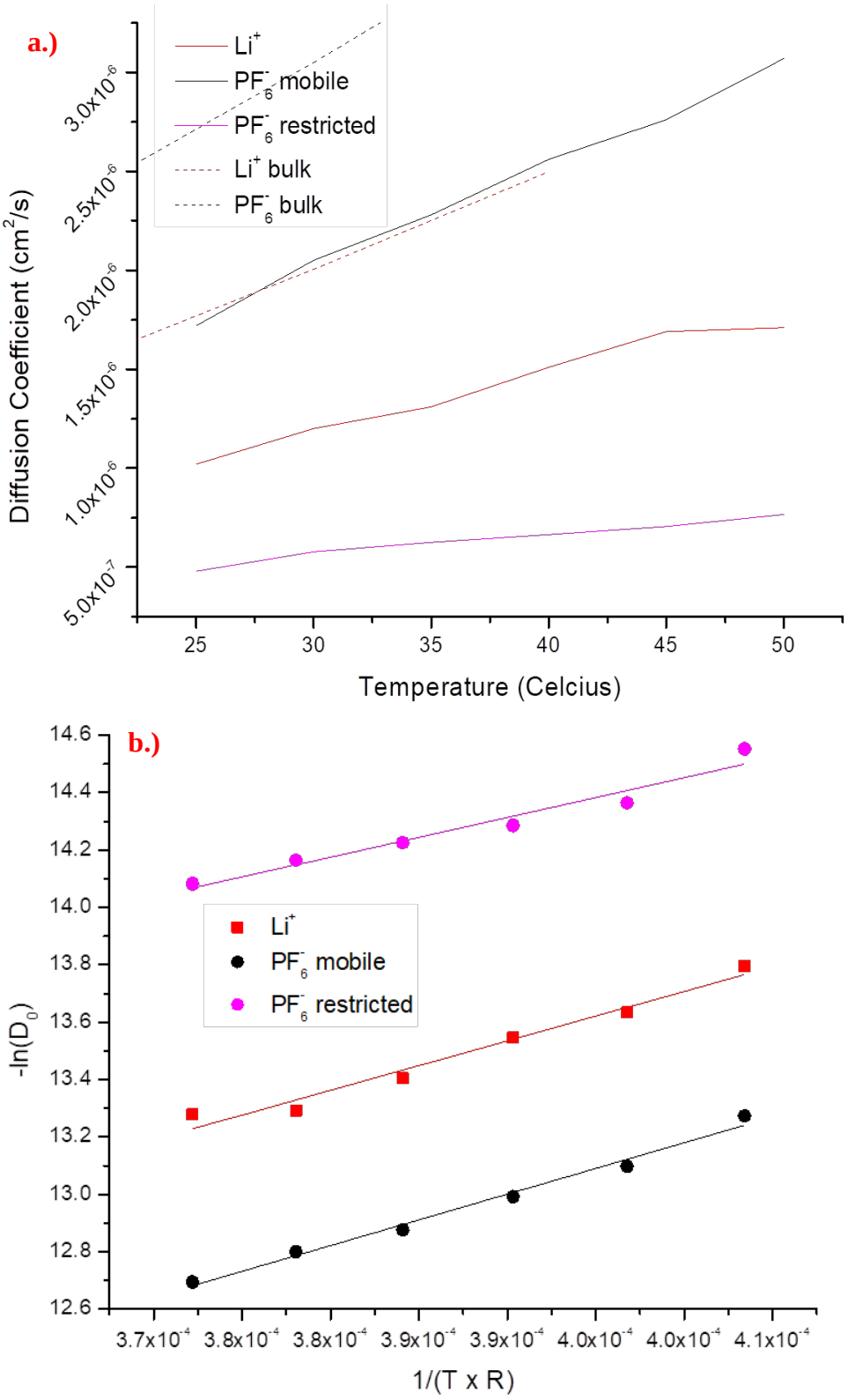

Figure 4.13: Self-diffusion coefficient values of Li^+ and PF_6^- in the electrolyte-film mixture at varying temperatures (a), negative logarithm of the self-diffusion coefficients versus inverse temperature – R with linear fit (b). Dotted lines show superimposed bulk diffusion values. Courtesy of Benjamin Porcheron.

Table 4.9: Energy of activation values for Li^+ and the two component PF_6^-. *Courtesy of Benjamin Porcheron.*

Nucleus	**Li^+**	**PF_6^- (Fast)**	**PF_6^- (Restricted)**
Ea (kJ)	17.2	17.9	13.8
Ea (eV)	0.18	0.19	0.14

4.10) Conclusion

We have successfully determined several diffusion coefficients of LP30 electrolyte species in both restricted and free environments. Firstly, DMC has the fastest diffusion coefficient due to viscosity changes, solvation affinity and how the diffusion spectra decays faster than that of EC Secondly, we have also identified, in accordance with existing literatures, that binder swelling due to DMC absorption can decrease Li diffusion in the bulk. This was manifested through the observed T_2 values and in turn the very difficult observation of the spin echo spectra for Li^+. Polymer swelling induces concentration gradients shifting viscosity values both in the polymer wells and in the bulk electrolyte. These reductions in diffusion coefficients relative to the bulk diffusion greatly highlight how interactions can affect the diffusion coefficients of the electrolyte species. Unfortunately, the magnitude of these strong interactions between the electrolyte species and the binder could've greatly impeded our ability to detect the effects of tortuosity with the self-diffusion coefficients. Although this might be the case, these determined values give us benchmark values pertaining to tortuosity effects of electrolyte-polymer systems with diffusion. Nevertheless, these values might shed some light for our model in order to identify ionic conductivity limitations by interactions and/or by tortuosity.

[1] Tambio, S. J. et al. Self-diffusion of electrolyte species in model battery electrodes using Magic Angle Spinning and Pulsed Field Gradient Nuclear Magnetic Resonance. *J. Power Sources* **362**, 315–322 (2017).
[2] H.T. Pinnick, Magnetic Susceptibility of Carbons and Polycrystalline Graphites. I*. *Phys. Rev.* **94,** (1954).
[3] J.B. Donnet, *Carbon Black: Science and Technology*, second ed., CRC Press 1993
[4] D.R. Lide, *Magnetic susceptibility of the elements and inorganic compounds, in: Handbook of Chemistry and Physics*, CRC Press, Boca Raton (FL, USA), 2005, pp. 130–135.
[5] Creer, J. G. & Troup, G. J. The magnetic susceptibility of $LiFePO_4$ and $LiCoPO_4$. *Phys. Lett.* A **32**, 439–440 (1970).

[6] Mohanty, D. et al. Neutron diffraction and magnetic susceptibility studies on a high-voltage $Li_{1.2}Mn_{0.55}Ni_{0.15}Co_{0.10}O_2$ lithium ion battery cathode: Insight into the crystal structure. *Chem. Mater.* **25**, 4064–4070 (2013).
[7] Mohanty, D. et al. Correlating cation ordering and voltage fade in a lithium-manganese-rich lithium-ion battery cathode oxide: a joint magnetic susceptibility and TEM study. *Phys. Chem. Chem. Phys.* **15,** 19496–509 (2013).
[8] Hertz, J. T. et al. Magnetism and structure of $LixCoO_2$ and comparison to Na_xCoO_2. *Phys. Rev.* B **77,** 75119 (2008).
[9] Motohashi, T. et al. Synthesis and properties of CoO_2, the x = 0 end member of the Li_xCoO_2 and Na_xCoO_2 systems. *Chem. Mater.* **19,** 5063–5066 (2007).
[10] Tasaki, K. et al. Solubility of lithium salts formed on the lithium-ion battery negative electrode surface in organic solvents. J. Electrochem. Soc. **156**, 1019–1027 (2009).
[11] Skarmoutsos, I., Ponnuchamy, V., Vetere, V. & Mossa, S. Li+ solvation in pure, binary, and ternary mixtures of organic carbonate electrolytes. *J. Phys. Chem. C* **119**, 4502–4515 (2015).
[12] Xu, K. Nonaqueous liquid electrolytes for lithium-based rechargeable batteries. *Chem. Rev.* **104**, 4303–4417 (2004).
[13] Zhang, Y., Narayanan, A., Mugele, F., Cohen Stuart, M. A. & Duits, M. H. G. Charge inversion and colloidal stability of carbon black in battery electrolyte solutions. *Colloids Surfaces A Physicochem. Eng. Asp.* **489**, 461–468 (2016).
[14] Youssry, M. *et al.* Non-aqueous carbon black suspensions for lithium-based redox flow batteries: rheology and simultaneous rheo-electrical behavior. *Phys. Chem. Chem. Phys.* **15**, 14476–86 (2013).
[15] Saunier, J., Gorecki, W., Alloin, F. & Sanchez, J. Y. NMR study of cation, anion, and solvent mobilities in macroporous poly(vinylidene fluoride). *J. Phys. Chem. B* **109,** 2487–2492 (2005).
[16] Richardson, P. M., Voice, A. M. & Ward, I. M. NMR self diffusion and relaxation time measurements for poly (vinylidene fluoride) (PVDF) based polymer gel electrolytes containing $LiBF_4$ and propylene carbonate. *Polymer (Guildf).* **97,** 69–79 (2016).
[17] Kataoka, H., Saito, Y., Sakai, T., Quartarone, E. & Mustarelli, P. Conduction Mechanisms of PVDF-Type Gel Polymer Electrolytes of Lithium Prepared by a Phase Inversion Process. *J. Phys. Chem. B* **104,** 11460–11464 (2000).
[18] Chapiro, A., Mankowski, Z. & Schmitt, N. Unusual swelling behavior of films of polyvinyl- and polyvinylidene/fluorides in various solvents. *J. Polym. Sci. Polym. Chem. Ed.* **20,** 1791–1796 (2003).
[19] Saunier, J., Alloin, F., Sanchez, J. Y. & Barrière, B. Plasticized Microporous Poly(vinylidene fluoride) Separators for Lithium-Ion Batteries. I. Swelling Behavior of Dense Membranes with Respect to a Liquid Electrolyte - Characterization of the Swelling Equilibrium. *J. Polym. Sci. Part B Polym. Phys.* **42**, 532–543 (2004).
[20] Krachkovskiy, S. A., Pauric, A. D., Halalay, I. C. & Goward, G. R. Slice-selective NMR diffusion measurements: A robust and reliable tool for in situ characterization of ion-transport properties in Lithium-ion battery electrolytes. *J. Phys. Chem. Lett.* **4**, 3940–3944 (2013).
[21] Huynh, T. V. *et al.* Restricted lithium ion dynamics in PEO-based block copolymer electrolytes measured by high-field nuclear magnetic resonance relaxation. *J. Chem. Phys.* **147**, (2017).

CHAPTER 5: ELECTROCHEMISTRY METHODOLOGY AND RESULTS

5.1) Introduction

Evaluating power performance in relation to electrode parameters and Li^+ transport is the end goal of this study. We cannot stress enough the importance of performing electrochemical measurements as a means to validate tortuosity and interaction effects on electrode power performance. This is attainable only by performing traditional electrochemical cycling of NMC based electrodes. We would also like to highlight that this study focuses on relatively thick electrodes with loading values almost double or triple than those found in numerous literatures (see Table 2.2). This enables us to really evaluate power performance at increased energy density especially from an application perspective. We will concentrate on the following aspects that in evaluating the electrochemical performance of our electrodes namely: delivered capacity, cell resistances, nominal capacity (Q_0) determination and PD (penetration depth) modeling. Our comparisons will center on two similarly thick but compositionally different electrode families as a means of exhaustively comparing formulation effects. The electrochemical performances will then be evaluated with PD and the electrode's corresponding cell resistance as to determine the operational limiting factors. The PD model will then allow us to determine power limitations and diffusion coefficients and if possible compare the values against those determined with NMR and draw relevant conclusions.

5.2) Electrodes

5.2.1) Electrode Compositions and Specifications

Electrodes with varying amounts of NMC 532, carbon black, and PVdF were used as received from RENAULT. The electrode specifications are presented in Tables 5.1 to 5.3. They differ by their CB and PVdF contents, respectively 2.2 and 1.8wt% for the NAx series, and 3.2 and 2.6wt% for the NAxb one. NA3, NA2, and NA2b have lower densities (higher porosities) than NA7, NA3b, NA4b, NA7b. NA8 has slightly lower density than the last four electrodes. NA3 and NA3b have lower thicknesses and NA4b has higher thickness than NA7, NA8, and NA7b.

Table 5.1: Weight percentages of the electrode components for NAx and NAxb

Percent Weight Compositions of the NMC532 Positive Electrode Sets			
Batch	**NMC**	**CB**	**PVdF**
NAx	96	2.2	1.8
NAxb	94.2	3.2	2.6

Table 5.2: Electrode specifications of the NAx set (average manufacturer, actual loading in parenthesis).

NAx Electrode Specifications								
Electrode	**Density**	**Loading tot**	**Qsurf**	**Thickness**	**Porosity**	**NMC**	**CB**	**PVdF**
	(g/cm3)	(mg/cm²)	(mAh/cm²)	(µm)	Volume fractions (%)			
NA2	3.2	26.0 (24.4)	4.2	81.4	28.0	64.8	3.6	3.6
NA3	3.2	15.6 (14.9)	2.5	48.8	28.0	64.8	3.6	3.6
NA7	3.5	26.0 (25)	4.2	74.4	21.2	70.9	3.9	4.0
NA8	3.4	26.0 (24.7)	4.2	76.6	23.5	68.9	3.8	3.9

Table 5.3: Electrode specifications of the NAxb set (average manufacturer, actual loading in parenthesis).

NAxb Electrode Specifications								
Electrode	**Density**	**Loading tot**	**Qsurf**	**Thickness**	**Porosity**	**NMC**	**CB**	**PVdF**
	(g/cm3)	(mg/cm²)	(mAh/cm²)	(µm)	Volume fractions (%)			
NA2b	3.2	26.5 (25.3)	4.2	82.9	26.0	63.6	5.2	5.1
NA3b	3.5	15.9 (14.6)	2.5	45.5	19.1	69.9	5.7	5.6
NA7b	3.5	26.5 (25.35)	4.2	75.8	19.1	69.6	5.7	5.6
NA4b	3.5	41.7 (40.7)	6.7	119.1	19.1	69.6	5.7	5.6

5.2.2) Basic Characterizations (SEM and electrical measurements)

Electrode images were taken using a Jeol 7600 Scanning Electron Microscope (IMN Nantes) with varying magnifications. Samples were mounted on a SEM stub fitted with carbon tape for adhesion. Gold sputtering was automatically done and silver paste was also added whenever needed. Electron energy was set at 5eV and the majority of images were taken using secondary electrons. Backscattered electron imaging was also done whenever necessary. Images include the electrode surface and the electrode cross section.

SEM images reveal the various particles included in the composite electrode. Porosity can be instantly seen from the electrodes which is essential for electrolyte impregnation and eventually allow electrochemical cycling. The pore sizes in NA7 (densest electrode in the NAx set) are qualitatively smaller than that of NA2 or NA3 which supports the compaction specifications of

the electrodes. Comparing NAx and NAxb electrodes also shows that the pores in NAxb electrodes are more filled with the CB-binder complex confirming the additional amounts of additives. This is seen from the backscattered images of the NAxb electrodes (Figure 5.1h,f) wherein the CB-PVdF is highlighted by its darker contrast than that of the AM. AM particle cracking can also be seen as a result of the calendering step (Figure 5.1b). From an electronic percolation perspective, these particle cracks can contribute to loss in electronic wiring. Images of the electrode-current collector interface also show no minimal indication of binder accumulation [1] nor NMC settling [2] on the current collector surface (Figure 5.1i). Heavy dentations due to AM compaction were also seen on the current collector surface. Cross section images suggest that the porous network somehow exists throughout the electrode. This will be better supported by FIB-SEM tomography.

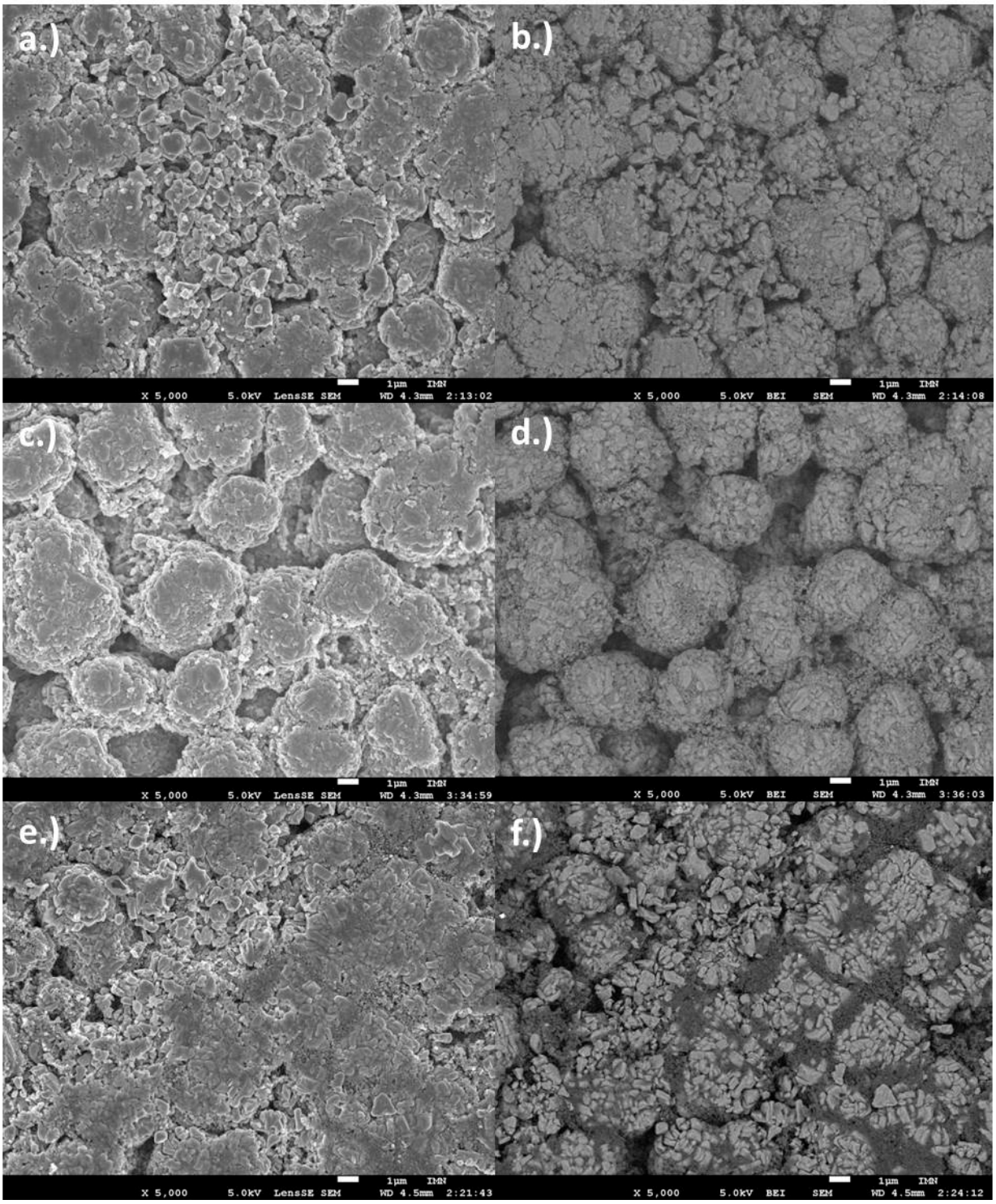
a.)
X 5,000 5.0kV LensSE SEM 1µm IMN WD 4.3mm 2:13:02
b.)
X 5,000 5.0kV BEI SEM 1µm IMN WD 4.3mm 2:14:08
c.)
X 5,000 5.0kV LensSE SEM 1µm IMN WD 4.3mm 3:34:59
d.)
X 5,000 5.0kV BEI SEM 1µm IMN WD 4.3mm 3:36:03
e.)
X 5,000 5.0kV LensSE SEM 1µm IMN WD 4.5mm 2:21:43
f.)
X 5,000 5.0kV BEI SEM 1µm IMN WD 4.5mm 2:24:12

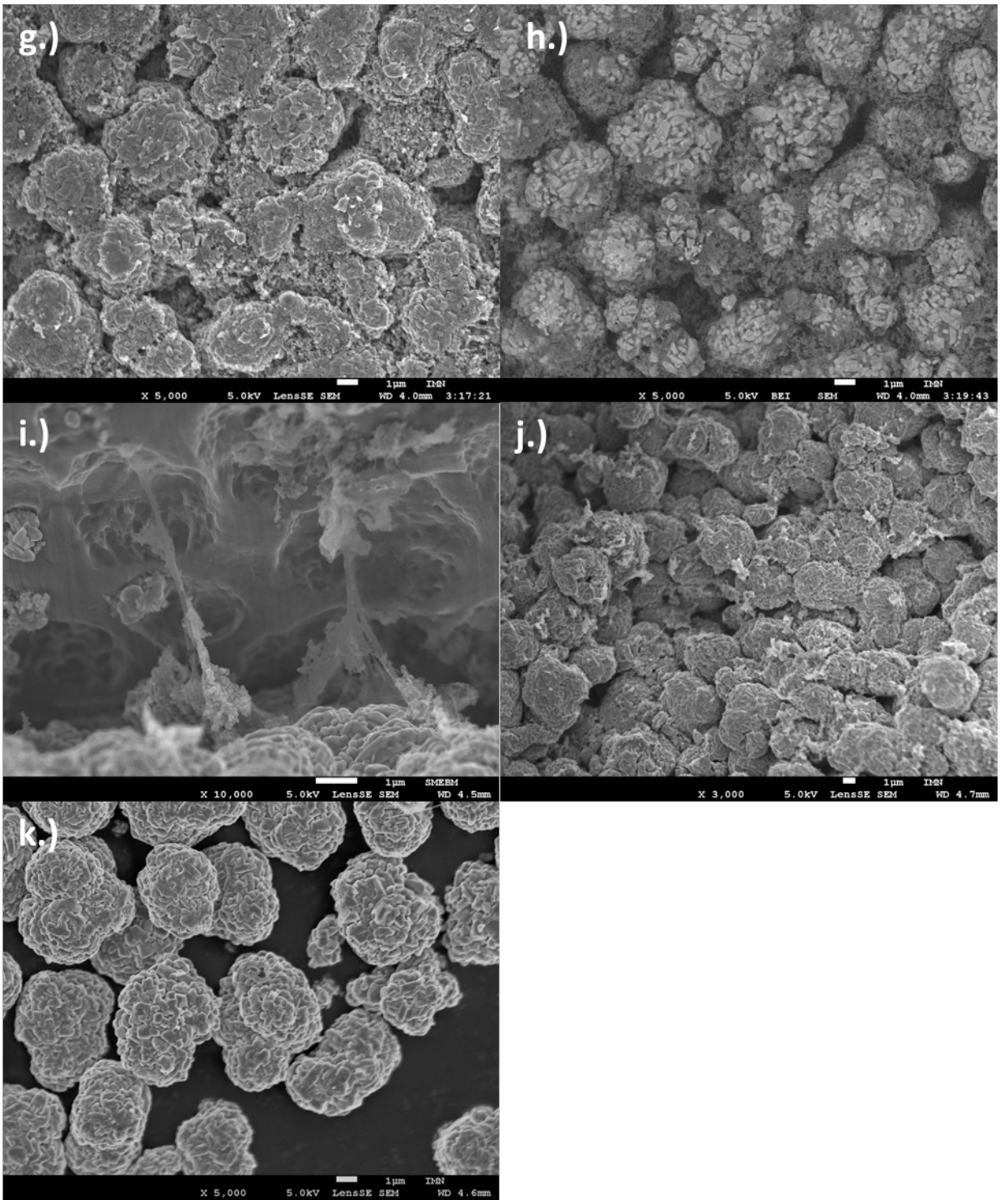

Figure 5.1: Electrode surface images of NA7 (a,b), NA2 (c,d), NA7b (e,f), NA2b (g,h) at 5,000 magnification with secondary electron (a,c,e,g) and backscattered electron (b,d,f,h) images. Eletrode-current collector interface image (i) and cross section image (j) of NA2 electrode. Pristine secondary particles of NMC (k).

5.2.3) XRCT and FIB/SEM Tomography Characterizations

Architectural relationships and examination were done by combining both X-ray computed tomography (XRCT) and focused ion beam/ scanning electron microscopy (FIB/SEM). Both have been used to quantify 3D microstructure parameters [1,3]. Characterizations were done by F. Cadiou in the course of his PhD thesis at MATEIS laboratory [4]. Experimental details are found in his thesis manuscript and all results presented here are for the purpose of interpreting the electrochemical performance of the electrodes.

XRCT of the pristine NMC secondary particles shows that particle size distribution centers at 5 µm with a 3-4 µm minimum particle size and a 16 µm maximum particle size. XRCT is limited in range and can only examine areas with large features (typically > 10 µm) making it difficult to render NMC cluster size distribution and micro/nano features less than 10 µm. However, XRCT reveals the presence of big heterogeneities such as large NMC clusters, pores and CB/PVdF agglomerates in all electrodes. These are distributed randomly along the electrode and the volume fraction depicted in a sample volume (typically 600 x 400 x electrode thickness μm^3) is always lower than 1%. Figure 5.2 shows projections of these big heterogeneities on a plan parallel to the current collector (left) and on a perpendicular one (right), where large NMC clusters appear in blue and large pores or CB/PVdF agglomerates appear in red for one representative sample.

2D SEM characterization was then done to complement the XRCT maps. Cross sections of 200 x electrode thickness μm^2 dimensions were scanned with SEM. Figure 5.3 shows image scans for the NA4b electrode. Two black regions were identified as CB/PVdF agglomerates (Figure 5.3a) and particle cracking was observed when the images were zoomed-in (Figure 5.3b). Quantification over the cross-sections of various electrodes revealed that there is 47% fragmentation ratio with the less calendered electrodes (NA2, NA3, and NA2b) in comparison with 57% fragmentation ratio with the most calendered electrodes (NA7, NA4b and NA7b). This fracturing is observed mostly at the grain boundaries, as in other work [5]. Figure 5.4 show the presence of the large CB/PVdF agglomerates in NA2b and NA7b.

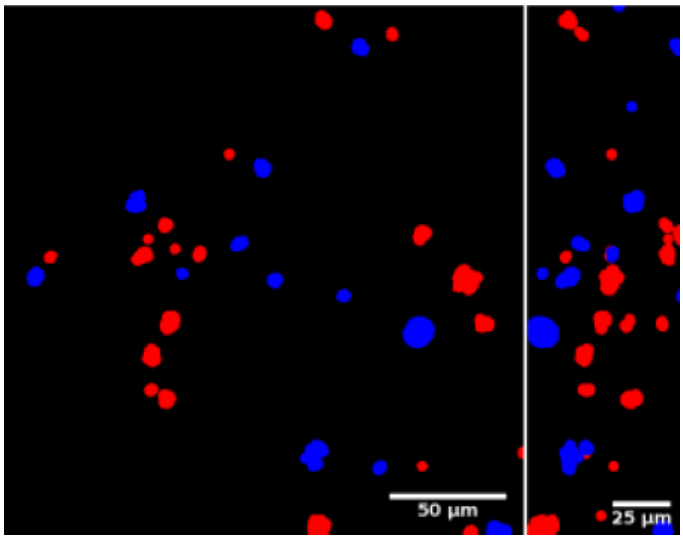

Figure 5.2: Projections of the big heterogeneities on a plan parallel to the current collector (left) and a perpendicular one (right), blue is for NMC and red for the pores/PVdF/CB phase. Courtesy of François Cadiou.

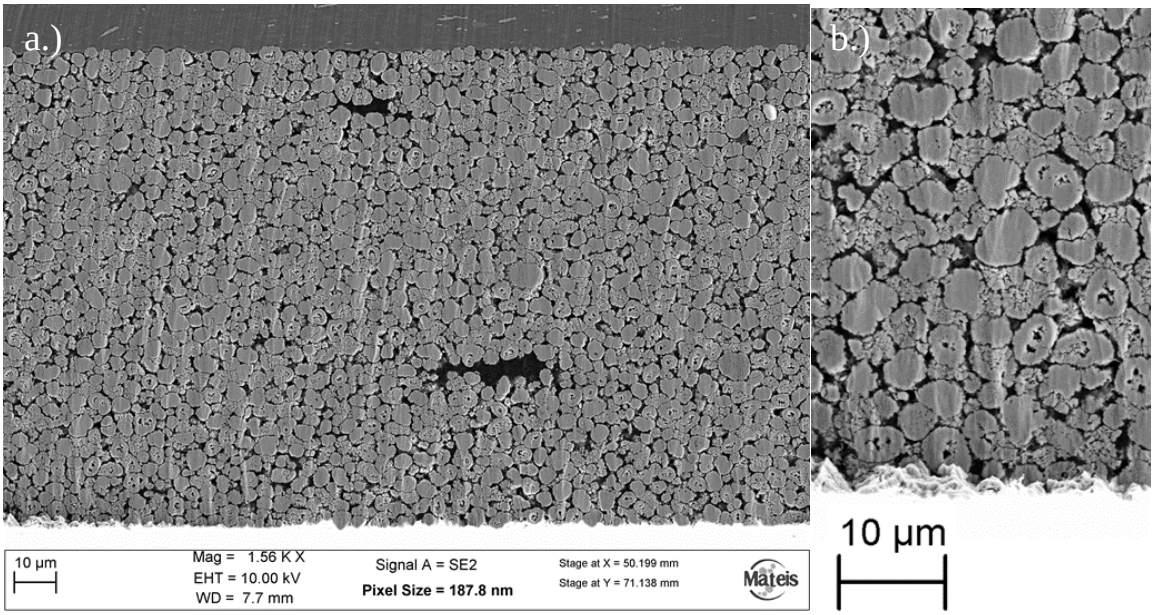

Figure 5.3: SEM views of NA4b cross-section at low (a) and high (b) magnification. Courtesy of François Cadiou.

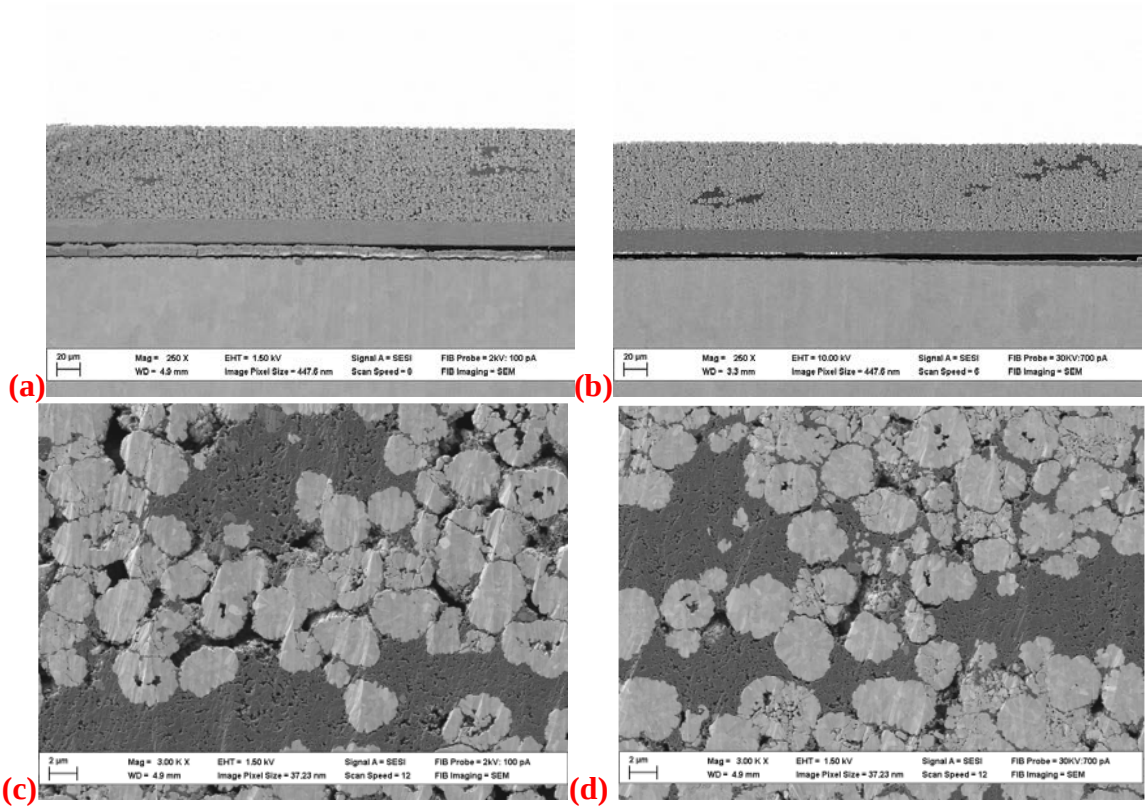

Figure 5.4: SEM views of cross sections and CB/PVdF large agglomerates (grey regions) in (a,c) NA2b and (b,d) NA7b. Courtesy of François Cadiou.

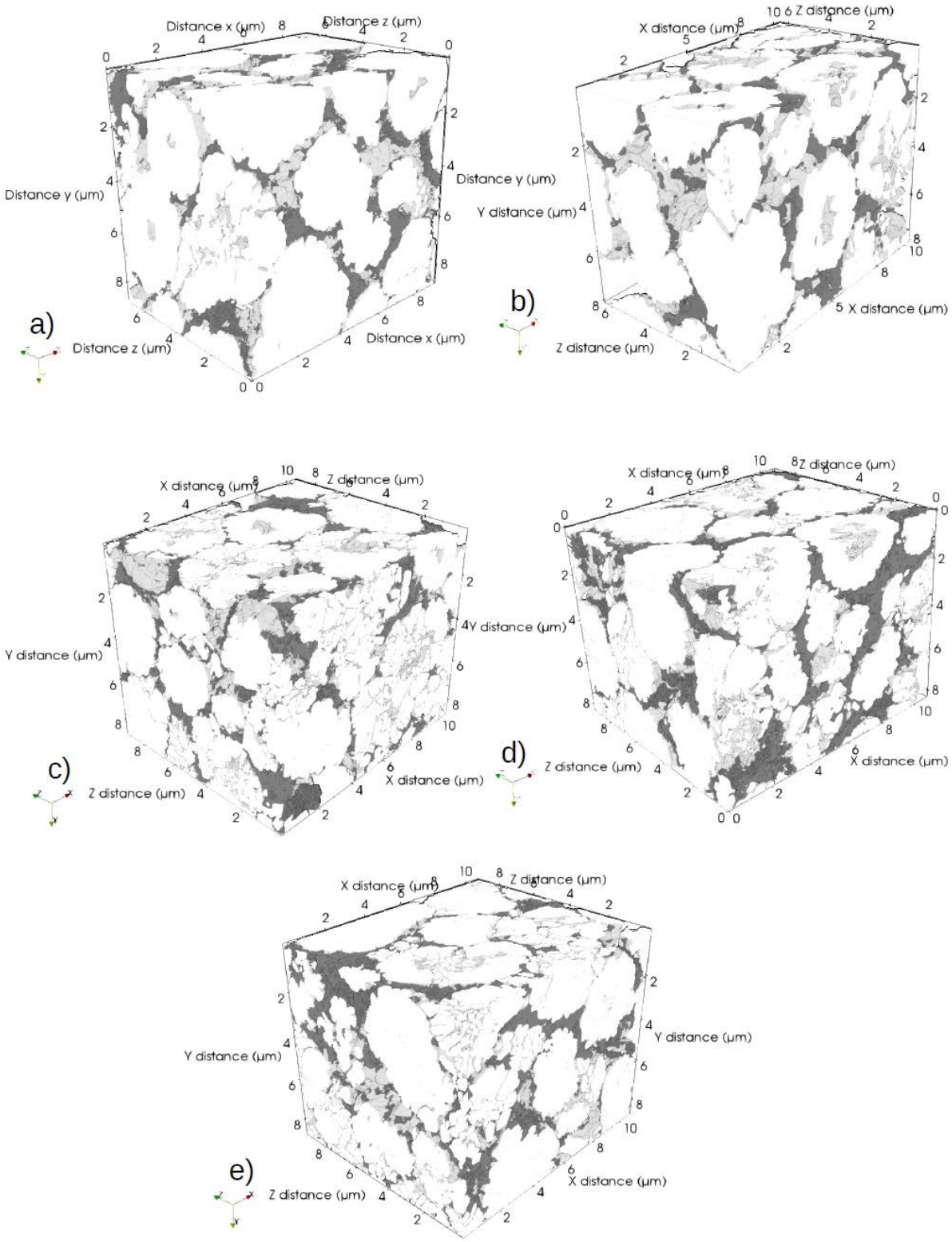

Figure 5.5: 3D views of reconstructed FIB/SEM volumes for (a) NA2, (b) NA3, (c) NA7, (d) NA2b and (e) NA7b. Grey areas show CB-PVdF rich regions. Courtesy of François Cadiou.

Table 5.4: Morphological parameters quantified from the FIB/SEM volumes. Courtesy of François Cadiou.

	NMC		CB/PVdF		Porosity	
	Volume fraction (%) Electrode FIB/SEM (Relative ≠)	**Intra-connectivity (%) Geometrical tortuosity**	**Volume fraction (%) Electrode FIB/SEM (Relative ≠)**	**Intra-connectivity (%) Geometrical tortuosity**	**Volume fraction (%) Electrode FIB/SEM (Relative ≠)**	**Intra-connectivity (%)**
NA2	64.8 70.4 (9)	100 1.06	7.2 4.8 (-33)	71 1.21	28.0 24.7 (-12)	97
NA3	64.8 61.0 (-6)	96 1.04	7.2 4.7 (-35)	31 1.26	28.0 34.4 (23)	98
NA7	70.9 69.1 (-2)	100 1.02	7.9 5.0 (-37)	63 1.22	21.2 25.9 (22)	98
NA2b	63.6 68.6 (8)	100 1.03	10.4 8.3 (-20)	97 1.29	26.0 23.1 (-11)	98
NA7b	69.6 72.4 (4)	100 1.00	11.3 7.9 (-40)	95 1.31	19.1 19.8 (4)	98

Table 5.4 recaps the electrode architectural parameters of the corresponding electrodes. 3D FIB/SEM reconstructions of the electrodes are shown in Figure 5.5 for NA2(a), NA3(b), NA7(c), NA2b(d), and NA7b(e). Comparison between the volume fractions in the electrodes and in the FIB-SEM volumes indicates some deviations. The CB/PVdF volume fraction is systematically lower by about 30% in the FIB/SEM volumes, i.e. at the local scale, compared to the electrode scale, which can be attributed to the presence of the CB/PVdF agglomerates along the electrode matrix (Figure 5.5). NA2 and NA3, having similar average compositions, showed differences in local morphologies. NA2 has larger NMC volume fraction and is less porous while NA3 has smaller NMC volume fraction and is more porous. NA2 and NA7 show similar local volume fractions despite their differences in composition. Interestingly, NA7 appears to have more fragmented NMC clusters which could be a result of NA7's calendering. The measured geometric surface area of NA7 and NA2 are 5.2 and 2.55 $\mu m^2/\mu m^3$ respectively. NA2b, being denser than NA2 is also seen to be less porous than the latter. NA7b is also seen to have a FIB/SEM composition close to electrode values but with less CB/PVdF amount.

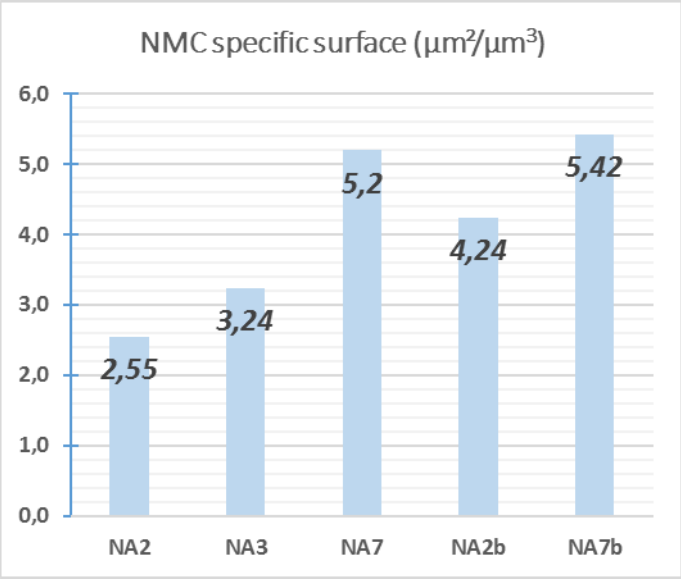

Figure 5.6: NMC phase specific surface in the different reconstructed FIB/SEM volumes. Courtesy of François Cadiou.

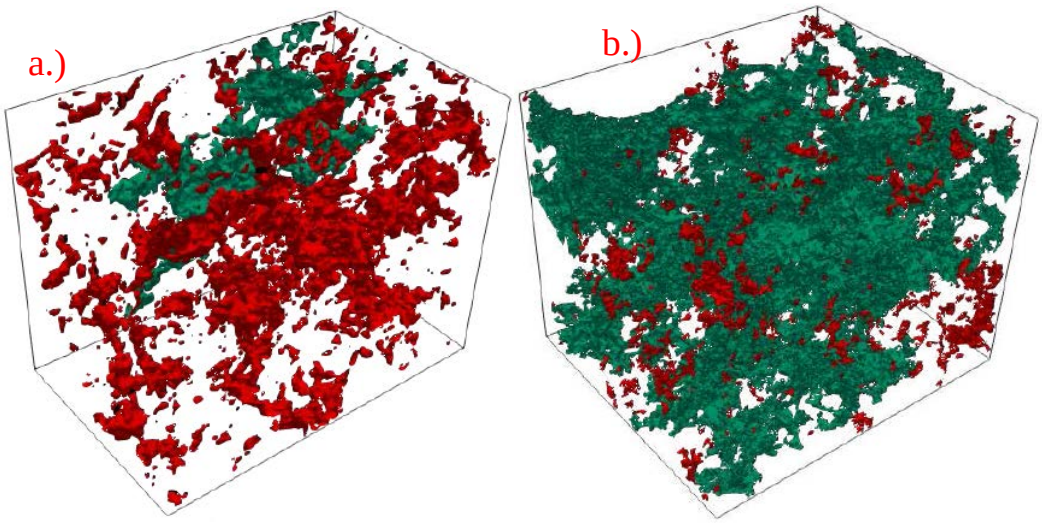

Figure 5.7: Visualization of the CB/PVdF phase in (a) NA3 and (b) NA7b FIB/SEM volumes. The most voluminous agglomerate is colored in green and others in red. Courtesy of François Cadiou.

Intraconnectivity is defined as the volume fraction of the most voluminous agglomerate of a phase found in a certain volume. The value of 100% means all voxels of the phase is a part of a unique agglomerate indicating the percolation of the phase. It appears that in all volumes, the porosity is well percolated. The CB/PVdF phase however, appears to be poorly/non-percolated in NA2, NA3 and NA7 electrodes. This is supported by FIB/SEM images showing the localization of the CB/PVdF phase (Figure 5.7). The most voluminous agglomerate is colored in green.

The geometrical tortuosity of a given porous matrix can be mathematically described as:

$$\tau = \frac{L_{pore}}{L_{straight}} \qquad \textit{(eq. 5.1)}$$

where L_{pore} is the effective actual path length through the pores from point A to B and $L_{straight}$ is the straight Eucledian distance. NMC exhibits values of 1 indicating that most of the volume can be crossed in an almost rectilinear line. CB/PVdF clusters however possess higher tortuosity values owing to their intricate morphology.

Upon closer inspection of the FIB/SEM volumes, four different types of porosity were identified: (i) occluded inside hollow and closed NMC clusters, (ii) macroporosity formed by the cavities in the stacking of NMC clusters, (iii) mesoporosity in the CB/PVdF phase, and (iv) mesoporosity localized in grain boundary cracks of fragmented NMC clusters (Figure 5.8). Their respective quantified values are shown in Table 5.5. Macroporosity constitutes the majority of the observed porosity with more than 90% for NA2, NA3 while it is 85% or less for NA7, NA7b and NA2b. Further calendering and CB/PVdF addition increases the contribution of mesoporosity as seen with NA7b. Tortuosity of the macroporosity was determined to be at 1.1 (average value over all FIB/SEM volumes) while the tortuosity for mesoporosity ranged between 1.5 and 2.0.

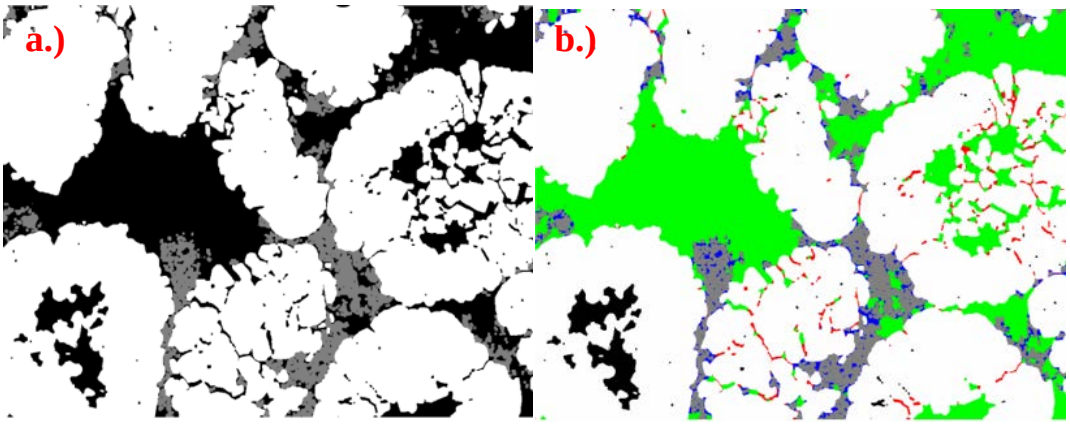

Figure 5.8: (a) 2D FIB/SEM reconstructed view of NA2b with NMC in white, porosity in black and CB/PVdF in grey. (b) The same view with the various types of porosity identified by a different color: closed porosity (black), macroporosity (green), mesoporosity confined within the CB/PVdF phase (blue) and mesoporosity confined at cracked grain boundaries of fragmented NMC clusters (red). Courtesy of François Cadiou.

Table 5.5: Distribution of different porosity types within the overall phase for all FIB / SEM volumes studied. Courtesy of François Cadiou.

	Volume fraction of the total porosity (%)	Contribution to the total porosity (%)			
		Macroporosity	Closed porosity	Mesoporosity in CB/PVdF	Mesoporosity in cracked NMC
NA2	24.7	92	3	1	4
NA3	34.4	96	2	< 1	1
NA7	25.9	83	2	7	8
NA2b	23.2	84	2	4	9
NA7b	19.8	78	1	11	10

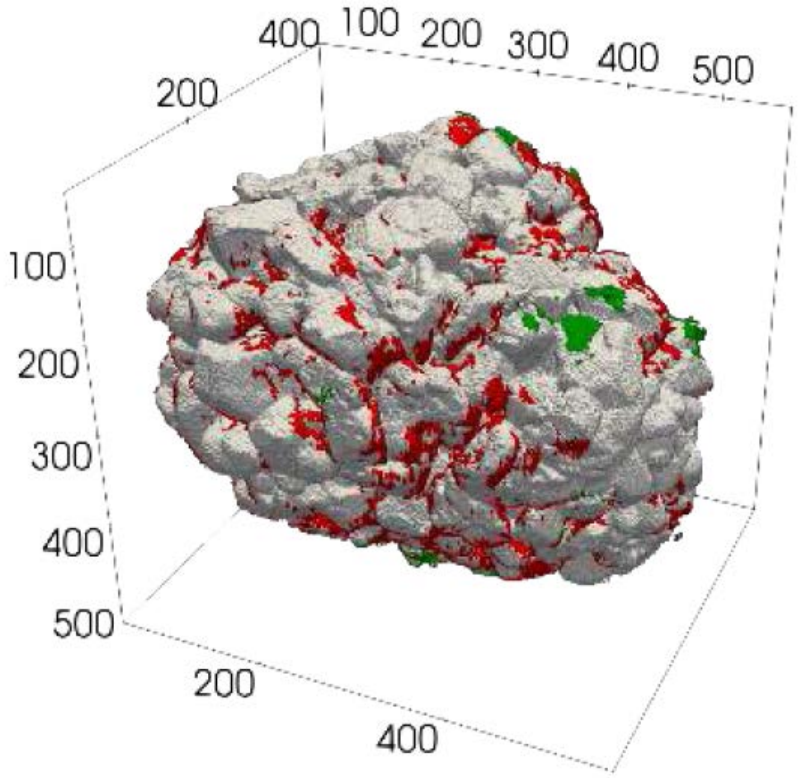

Figure 5.9: 3D view of an NMC cluster (NA2) and its interfaces with CB/PVdF (in red) and other clusters of NMC (green), the rest of the surface is in contact with the porosity. The scale is in voxel, 1 voxel = 10x10x10nm^3. Courtesy of François Cadiou.

Interconnectivity values were also determined for both NMC and CB/PVdF phases. Figure 5.9 shows the NMC cluster of NA2 with surfaces in contact with the pores colored in grey, surfaces in contact with CB/PVdF are colored red and surfaces in contact with NMC are colored green. Interconnectivity can be expressed either as: 1.) the interface quantity between phases (in µm^2) (NMC vs. CB/PVdF, etc.) relative to the volume a certain phase or; 2.) the ratio between the

amount of interface between phases relative to the amount of surface of a certain phase. Due to that the degree of fragmentation in NMC being different from one another, and NMC having a specific surface area different from one volume to another, both quantifications of interconnectivity tell contrasting schemes. Previous work by Besnard et al. [3] states that large amounts of interface are crucial for lithium insertion/disinsertion facilitation. This will be better explained with the results of the electrochemical tests.

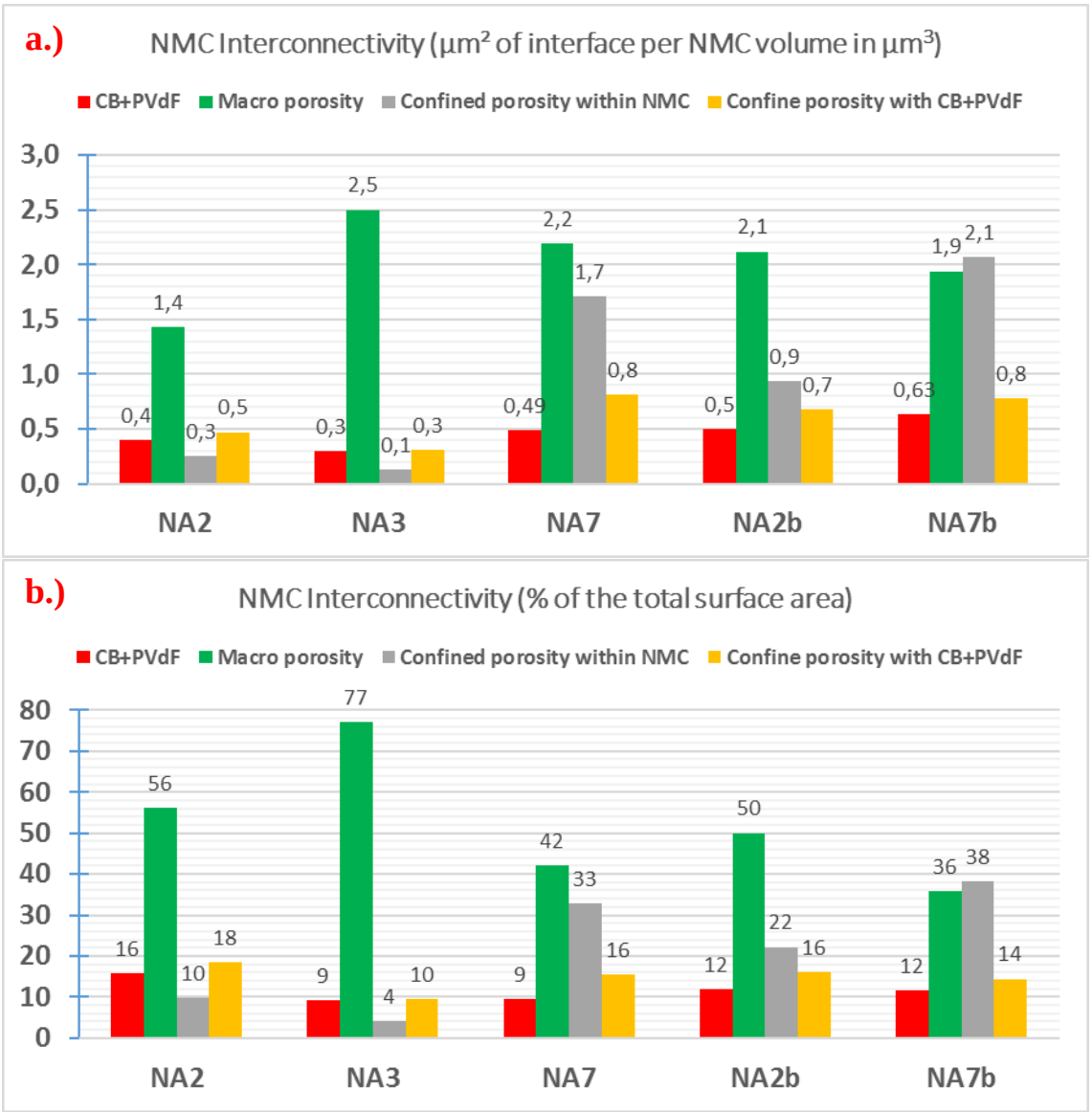

Figure 5.10: Interconnectivity of the NMC phase with: the CB/PVdF phase, the macroporosity, the mesoporosity confined within the CB/PVdF phase and at cracked NMC grain boundaries given in µm² of interface per µm³ of NMC in (a) and in % of the total surface area of the NMC phase in (b). Courtesy of François Cadiou.

5.2.4) Electrical Characterizations

Electrical properties of these electrodes were measured by Broad band Dielectric Spectroscopy (BDS). Characterizations were done by A. Agrawal in the course of his PhD thesis at GeePs laboratory [6]. BDS is a complex but powerful technique that may allow to determine the electrical properties of a composite material at its multiscales [7,8,9]. At the time of writing, the analysis of the measurements made on the study materials is still being consolidated. We will limit ourselves to summarize the salient points. Table 5.6 gives the conductivity at room temperature and in the dry state, as well as the energy of activation for an NMC532 sample (in the form of a pellet binded by a few wt% of PVdF) and for some of the electrodes of the project.

Table 5.6: Conductivity at room temperature in dry state measured by BDS and approximate values of their activation energy for the NMC532 material and the electrodes. Courtesy of Anshuman Agrawal. Ionic conductivity determined by numerical simulations. Courtesy of François Cadiou.

		Conductivity at RT dry state ($S.m^{-1}$)	**Energy of activation (eV)**	**Ionic conductivity at RT (wet state) ($S.m^{-1}$)**
NMC	**Pellet**	0.00136	0.27	-
	Cluster	0.58 (effective)	0.20	-
	Grain	87 (effective)	0.10	-
NA3		0.035	0.10	0.110
NA2				0.061
NA7		0.06	0.05	0.076
NA2b		0.65	0.005	0.056
NA7b		0.85	0 (metallic)	0.032
CB/PVdF		~250 - 300	0 (metallic)	-

The effective conductivity depends on the volume fraction of the material in the measured sample and is lower than the true conductivity.

For NMC, the conductivity at the various scales is established. The conductivity of the grains is high and shows fairly low energy of activation, as a consequence of the high Ni content, compared to NMC333 [9]. The large conductivity drop from the grain to the cluster scale is due to the grain boundaries. The very large conductivity drop from the cluster to the sample scale is due to the small inter-cluster contact points (bottlenecks). The true conductivity of the CB/PVdF mixture is also reported. This one was measured on a bulk CB/PVdF film [10] and also determined through numerical simulations by F. Cadiou [11]. The comparison with the NMC grain conductivity value highlights the high conductivity of the NMC at the grain level. With

respect to the electrodes, the conductivity differs by one order of magnitude between the NAx and NAxb formulations, in agreement with the FIB/SEM tomography analysis that showed the CB/PVdF mixture is only percolated in NAxb. The close inspection of the BDS data (not detailed here) reveals two types of electrical paths in the electrodes, as schematized in Figure 5.11. In the non-percolated NAx electrodes, gaps in the incomplete CB-PVdF network are filled by NMC grains or clusters. In the percolated NAxb ones, there are two types of paths in parallel. Path 1 represents percolated CB/PVdF mixture and path 2 represents composites like NAx series. Whatever the electrodes the contact resistance at the interface with the current collector/electrode was found negligible (maximum value is 0.02 ohm for NA2).

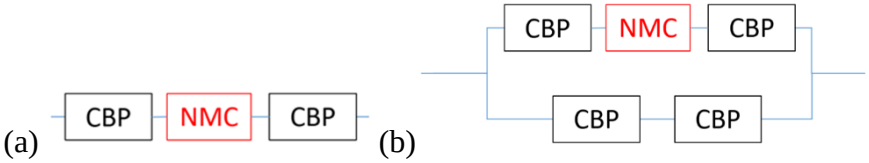

Figure 5.11: Equivalent electrical circuits for the non-percolated NAx (a) and percolated NAxb (b) electrodes. Courtesy of Anshuman Agrawal.

The electrical properties were also measured in the wet state, when the electrode is impregnated by an electrolyte. Confirming the earlier work of Seid et al. [12] and Panabière et al. [13], these measurements revealed a strong decrease in the conductivity of the CB/PVdF aggregates when wetted by the liquid electrolyte, due to the adsorption of the electrolyte ions, while that one of NMC remains much less altered. The ionic conductivity of the electrodes wetted by the electrolyte was determined by numerical simulation by F. Cadiou. It obeys an Archie law [4]

$$\sigma_{ionic} = \sigma_{electrolyte}\phi^2_{porosity} \qquad \textit{(eq. 5.2)}$$

with σ_{ionic} and $\sigma_{electrolyte}$ the ionic conductivities of the electrode in the wet state and of the liquid electrolyte (1 $S.m^{-1}$), and $\phi_{porosity}$ the porosity volume fraction. There is acceptable agreement between numerical results and preliminary analysis of BDS measurements. For NA2, the experimental ionic conductivity is 0.063 $S.m^{-1}$. For NAx electrodes, their ionic conductivity is higher than their electronic conductivity (in the dry state).

5.3) Experimental Protocol for Electrochemical Measurements

Samples of 12 mm and 7 mm diameter were punched out from the positive electrode laminates. They were dried in a 90°C vacuum oven for 16 h before assembly. Coin cells were assembled in half-cell configuration in an argon atmosphere controlled glove box. The metallic parts of the coin cells were cleaned in acetone in an ultrasonic bath for 2 hrs and dried at 90°C under vacuum before being introduced in the glove box. Lithium disc (Sigma Aldrich, 0.75mm thickness) of 12 mm diameter was used as the negative electrode, Whatman™ GF/D glass fiber was used as separator (dried at 120°C under vacuum before being introduced in the glove box) and LP30 ($LiPF_6$ 1 molar in 1:1 v:v ethylene carbonate : dimethylcarbonate, Solvionic™) was used as electrolyte. Coin cells were sealed using a MSK 160D Crimper and were rested overnight before cycling. Three coin cells at least were assembled to allow for statistical verification (reproducibility).

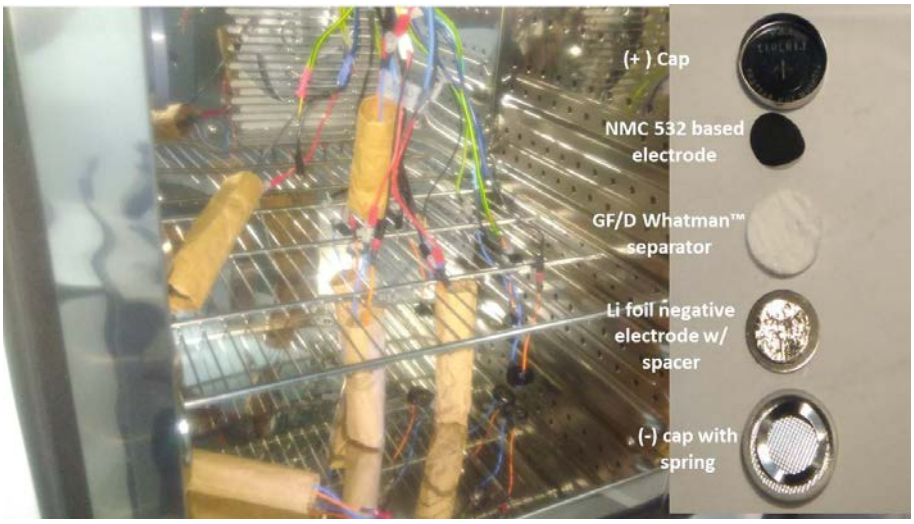

Figure 5.12: Schematics of the half-cell coin cell assembly (right). Cell setup in the controlled temperature chamber (left)

Galvanostatic measurement is a prominent electrochemical technique to evaluate electrode performance. It measures a system's voltage response (in this case the difference between the potential at the NMC positive electrode and metal lithium at the negative electrode) under a constant current. These measurements are deemed practical due to that real world applications of batteries tend to rely on their performance under varying exchange current densities. Moreover, the reactions at the electrodes can be evaluated using dQ/dV curves which relate the anodic and

cathodic peak to the thermodynamics of the electrode reactions [14]. The majority of the galvanostatic charge-discharge sequences found in most literatures involve the application of a constant current that corresponds to a "C-rate". This is derived from the practical/theoretical gravimetric capacity of an active material and the electrode loading. In general, the theoretical capacity can be determined from the equation:

$$Q = nF/M \qquad \textit{(eq. 5.3)}$$

Where M is the molar mass of the active material, F is the Faraday constant and n is the number of electrons participating in the overall redox reaction. The capacity taken from this equation translates to the specific capacity of the material (the attainable theoretical capacity per gram of material (mAh/g). In electrochemical studies, capacity is reported in many terms. To better define capacity terms, gravimetric capacity is the attainable capacity per gram of electrode, nominal capacity is the maximum practical capacity attainable, volumetric capacity is the capacity per volume of electrode and areal capacity is the capacity per geometric area of electrode.

Table 5.7: Table of sample currents used in cycling 12mm diameter positive electrodes (1.13cm²). Basis theoretical capacity for discharge was at 274mAh/g while the basis practical capacity in charge is 165mAh/g. C-rate labels in discharge are labeled against the practical capacity of 165mAh/g.

C-rate (Discharge)	**NA3 (mA)**	**NA2 (mA)**	**NA4b (mA)**	**C-rate (Charge)**	**NA3 (mA)**	**NA2 (mA)**	**NA4b (mA)**
C/12.5	0.231	0.372	0.630	**C/20**	0.139	0.225	0.379
C/6	0.461	0.744	1.259	**C/10**	0.278	0.449	0.759
C/3	0.922	1.488	2.518	**C/5**	0.556	0.899	1.518
C/1.2	2.305	3.720	6.295	**C/2**	1.389	2.247	3.794
1.66C	4.610	7.440	12.590	**C**	2.778	4.493	7.589
3.32C	9.220	14.880	25.180	**2C**	5.556	8.987	15.177
8.3C	23.050	37.200	62.950	**5C**	13.891	22.467	37.943
16.6C	46.100	74.400	125.900	**10C**	27.781	44.934	75.885
C/60 (floater)	0.0461	0.074	0.126	**C/100 (floater)**	0.028	0.045	0.076

The applied current will charge or discharge this determined capacity of the electrode in a certain amount of time hence the C-rate is described with a factor. For example, 1C means that the applied current is theoretically enough to charge/discharge the nominal electrode capacity in 1hr.

2C means 1/2 hr and 0.5 C, 2 hrs. Moreover, the capacity response of the electrode during charge and discharge can allow evaluating the coulombic efficiency which is described as the capacity ratio between discharge:charge capacity (cathode) or charge:discharge capacity (anode).

Cycling sequence was patterned against the typical “power test” which evaluates the rate capability of a certain cell. Figure 5.13 illustrates the included sequences in the test. The test has three initial formation cycles followed by the real “power test”. The formation sequences are done to ensure the formation of a stable SEI layer and to allow for the full impregnation of the electrode porosity by the electrolyte. The lithiation (discharge) sequence focuses on the power performance during discharge. The formation cycles were done at C/6 for discharge and the power test had a CCCV charging step of C/6 with a float current of C/60 at 4.3V. The discharge is then varied with the following C-rates: C/12.5, C/6, C/3, C/1.2, 1.66C, 3.2C, 8C and 16.6C with a floor voltage of 2.1V. The delithiation sequence (charge) focuses on the power performance during charge and resembles the power test for the lithiation sequence but with the charge and discharge C-rates in vice versa. The formation cycles were done at C/10 for delithiation and the power test had a CCCV discharging step of C/10 with a float current of C/100 at 2.1V. The charge is then varied with the following C-rates: C/20, C/10, C/5, C/2, C, 2C, 5C and 10C with a floor voltage of 4.3V. Different C-rate values were considered between lithiation and delithiation wherein the theoretical capacity of 274 mAh/g was used by error for lithiation and the practical capacity of 165 mAh/g was used for delithiation. However, all C-rates are labeled against the practical capacity of 165 mAh/g in the following. Cycling was also done in varying temperatures namely 0°C, 10°C, 22°C, 30°C, 40°C. The cells were placed inside a Binder MK56 varying temperature chamber capable of delivering temperature control in both low and high temperatures. Formation sequence was done at the same temperature that the one for the power test.

Figure 5.13 shows examples of potential and current versus time profiles for the discharge and charge power tests, respectively. One can note that the floating is visible at 2.1V in the power charge test, but it is not at 4.3 V in the power discharge test. The latter exists but it is too short to be visible on the time scale. This suggests that it is easy to de-insert all the lithium ions that were inserted beforehand. But that it is more difficult to re-insert all the lithium ions that were

previously de-inserted, as the full re-insertion can only be achieved by constraining the system to remain at low potential. This may reflect different intrinsic kinetics of the active material in the delithiated than in the lithiated states.

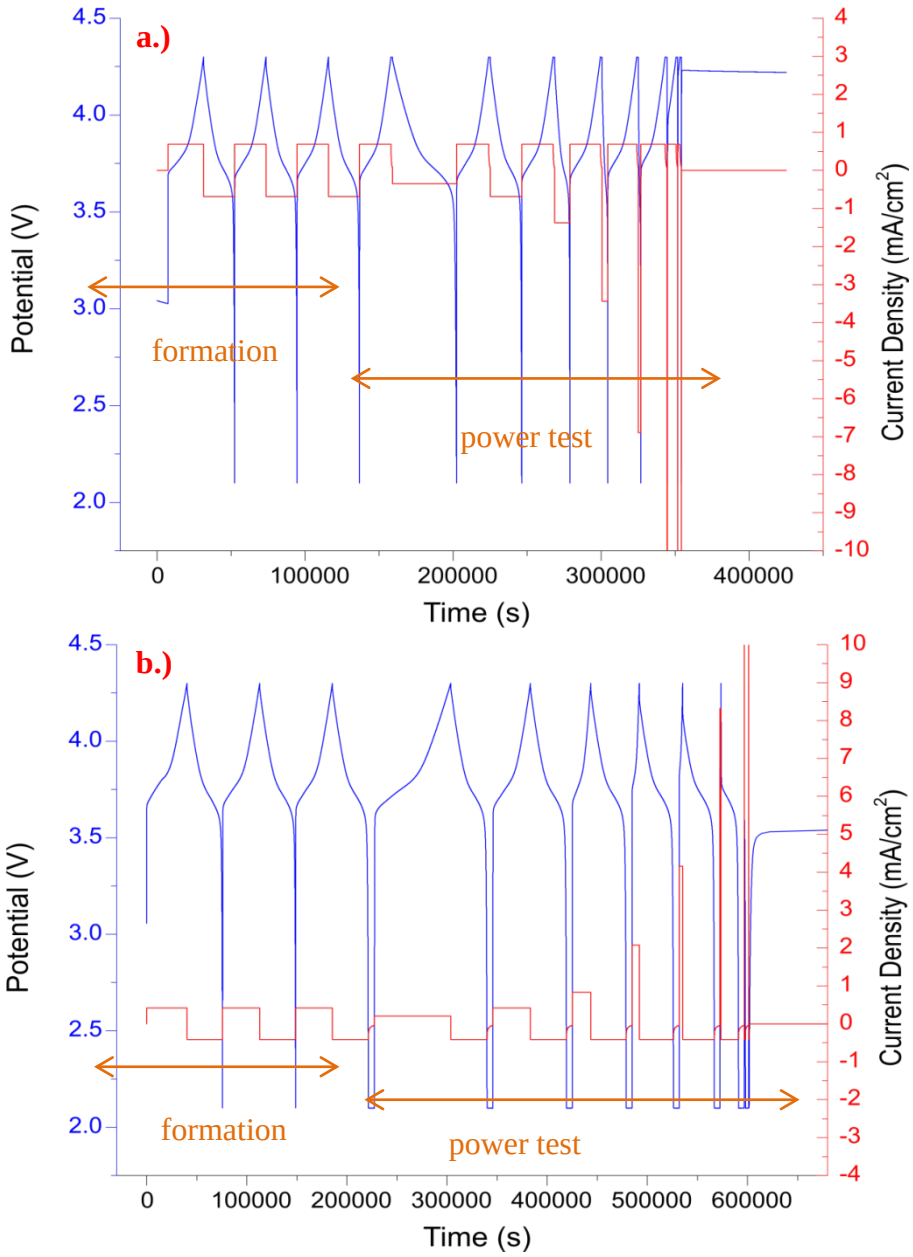

Figure 5.13: V vs. I vs. t graphs of lithiation (a) and delithiation (b) sequences. The formation cycles and the power cycle sections are shown. Applied current with "floater" is highlighted in red.

5.4) Standard Errors and Reproducibility

5.4.1) Introduction

Reproducibility is a key parameter in identifying the statistical eligibility of the results. Literatures have stressed the inevitable inhomogeneity of the electrode composite due to the various material components (AM, conductive additive, binder) and composite parameters (porosity, loading, density etc.) which can be minimized through thorough mixing, optimal formulation and proper electrode processing. This should result in electrode uniformity which in turn should produce electrodes capable of statistically achieving the same electrochemical performance. Moreover, it is known that measurements done with coin cells suffer from lack of reproducibility owing to the small surface area of the electrodes, which is then more sensitive to small defects or heterogeneities in the electrode coating [15].

In Figures Figure 5.14 and Figure 5.15, several examples of discharge and charge curves are shown. It can be seen that the reproducibility is getting worse at higher temperatures.

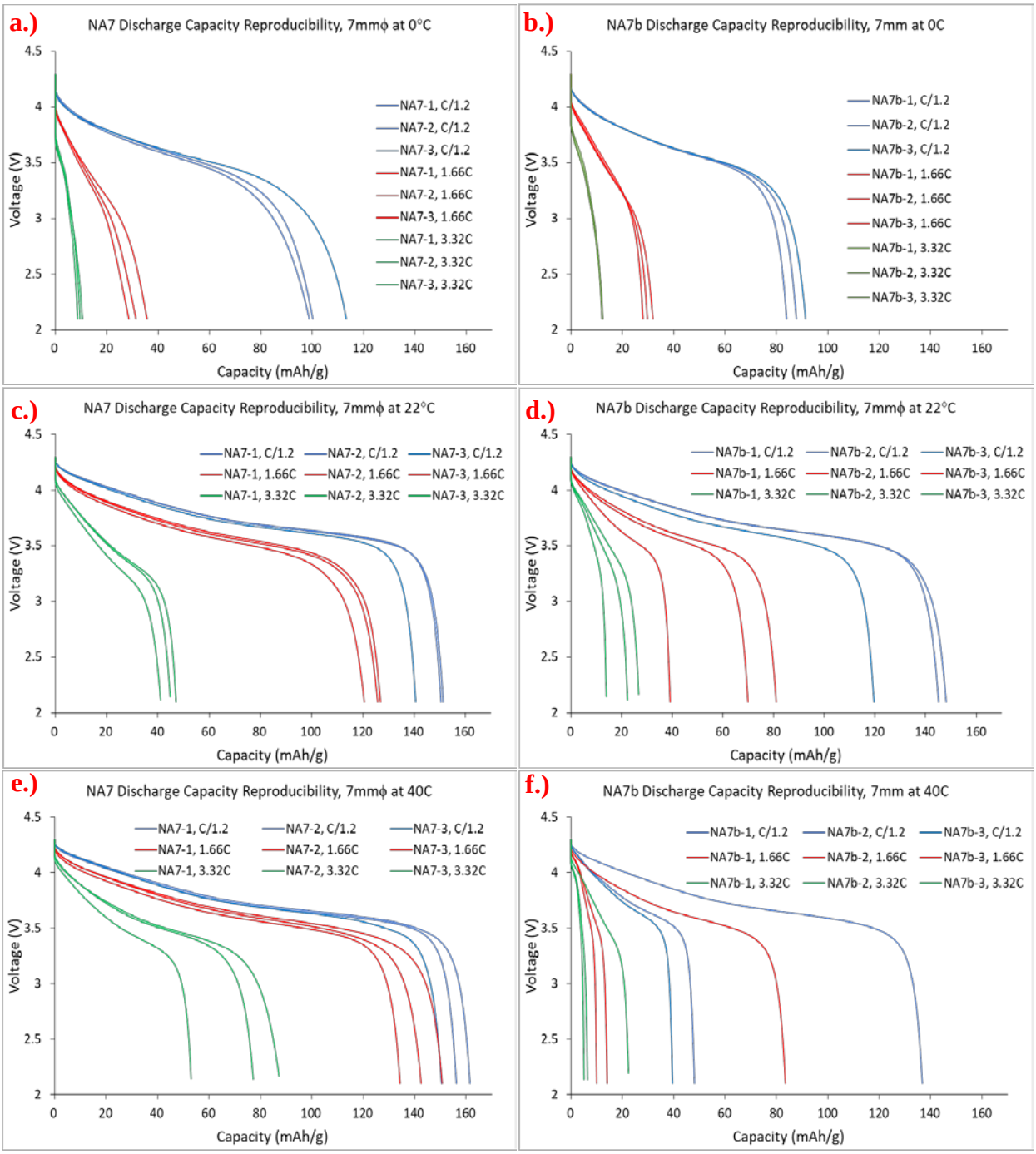

Figure 5.14: Discharge capacity reproducibilities of NA7 (left) and NA7b (right) per C-rate 7mmϕ disc radius at 0°C (a,b), 22°C (c,d) and 40°C (e,f).

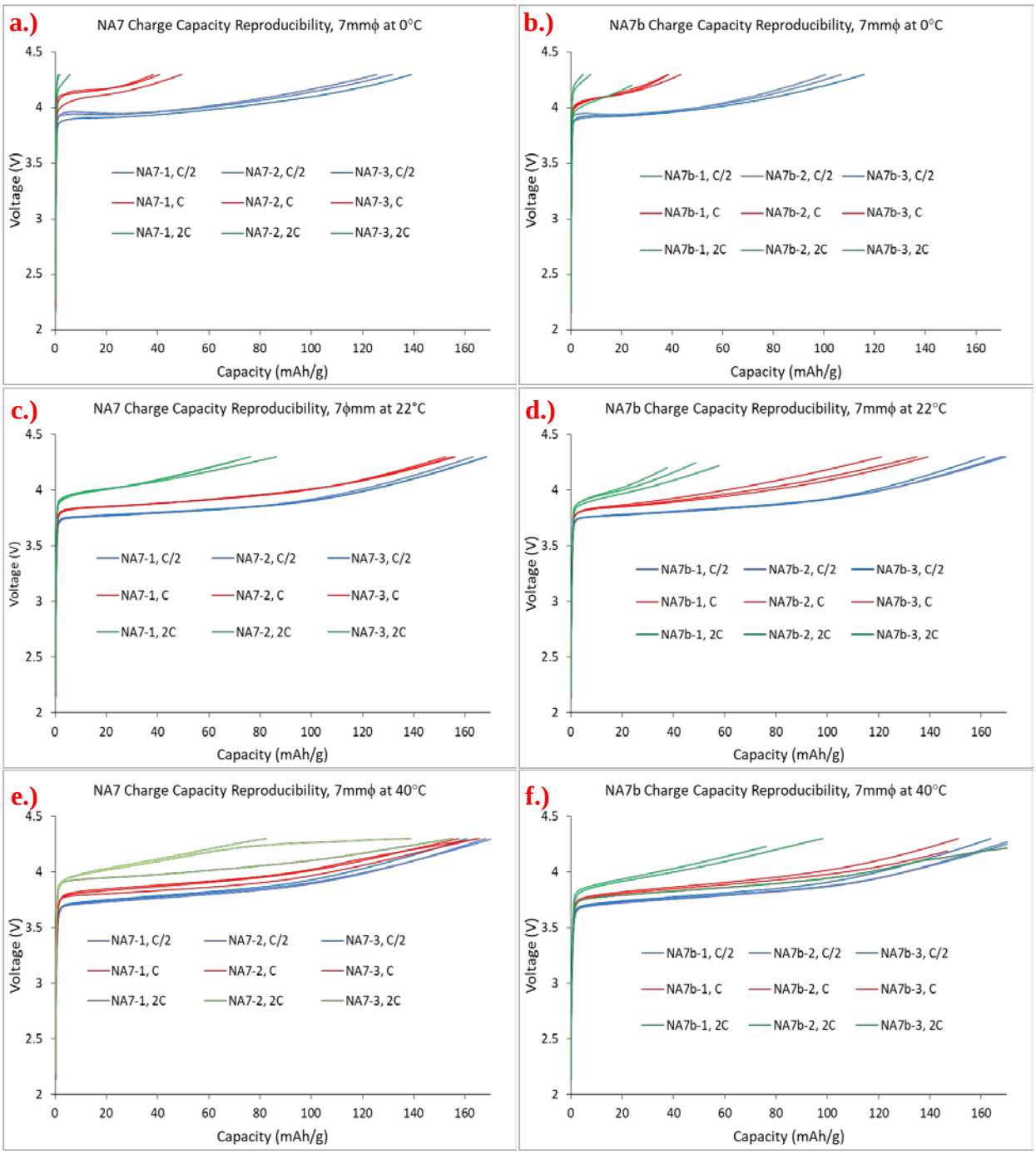

Figure 5.15: Charge capacity reproducibilities of NA7 (left) and NA7b (right) per C-rate 7mmϕ disc radius at 0°C (a,b), 22°C (c,d) and 40°C (e,f).

5.4.2) Mass loading variability

The operating current (C-rate) is based on the AM loading contained in each electrode. Non-uniform mass distribution along the electrode film could result in current distribution

inhomogeneity which can result into either inadequate electron transfer or increased polarization scattered within a given region. NA7 and NA2 electrodes were selected and circular electrodes (12 mm diameter) were punched in different areas along the width and length of the sheets. These were then weighed and compared to determine mass distributions. Mass statistics are shown in Table 5.8.Values show a minimum of 1.5% to a maximum of 3% error relative to both average weights and the manufacturers indicated mass loading. This meant that C-rates determined from the manufacturer's value would generate at least 3% error value.

Table 5.8: Mass loading distribution statistics

Electrode	**NA7**		**NA2**	
Region	**Length**	**Width**	**Length**	**Width**
Average wt. (mg)	9.43	9.55	9.73	9.70
Std. Deviation (vs. wt. average)	0.09	0.14	0.03	0.30
Error (vs. wt. average) (%)	0.91	1.49	0.35	3.07
Error (vs. actual wt.) (%)	1.49	0.24	4.22	3.86

5.4.3) Capacity Variations with Electrode Formulation and Temperature

Figure 5.16 shows the capacity relative errors for all electrodes in both charge and discharge based on 3 to 4 cells on average. The relative errors were computed form the standard deviation within and the average capacity as illustrated in the following equation:

$$\%Error = \left(\frac{capacity\ std.dev.of\ electrode(x)}{average\ capacity\ (x)}\right) \qquad \textit{(eq. 5.4)}$$

where x is the electrode type (NA7, NA8, NA2… etc.). For room temperature, results are compared for 7 and 12 mm radii. Error values for the capacities at rates below C* are in the range of 0-6%, which is similar or slightly higher than the values determined from the mass load errors. This suggests that the capacity deviations below C* can be attributed to the local mass loading distribution differences during the manufacturing process. These capacity errors gain considerable to dramatic increases at C-rates above C* in charge. The same observation can be said at varying temperatures. There is no clear dependency of error evolution at varying temperatures at first sight, but the error still tends to increase at C-rates above C*. It could be hypothesized that since ionic limitation dictates performance at rates above C*, the

inhomogeneity in particle distribution and architecture affects the tortuosity which in turn affects the reproducibility between electrodes at high rates. It can also be added that the relative error on the capacity will be all greater as the absolute value of the capacity is low, which is the case with a high current regime. The very high error values at high 5C and 10C during charge (Figure 5.17) could be attributed to the ceiling voltage of the power sequence as a moderate difference in the polarization of the cell may result in a significant difference in capacity. When one looks at the influence of the electrode composition, one can note that there is a trend of higher relative error in discharge for NAxb series, while the higher relative error in charge seems to happen more frequently with the NAx series. For example, in discharge, at 22°C (7 mm) the higher relative errors are observed for NA4b, NA7b, and NA2b. In charge, at 0°C, 22°C (7 mm), and 30°C, the higher relative errors are observed on the whole for NA2, NA8 and NA7. These trends could be the consequence of largest diffusion limitations for NAxb electrodes, and of larger cell resistances for the NAx ones, as we will see later.

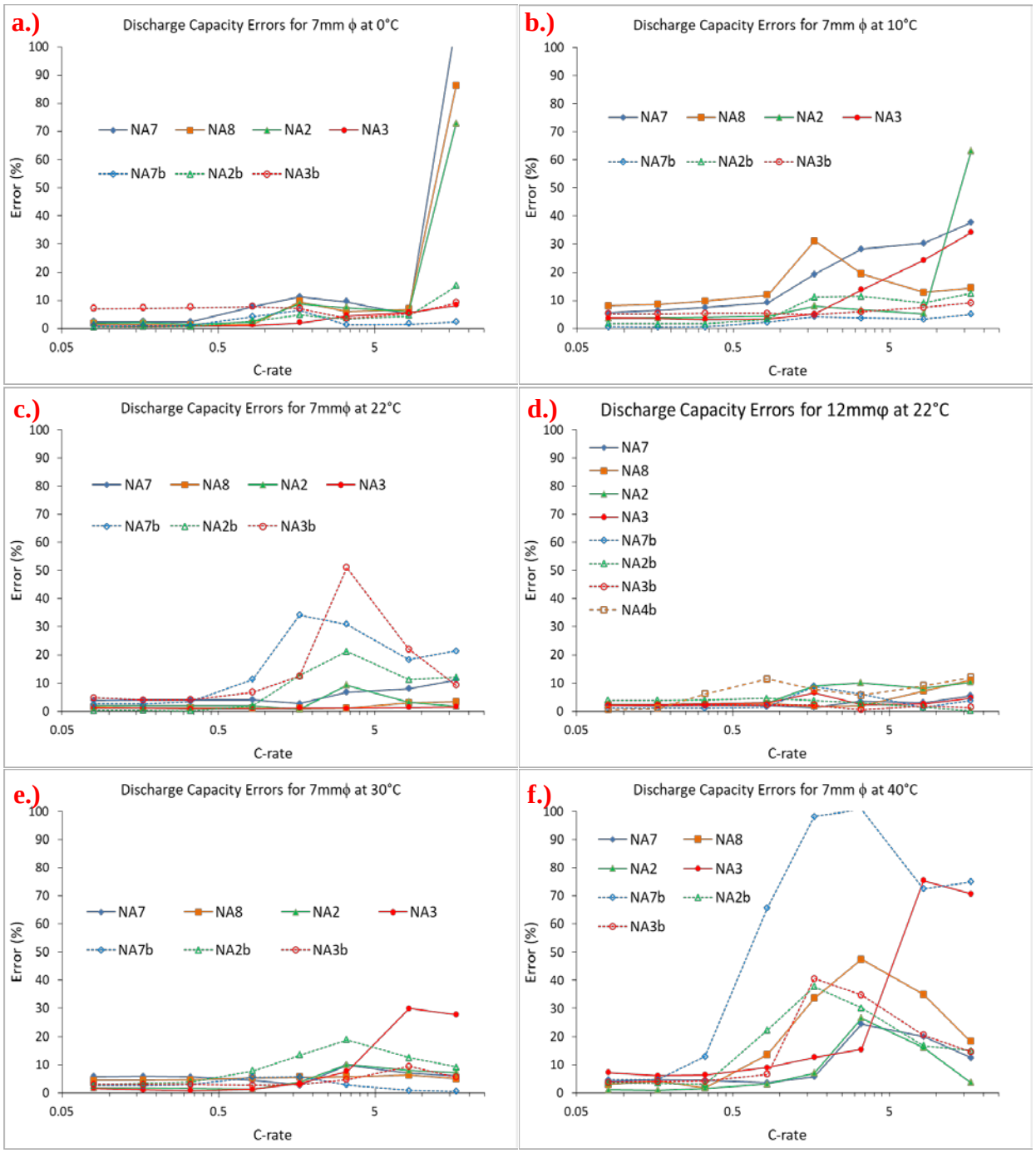

Figure 5.16: Discharge capacity error percentages per C-rate per electrode for 7 mmϕ disc radius at 0°C (a), 10°C (b), 22°C (c), 30°C (e), 40°C (f) and for 12 mmϕ disc radius at 22°C (d).

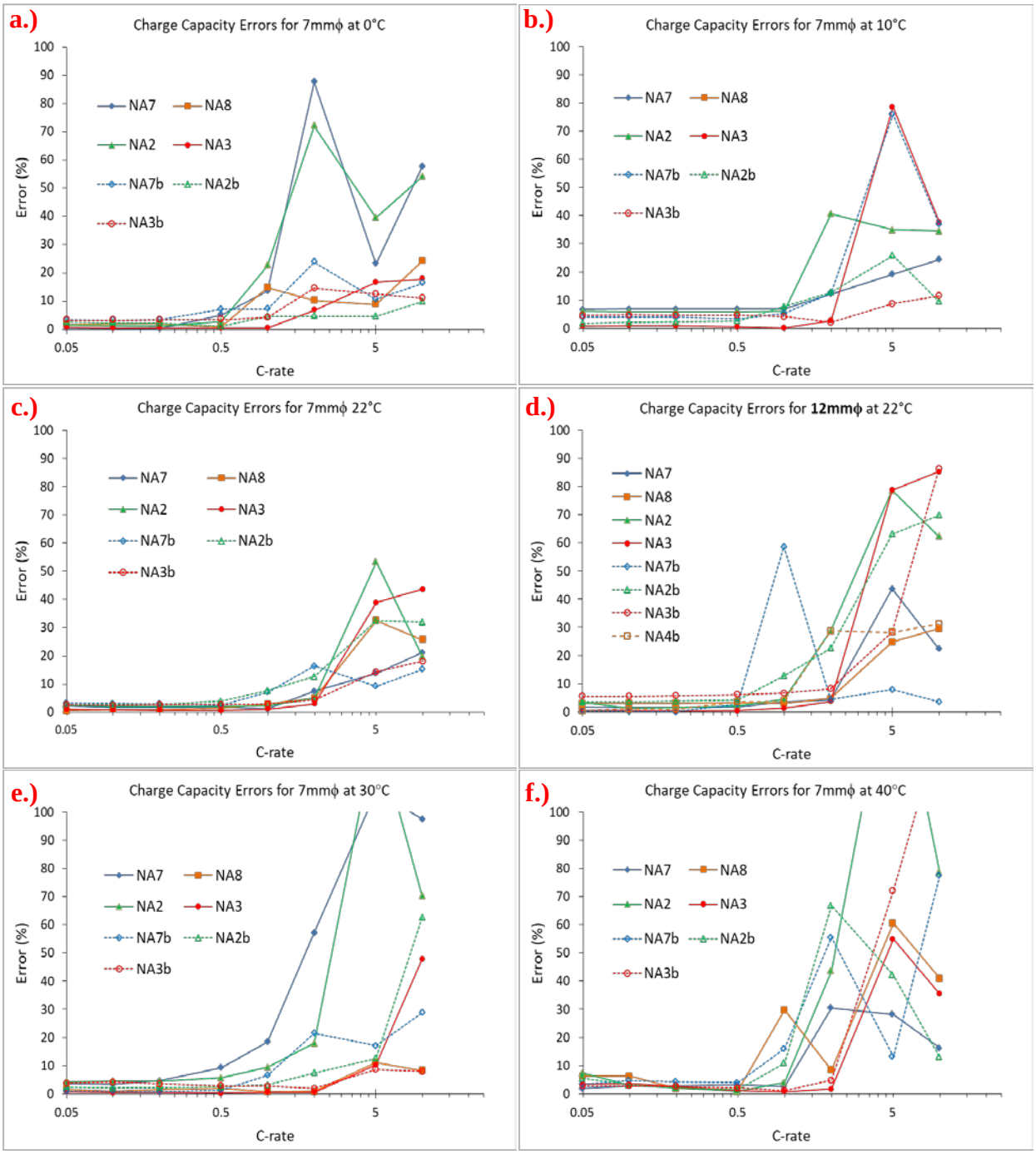

Figure 5.17: Charge capacity error percentages per C-rate per electrode for 7 mmϕ disc radius at 0°C (a), 10°C (b), 22°C (c), 30°C (e), 40°C (f) and for 12 mmϕ disc radius at 22°C (d).

5.4.4) Wettability Test

In an attempt to relate the strong relative errors observed above C* with the diffusion limitations, we performed wettability tests of the different electrodes by the electrolyte. Multiple 12mm diameter discs were punched from each electrode type and were soaked in excess electrolyte overnight. Tissue was used to remove excess electrolyte and masses were taken before and after soaking and were compared against the theoretical porosity volume from the electrode density. Volume quantification were done through the following equations:

The theoretical pore volumes were taken from the electrode densities as measured by the manufacturer:

$$pore\ volume = \left(\frac{electrode\ mass}{electrode\ density}\right) \times manufacturer\ porosity \qquad \textit{(eq. 5.5)}$$

and the penetrated electrolyte volume was determined through:

$$electrolyte\ volume = \left(\frac{mass_{wet} - mass_{dry}}{\rho_{LP30}}\right) \qquad \textit{(eq. 5.6)}$$

where $mass_{wet}$ is the mass of the fully soaked electrode, $mass_{dry}$ is the empty electrode and ρ_{LP30} is the density of LP30. The results are shown in Table 5.9 where the volume of absorbed electrolyte can be compared to the porous volume and the magnitude of the relative difference between these two highlights the fraction of the porosity that has not been penetrated by the electrolyte. Interestingly, the electrodes with the larger porosity are more entirely wetted by the liquid electrolyte. The poorer wetting of the lower porosity electrodes can come from the increased tortuosity and pore blockage posed by both the additional CB-PVdF and calendering as seen with FIB/SEM tomography and SEM. It should be noted that the wetting of the electrodes by the electrolyte in real conditions is possibly better than the results of these measurements suggest, where the impregnation duration has been limited, especially in view of the duration of the formation sequence and the low-rate cycles before the high-rate cycles, for which the lack of reproducibility is most striking. Moreover, the capacity measured at low-rate is generally close to the expected capacity, considering that the whole of the active mass participates in the discharge

(or the charge). It would have been interesting to carry out additional measurements to quantify the impregnation of the electrodes by the electrolyte in cycling conditions and eventually better understand the cause of the lack of repeatability of the electrochemical performance.

Table 5.9: *Standard deviation of the soaked electrode masses and relative errors of the soaked electrodes vs. theoretical porosity*

Electrode	**NA7**	**NA2**	**NA3**	**NA7b**	**NA2b**	**NA3b**
Mass gain (mg)	**2.6**	**3.8**	**2.2**	**2.1**	**3.3**	**2.0**
Std. Dev. (vs. average wt.)	0.2	0.0	0.3	0.4	0.1	0.3
Corresponding volume of electrolyte (µl)	**2.2**	**3.2**	**1.8**	**1.7**	**2.7**	**1.6**
Electrode sample volume (µl)	**9.7**	**10.2**	**7.0**	**10.8**	**10.9**	**6**
Porosity volume (µl)	**2.1**	**2.9**	**2**	**2.1**	**2.8**	**1.16**
Error (vs. theoretical volume, %)	9.7	0.0	16.9	30.9	4.6	43.1

5.4.5) Extra Charge Capacity

Still related to the repeatability of the measurements, we observed that some electrodes had excessive charge capacities. Table 5.9 corresponds to the discharge power test. Each discharge was followed by a charge at C/6, with a floating at 4.3V. One can see the difference between the measured capacity for the charge and the measured capacity for the discharge that preceded it. The reported data are averaged values on each series of electrodes at different temperatures. It appears that the charge capacity is systematically higher than the discharge capacity. This is described by: (i) long discharge (lithiation) times, therefore more lithium has been extracted from the material during charge and (ii) high temperatures (thermal activation).

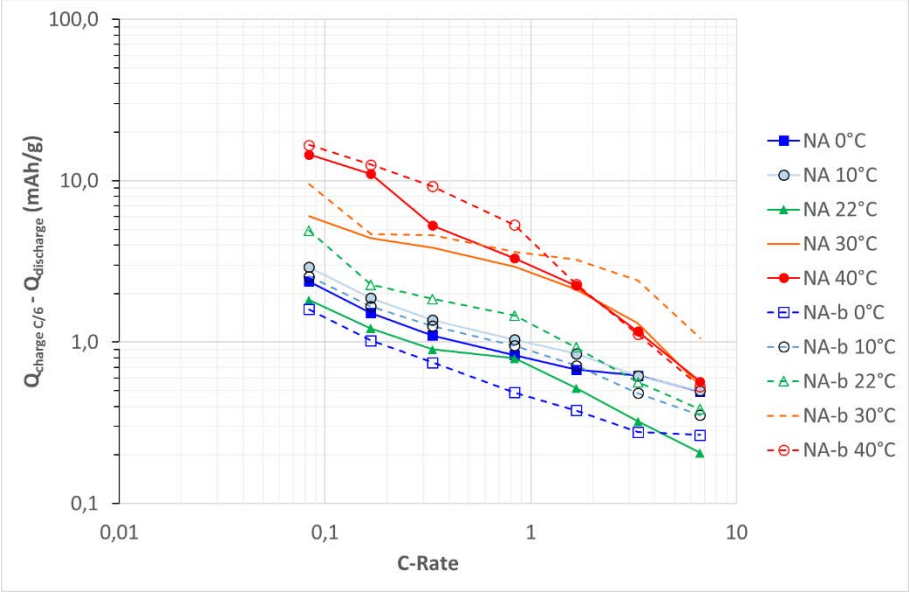

Figure 5.18: Difference between the measured capacity for the charge and the measured capacity for the discharge that preceded it (Log scale). The reported data are averaged values on each series of electrodes at different temperatures.

This extra charge can be due to the existence of a parasitic reaction of the electrolyte at high-potential with the active material, because it is amplified by a rise in temperature and by an increase in the duration in the high potential region. We would also like to note that these kinds of side reactions are expected to occur at temperatures higher than 40°C and higher voltage ceilings in literature [16,17] and therefore we would like to consider such side reaction occurring at relatively low temperatures as unique to our system. We then examined the possibility that this parasitic reaction may be a factor in the lack of repeatability of our discharge measurements. Indeed, it appears that for a given electrode formulation and for a given temperature, some batteries have an extra capacity very different from the average. This is the case for NA2-2 at 0°C, NA7-4 at 30°C, NA8-3 at 40°C, and NA7b-2 at 40°C (Figure 5.20 a, c , e, g). However, these electrodes do not systematically have aberrant discharge performance. For example NA2-2 and NA8-3 have performance absolutely equal to those of their sisters. In contrast, NA7-4 shows lower performance than those of its sisters and NA7b-2 higher performance (Figure 5.20 b, d , f, h).

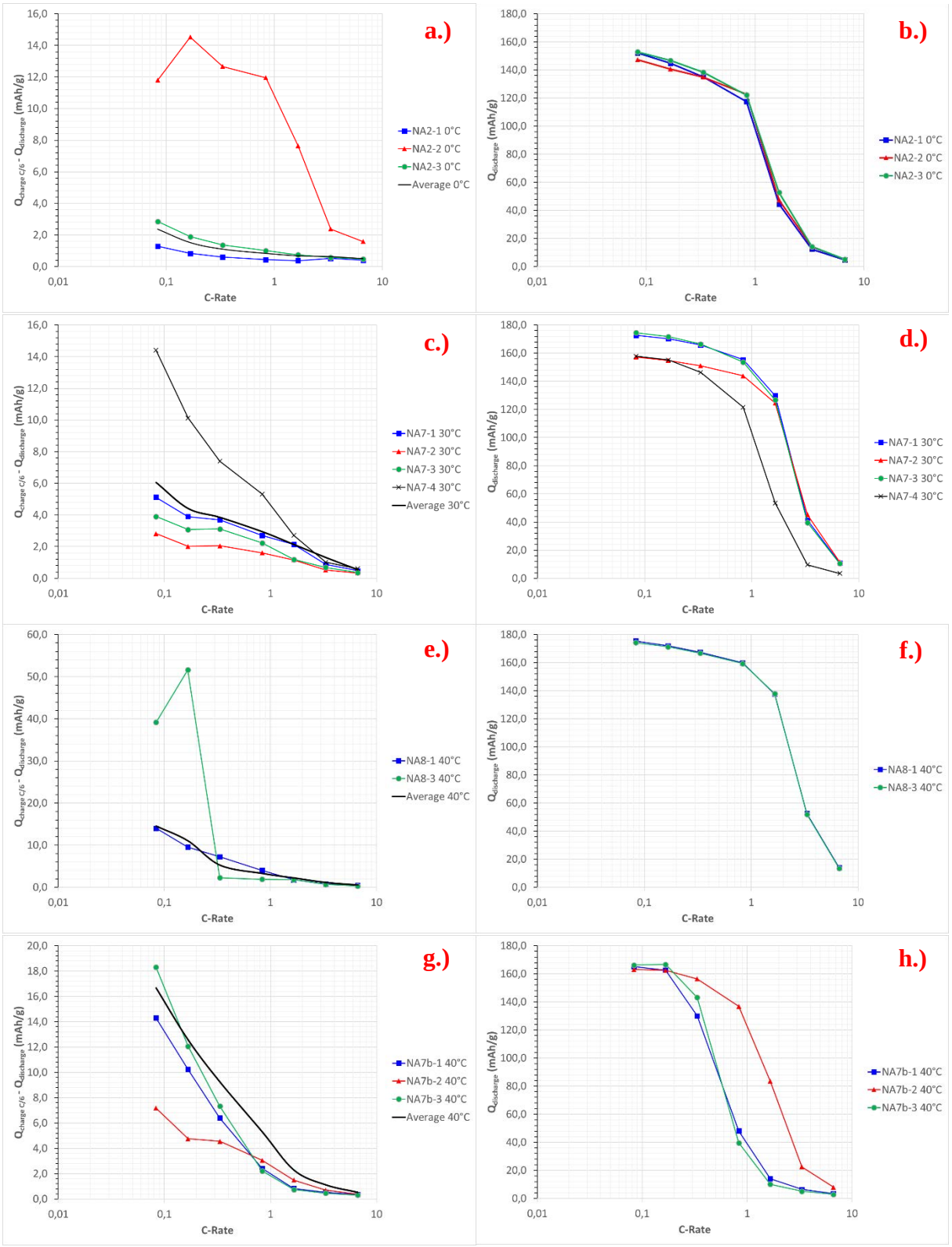

Figure 5.19: Difference between the measured capacity for the re-charge (always at C/6) and the measured capacity for the discharge (various C-rates) that preceded it (Linear scale). The reported data corresponds to single cells of NA2 at 0°C (a), NA7 at 30°C (c), NA8 at 40°C (e) and NA7b (g) at 40°C. The corresponding discharge power tests are given in (b), (d), (f) and (h).

Figure 5.21 corresponds to the charge power test. Each charge was followed by a discharge at C/10, with a floating at 2.1V. Figure 5.21 illustrates the difference between the measured capacity for the charge and the measured capacity for the discharge that followed it. The reported data are averaged values on each series of electrodes at different temperatures. It appears that the discharging capacity is systematically lower than the charge capacity, again all the more: (i) that the charge has been long, and (ii) the temperature is high. Moreover, some spikes can be seen on the capacity difference curves at high rates and high temperature. Again, we tentatively attribute this extra charge capacity to a parasitic reaction occurring in the high potential region of the electrolyte at the active material surface. This extra charge capacity could also be due to the fact that the float current operated at the end of the discharge was not sufficient to re-insert all the lithium de-inserted during the previous charge. But this assumption seems less likely than the former one because the discharge was carried out at a slow rate (C/10) and ended with a floating at 2.1V until the current reaches a minimal value (corresponding to a C/100 regime).

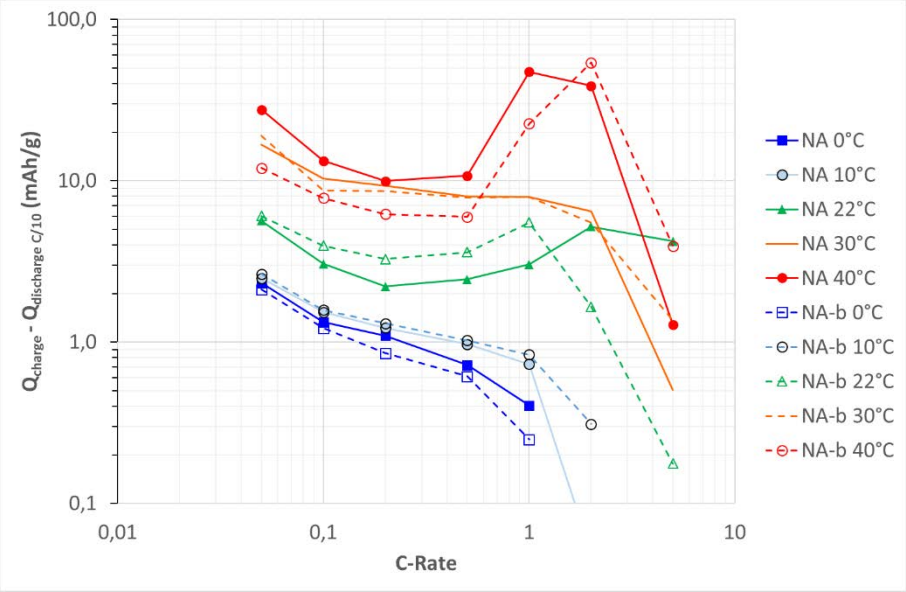

Figure 5.20: Difference between the measured capacity for the discharge and the measured capacity for the charge that preceded it (Log scale). The reported data are averaged values on each series of electrodes at different temperatures.

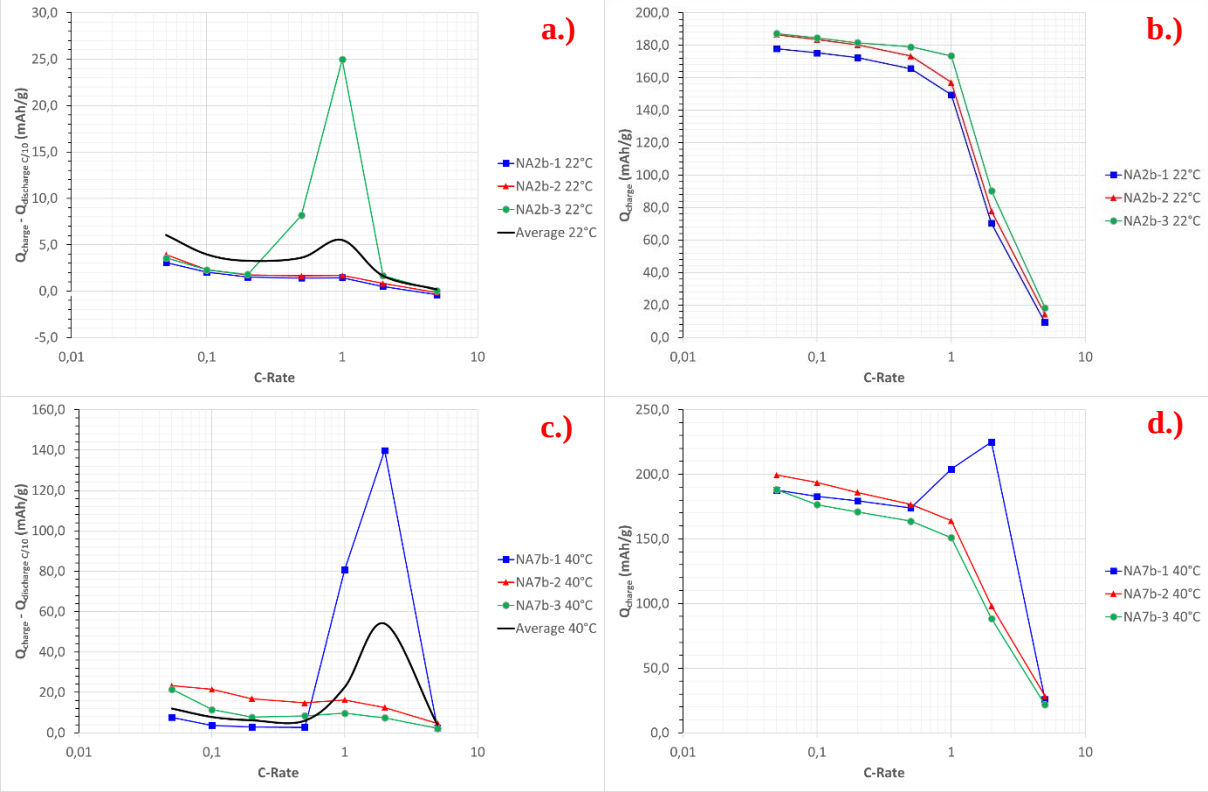

Figure 5.21: Difference between the measured capacity for the discharge (always at C/10) and the measured capacity for the charge (various C-rates) that succeeded it (Linear scale). The reported data corresponds to single cells of NA2b at 22°C (a), and NA7b at 40°C (c). The corresponding discharge power tests are given in (b) and (d).

5.4.6) Conclusion

This extra charge capacity is a major problem with regard to the performance analysis of the electrodes in charge. We tried to solve it in the following way. We will then report, for a given current regime, the measured charge capacity and the capacity measured at the next discharge (this one measured at C/10 + floater current). Quantitative analyzes will focus on the discharge capacity, based on the hypothesis that lithium re-inserted during the discharge can only be in sites left vacant during the charge. Furthermore, for the performance analysis of the electrodes both in charge and in discharge, we used average values for the cell resistances and Q_0, but we kept track of each individual cell for the diffusion modelling (PDM model).

5.5) Electrochemical Behavior – Qualitative Trends

Figure 5.23a shows the first charge-discharge capacities for NA7 electrode as part of the formation cycle. The discrepancy between the capacities of both first charge and first discharge indicates irreversible capacity that is associated on one hand with irreversible structural modification when the material is delithiated for the first time [18] and eventually a parasitic reaction as seen previously. And on the other hand with intrinsic kinetic limitations of the active material, as part of this capacity loss can be recovered with a constant voltage step at 4.3 V or by cycling at higher temperature. [19]. This was also observed for all electrodes in both NA and NAb series and is typical for cells using NMC 532 as their active material. The first cycle efficiency showed by all of the electrodes varied from 70%-80% indicating a 20% capacity loss.

Figure 5.23b and Figure 5.23c shows typical voltage-capacity curves for NMC 532 at various rates. Both the capacity of our NMC and the operating voltages were decreasing at increasing C-rate. The voltage plateaus also showed varied slopes at various regimes and the slope was getting steeper at increasing current densities. The decrease in both capacity and voltage are due to resistance contributions both electronic and ionic which will be further elaborated in the resistance and PDM model sections. In the following, the influence of the several parameters studied in this work (temperature, electrode additive content, porosity or density, thickness or mass loading) will be illustrated for discharges. Same trends were observed for charges.

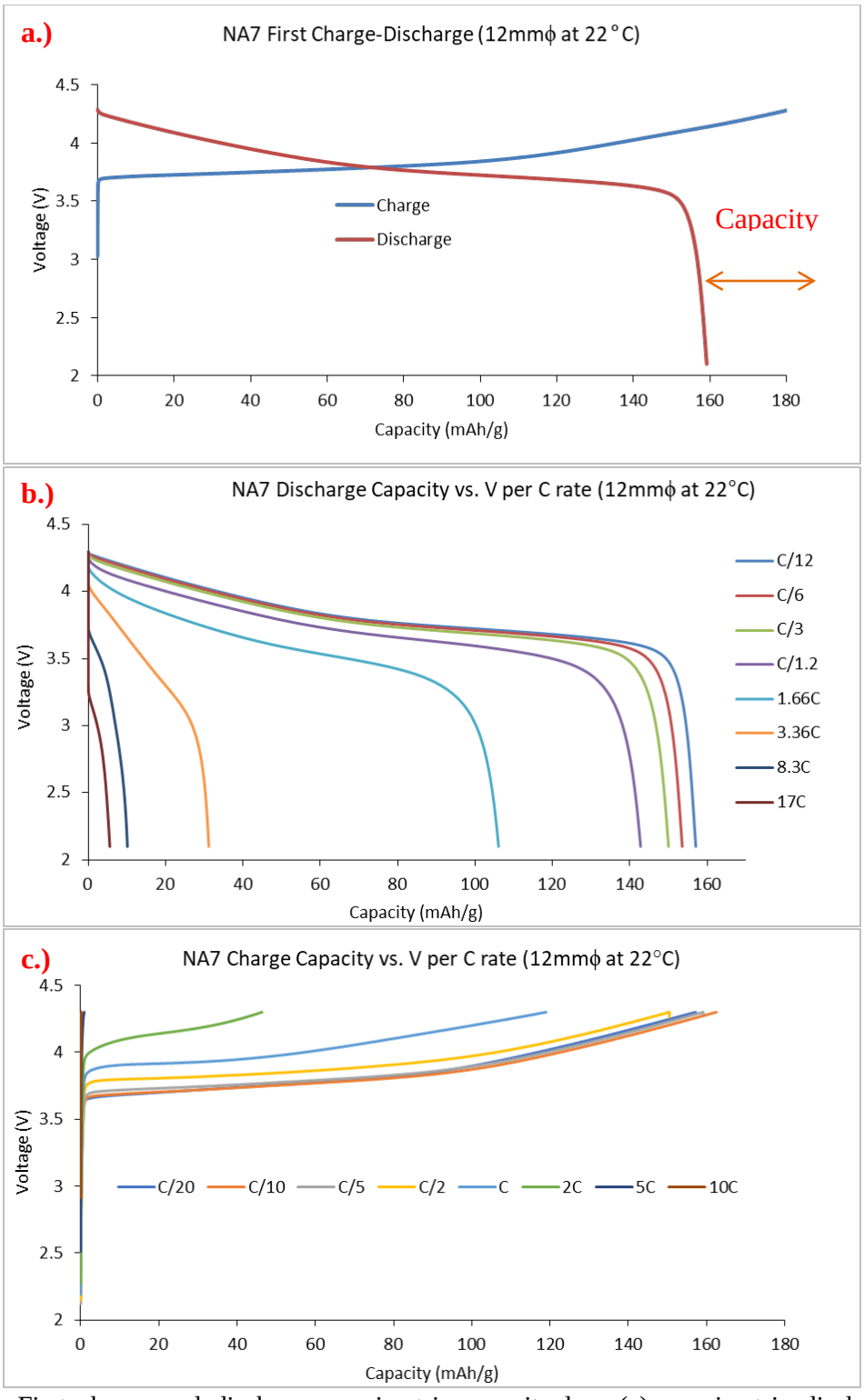

Figure 5.22: First charge and discharge gravimetric capacity loss (a), gravimetric discharge (b) and charge (c) capacities at various C-rates.

5.5.1) Influence of Temperature

Figure 5.24 shows the discharge and charge curves of NA7 at varying temperatures at a rate of 1.66C. Increasing capacity is seen at increasing temperatures both in discharge and in charge at this constant C-rate. Figure 5.25 shows the capacities of NA7 at varying temperature and multiple rates in discharge and in charge. In the latter case, the corresponding discharge capacities are also plotted. The discharge capacity experienced brutal drop from 151 to 36 mAh/g at a rate of 1.66C when the temperature decreases from 40 to 0°C, which is relatively large vs. the other C-rates indicating the change in the critical C* regime with the temperature (See bibliographical part for the definition of C*). Similarly in charge, the capacity drops from 155 mAh/g at 22°C to 49 mAh/g at 0°C. The increase in the nominal (low rate) capacity at increasing temperature could be due to minimized intrinsic kinetic limitations of the active material [19]. At higher temperatures, both electronic conductivity of the active material and electrolyte salt mobility are increased improving the electrochemical performance at all rates. Their contributions will be further discussed later.

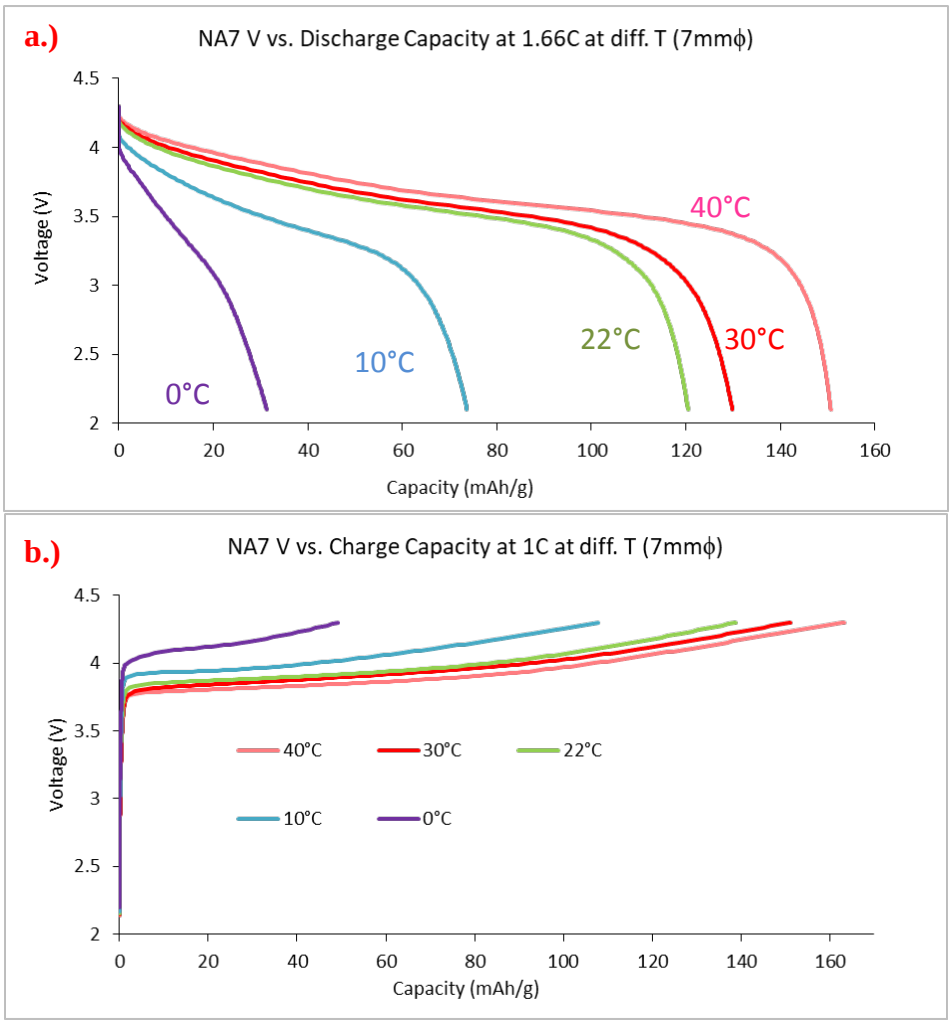

Figure 5.23: Gravimetric discharge capacities at 1.66C (a) and charge capacities at C (b) at various temperatures.

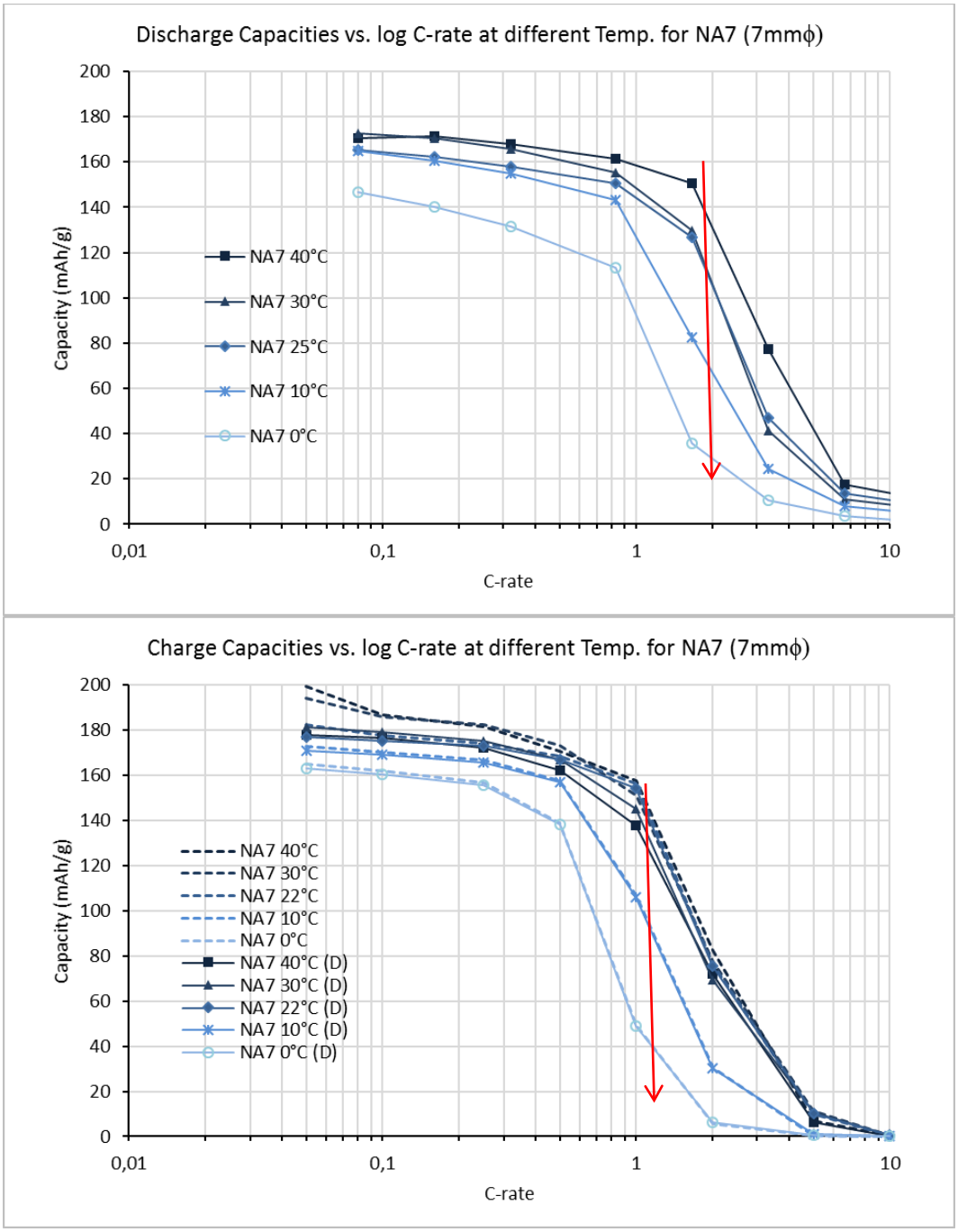

Figure 5.24: Gravimetric discharge (a) and charge (b) capacities at various temperatures. Capacity drop around C to 1.66C is highlighted by and arrow. The corresponding discharge capacities after charge are labeled as (D).

5.5.2) Influence of Additive Content

Figure 5.26 shows the potential vs. capacity curves of both NA7 and NA7b at varying C-rates. Interestingly, the increased CB/PVdF additive content decreases the practical capacity, in

particular at high C-rates (> 1). The same phenomena can be observed with the rest of the electrodes. Even NA2 and NA3, in which the CB/PVdF phase is not percolated, clearly show superior rate performance than, respectively, NA2b and NA3b, in which the CB/PVdF phase is well percolated. This result was unexpected when one refers to previous experimental work on others active materials such as $LiCoO_2$ [20,21], $Li_{1.1}V_3O_8$ [22], $LiMn_2O_4$ [23], $LiFePO_4$ [24], $LiNi_{0.8}Co_{0.15}Al_{0.05}O_2$ [25], or review articles [26] that indicate that the percolation of the electron-conducting network, here the CB/PVdF phase, is absolutely necessary to achieve both high nominal capacity and good power performance. This result likely indicates that the intrinsic electronic conductivity of the active material used here is sufficiently high that it is not necessary to form an extrinsic percolating electronic conductive network around this active material. The amount of CB/PVdF contained in the electrodes of the NAxb series is then excessive and probably penalizes the resistance to charge transfer, by reducing the amount of interface between the active material and the electrolyte, and/or penalizes the diffusion of the electrolyte species through the electrode by increasing the tortuosity of the porosity. This will be studied with more details later.

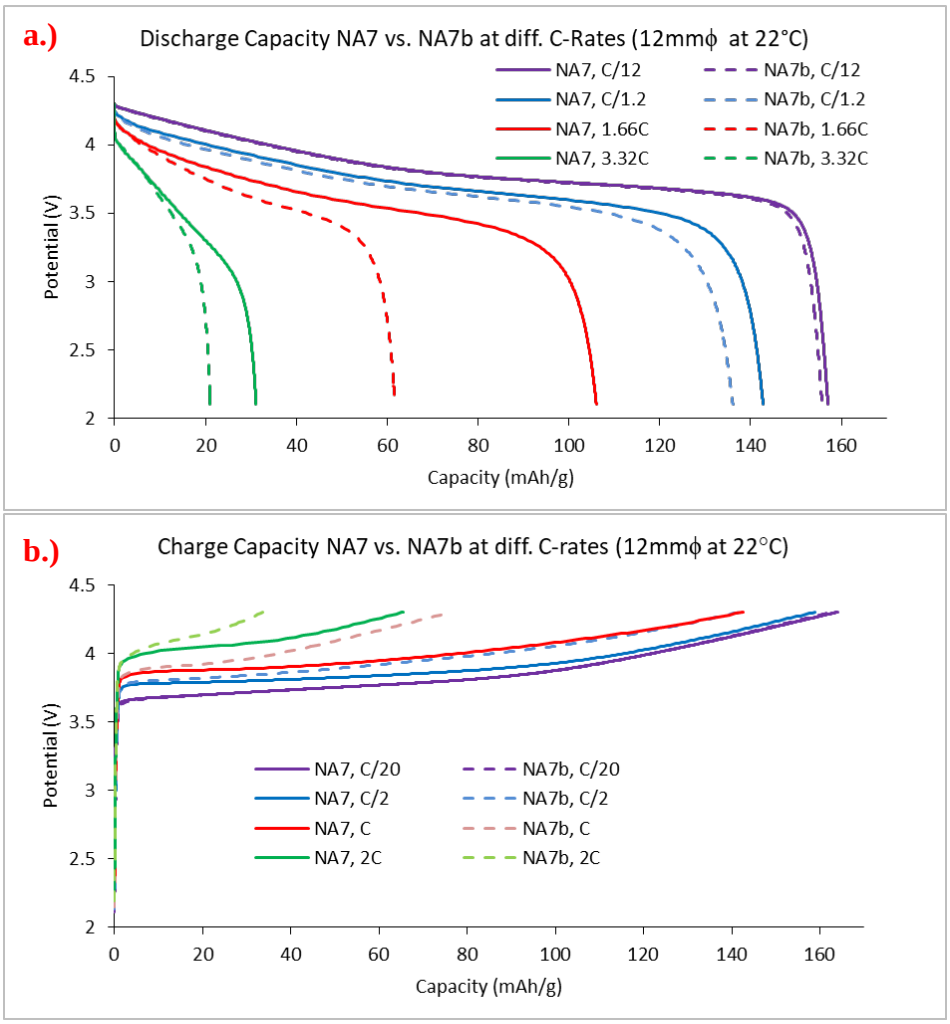

Figure 5.25: NA7 Gravimetric discharge (a) and charge (b) capacities at various rates at 12 mmϕ and 22°C.

5.5.3) Influence of Porosity

Dense electrodes generally have better electronic wiring but porous electrodes generally have better ionic wiring, which could affect performances at different regimes [27]. Figure 5.27a shows the potential vs. capacity curves of NA2, NA8 and NA7 at 1.66C. Increased capacities are seen at increasing porosities. NA2 share the same mass loading with NA7 but has higher porosity. NA2 delivered 25% more capacity than NA7 at a C-rate of 1.66C during discharge. This is also observed with the denser electrodes of the NAxb set as NA2b exhibited also 25% higher nominal discharge capacity than NA7b at a rate of 1.66C (not shown). The increased porosity has likely improved ion access resulting in better AM utilization at 1.66C. Furthermore, density effects can also be seen in the plots of capacity vs. current density (Figure 5.27b). Denser

NA8 electrode exhibited higher capacities at low current than NA2, but this hierarchy is reversed at higher current densities. Interestingly, both NA8 and NA2 almost have the same capacities during the charge power test (Figure 5.28).

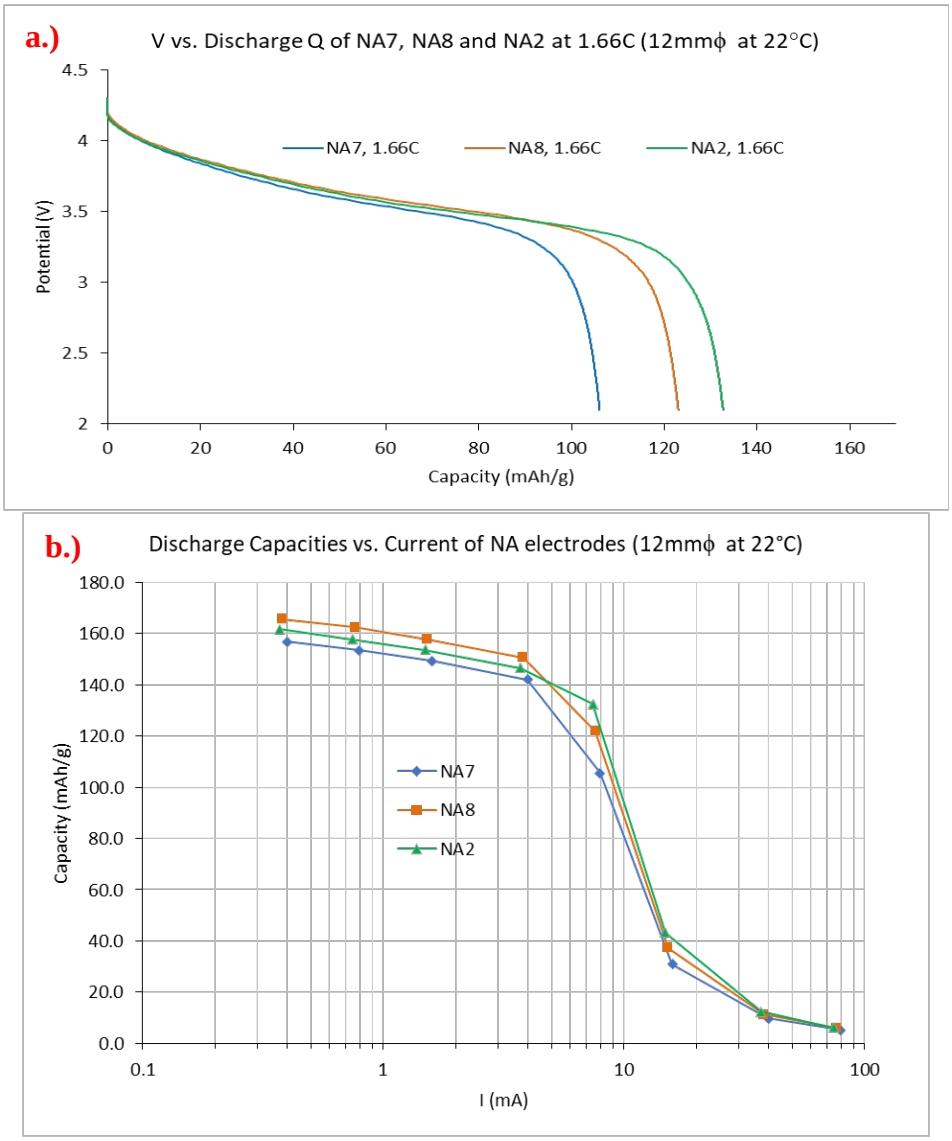

Figure 5.26: Discharge gravimetric capacities of NA7, NA8 and NA2 at 1.66C (a) and at different currents (b).

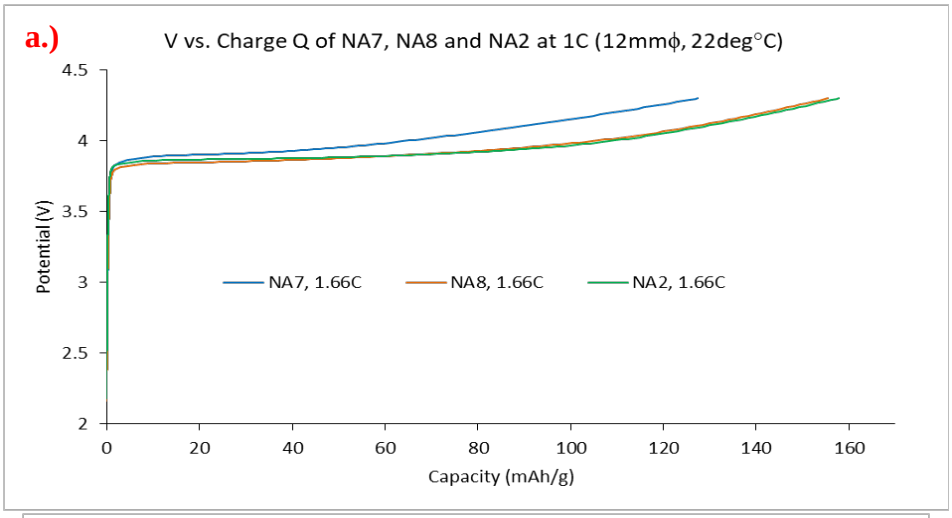

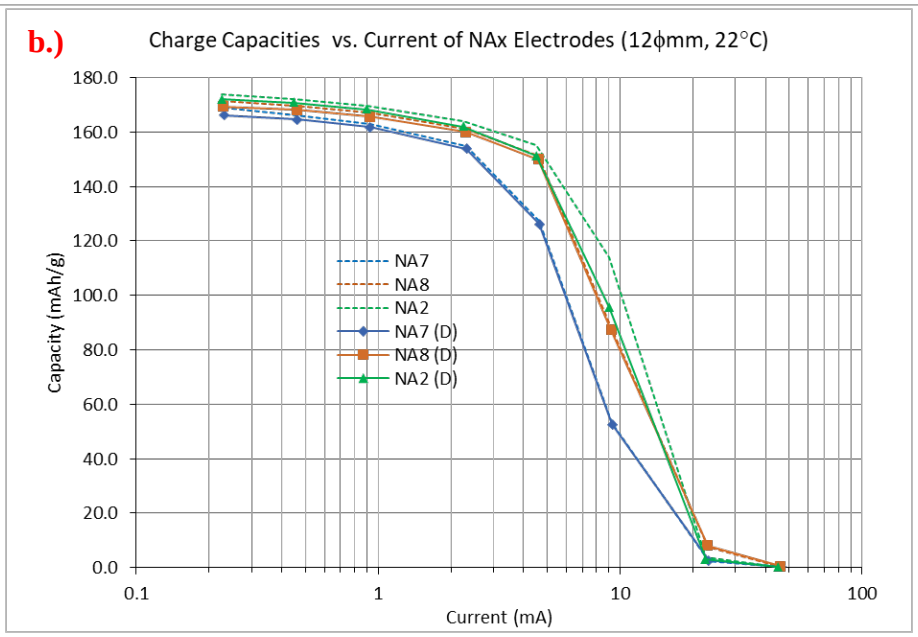

Figure 5.27: Charge gravimetric capacities of NA7, NA8 and NA2 at C (a) and at different currents (b). The corresponding discharge capacities after charge are labeled as (D).

5.5.4) Influence of Mass Loading

Figure 5.29 allows to compare the potential vs. capacity curves both in discharge and charge at 1.66C and 1C, respectively, of NA3b, NA7b and NA4b that have all same composition and density but different active mass loadings. The obtained specific capacity clearly decreases when the active mass loading increases. In complement, Figure 5.30 and Figure 5.31 show the variation of the specific and areal capacities of NA7b, NA4b and NA3b in both charge and discharge with the rate and the current density. NA4b bears the highest mass loading of all the electrodes in this study which allows it to have the highest areal capacity of all the electrodes. In

terms of specific capacity, NA4b full capacity can only be optimally extracted at lower C-rates. At increasing C-rates, the extractable capacity starts to drop severely for NA4b starting from a low C-rate of C/5. This is remarkable relative to other electrodes in this study since that the severe capacity drop is only observed starting from a C-rate of C. These observations somehow support the idea of ionic limitations and how it affects C*. NA4b's increased thickness increases the distance over which the electrolyte species must diffuse. This results to earlier salt depletion in the deeper regions of the pore matrix consequently terminating the electrochemical reaction even at a low rate of C/5. Nevertheless, the power performance of this electrode is not bad in light of the state of the art. Table 5.10 below summarizes previous works. The critical state C* of the electrodes of the state-of-the-art is a little higher than that of NA4b, but it will be noted that their porosities are twice as high. Charge capacities appear to decrease from C* and beyond owing to the limitation of the charge ceiling potential (4.3V).

Table 5.10: NA4b's composition (first line) in comparison to electrodes of existing literatures.

NMC **Electrode formulation** **NMC/C/B**	**Capacity (mAh/cm²)** ***Active mass loading (mg/cm²)***	**Porosity (%)** ***Thickness (µm)***	**C***	**Ref.**
532 94.2:3.2:2.6	6.7 *41.7*	19.1 *119*	C/5	here
333 90:7:3	8 *67*	40 *255*	C/2	[28]
333 93.6:4.4:2	10 *71*	44 *295*	C/2	[29]

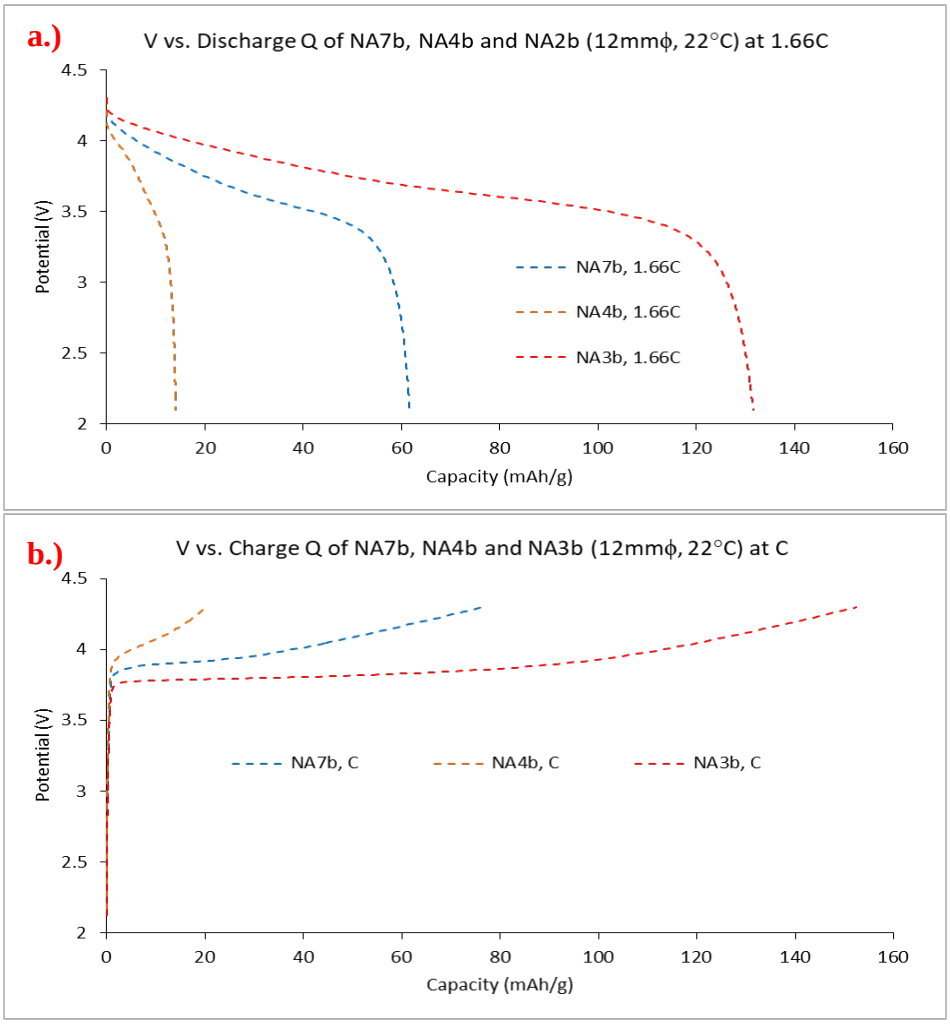

Figure 5.28: Gravimetric discharge (a) and charge (b) capacities of NA7b, NA4b and NA3b at 1.66C (a) and C

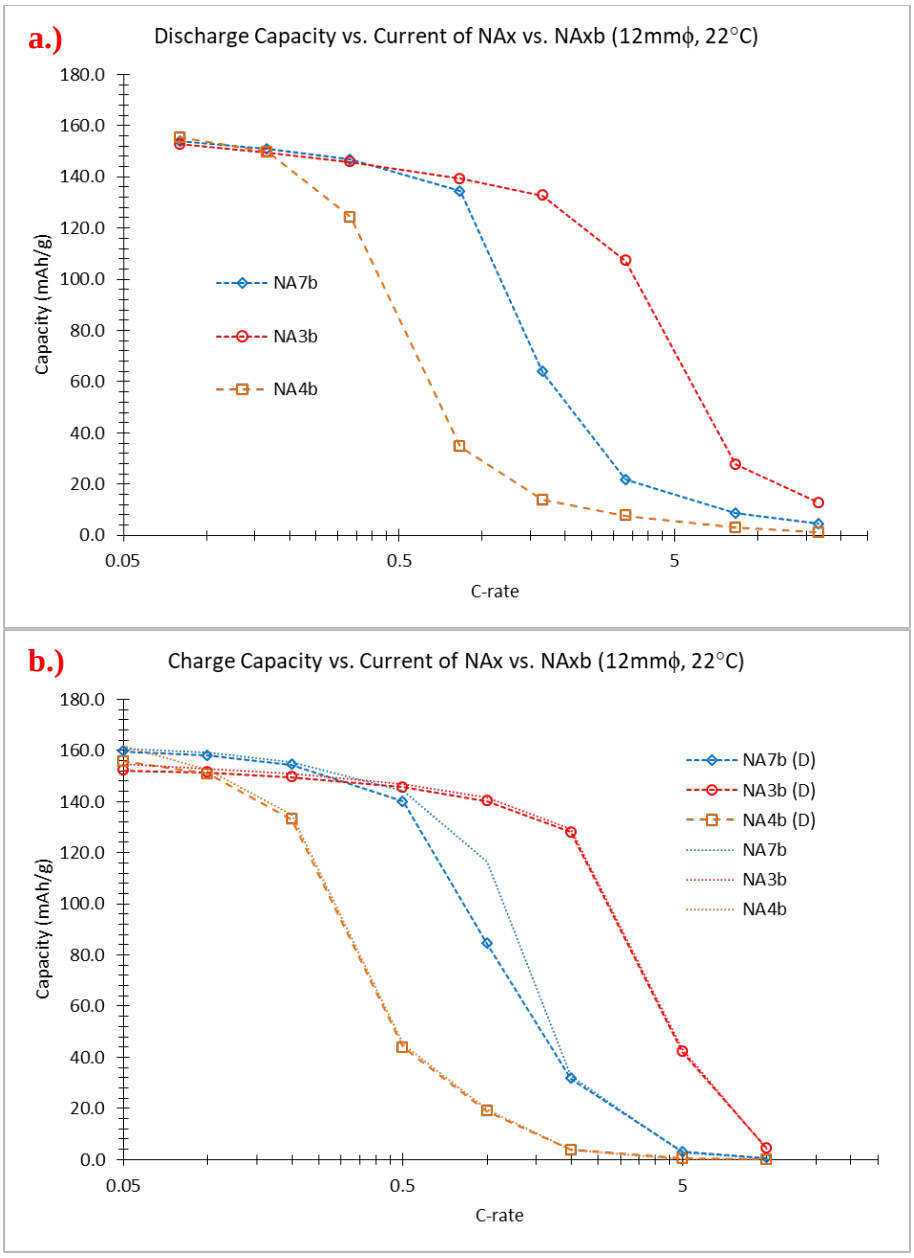

Figure 5.29: Gravimetric (a) and charge (b) capacities of NA7b, NA4b and NA3b at varying C-rates. The corresponding discharge capacities after charge are labeled as (D).

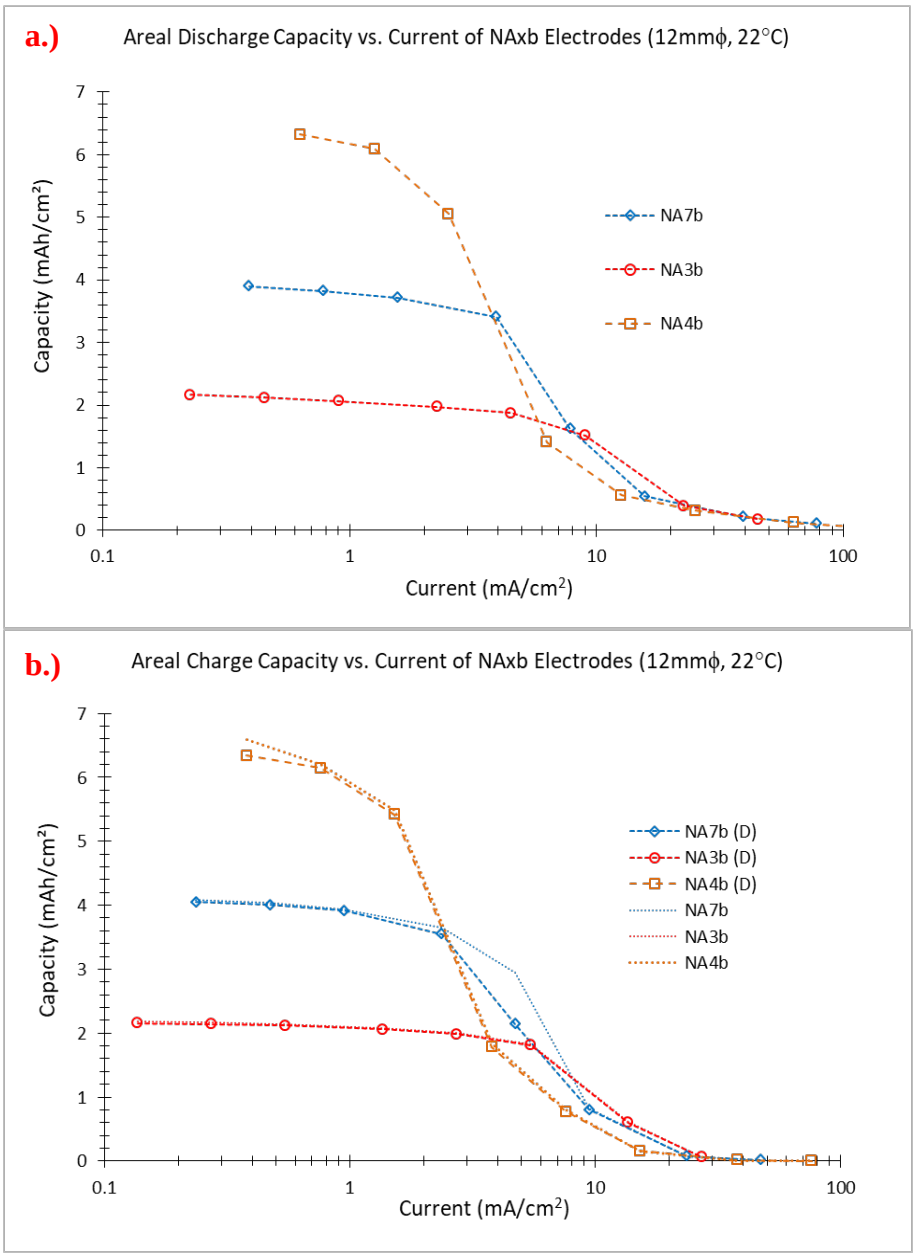

Figure 5.30: Areal discharge (a) and charge (b) capacities of NA7b, NA4b and NA3b at varying C-rates. The corresponding discharge capacities after charge are labeled as (D).

5.6) Quantitative Analysis Methodology

Our initial qualitative analyses reconfirmed the presence of multiple limiting factors in electrochemical performance as demonstrated from past literature. Since this study deals with electrode design and formulation, it is best to quantify these limitations to be able to optimally identify industrially relevant parameters. The succeeding sections will deal with these various parameters specifically cell resistance, C*, Q*, and penetration depth. We would also like to

remind the reader that results that deal with temperatures effects were done with coin cells having 7 mm diameter positive electrodes and results that compare electrode compositions and properties (at room temperature) were done with coin cells having 12 mm diameter positive electrodes.

5.6.1) Cell Resistances

The cell resistances were determined from the cell polarization and the absolute operating current. This cell polarization is defined as the difference in potential between the operating voltage and the voltage observed for the lowest measuring current as illustrated in Figure 5.32 When the cell polarization is plotted versus the absolute current, a very clear linear trend is observed for discharge (Figure 5.33b). This corresponds to the simple Ohm's law relation V=IR where V is the potential difference, I is the current and R is the cell resistance.

For the charge, a nearly linear behavior is observed only for the lower currents, corresponding to C-rates up to 2C. We believe that the operating voltages at charging rates of 5C and 10C are too close to the ceiling voltage (4.3V) to be able to extract a proper voltage difference. Thus, we have considered the charge cell resistance value coming only from the linear part of the voltage difference-current curves. One can also observe on the voltage-capacity plots that the voltage difference is much higher in charge than in discharge. For example, at the charging rate of 2C the voltage difference equals about 0.5 V, while at the discharging rate of 3.2C it only equals about 0.2 V. Logically, cell resistances during charge also appear to be much higher in charge (108.5 Ω) than during discharge (24.2 Ω) (Figure 5.33a), which will be discussed later.

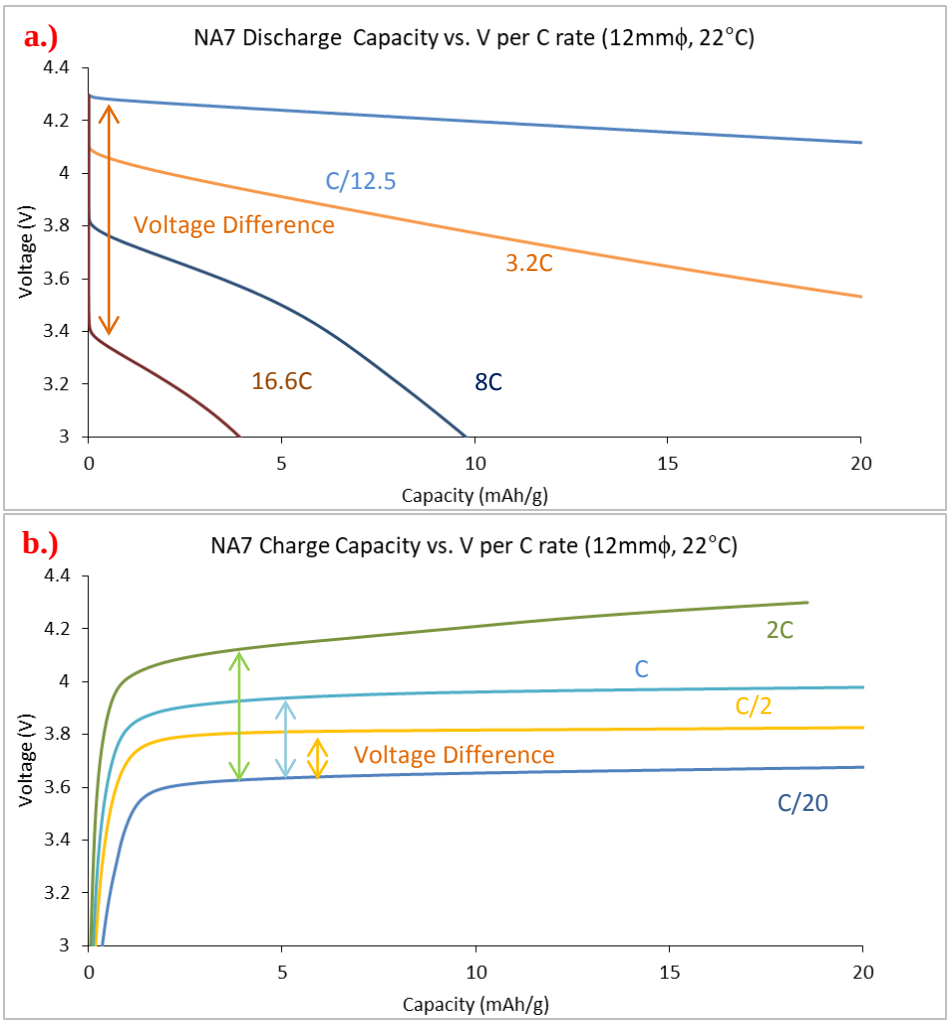

Figure 5.31: Determination of voltage difference by subtracting the operating voltage to the C/12.5 voltage (lithiation, a) and subtracting the operating voltage at C/20 to operating voltage of other C-rates (delithiation, b). Voltage differences at 5C and 10C charge rates were omitted.

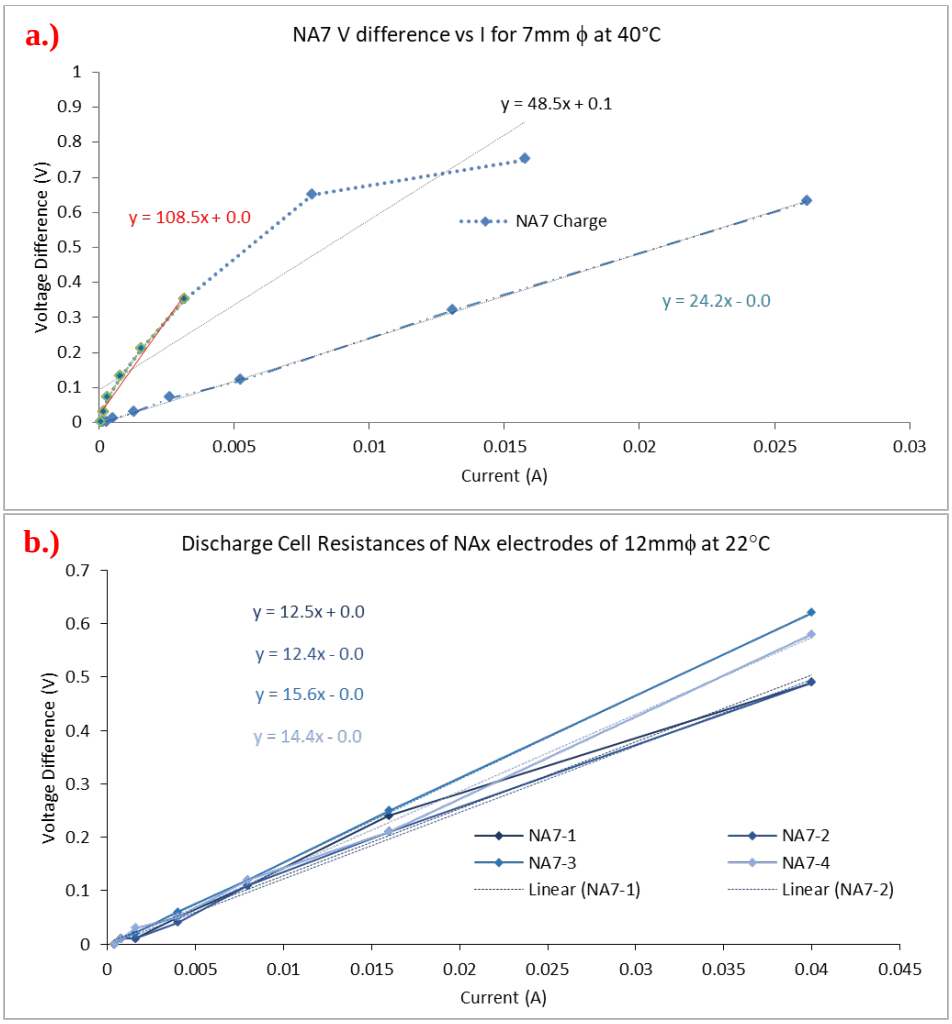

Figure 5.32: Linear fitting example for NA7 charge and discharge cell resistances (a). Fitting correction for charge was done by taking out points at high C-rate due to ceiling voltage (red line). Statistical presentation of cell resistances for the four cells of NA7 with 12mmϕ cathode diameter at 22°C (b).

5.6.2) Nominal Capacity (Q_0) and Critical Regime (C*)

Figure 5.34 illustrates the identification of Q_0 and C*. Q_0 is defined as the maximum practical capacity (= nominal) and C* is the C-rate at which there is a noticeable decline in capacity. Q_0 is best taken at the lowest C-rates of our power tests, i.e. C/12.5 in lithiation and at C/20 in delithiation. This criterion is best supported by complementary tests at C/60 wherein there is still a significant increase in discharge power capacity when discharging at very low rates. Q_0 is higher in charge than in discharge, which may reflect the better intrinsic kinetics of the active material in the delithiated than in the lithiated states. C* shifts from higher C-rates to lower C-rates specifically: between 1.66C and 3.2C for lithiation, and between C and 2C for delithiation.

The difference in C* with charge and discharge could be again attributed with the charge ceiling voltage (4.3 V). The proximity of the latter with the charge operating voltage results in premature end of charge at higher C-rates.

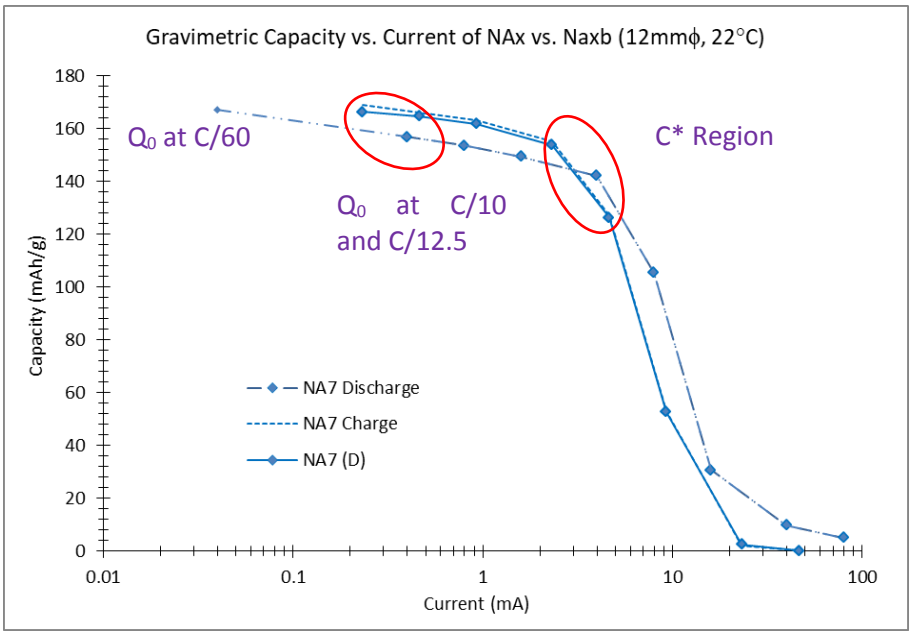

Figure 5.33: Charge and discharge capacities of NA7 showing the areas of Q_0 and C evaluation. The corresponding discharge capacities after charge are labeled as (D).*

5.6.3) Penetration Depth Model

Modeling in scientific research has helped better understand observable phenomena. In the battery industry, models also serve as a form of alternative research at a reduced cost. In the context of this study, analytical modelling is employed to both understand how the electrode parameters affect the electrochemical performance of electrodes but also to help develop a simple model that could help tailor optimized electrodes in an industrial setting. West et.al. [30] formulated a model focused on the correlation of electrochemical performance of porous insertion electrodes with the diffusion of the salt in the electrode pores. The main assumptions of the model are that the charge-transfer overpotential is negligible and the pore geometry consists of ideal shapes namely cylinders, spheres and columns. The transport in the electrolyte was treated as one-dimensional diffusion and migration according to the Nernst-Planck equation. It was concluded that the electrolyte depletion is the principal limiting factor in the capacity obtained during discharge. Fuller et. al.'s model dealt with thickness effects on power

performance [31]. This included a multi-pronged approach wherein they correlated ion concentrations both in the AM and electrolyte, the electrode potential, and Butler-Volmer kinetics to predict the electrochemical performance of electrodes.

As described earlier in the literature review by Gallagher et.al. [32], salt depletion at the deeper recesses of the pore network dictates performance at high C-rates. This salt depletion happens when the intercalation reaction is fast enough but the pore reservoirs are unable to replenish the concentration of lithium ions therefore halting the electrochemical reaction. Johns et.al. proposed a direct approach in relating the current density and the depth of discharge [33]. The model mostly revolves on how the transference number of the electrolyte salt performs during the depletion phenomenon. Transference number is the number of moles of a charged specie that migrates to an electrode after the passage of a Faraday of charge. In the case of lithium, the number that successfully reached the electrode by migration is assigned as t_+. Its complement $(1 - t_+)$ or t_- defines the number of moles of lithium that cannot take part in the electrode reaction until they have reached the active particle surfaces by salt diffusion. The discharge front generated via the depletion phenomena is schematized in Figure 5.35.

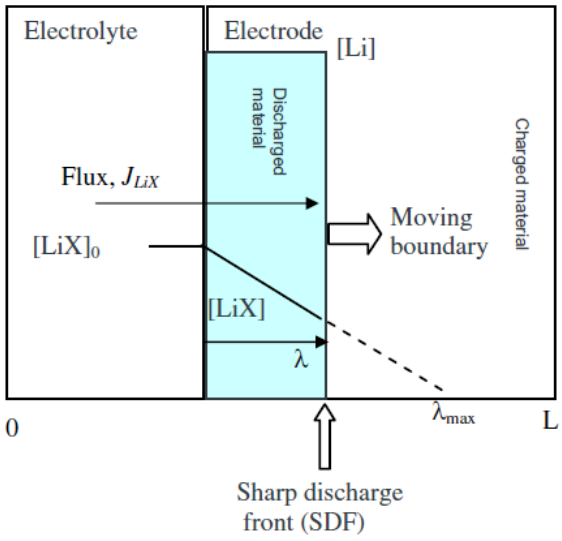

Figure 5.34: Representation of the sharp discharge front model.

The aim of this approach is to assess the significance of restricted lithium salt diffusion in the composite battery electrode. This model is simple as it only accounts for the diffusion of the

lithium salt in this moving boundary. Johns et.al. also included the following assumptions for their model:

- A sharp planar boundary between discharged and charged material perpendicular to the current direction.
- A negligible initial concentration of lithium salt LiX in the composite compared with the total demand for lithium during discharge.
- Constant [LiX] = $[LiX]_o$ in the separator.
- Constant values of the diffusion coefficient D_{LiX} and lithium transference number T_+.

This meant that the assumptions heavily state that the diffusion coefficient of the ion species is constant throughout the rest of the cell and that early termination of the electrochemical reaction happens when $[LiX]_1$ (the concentration of Li at area/region of the discharge front (the planar moving boundary)) approaches zero. Ionic resistance is also the sole resistance present and all electronic limitations are negligible. The general diffusion equation of the moving boundary is stated as:

$$J_{LiX} = \left(\frac{jt_-}{F}\right) = -D_{LiX}\left(\frac{d[LiX]}{dx}\right) \qquad \textit{(eq. 5.7)}$$

$$\left(\frac{d[LiX]}{dx}\right) = -\frac{jt_-}{FD_{LiX}} \quad \rightarrow \quad [LiX]_1 = [LiX]_0 + \lambda\left(\frac{d[LiX]}{dx}\right) \qquad \textit{(eq. 5.8 and eq. 5.9)}$$

where λ is the thickness of the discharged region. *j* denotes current density, J_{LiX} the flux of salt in the electrolyte and F is the Faraday constant. A premature end of discharge occurs when $[LiX]_1$ = 0 and $\lambda = \lambda_{max}$:

$$\lambda_{max} = \frac{-[LiX]_0}{\left(\frac{d[LiX]}{dx}\right)} = \frac{FD_{LiX}[LiX]_0}{jt_-} \qquad \textit{(eq. 5.10)}$$

where λ_{max} is the maximum discharge front, and $[LiX]_0$ is the concentration of lithium in the electrolyte bulk. The degree of discharge, DoD, therefore depends on the current density j as follows:

$$DoD = \frac{discharge\ capacity\ obtained}{theoretical\ capaciyt} = \frac{\lambda_{max}}{L} = \frac{FD_{LiX}[LiX]_0}{jt\_L} \quad \textit{(eq. 5.11)}$$

where L is the electrode thickness. The model illustrated well the relationship between the depth of discharge at high rates but was concluded to better describe supercapacitor systems than batteries.

Shifts in current distribution can occur due to the concentration gradients that are generated during the mass transfer of ions from the separator to the electrode surface and vice versa. These concentration gradients will approach a pseudo steady-state at time t_{ss} leading to a penetration depth in the electrode pore matrix L_d. If the said penetration depth is larger than the electrode thickness, then the electrochemical reaction is not bound by ionic transport and vice versa. Gallagher et.al. used concentrated solution theory and had the following assumptions:

- convection and changes in solvent concentration are negligible,
- the salt is composed of a univalent cation and anion

The resulting equation is as follows:

$$L_d = \frac{\epsilon}{T}\frac{D_0 C_0 F}{(1-t_+)I} \quad \textit{(eq. 5.12)}$$

Where ε is the electrode porosity, T is the tortuosity factor, D_0 is the salt diffusion coefficient in electrolyte, C_0 is the electrolyte salt concentration and I is the current density. The difference between this equation and John's is that it takes into account the electrode porosity effects on the local concentration of salt in the pores and also that the diffusion is affected by the tortuosity. These allow only a rough estimation of DoD when considering the values of D_0, t_+ and C_0. We then combine both John's and Gallagher's equations which results to:

$$PD = \frac{Q_{C-rate}}{Q_{low\ rate}} = \frac{L_d}{L} = \frac{\epsilon}{TL}\frac{D_0 C_0 F}{(1-t_+)I} \quad \textit{(eq. 5.13)}$$

which is our attempt to better quantify the effects of electrode microstructure in the electrochemical performance of battery electrodes. Three approaches were taken in the fitting of the model: adjusting D_0, adjusting T, and adjusting ε.

D_0 was adjusted first to compare its order of magnitude with the lithium salt diffusion coefficient measured by PFG-SE NMR for bulk electrolyte at different temperatures. To perform the fit, we considered the total porosity of the electrodes and a tortuosity factor from a well-recognized literature [34]. We used the lower bound of the modified Bruggeman-type function established by Usseglio-Viretta et al. for a NMC532–based electrode (see bibliographical section).

$$T = 1.3\epsilon^{-0.59} \qquad \textit{(eq. 5.14)}$$

As an output result, the difference between the effective diffusion coefficient (the fit result) and that of the electrolyte could be interpreted as a consequence of the physico-chemical interactions of the electrolyte with the electrode materials. In fact, some studies have shown an impact of the interactions at the solid / liquid interfaces on the diffusion of the species of the electrolyte. [35,36,37,38]

Tortuosity factor adjustment was then done through using the D_0 values taken from PFG-SE NMR measurements of the bulk LP30 electrolyte at varying temperatures and also using the porosity assigned by the manufacturer (the total porosity). Indeed, a number of studies conclude that the geometric tortuosity determined by tomography overestimate the ion mass transport including electrolyte diffusivity and conductivity. [39] Experimentally determined effective tortuosity, through the measurement of effective ionic resistivity of the electrode by impedance spectroscopy [40,41] or by polarization-interrupt experiment [34], or through gas transport resistance measurement method [42], give larger values than typical geometrical tortuosity (typically several times).

Finally, starting from the analysis conducted by François Cadiou concerning the different porosities observed in the FIB/SEM volumes, porosity adjustment was done using the same bulk D_0 approach and assigning tortuosity with the value of “maximum free tortuosity” calculated via FIB-SEM tomography. In doing so, we verified our hypothesis that macroporosity plays a key role in the replenishment of lithium concentration by salt diffusion through the electrode.

The shapes of the curves were matched with the points along the C* region (either 2C or C depending on the electrode and the temperature). This matching was done to generate three values namely D_{eff}, T_{eff} and ε_{eff}. This was to illustrate how the 3 values change while the other values remain constant.

Figure 5.36 shows the fitted curves for NA7 using the PDM model and the modified values presented in Table 5.11. The PDM model was only applied at C-rates containing C* and above due to that the model only applies for diffusion limited processes (high C-rates) therefore there is no model curve below C*. The PDM model curve somehow captures the capacity drop starting from C* and the curve of capacity decrease is almost as the same shape as the experimental curve. The discrepancy between the model and the experimental curve may stem from how the model is a rough estimate that does not take into account neither the electronic limitations on the practical capacity nor the influence of the cell polarization. Even so, the shape of the curve mimics the experimental behavior even at varied values of D_{eff}, T_{eff} and ε_{eff}. The adjusted parameters D_{eff}, T_{eff} and ε_{eff} will all be further discussed quantitatively.

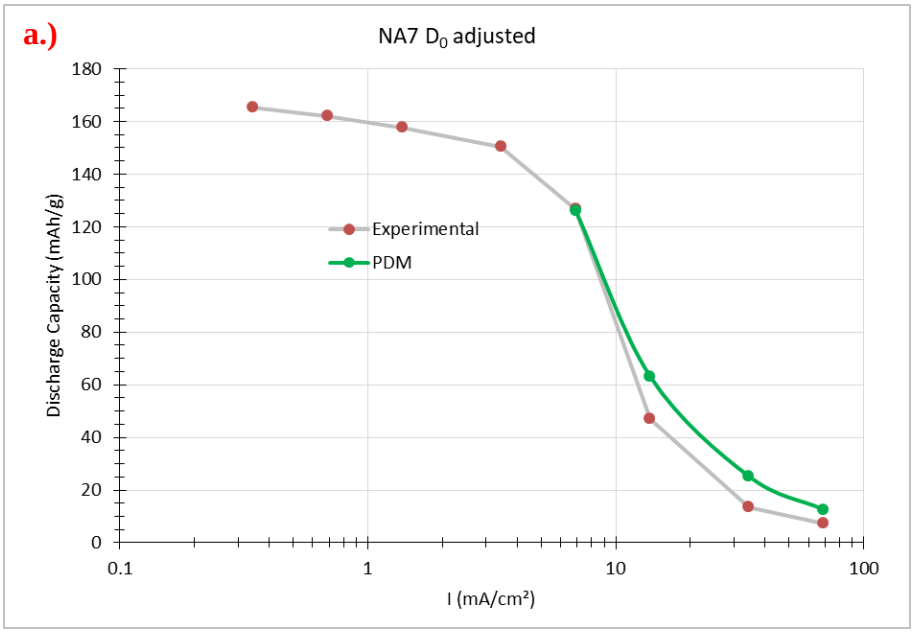

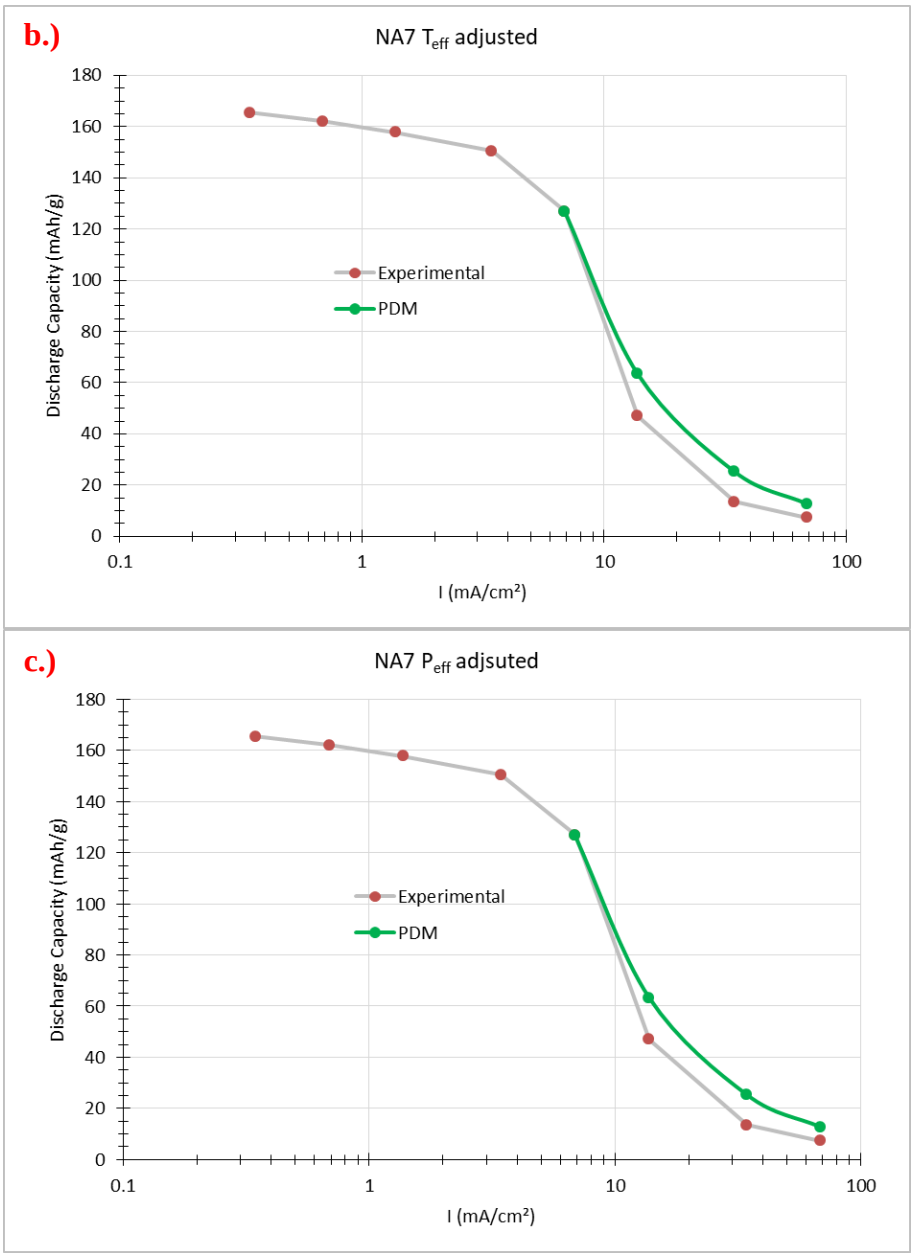

Figure 5.35: NA7 discharge PDM fits optimized with D_0 (a), T_{eff} (b) and P_{eff} (c).

Table 5.11: Table of values used in the model. Values in bold represented manually adjusted values for the fit. F, Faraday's constant is in A.s/mol. The electrode is NA7 at 22°C.

Graph	Q_0 (mAh/g)	D_0/D_{eff} (cm^2/s)	T_0/T_{eff}	$\varepsilon_0/\varepsilon_{eff}$	I (A/cm^2)	L (cm)	t_+	C_0 (mol/cm^3)
D_0 adjusted	165.5	***3.5 x 10^{-6}***	3.8	0.212	0.00344	0.0074	0.383	0.001
T_{eff} adjusted	165.5	1.6 x 10^{-6}	***1.36***	0.212	0.00344	0.0074	0.383	0.001
ε_{eff} adjusted	165.5	1.6 x 10^{-6}	1.2	***0.184***	0.00344	0.0074	0.383	0.001

5.7) Cell Resistances

5.7.1) Influence of the Electrode Diameter and/or the Active Mass Loading

Cell resistances in discharge at 22°C were taken at varying electrode radii to study loading effects. Figure 5.37a shows the cell resistances plotted against the active mass (increasing radii) and Figure 5.37b against the inverse of the active mass.

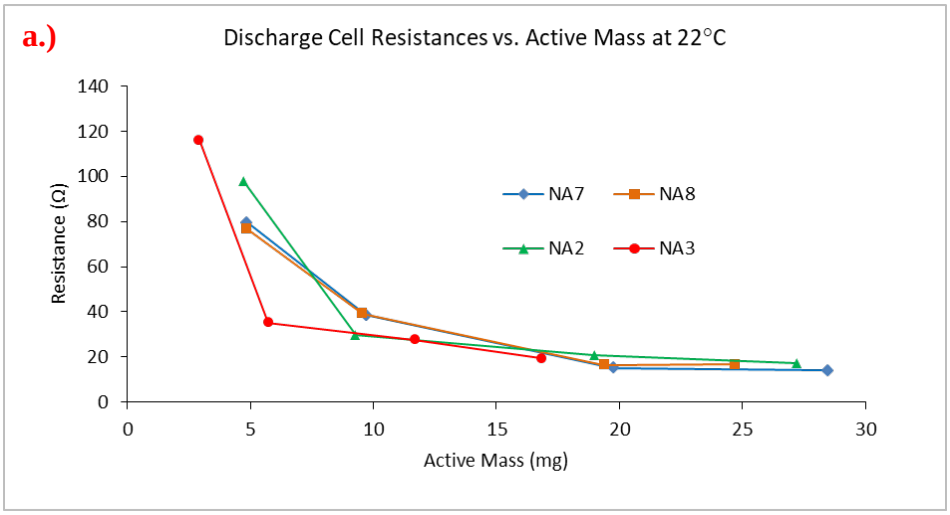

Figure 5.36: Discharge cell resistances of the NAx electrodes vs active masses.

The cell resistance decreases with increasing active mass and tends toward a plateau value at high active mass. It has been shown that the total electrode polarization resistance can be decomposed in two terms. [43,44,45,46] The first one, R_w, gathers the electronic and ionic wires resistances, with (i) the contributions of the electrode/current collector interface (the contact resistance) and the electronic conductive network (in general the conducting agent/binder), and (ii) the contribution of the liquid electrolyte network in the electrode's porosity for the ionic wires. The second one, which is called the charge transfer resistance R_{ct}, reflects the resistance to lithium insertion (de-insertion) into the active particles. It depends on (i) the lithium insertion reaction mechanism, which may involve the migration of lithium ions through the SEI and (ii) the interconnectivity of the active mass with the electronic and ionic wires.

The Li^+ charge transfer process involves the desolvation of the solvated Li^+ in the liquid electrolyte, crossing of Li^+ through the SEI layer formed at the electrolyte/electrode interface and

the acceptance of an electron from the external circuit while intercalating into the electrode material. Ogumi and Abe, using an AC impedance technique, studied Li^+ charge transfer kinetics at the interface between thin film lithium transition metal oxide electrodes such as $Li_4Ti_5O_{12}$ [47], $LiMn_2O_4$ [48], and $LiCoO_2$ [49] and Li^+ liquid electrolyte. They concluded that the kinetics of the Li^+ charge transfer is limited by the de-solvation step, when the Li^+ moves between a solvated state in the liquid to a de-solvated state in the solid. For porous composite electrodes, which contain a binder and a carbon conductor, the charge transfer resistance also depends on the quality of the ionic and electronic wiring of the active mass. Xu et al. found a dependence of the cell impedance and of its activation energy with the type of binder. A lower resistance and activation energy being observed for CMC compared to PVdF [50]. Huang et al. predict a decrease of the charge transfer resistance with the decrease of NMC clusters size [51]. Heubner et al. found for NMC622-based composite electrode an increase of the charge transfer resistance with a decrease of the porosity, i.e. a decrease of the interconnectivity between the active mass and the liquid electrolyte [52]. Zheng et al. [53] found for NMC333-based composite electrodes by electrochemical impedance spectroscopy that charge-transfer resistance with calendering varied greatly with inactive material content. When the electrode contains low levels of inactive material (2% PVDF and 1.6% carbon), calendering reduced R_{ct}. With high levels of inactive material (8% PVDF and 6.4% carbon), R_{ct} increased with increased calendering. This means that increased calendaring compensates for the lack of particle interconnectivity within electrodes containing less carbon. In the case of the electrodes containing higher amounts of carbon, the additives somehow block ionic access on the surface of the active material. When combined with low porosities, these additives further close the ionic pathways therefore increasing charge transfer resistance. Besnard et al. [3] observed an increase of the cell polarization for NMC333-based composite electrodes when the interconnectivity between the NMC and the electrolyte was decreased below 80% as the inactive material content was increased (from 5% PVdF and 3% carbon to 7.5% PVdF and 4.5% carbon). On the other hand, an increase of the cell polarization was observed for NMC333/LFP-based composite electrodes when the interconnectivity between the NMC and the PVdF/carbon network was decreased from 8% to 3% as the inactive material content was decreased (from 7.5% PVdF and 4.5% carbon to 5% PVdF and 3% carbon). Here the interconnectivity between NMC and the PVdF/carbon network varies between 9 and 16%,

and the interconnectivity between NMC and the total porosity varies between 91 and 84% (respectively for NA7 and NA2).

R_w and R_{ct} vary differently with the active mass loading, m. If the contact resistance is negligible, as here according to electrical measurements [6], R_w increases more or less linearly with m ($R_w \propto m$) because the lengths of the electronic and ionic paths increase with the electrode thickness (which increases with m). [43-46,53] Contrarily, R_{ct} typically decreases with m and an inverse proportionality with m is expected, ($R_{ct} \propto m^{-1}$, which is in fact an inverse proportionality with the active mass available surface for reaction) if all particles behave as parallel strands through which the current flows. Then, the analysis of the dependence of the cell resistance with the electrode loading can be instructive. Here, the nearly inverse proportionality of the cell resistance with m suggests that it is likely dominated by the charge transfer reaction for low active mass loading (small radii). Note that as we varied the electrode radius to play on the loading m, the thickness is kept constant for a given electrode and thus we expect that R_w is a constant for a given electrode. Then, the plateau value observed at high active mass loading (large radii) could indicate that the cell resistance is in this case significantly contributed by R_w, as this one is independent on the electrode radii. In what follows, all the measurements were carried out with electrodes of diameter greater than or equal to 7 mm. The corresponding loadings give rise to a resistance value which is on the plateau of the variation curve of the resistance with the loading of the electrode. We can therefore conclude that this resistance mainly reflects the resistance of the conductive paths.

5.7.2) Dependence on Electrode Parameters and Temperature

Cell resistances were taken at varying temperatures to study temperature effects. Figure 5.38 shows how the cells resistance during discharge decrease at increasing temperature. One can note that NAxb electrodes have lower cell resistances than the electrodes of the NAx series, in particular in the low temperature range. The gap between NAxb and NAx becomes diminished at higher temperatures. Knowing that NAxb electrodes are better percolated than NAx electrodes, with respect to CB/PVdF, we can assume that the electronic wires have significant contributions on the cell resistance, especially at lower temperatures. Energies of activation could be

determined by plotting the logarithm of the inverse of the resistance versus the logarithm of the inverse of the temperature. Indeed, it is generally observed that charge transfer across the interface is a thermally activated process, and that R_{ct} follows the relationship [54]:

$$\frac{1}{R_{ct}} = \frac{1}{R_{ct0}} e^{\frac{-E_{a,ct}}{RT}} \qquad \textit{(eq. 5.15)}$$

On another hand, as R_w depends on transport properties themselves activated by temperature, such as electronic and ionic conductivities, one can also write:

$$\frac{1}{R_w} = \frac{1}{R_{w0}} e^{\frac{-E_{a,w}}{RT}} \qquad \textit{(eq. 5.16)}$$

which leads in both cases to

$$ln\,\tfrac{1}{R} = ln\,\tfrac{1}{R_0} \times \left(\tfrac{-E_a}{RT}\right) \qquad \textit{(eq. 5.17)}$$

$$slope\left(ln\,\frac{1}{R}\ vs.\ \frac{1000}{T}\right) = \left(\tfrac{-E_a}{R\times 1000}\right) \qquad \textit{(eq. 5.18)}$$

where R_0, E_a, R and T are a constant, the activation energy, the gas constant and the temperature in Kelvin, respectively.

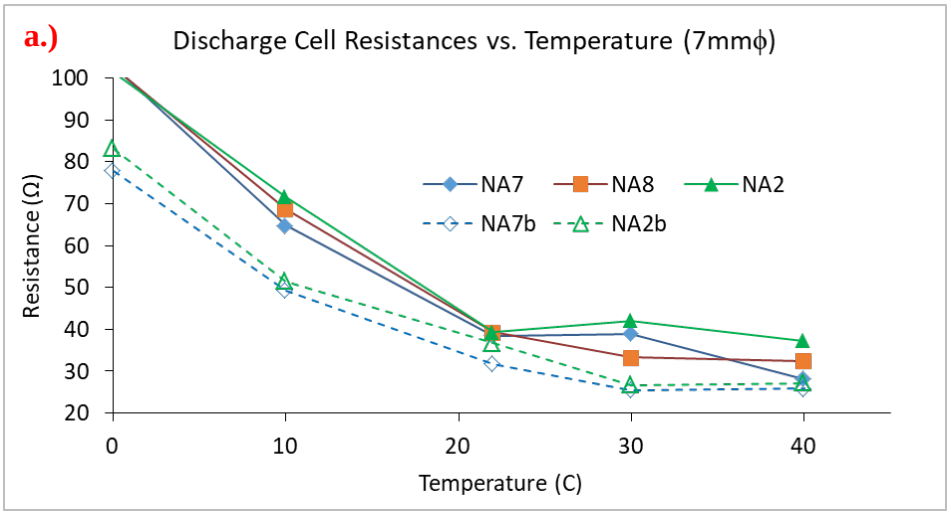

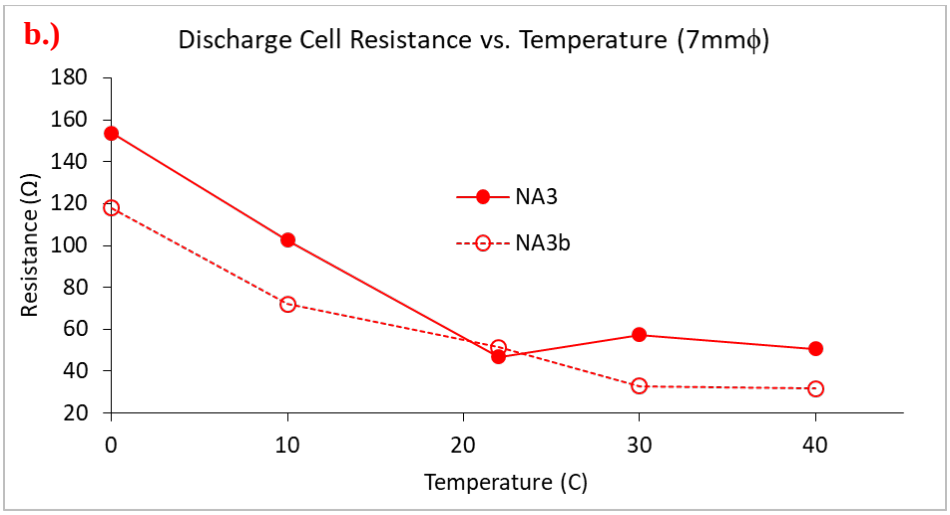

Figure 5.37: Discharge cell resistances vs. T of the thick electrodes (a) and thin (b) electrodes.

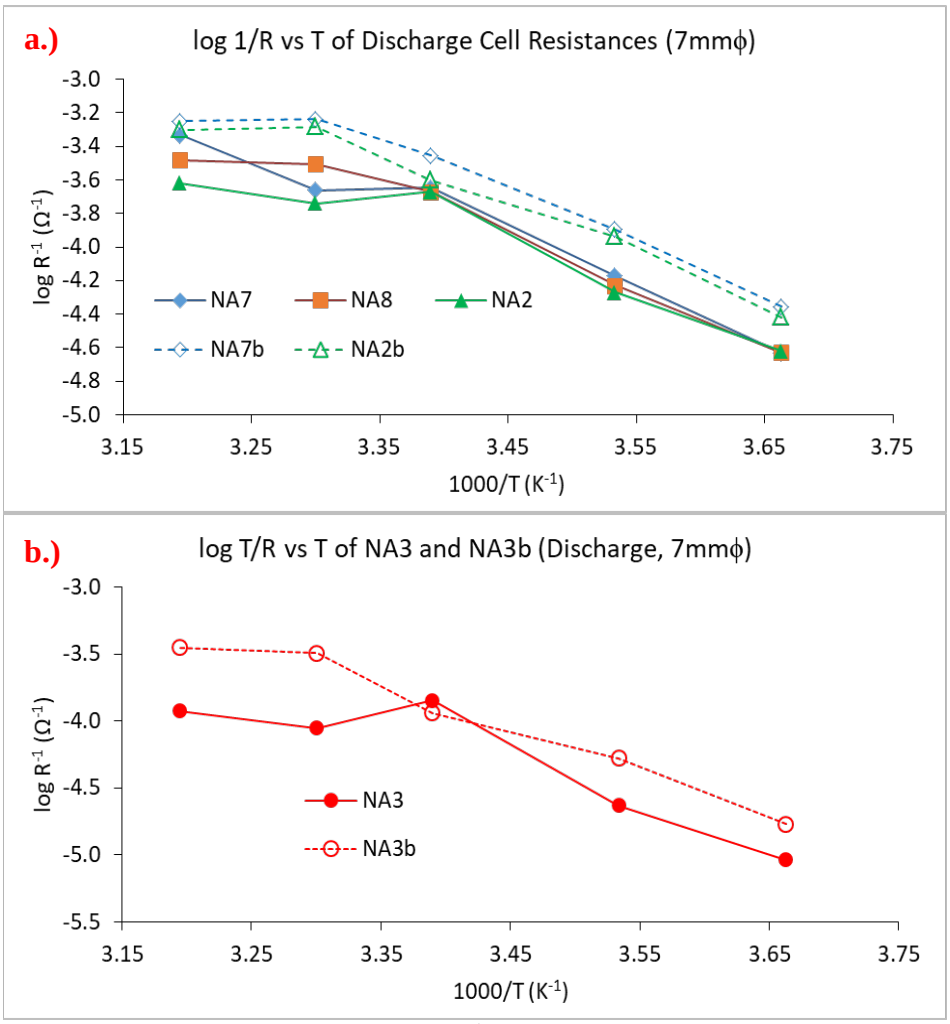

Figure 5.38: Inverse discharge cell resistances vs. T^{-1} of the thick electrodes (a) and thin (b) electrodes.

Ln(1/R) vs 1/T curves of the electrodes are shown in Figure 5.39. Two distinct regimes during discharge are seen more clearly with the given curves. One can note that for the NAxb electrodes the temperature at which the transition occurs is higher. Indeed, a first linear dependence of Ln(1/R) with 1/T is observed from 0 to 30°C for NAxb, with a plateau on the curve from 30 to 40°C, while for NAx the transition happens at 22°C. The activation energy values are shown in Table 5.12. There is a clear difference between the E_a at high and low temperatures further supporting the hypothesis of two distinct regimes. In the high temperature range, E_a is negligible for all electrodes, whatever their thickness, composition and density. In the low temperature range, the activation energy values show limited variation with the electrode parameters with values of 0.26 – 0.31 eV. These values are significantly lower than typical charge transfer activation energies. Indeed, for NMC333-based composite electrodes, Xu et al. found 36 kJ/mol (0.37 eV) in the [27;49°C] range with PVdF as the binder [50], and Qiu et al. found 65 kJ/mol (0.67 eV) in the [-20;25°C] range. They are also lower than the activation energies (typically 45-50 kJ/mol, 0.47-0.52 eV) found by the group of Ogumi and Abe for the charge transfer process at the interface between thin film electrode material and liquid electrolyte [47-49]. Jow et al. [54] found 50 kJ/mol (0.52 eV) for $LiNi_{0.80}Co_{0.15}Al_{0.05}O_2$ (NCA)-based composite electrodes. This tends to confirm that the cell resistance is dominated by R_w, with a major contribution from the electronic wires, as NAxb electrodes show lower resistances than NAx ones. However, the activation energy values at lower temperatures are close to the conductivity activation energy found for the NMC532 material (0.27 eV at the sample scale and 0.20 eV at the cluster scale). This may suggest that the polarization resistance (at the beginning of the discharge) is dominated by R_w, which is itself dominated by the resistance associated with electronic transport in the electrode, and that the latter is limited by the conductivity of the active material. One may recall that in the NAx electrodes, the electronic wires are constituted of CB/PVdF aggregates in series with NMC grains or clusters (section 5.2.4). In this case, it sounds reasonable that the temperature dependence of the cell resistance is determined by the temperature dependence of the NMC conductivity. In the NAxb electrodes, two types of electronic wires exist (in parallel), the first ones constituted of CB/PVdF aggregates in series with NMC grains or clusters as in NAx, and the second ones constituted of percolated CB/PVdF aggregates. It could then be expected that the temperature dependence of the cell resistance is very low, being determined by that of the most conductive wires, which are not or only weakly thermally activated in their dry

state. However, the experimental measurements of A. Agrawal, confirming the earlier work of Seid et al. [55] and Panabière et al. [13], reveal a strong decrease in the conductivity of the CB/PVdF aggregates when wetted by the liquid electrolyte, due to the adsorption of the electrolyte ions, while that one of NMC remains much less altered. This could explain that even in the NAxb electrodes the polarization resistance has a temperature dependence determined by the temperature dependence of the conductivity of the active material. Regarding the lack of temperature dependence of the polarization resistance above 22 or 30°C for NAx and NAxb respectively, it is difficult at this stage to propose a solid interpretation.

Table 5.12: Discharge energy of activation values at low temperature per electrode.

E_a (Discharge, 7mm) in eV ***[T° range]***						
NA3	**NA2**	**NA7**	**NA8**	**NA3b**	**NA7b**	**NA2b**
0.38 *[0 – 22°C]*	0.30 *[0 – 22°C]*	0.31 *[0 – 22°C]*	0.30 *[0 – 22°C]*	0.29 *[0 – 30°C]*	0.27 *[0 – 30°C]*	0.26 *[0 – 30°C]*

The comparison of the discharge and charge cell resistances shows a significant change in the cell resistance between the two different electrochemical processes. The cell resistance is significantly higher in charge than in discharge (Figure 5.40). For example, for NA2 it equals ~180 Ω at 0°C and ~120 Ω at 40°C in charge versus ~100 Ω and ~35 Ω in discharge. For NA2b, it equals ~135 Ω at 0°C and ~80 Ω at 40°C in charge versus ~80 Ω and ~25 Ω in discharge. Seid et al. [55], Qiu et al. [56], and Amin and Chiang [57] report up to one order of magnitude decrease of the conductivity of NMC333 and NMC532 between delithiated and lithiated states (Figure 5.42). The decrease in conductivity is due to the decrease in the number of holes corresponding to the increase of Li^+ content in the NMC. The NMC lower conductivity in lithiated state and thus at the beginning of charge may well explain the higher value of the cell resistance in charge than in discharge. As the cell resistance appears dominated by the electronic wires and the NMC conductivity, observing higher values for charge resistances especially for NA2 and to a lesser extent for NA8 compared to NA7, NA2b and NA7b, is consistent with the above interpretation. Because these electrodes are those which contain the least CB/PVdF, which are the least calendered, particularly NA2, and are therefore those which are then the most sensitive to the lower conductivity of the NMC in the lithiated state. Finally, the non-linearity of

the inverse resistance curves makes it difficult to determine the activation energy through linear fitting.

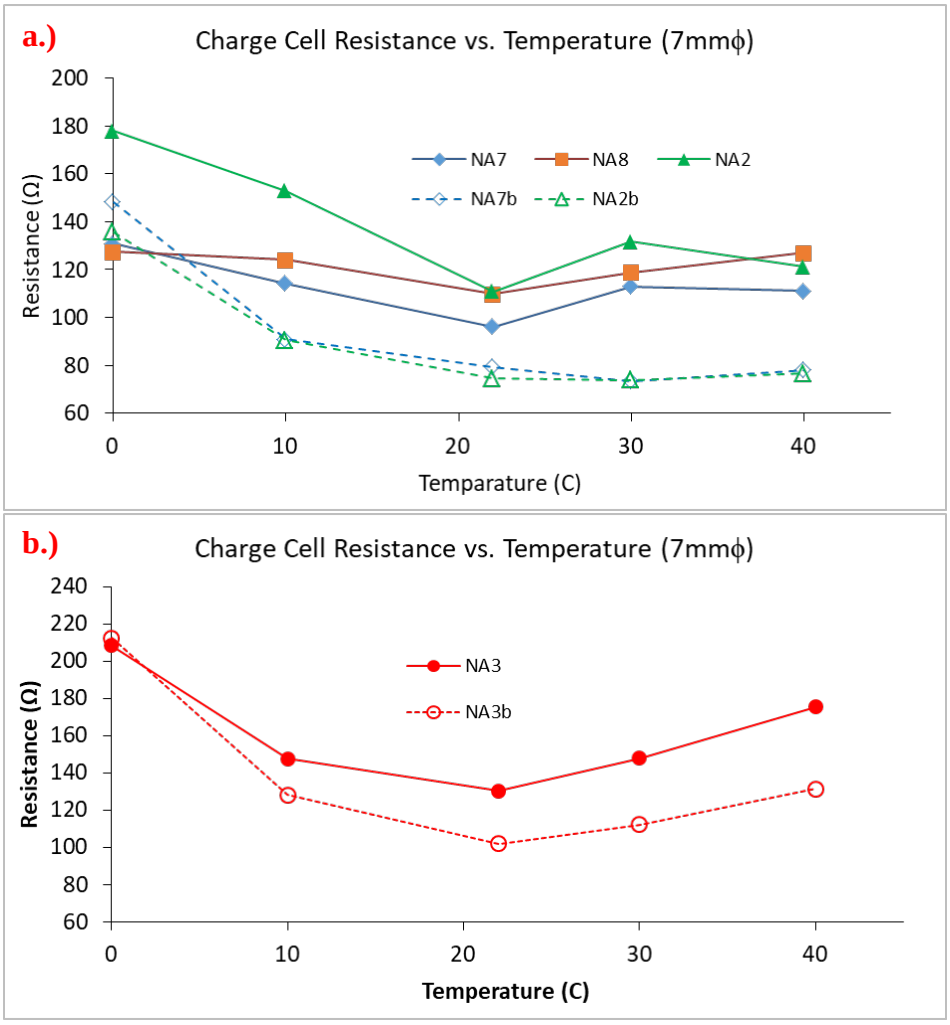

Figure 5.39: Charge cell resistances vs. T of the thick electrodes (a) and thin (b) electrodes.

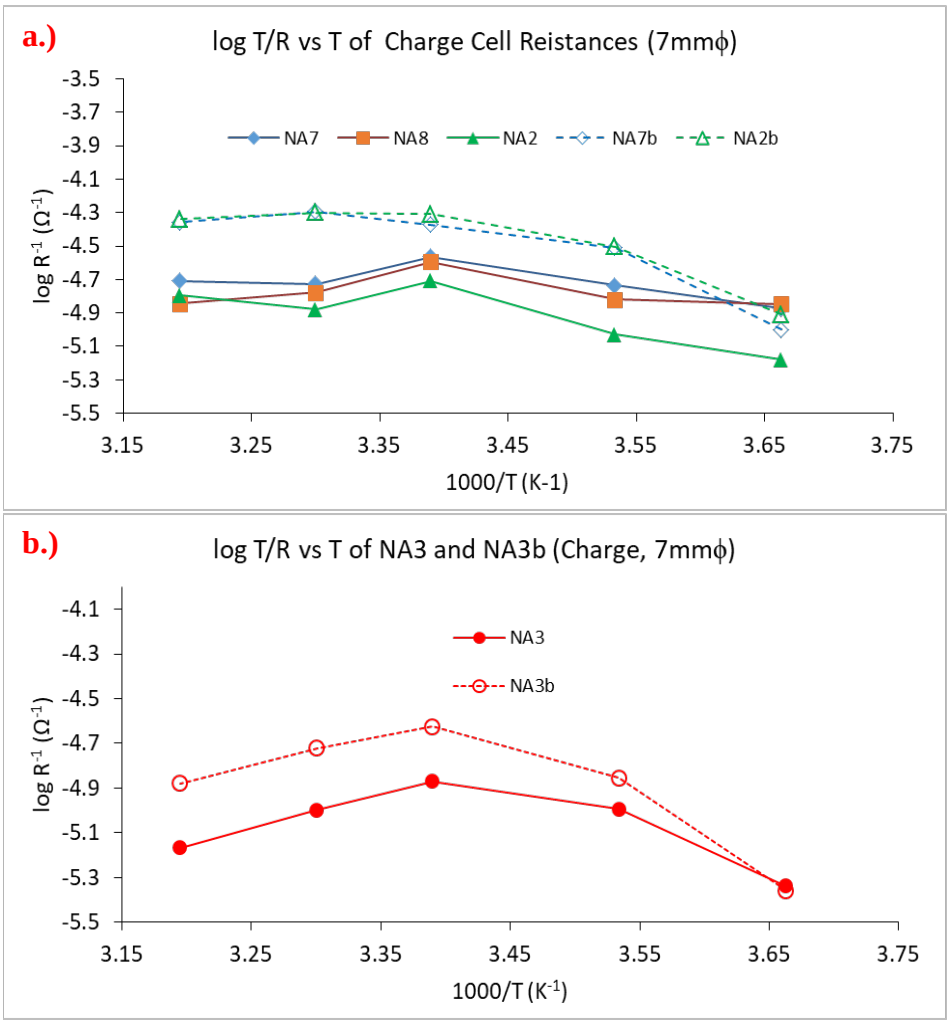

Figure 5.40: Inverse discharge cell resistances vs. inverse T of the thick electrodes (a) and thin (b) electrodes.

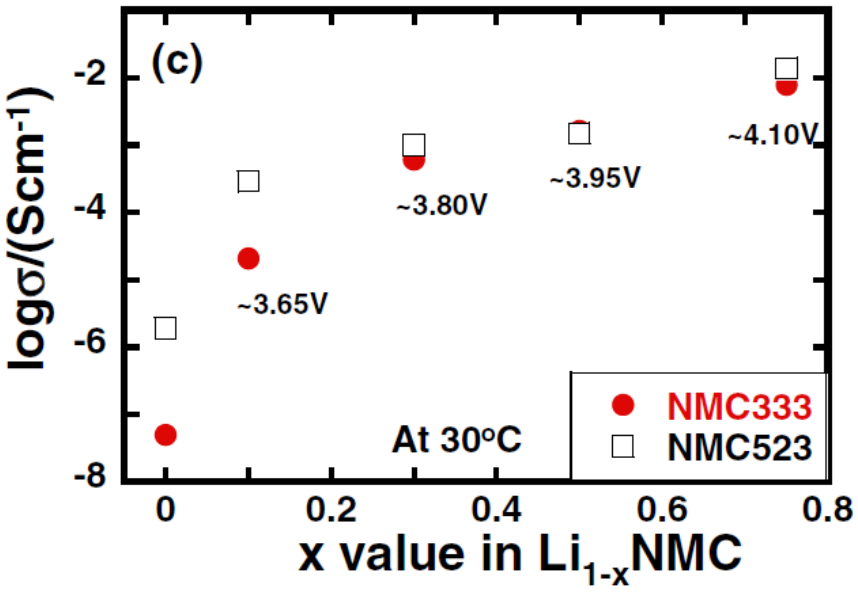

Figure 5.41: The electronic conductivity of NMC ($Li_{1-x}NMC$) as a function of x value in $Li_{1-x}NMC$ at 30°C obtained from DC measurement [57]. x = 0 corresponds to the end of discharge (fully lithiated state) and x = 0.5 to the end of charge.

5.7.3) Conclusion

The cell resistances at the beginning of the discharge and charge were extracted and we have shown, by studying their dependence with the quantity of conductive additive and the temperature that for our electrodes, these resistances are mainly attributable to the electronic transport properties of the electrodes. These appear influenced by the amount of conductive additive and by the intrinsic conductivity of the active material, different at the beginning of discharge and charge. In this regard, the Figure 5.43 shows that these cell resistances decrease with increasing electronic conductivity and are lower at the beginning of discharge, or when the active material has the highest electronic conductivity. The thermal activation energies of cell resistances suggest that the electronic conductivity of the electrodes when they are impregnated with electrolytes is dominated by the conductivity of the active material, confirming the measurements made elsewhere which observe a significant decrease in the conductivity of the mixture. CB / PVdF when impregnated with the electrolyte. Thus, even if the amount of CB/PVdF in the NAx electrodes is insufficient to reach the percolation of this mixture, and that this results in an electronic conductivity approximately 10 times less in the dry state (approximately) than that of the NAxb electrodes, the cell resistance of the NAx electrodes is

only 2 times lower (approximately) than that of the NAxb electrodes. In addition, the electrochemical performances of the NAx electrodes are equivalent to, or even greater than those of the NAxb electrodes, as has been seen in the preceding sections. It is therefore clearer here that the high conductivity of NMC532, compared to NMC333, allows to reduce the amount of CB/PVdF additives (by about 50% with respect to the study by Besnard et al.). This is significant since we can operate electrodes at a much lower additive content to an extent that is sufficient for electronic conduction in combination with the electrolyte but does not hinder ionic wiring and conduction for the Li^+ to approach the active material surface.

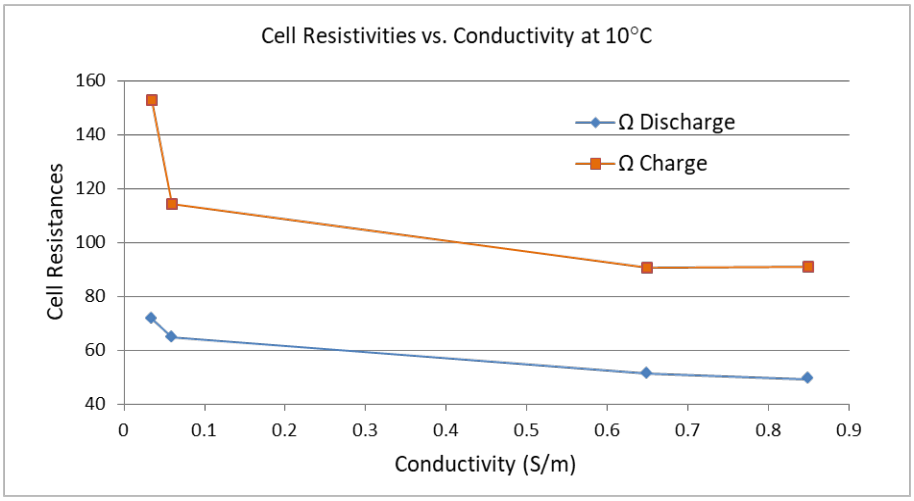

Figure 5.42: Cell resistances vs. electrode conductivity values in the dry state determined by BDS. Measurements courtesy of Anshuman Agrawal.

5.8) Nominal Capacity (Q_0)

Nominal capacities are taken from low C-rates to allow maximum pseudo-steady state diffusion and in turn maximize active material utilization. Nominal capacities are thus generally independent of the electrode parameters such as thickness and porosity, and of the electrode formulation. Except for the cases where the electrode has fairly inhomogeneous distribution of its components [58], and/or is loosely and insufficiently calendered [27], and/or has not well-balanced formulation (excess of binder or lack of conductive additive) [59], the nominal capacity (or the gap between this nominal capacity and the theoretical capacity based on the lithium stoichiometry in the active material) solely reflects the intrinsic kinetic limitations of the active material. Figure 5.44 compares the discharge (taken at the C/12.5 rate) and the discharge following the charge (taken at the C/10 rate) Q_0 values averaged over all electrodes as a function

of the temperatures with errors bars representing the standard deviations. Both the discharge and charge Q_0 values tend to increase at increasing temperature on the whole meaning it is easier for the reaction to proceed for the bulk of the active material hence maximizing higher utilization. Q_0 is higher and is less distributed (lower standard deviation) in charge than in discharge. The kinetic hindrance to the lithiation process at high lithiation state [19] (when x_{Li} in Li_xNMC is tending toward 1) likely explains that higher Q_0 values are obtained in charge than in discharge. Then, the increase of Q_0 with the temperature likely reflects an improvement of the active material intrinsic kinetic limitations. The more distributed Q_0 values in discharge is likely due to the kinetic hindrance at high lithiation state that makes Q_0 more dependent on the electrode formulation or microstructure in discharge than in charge. It can be seen, however, that the nominal capacity tends towards a threshold value, reached at 22°C in charge and 30°C in discharge, respectively equal to 174.5 and 170 mAh/g.

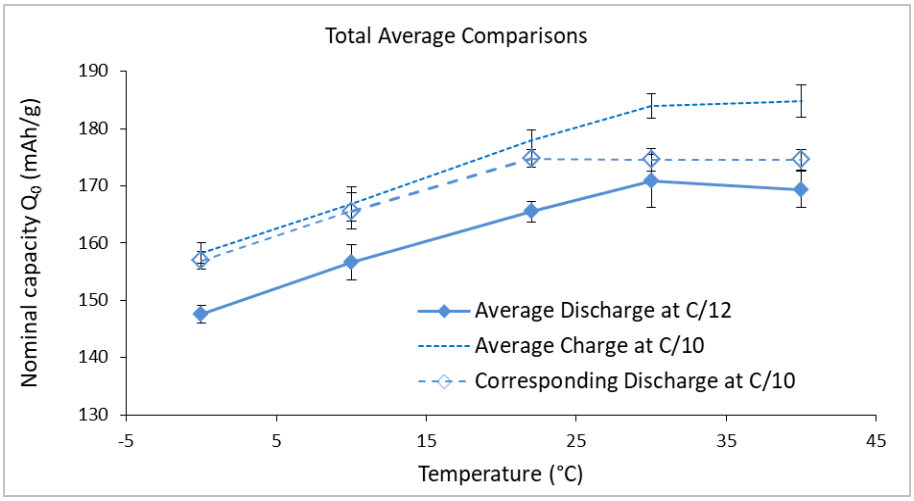

Figure 5.43: Q_0 values averaged over all electrodes as a function of the temperatures in discharge and charge. For charge, the corresponding discharge is also shown.

Figure 5.45 compares the average nominal capacities, Q_0, both in discharge and charge, as a function of the temperature for NA2, NA8, NA7, NA2b and NA7b. Let's remind that for the charge, because of the extra-charge capacity phenomenon, it is the corresponding discharge at C/10 that is plotted instead (see section 5.4.5). In discharge, one can see that NAxb electrodes have the highest discharge nominal capacities at lower temperatures than NAx ones, and that in the latter series NA2 has higher Q_0 than NA8 and NA7. At higher temperature, however, the hierarchy between NAxb and NAx is reversed. The higher Q_0 at low temperature for NAxb than

for NAx may reflect the better electronic wiring in the former electrodes due to the better percolation of the CB/PVdF mixture. This way, the higher Q_0 for NA2 than for the more calendered NA8 and NA7 might indicate the detrimental influence of the fragmentation of the NMC clusters into primary grains on the electronic wiring of the active mass. This inversion of the hierarchy at high temperature between NAx and NAx electrodes suggests a detrimental influence of the excess PVdF / carbon on the accessibility of the active material for these temperatures. This could be attributable to the swelling of the PVdF following an electrolyte absorption, leading to a decrease in the electronic conductivity by increasing the distances between carbon particles or to a closure of certain pores by the gelled mass. The trends are less clear on the Q_0 values in charge likely because the conductivity of NMC is higher in the delithiated step/at the end of charge than in the lithiated step/at the end of discharge [55,56,57].

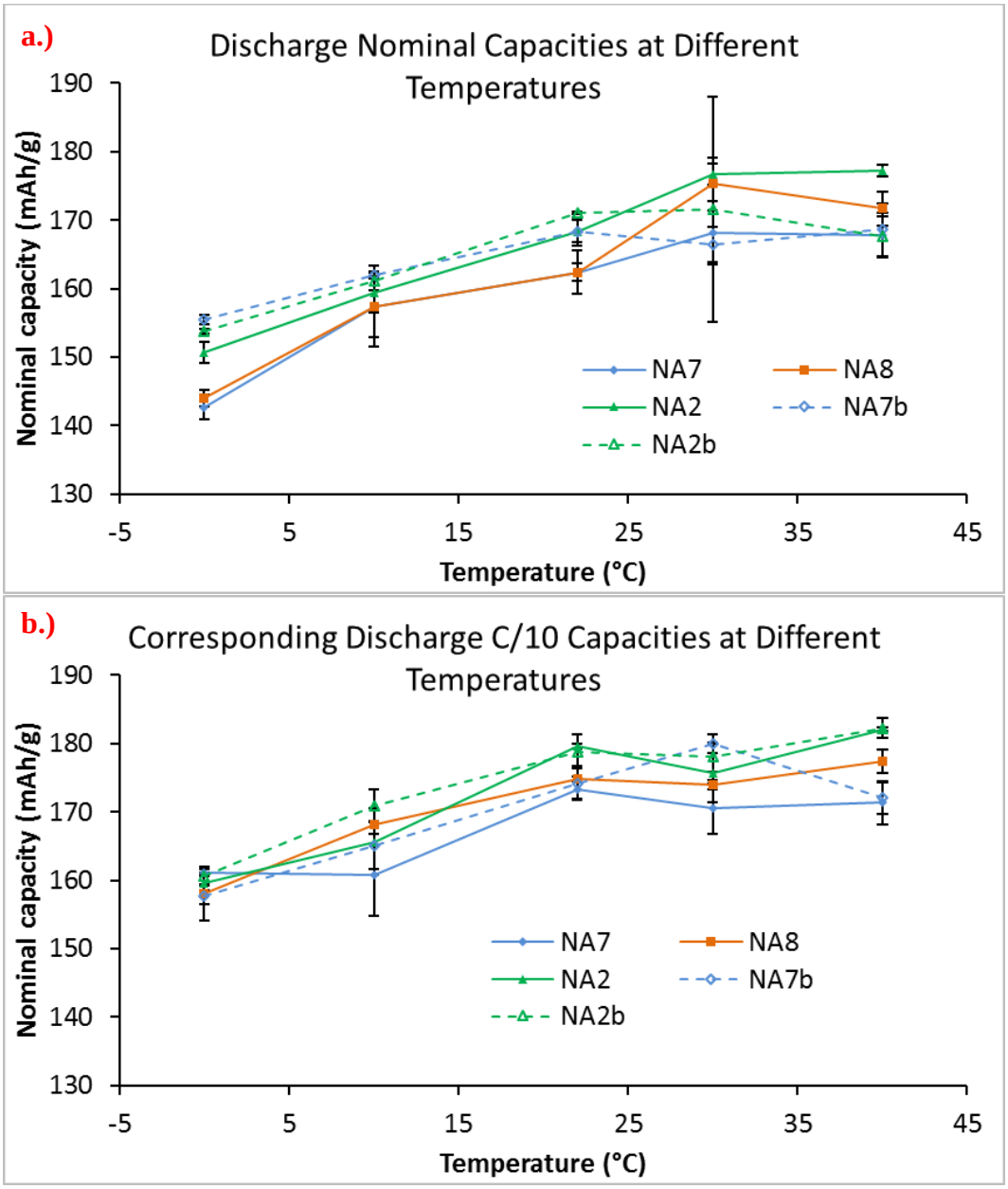

Figure 5.44: Average nominal capacities, Q_0, in (a) discharge (taken at the C/12.5 rate) and in (b) charge (taken at the C/10 rate) as a function of the temperature for NA2, NA8, NA7, NA2b and NA7b. Instead of the charge capacities, the corresponding discharge capacities are plotted (see section 3.2.4 for explanation)

5.8.1) Conclusion

The nominal capacities exhibited by the various electrodes are higher in charge than in discharge and increase with the temperature, up to plateau values reached at 22°C in charge and 30°C in discharge, respectively equal to 174.5 and 170 mAh/g. These behaviors likely reflect the better

intrinsic kinetics of the active material in the delithiated state and at higher temperature. As a consequence, some slight variations of the nominal capacity with the electrode formulation and microstructure are observed for the discharge.

5.9) Penetration Depth Model

We would like to remind the reader that the penetration depth model is mostly valid for relatively thick electrodes. Therefore, the evaluations in this section will mostly deal with NA7, NA8, NA2, NA7b and NA2b. Also, the bulk diffusion coefficients extracted from NMR spectroscopy, even though they are self-diffusion values, are assumed to be the same for diffusion of the bulk electrolyte. The PDM equation is rewritten below. As explained in the methodology section, D_0, or T or ε were adjusted in order that the calculated capacity $Q_{C\text{-rate}}$ matches the experimental capacity at C*. The definition, unit and value for each parameter is given in Table 5.13.

$$Q_{C-rate} = Q_0 \frac{\epsilon}{TL} \frac{D_0 C_0 F}{(1-t_+)I} \qquad \textit{(eq. 5.19)}$$

Table 5.13: Definition, unit and value of the PDM equation.

Parameter	Definition	Unit	Value
D_0	Bulk diffusion of Li^+ in pure electrolyte (cm^2/s)	cm^2/s	Variable
C_0	Bulk concentration of Li^+ in the electrolyte	mol/cm^3	0.001
t_+	Lithium transference number	-	See Table 4.5 in NMR section
ε	Porosity	Volume fraction	Variable
T	Tortuosity factor	-	variable
L	Electrode Thickness	cm	See Table 5.2 and Table 5.3 (Electrodes specifications)
F	Faraday's Constant	A·s/mol	96500
I	Current Density	A/cm^2	$0.344\ 10^{-3}$ to $69\ 10^{-3}$
Q_0	Nominal Capacity	mAh/g	Determined at the lowest rate for each electrode

5.9.1) Effective diffusion coefficient

We used the lower bound of the modified Bruggeman-type function established by Usseglio-Viretta et al. for a NMC532–based electrode. The corresponding tortuosity factor values are given in Table 5.14. The matching between the experimental and calculated capacities with the PDM equation are shown for NA7 as examples at the different temperatures in Figure 5.46. The effective diffusion coefficients, D_{eff}, extracted from this fitting procedure are all gathered as a function of the temperature in Figure 5.47. In this case, only the best cells were considered for each electrode formulation at each temperature.

Table 5.14: Tortuosity factors used to perform the PDM fitting of the discharge capacity vs. current curves.

Electrode	NA2	NA8	NA7	NA2b	NA7b
Porosity volume fraction	0.28	0.235	0.212	0.26	0.191
Tortuosity factor	2.75	3.06	3.25	2.88	3.45

Bulk diffusion values from NMR measurements serves as our control for the comparison of diffusion values from the PDM model. A first striking result is that the order of magnitude as well as the temperature dependence of the effective diffusion coefficients are close to that of the diffusion coefficient determined by NMR on the bulk electrolyte (not confined in the porosity of the electrode), except for singular cases that we will come back to later. These observations are encouraging because they support the validity of our approach and are a confirmation that the sudden drop in discharge capacity with the increase of the current beyond the critical regime C* is due to the diffusional limitations in the electrode. A second striking result is that the effective diffusion coefficients are higher than D_0. At the fundamental level, it is known that the ion diffusion is governed by the diffusion of the solvent, and can be described by the Stokes-Einstein equation [60]

$$D = \frac{kT}{6\pi\eta r_s} \qquad \textit{(eq. 5.20)}$$

in which η is the solvent viscosity, D is the self-diffusion coefficient, r_s is the effective hydrodynamic radius, T is the temperature, and k is the Boltzmann constant.

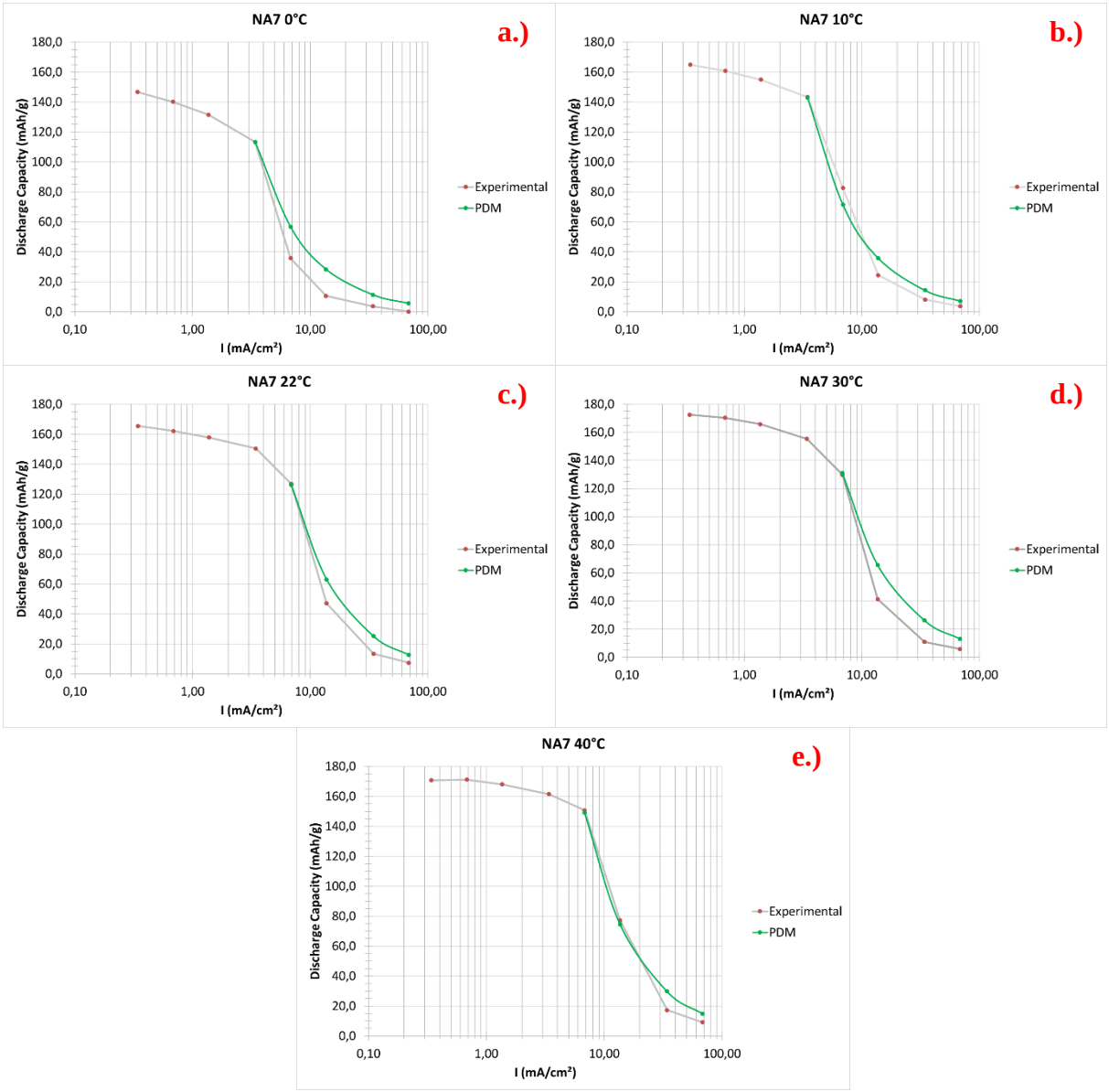

Figure 5.45: NA7 D_{eff} PDM fits (green line) at different temperatures: 0°C(a), 10°C(b), 22°C(c), 30°C(d), 40°C(e).

A value of D_{eff} higher than D_0 would mean that the temperature in the electrode is higher (up to three times for NA7) than in the measuring chamber, or that the viscosity of the solvent or the effective hydrodynamic radii are reduced when confined in the electrode, which are all unrealistic hypotheses. It is more likely that the tortuosity values postulated to perform the

modeling are simply too high for our electrodes. Another hypothesis is that the increased D_{eff} can be attributed to viscosity changes brought about by concentration variations in both the electrolyte and in the pore matrix. Lower salt concentrations decreases viscosity and therefore increases diffusion [61].

Some literature also suggests that specific interactions at the solid/liquid interfaces can have significant effects on the diffusion of species in the liquid, but it is for example ultra-confined systems on a nanometric scale, which does not correspond to our materials [62]. In the following, therefore, we have taken the effective diffusion coefficient equal to that of the bulk electrolyte, considering that the diffusion properties of the electrolyte are not affected by its confinement in the porosity of the electrode, and we then sought to determine an effective tortuosity factor for each electrode. The latter was therefore a variable in the PDM model equation.

Before going on to this second part, we can notice that the effective diffusion coefficients tend to increase less rapidly than the bulk diffusion coefficient at the highest temperatures (case of NA7 and NA8), or even tend towards a plateau value (case of NA2 and NA7b), or even decrease (case of NA2b). We will return later to the possible causes of these results.

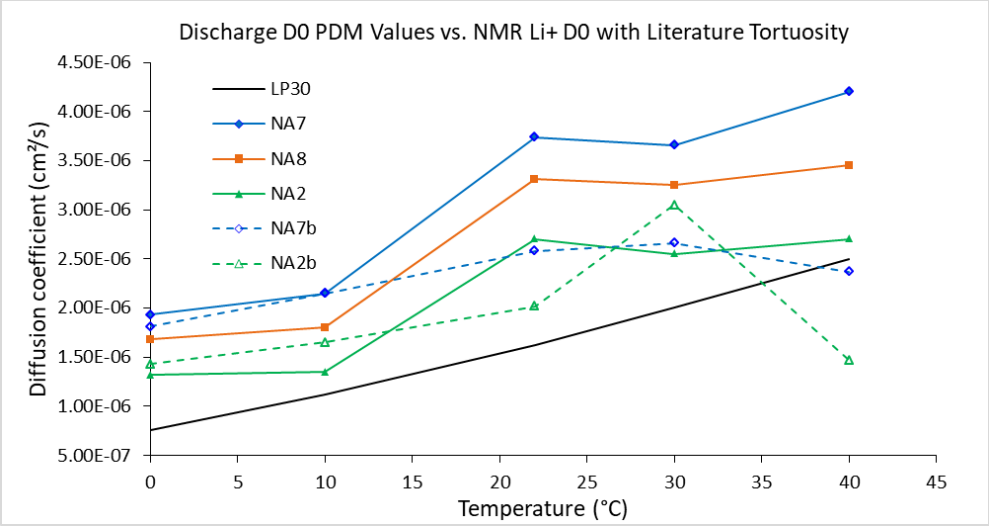

Figure 5.46: Determined values for D_0 from tortuosity values specified by Usseglio-Vireta.

5.9.2) Effective Tortuosity

Then, we hypothesized that the diffusion coefficient is the same as in the bulk electrolyte and we fitted the experimental curves with the PDM equation taking the tortuosity factor as a variable parameter. The matching between the experimental and calculated capacities with the PDM equation are shown for NA7b as examples at the different temperatures in Figure 5.48. The effective tortuosity factors, T_{eff}, extracted from this fitting procedure are all gathered as a function of the temperature in Figure 5.49. The points correspond to each of the three cells that were cycled per electrode at varying temperatures. The horizontal red lines correspond to tortuosity factors that describe both macroporosities and mesoporosities identified by FIB/SEM tomography. Macroporosities are the porous volumes formed by the large cavities in the stacking of NMC clusters and mesoporosities are the small porous volumes confined within the CB/PVdF mixture and at the grain boundary cracks of fragmented NMC clusters. The majority of the points lie in between these two realistic bounds, suggesting that the T_{eff} in our electrodes correspond to average values of both macro and mesoporosities. This is another encouraging result, since all the parameters used in the PDM model equation are real and justified from the point of view of the properties of the electrolyte (C_0, D_0 and t_+), the microstructure of the electrode (L and ε), electrochemical properties of the active material (Q_0), and finally cycling conditions (I).

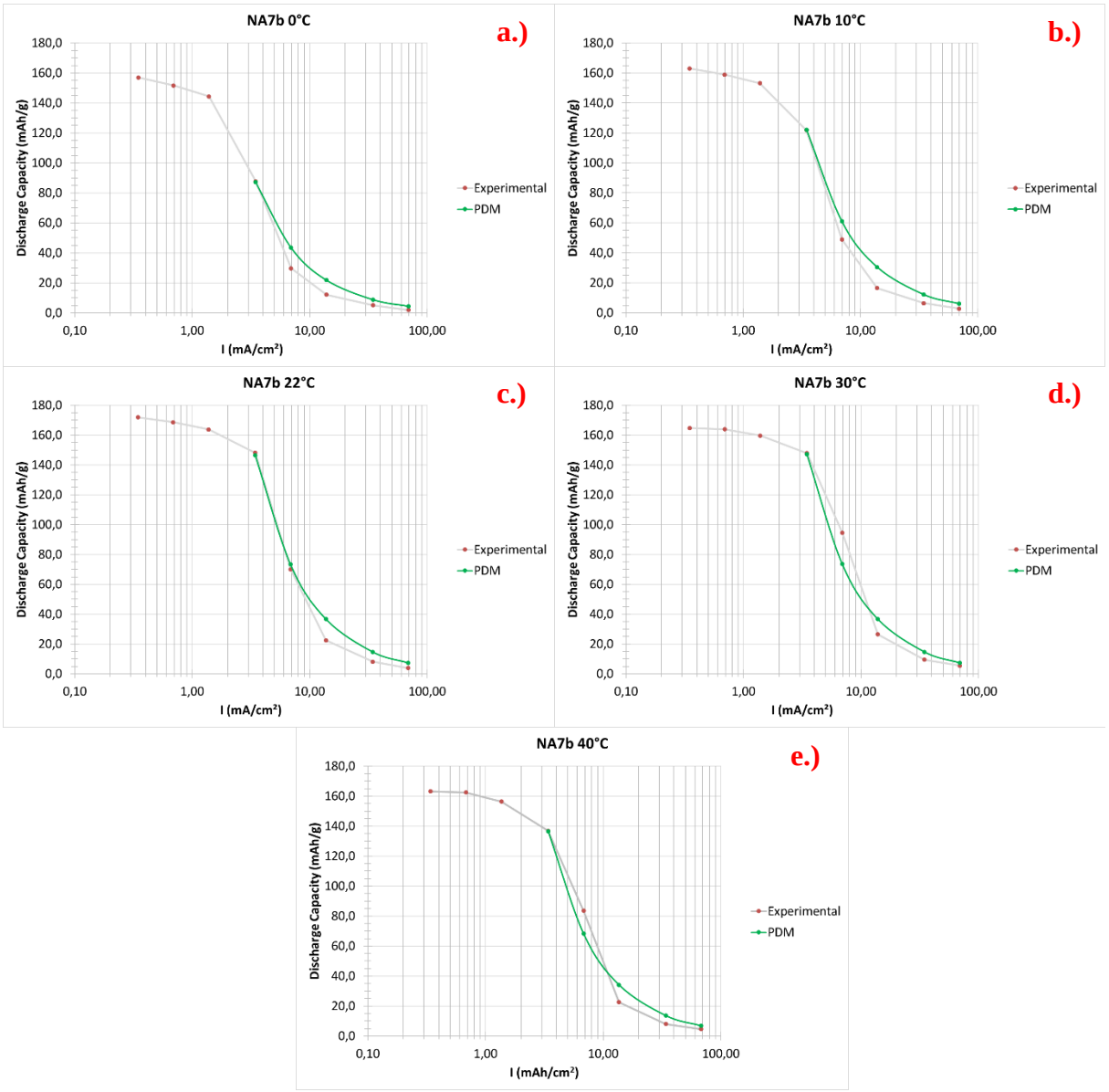

Figure 5.47: NA7b T_{eff} PDM fits (green line) at different temperatures: 0°C(a), 10°C(b), 22°C(c), 30°C(d), 40°C(e).

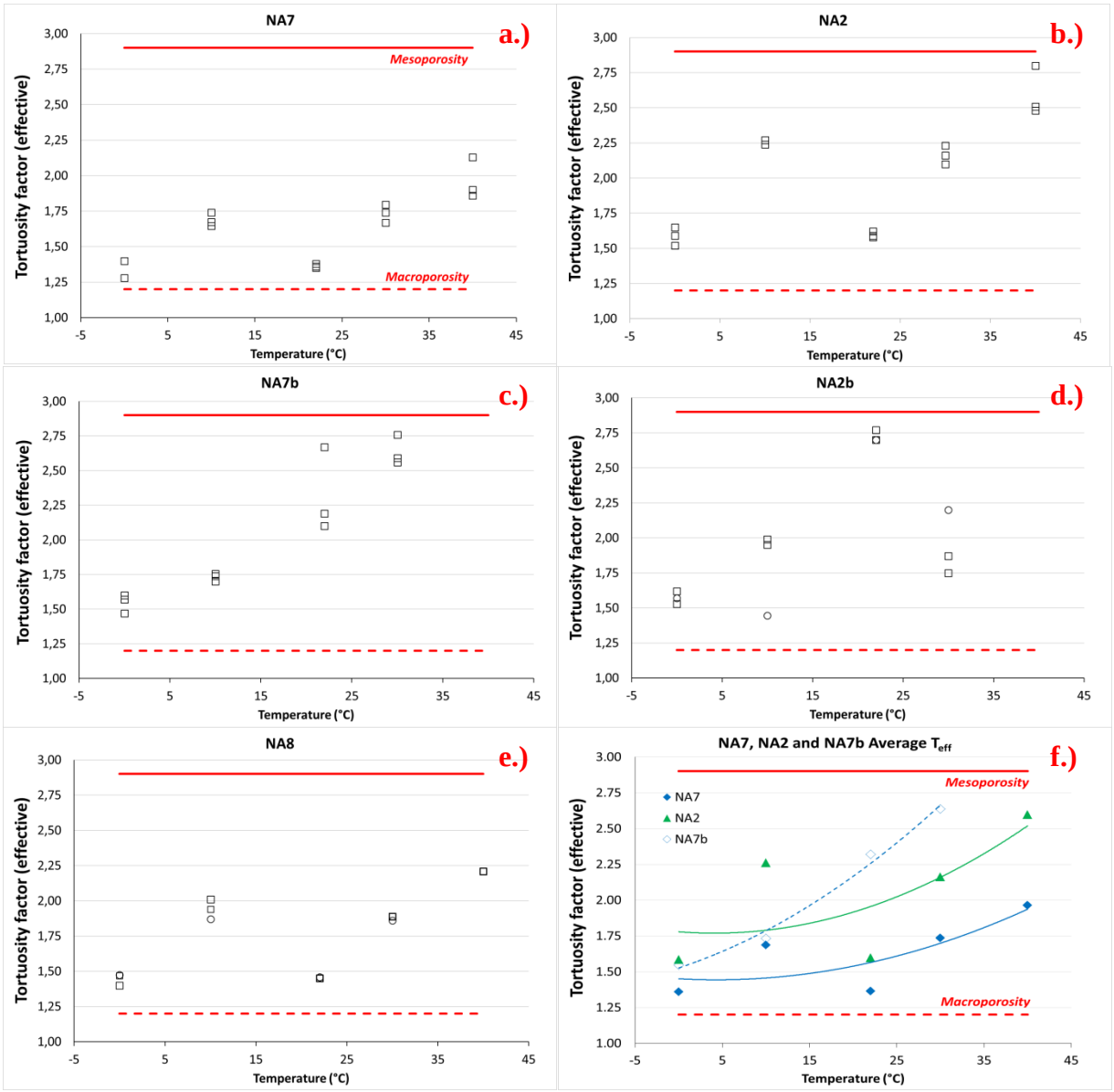

Figure 5.48: T_{eff} PDM fits of NA7(a), NA2(b), NA7b(c), NA2b(d), NA8(e) electrodes at various temperatures. Average tortuosity values of NA7, NA2 and NA7b are comparted with each other (f).

T_{eff} values also appear to increase at increasing temperature, especially when the electrode contains more CB/PVdF. This is better illustrated in Figure 5.49f where the average values of T_{eff} for NA7 and NA7b can be compared. This trend could be due to some swelling of the CB/PVdF phase by the electrolyte. This phenomenon is documented in the literature. Saunier et al. [63] found that dense PVdF films could absorb increasing liquid electrolyte amounts with increasing temperature. The swelling ratios for pure DMC, pure EC, and DMC/EC mixtures are reported in Figure 5.50. At 40°C, the swelling ratio (obtained by the differential weighing of the

samples before and after swelling) of PVdF by DMC/EC is ~125%. However, only a small amount of salt permeates through the polymer and the salt concentration in the electrolyte trapped in the gel is much lower than the salt concentration in the bulk electrolyte, 0.2 vs. 1.0 M respectively. In the case of porous electrodes with PVdF binder, this differential trapping of electrolyte species in the PVdF may be at the origin of a decrease of the ionic diffusivity and conductivity, due to the increase of the salt concentration in the electrolyte within the porous phase, a modification of the salt dissociation, and of the increase of the swollen PVdF/CB phase volume. The latter phenomenon may lead to the more drastic effect if some pores are clogged by the swollen PVdF/CB phase in which diffusion is ultra-slow. For example, Kataoka et al. [64] found that the conduction mechanism of a PVdF porous membrane infiltrated by a liquid electrolyte is essentially dominated not by the solution-rich region, which are trapped in the cavities, but by the polymer-rich region of the swollen polymer, which are forming the walls of the cavities. Another study by Saunier et al. [60] was in contradiction with this result but the microstructure of their porous PVdF membrane appears different to that of Katakoa et al., the latter showing smaller pores.

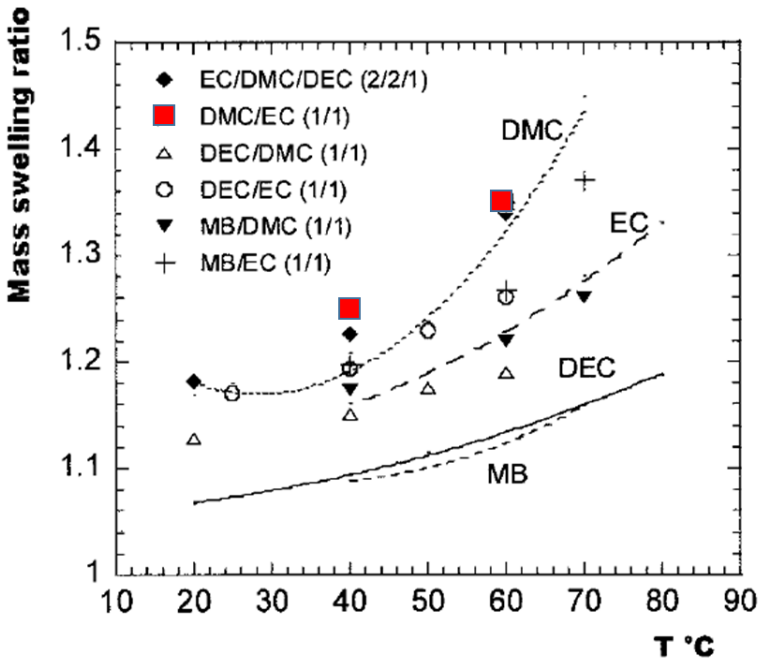

Figure 5.49: Mass swelling ratios of a PVdF dense film in equivolume solvent mixtures. The lines are associated with the pure solvents. [63]

5.9.3) Effective Porosity

All these observations led us to a third way to use the PDM model. The fit was then performed by taking as diffusion coefficient that of the electrolyte, as the tortuosity factor that of macroporosity (considered equal to 1.2 for all samples), and then to vary the porosity in the equation of the PDM. In other words, we are making the hypothesis that the homogenization of the concentration of species of the electrolyte in the electrode is made possible mainly via the channels formed by the so-called macroporosity, which are large and of low tortuosity, in which a greater number of species can diffuse more rapidly, than in the smaller, more tortuous channels formed by confined mesoporosity. The result of the fit will be a value of effective porosity, lower than the total porosity, which we will compare to the macroporosity value determined by F. Cadiou on the FIB/SEM volumes.

The matching between the experimental and calculated capacities with the PDM equation are shown for NA2 as examples at the different temperatures in Figure 5.51. The effective porosity, ε_{eff}, extracted from this fitting procedure are all gathered as a function of the temperature in Figure 5.52. The points correspond to each of the three cells that were cycled per electrode at varying temperatures. The horizontal red lines correspond to the total porosity and to the macroporosity calculated from the FIB/SEM volumes.

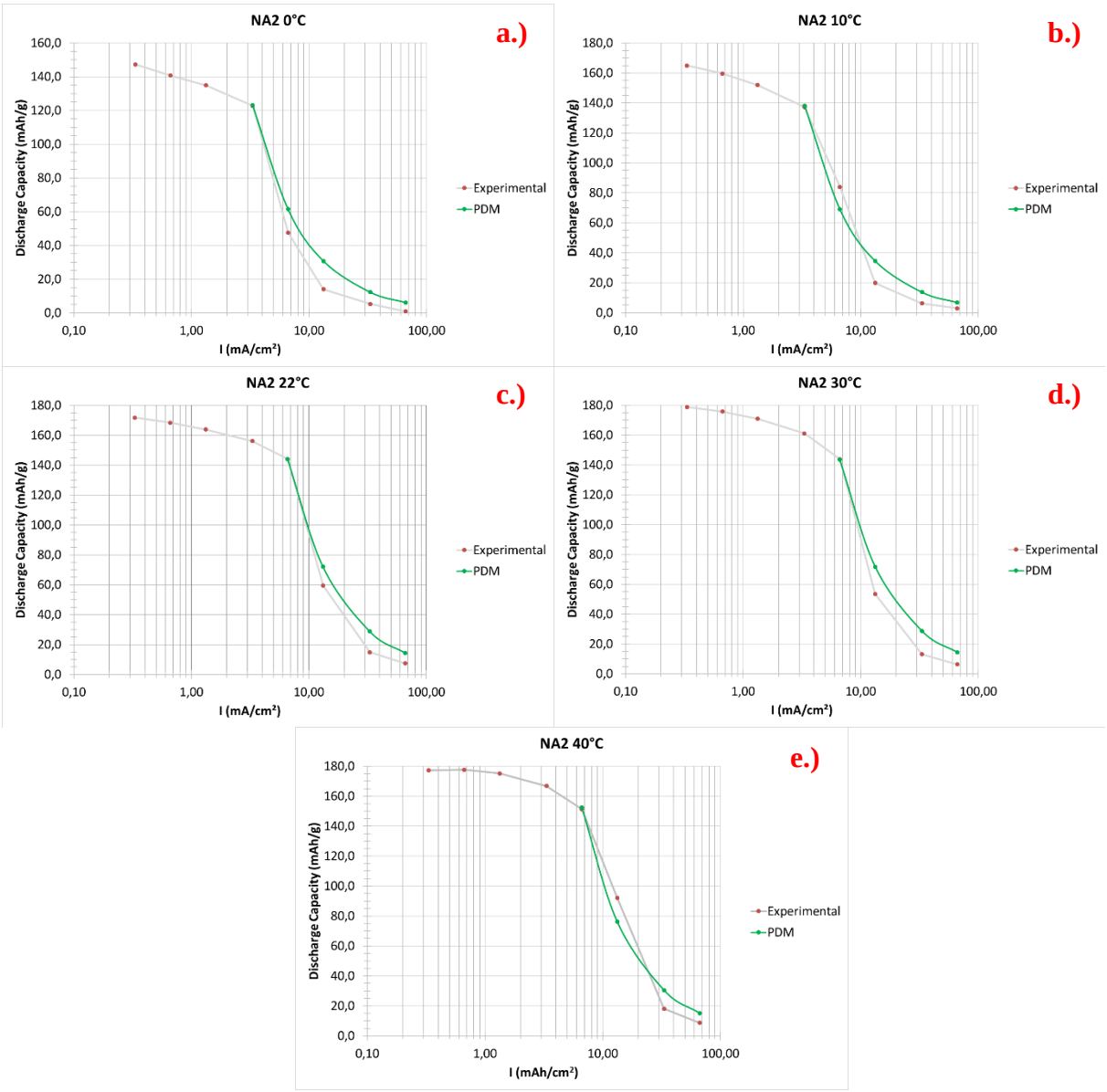

Figure 5.50: NA2 P_{eff} PDM fits (green line) at different temperatures: 0°C(a), 10°C(b), 22°C(c), 30°C(d), 40°C(e).

All ε_{eff} values are in the region below the total porosity line, suggesting that the entire porosity of the electrode does not participate effectively in the homogenization of the salt concentration. Apparently, the ε_{eff} values are closer to the macroporosity line, in particular for NA7, an electrode for which a fairly good match is observed at all temperatures except for 40°C. For the other electrodes, ε_{eff} is equal to the macroporosity at low temperature, then drops, and all the more severely as the electrodes contain PVdF/CB, which can be attributed as we have seen previously to the swelling of PVdF/CB islands by the solvent of the electrolyte, which would

result in a closure of certain pores. For NA7b and NA2b the phenomenon would be so critical that the effective macroporosity is decreased at a very low volume fraction at 40°C, of the order of 5 to 7% of the volume of the electrode. This does not mean that the macroporosity decreases so much with temperature, but rather illustrates how effective or useful porosity decreases with temperature. The swelling of the islands of PVdF/CB created zones of congestions that would harm the proper functioning of the macroporosity network vis-à-vis the diffusion of the species of the electrolyte, for example by breaking its percolation. This gives the picture that these are "defect points" that are the cause of the brutal capacity drop with the increase of the current beyond the critical regime. Careful observation of the cross-section of the electrodes (see Figure 5.3) shows that there is an alternation of non-fractured and fractured NMC cluster. There is therefore in the porous network an alternation of macroporosity type zone and confined porosity type zone. These last break the channels for the fast diffusion of the species of the electrolyte.

The average values of ε_{eff} are compared for all electrodes in Figure 5.52f. It can be noted that the effective porosity is close for NA7 and NA2, 0.19 and 0.21 respectively, while their total porosity is significantly different, 0.21 and 0.28 respectively. This suggests that the microstructure of NA2 is much less efficient than that of NA7. This may point to an influence of the poorer electronic wiring of the active mass in NA2 compared to NA7. The heterogeneity of the electronic wiring of the active mass to the electron collection network would lead to heterogeneous functioning of the electrode, critical for high current regimes. The best connected NMC clusters sucking the ionic fluxes, the diffusional limitations would then appear earlier than in the case of an electrode such as NA7 where the greater compactness homogenizes the electronic wiring and the electrode functioning.

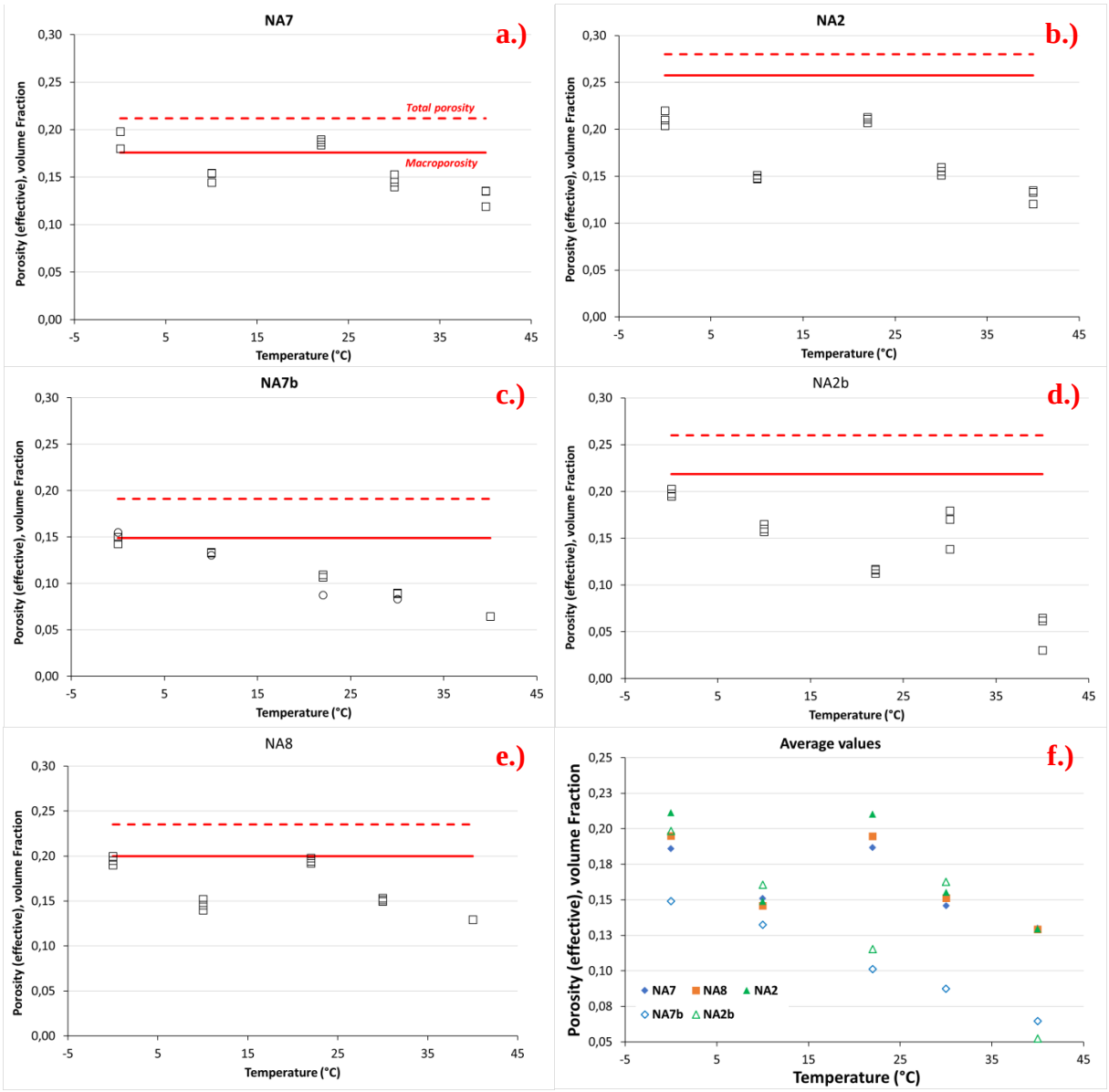

Figure 5.51: ε_{eff} PDM fits of NA7(a), NA2(b), NA7b(c), NA2b(d), NA8(e) electrodes at various temperatures. Average P_{eff} of all the electrodes are comparted with each other (f).

5.9.4) Influence of the Active Mass Loading

Discharge experimental areal capacities at 12 mmϕ, 22°C were then fitted with the PD model on NA2 and NA3 on one hand, and NA3b, NA7b and NA4b on the other hand to test its consistency on electrodes with significantly differing active mass loadings. Indeed, NA2 and NA3 (NA3b, NA7b and NA4b) have same CB/PVdF content and same porosity, but different active mass loadings. Table 5.15 shows the parameters involved in the fitting. The fitting technique used in this case is varying the ε_{eff} value. The model still captures the capacity decrease past the C*

region in both 7 mmϕ and 12 mmϕ electrodes. More importantly, the ε_{eff} values are almost the same for each electrode for both the 7 mm and 12 mm electrode diameter (Table 5.15 and Figure 5.52). This underlines the versatility of the PD model. NA3b, NA7b and NA4b tend to have the same ε_{eff} at this temperature, respectively 0.12, 0.11 and 0.10. As they have same composition and density, their macroporosity expected is expected to be similar, about 0.15. This trend of decreased ε_{eff} values with increased thickness (active mass loading) is somehow expected. Indeed, the increased thickness could increase the probability of the "defect points" aforementioned in the previous section. Unexpectedly, NA2 exhibits a larger ε_{eff} than NA3. One may notice that NA2 and NA3 surprisingly have comparable C* and comparable areal capacities at rates beyond C*. This suggests that NA3 has a different microstructure than NA2, less efficient with respect to electronic and ionic wirings of the active mass. This may result from a poor manufacturing. The electrode tapes were manufactured elsewhere and are one shots. We were not able to check the reproducibility of their manufacturing. Another hypothesis is that the smaller thickness of NA3 leads during the calendering to a less homogeneous crushing of this electrode than for NA2, resulting in a less homogeneous microstructure and having a greater number of "defect points". This problem would not be seen with NA3b due to the higher amount of CB/PVdF. The plastic mechanical behavior of the PVdF [65] and the carbon lubrication properties would allow a better accommodation of the compression imposed on the electrode film.

Table 5.15: Table of parameters for ε_{eff} PDM fitting of various eletrodes of 12mmϕ cycled at 22°C.

Graph	Q_0 (mAh/cm^2)	D_0 (cm^2/s)	T_{0f}	ε_{eff}	I (A/cm^2)	L (cm)	t_+	C_0 (mol/cm^3)
P_{eff} adjusted NA2	***4.35***	*1.6 x 10^{-6}*	1.2	***0.20***	$0.352\cdot10^{-3}$ to $65.8\cdot10^{-3}$	0.0074	0.393	0.001
P_{eff} adjusted NA3	***2.78***	1.6 x 10^{-6}	1.2	***0.13***	$0.204\cdot10^{-3}$ to $40.8\cdot10^{-3}$	0.00445	0.393	0.001
P_{eff} adjusted NA7b	***4.46***	1.6 x 10^{-6}	1.2	***0.11***	$0.347\cdot10^{-3}$ to $69.4\cdot10^{-3}$	0.00744	0.393	0.001
P_{eff} adjusted NA4b	***7.17***	1.6 x 10^{-6}	1.2	***0.10***	$0.557\cdot10^{-3}$ to $69.4\cdot10^{-3}$	0.00814	0.393	0.001
P_{eff} adjusted NA3b	***2.5***	1.6 x 10^{-6}	1.2	***0.12***	$0.200\cdot10^{-3}$ to $40\cdot10^{-3}$	0.00446	0.393	0.001

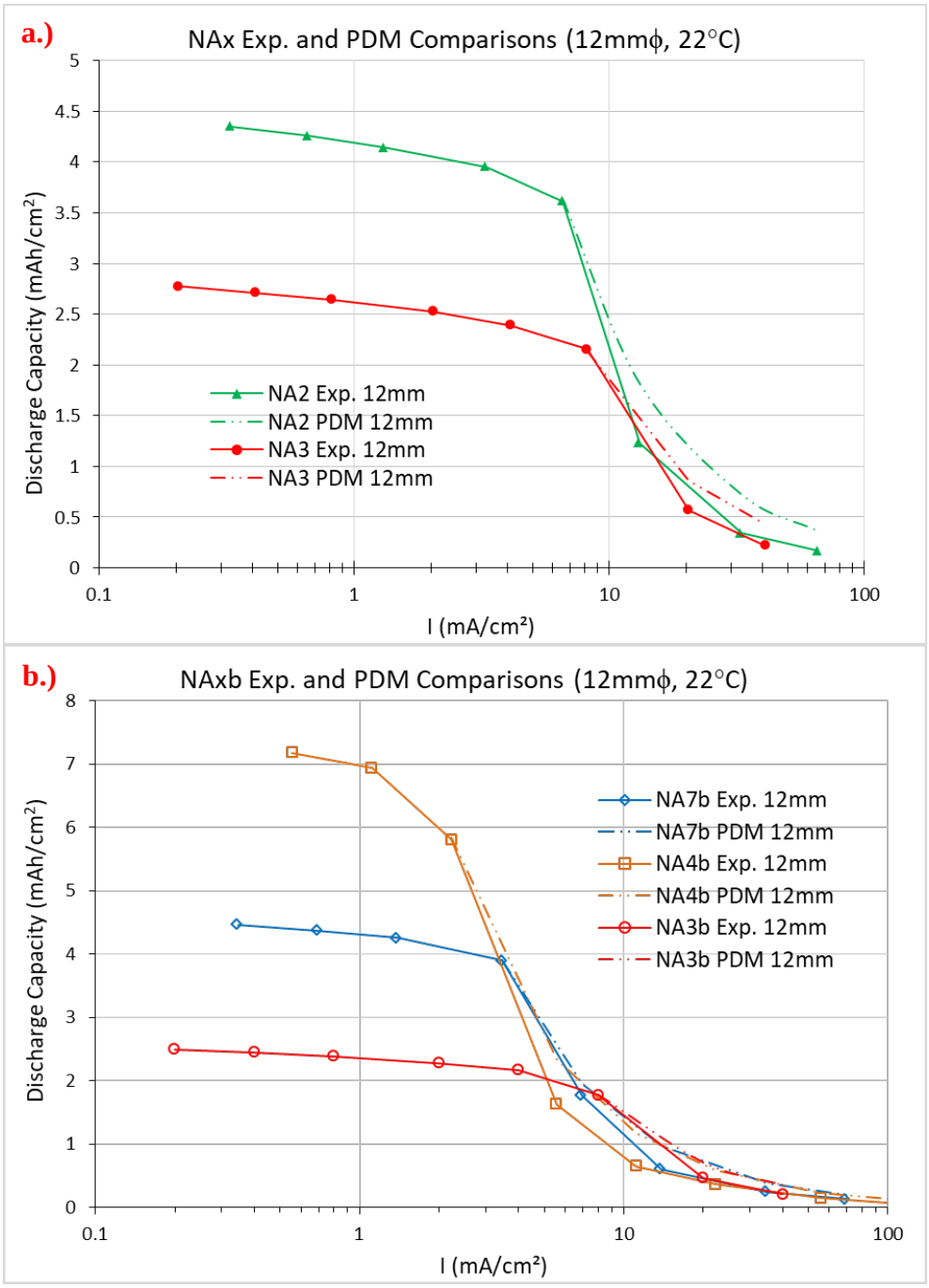

Figure 5.52: PDM ε_{eff} fits of NA2 vs NA3 (a) and NA7b vs NA4b vs NA3b (b)

5.9.5) Analysis of Power Behavior in Charge

Due to the manifestation of a possible side reaction that greatly increased our capacity during charge, we came into the conclusion that the next best step to describe the capacities during charge is via the corresponding discharge capacities for each power step. Hypothetically, the true reversible capacity should be able to be recovered via the amount of Li that is put back into the active material during the lithiation step (discharge). Figure 5.54 shows the comparison between the power discharge capacities (lithiation) and the corresponding discharge C/10 capacities ((D) delithiation) between NA7, NA2, and NA7b. Figure 5.55 gives us a closer look with the capacities in the C and 2C regions.

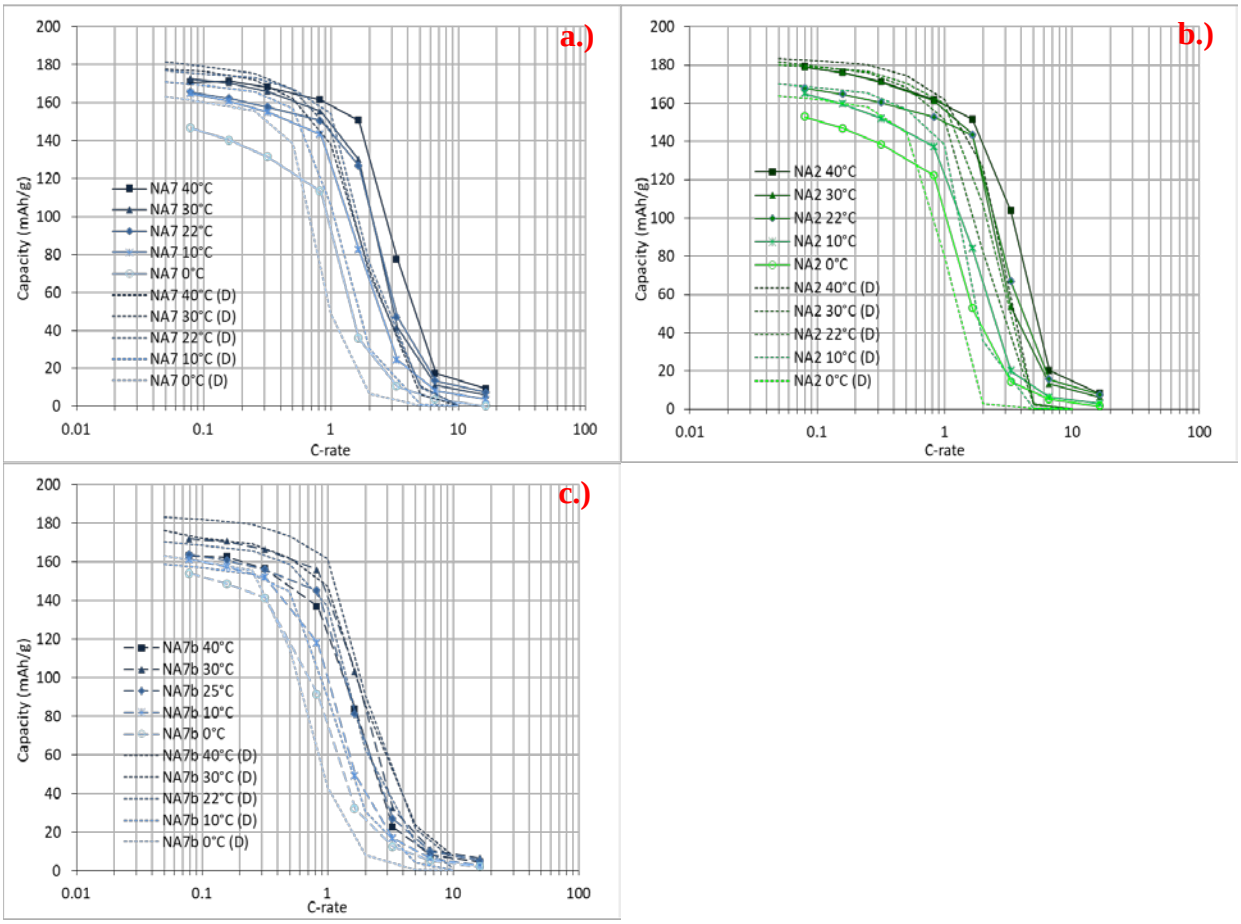

Figure 5.53: Lithiation discharge capacities (marked lines) vs corresponding discharge capacities from delithiation (dotted lines) of NA7(a), NA2(b) and NA7b(c).

The most striking features are that: (i) the charge capacity (measured through the corresponding discharge capacities (D)) is higher at low rate than the discharge capacities; but (ii) the C* region is decreased in charge, which means the brutal drop in capacity appears for a lower current in charge that in discharge. The first feature is a reflection of the better intrinsic kinetics of the active material in the lithiated state leading to higher Q_0. The second feature is a reflection of the lower conductivity of the active material in the delithiated state and thus larger cell resistance and then larger polarization (operating voltage closer to the ceiling voltage) in charge. We can observe that the capacities at lower temperatures for the corresponding discharges (D) are lower than those of the power discharge capacities for all electrodes which could come from the combined low thermal activation of the active material and the low conductivity of the active material at the beginning of charge. A bigger gap can be seen at a higher rate (2C) especially for NA7 and NA2 which is the manifestation of the lower electrical conductivity in comparison to NA7b where the gap is closer. Finally, NAx still has a higher overall capacity at higher rates than NAxb due to the less tortuous/blocked pore architecture.

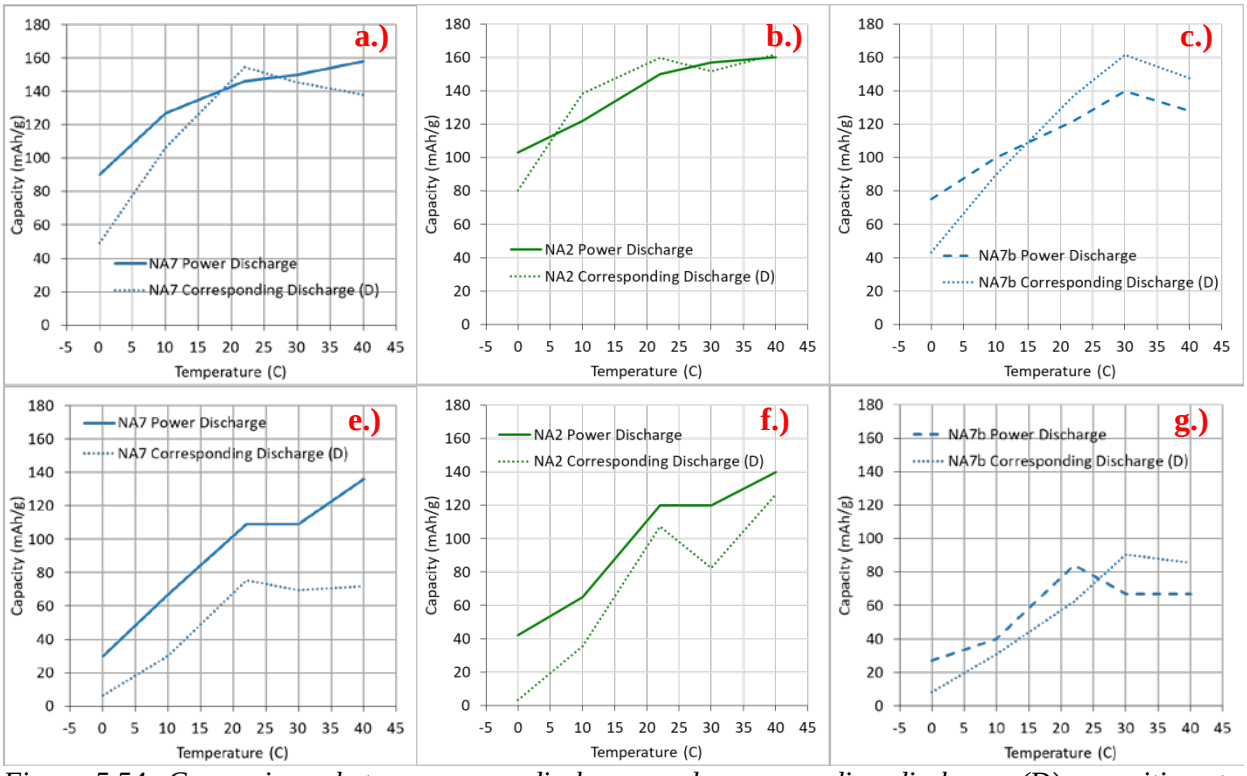

Figure 5.54: Comparisons between power discharge and corresponding discharge (D) capacities at a rate of C (top row) and 2C (bottom row) for NA7 (right column), NA2 (middle column) and NA7b (right column).

5.9.6) Conclusion

The simple PD model that we tested offered reasonable parameters concerning the three individual parameters of D_{eff}, T_{eff} and ε_{eff}. The same order of magnitude for diffusion determined for D_{eff} and D_0 at varying temperatures illustrates that our model is "in range" in determining diffusion coefficients in the electrode, although this was offset by the high tortuosity values taken from the study by Usseglio-Vireta *et. al.* The T_{eff} values not only reflected the average tortuosity in the electrode matrix but also demonstrated how increased binder-electrolyte interactions at increasing temperatures and increased CB-PVdF content can affect the paths in the pore matrix. Finally, the determined ε_{eff} values were not only realistic but also revealed the degree of available pore space that effectively homogenizes the electrolyte concentration. The ε_{eff} values tend to decrease at increasing density and CB-PVdF content demonstrating the concept of defect points that chokes ion transport within the pore matrix.

The power capacities during charge were analyzed via the corresponding discharge capacities after the preceding charge. We were able to extract reasonable (D) capacities and when compared to the power discharge capacities, it was seen that the capacities during charge (via (D)) were lower on average than that of the capacities during the power discharge. This was attributed to the change of the intrinsic conductivity of the active material. The lowering of the capacity during charge seen with both NAx and NAxb electrodes tells us that this is a significant limiting factor of the electrode performance during charge. Even so, at higher rates, the pore microstructure still holds a great effect as seen through how the NAxb electrodes have lower capacities than that of the NAx series during charge.

---

[1] A. Etiemble, N. Besnard, A. Bonnin, J. Adrien, T. Douillard, P. Tran-Van, L. Gautier, J.-C. Badot, E. Maire, B. Lestriez, Multiscale morphological characterization of process induced heterogeneities in blended positive electrodes for lithium–ion batteries. *J. Mater. Sci.* **52**, 3576–3596 (2016).
[2] Porcher, W., Lestriez, B., Jouanneau, S. & Guyomard, D. Design of aqueous processed thick LiFeP O4 composite electrodes for high-energy lithium battery. *J. Electrochem. Soc.* **156**, (2009).
[3] Besnard, N. *et al.* Multiscale Morphological and Electrical Characterization of Charge Transport Limitations to the Power Performance of Positive Electrode Blends for Lithium-Ion Batteries. *Adv. Energy Mater.* **7**, (2017).

[4] F. Cadiou, Étude de l'impact de la microstructure sur les propriétés effectives électriques des batteries lithium ion; acquisition et simulations sur des microstructures réelles et génération d'architectures numériques, PhD thesis, INSA de Lyon, 2019.
[5] Dang, D., Wang, Y. & Cheng, Y.-T. Communication—Fracture Behavior of Single $LiNi_{0.33}Mn_{0.33}Co_{0.33}O_2$ Particles Studied by Flat Punch Indentation . *J. Electrochem. Soc.* **166**, A2749–A2751 (2019).
[6] A. Agrawal, PhD thesis.
[7] Badot, J. C., Ligneel, E., Dubrunfaut, O., Guyomard, D. & Lestriez, B. A multiscale description of the electronic transport within the hierarchical architecture of a composite electrode for lithium batteries. *Adv. Funct. Mater.* **19**, 2749–2758 (2009).
[8] Seid, K. A. *et al.* Multiscale electronic transport mechanism and true conductivities in amorphous carbon-$LiFePO_4$ nanocomposites. *J. Mater. Chem.* **22**, 2641–2649 (2012).
[9] Seid, K. A. *et al.* Multiscale electronic transport in $Li_{1+x}Ni_{1/3-u}Co_{1/3-v}Mn_{1/3-w}O_2$: A broadband dielectric study from 40 Hz to 10 GHz. *Phys. Chem. Chem. Phys.* **15**, 19790–19798 (2013).
[10] Zheng, H., Yang, R., Liu, G., Song, X. & Battaglia, V. S. Cooperation between active material, polymeric binder and conductive carbon additive in lithium ion battery cathode. *J. Phys. Chem. C* **116**, 4875–4882 (2012).
[11] Cadiou, F. *et al.* Numerical Prediction of Multiscale Electronic Conductivity of Lithium-Ion Battery Positive Electrodes. *J. Electrochem. Soc.* **166**, A1692–A1703 (2019).
[12] Seid, K. A. *et al.* An in situ multiscale study of ion and electron motion in a lithium-ion battery composite electrode. *Adv. Energy Mater.* **5**, 1–10 (2015).
[13] Panabière, E., Badot, J. C., Dubrunfaut, O., Etiemble, A. & Lestriez, B. Electronic and Ionic Dynamics Coupled at Solid-Liquid Electrolyte Interfaces in Porous Nanocomposites of Carbon Black, Poly(vinylidene fluoride), and γ-Alumina. *J. Phys. Chem. C* **121**, 8364–8377 (2017).
[14] Yang, X. & Rogach, A. L. Electrochemical Techniques in Battery Research: A Tutorial for Nonelectrochemists. *Adv. Energy Mater.* **1900747**, 1–10 (2019).
[15] Mohanty, D. *et al.* Effect of electrode manufacturing defects on electrochemical performance of lithium-ion batteries: Cognizance of the battery failure sources. *J. Power Sources* **312**, 70–79 (2016).
[16] Tsukasaki, H. *et al.* Thermal behavior and microstructures of cathodes for liquid electrolyte-based lithium batteries. *Sci. Rep.* **8**, 1–9 (2018).
[17] Belharouak, I., Lu, W., Vissers, D. & Amine, K. Safety characteristics of $Li(Ni_{0.8}Co_{0.15}Al_{0.05})O_2$ and $Li(Ni_{1/3}Co_{1/3}Mn_{1/3})O_2$. *Electrochem. commun.* **8**, 329–335 (2006).
[18] Lu, P. *et al.* Observation of electron-beam-induced phase evolution mimicking the effect of the charge-discharge cycle in Li-rich layered cathode materials used for Li ion batteries. *Chem. Mater.* **27**, 1375–1380 (2015).
[19] Kasnatscheew, J. *et al.* The truth about the 1st cycle Coulombic efficiency of $LiNi_{1/3}Co_{1/3}Mn_{1/3}O_2$ (NCM) cathodes. *Phys. Chem. Chem. Phys.* **18**, 3956–3965 (2016).
[20] Kuroda, S., Tobori, N., Sakuraba, M. & Sato, Y. Charge-discharge properties of a cathode prepared with ketjen black as the electro-conductive additive in lithium ion batteries. *J. Power Sources* **119**–**121**, 924–928 (2003).
[21] Kuratani, K. *et al.* Controlling of dispersion state of particles in slurry and electrochemical properties of electrodes. *J. Electrochem. Soc.* **166**, A501–A506 (2019).

[22] Guy, D., Lestriez, B., Bouchet, R. & Guyomard, D. Critical Role of Polymeric Binders on the Electronic Transport Properties of Composites Electrode. *J. Electrochem. Soc.* **153**, A679 (2006).
[23] Lazarraga, M. G., Mandal, S., Ibañez, J., Manuel Amarilla, J. & Rojo, J. M. $LiMn_2O_4$-based composites processed by a chemical-route: Microstructural, electrical, electrochemical, and mechanical characterization. *J. Power Sources* **115**, 315–322 (2003).
[24] Guzmán, G., Vazquez-Arenas, J., Ramos-Sánchez, G., Bautista-Ramírez, M. & González, I. Improved performance of $LiFePO_4$ cathode for Li-ion batteries through percolation studies. *Electrochim. Acta* **247**, 451–459 (2017).
[25] Tran, H. Y. *et al.* Influence of electrode preparation on the electrochemical performance of $LiNi_{0.8}Co_{0.15}Al_{0.05}O_2$ composite electrodes for lithium-ion batteries. *J. Power Sources* **210**, 276–285 (2012).
[26] Wang, Y., Fu, X., Zheng, M., Zhong, W. H. & Cao, G. Strategies for Building Robust Traffic Networks in Advanced Energy Storage Devices: A Focus on Composite Electrodes. *Adv. Mater.* **31**, 1–29 (2019).
[27] Fongy, C., Gaillot, A.-C., Jouanneau, S., Guyomard, D. & Lestriez, B. Ionic vs Electronic Power Limitations and Analysis of the Fraction of Wired Grains in $LiFePO_4$ Composite Electrodes. *J. Electrochem. Soc.* **157**, A885 (2010).
[28] Singh, M., Kaiser, J. & Hahn, H. A systematic study of thick electrodes for high energy lithium ion batteries. *J. Electroanal. Chem.* **782**, 245–249 (2016).
[29] Zolin, L., Chandesris, M., Porcher, W. & Lestriez, B. An Innovative Process for Ultra-Thick Electrodes Elaboration: Toward Low-Cost and High-Energy Batteries. *Energy Technol.* **7**, (2019).
[30] West, K. Jacobsen, T. and Atlung, S. Modeling of Porous Insertion Electrodes with Liquid Electrolyte. *J. Electrochem. Soc.* **129**, 1480 (2006).
[31] Fuller, T. F., Doyle, M. & Newman, J. Simulation and Optimization of the Dual Lithium Ion Insertion Cell. *J. Electrochem. Soc.* **141**, 1–10 (1994).
[32] Gallagher, K. G. *et al.* Optimizing Areal Capacities through Understanding the Limitations of Lithium-Ion Electrodes. *J. Electrochem. Soc.* **163**, A138–A149 (2015).
[33] Johns, P. A., Roberts, M. R., Wakizaka, Y., Sanders, J. H. & Owen, J. R. How the electrolyte limits fast discharge in nanostructured batteries and supercapacitors. *Electrochem. commun.* **11,** 2089–2092 (2009).
[34] Zacharias N.A., Nevers, C. Skelton D.R., Knackstedt K., Stephenson D.E., Wheeler D.R., Direct Measurements of Effective Ionic Transport in Porous Li-Ion Electrodes. *J. Electrochem. Soc.*, **2013**, *160*, A306.
[35] Kataoka, H., Saito, Y., Sakai, T., Quartarone, E. & Mustarelli, P. Conduction Mechanisms of PVDF-Type Gel Polymer Electrolytes of Lithium Prepared by a Phase Inversion Process. *J. Phys. Chem. B* **104**, 11460–11464 (2000).
[36] Saunier, J., Gorecki, W., Alloin, F. & Sanchez, J. Y. NMR study of cation, anion, and solvent mobilities in macroporous poly(vinylidene fluoride). *J. Phys. Chem. B* **109**, 2487–2492 (2005).
[37] Saito, Y., Morimura, W., Kuratani, R. & Nishikawa, S. Ion transport in separator membranes of lithium secondary batteries. *J. Phys. Chem. C* **119**, 4702–4708 (2015).

[38] Saito, Y., Morimura, W., Kuse, S., Kuratani, R. & Nishikawa, S. Influence of the Morphological Characteristics of Separator Membranes on Ionic Mobility in Lithium Secondary Batteries. *J. Phys. Chem. C* **121**, 2512–2520 (2017).
[39] Tjaden, B., Brett, D. J. L. & Shearing, P. R. Tortuosity in electrochemical devices: a review of calculation approaches. *Int. Mater. Rev.* **63**, 47–67 (2018).
[40] Landesfeind, J., Hattendorff, J., Ehrl, A., Wall, W. A. & Gasteiger, H. A. Tortuosity determination of battery electrodes and separators by impedance spectroscopy. *J. Electrochem. Soc.* **163**, A1373–A1387 (2016).
[41] Malifarge, S., Delobel, B. & Delacourt, C. Determination of tortuosity using impedance spectra analysis of symmetric cell. *J. Electrochem. Soc.* **164**, E3329–E3334 (2017).
[42] DuBeshter, T., Sinha, P. K., Sakars, A., Fly, G. W. & Jorne, J. Measurement of Tortuosity and Porosity of Porous Battery Electrodes. *J. Electrochem. Soc.* **161**, A599–A605 (2014).
[43] Gaberscek, M. Towards optimized preparation of cathode materials: How can modeling and concepts be used in practice. *J. Power Sources* **189**, 22–27 (2009).
[44] Fongy, C., Jouanneau, S., Guyomard, D., Badot, J. C. & Lestriez, B. Electronic and ionic wirings versus the insertion reaction contributions to the polarization in $LiFePO_4$ composite electrodes. *J. Electrochem. Soc.* **157**, 1347–1353 (2010).
[45] Marino, C., Fullenwarth, J., Monconduit, L. & Lestriez, B. Diagnostic of the failure mechanism in $NiSb_2$ electrode for Li battery through analysis of its polarization on galvanostatic cycling. *Electrochim. Acta* **78**, 177–182 (2012).
[46] Mazouzi, D. *et al.* Very high surface capacity observed using Si negative electrodes embedded in copper foam as 3D current collectors. *Adv. Energy Mater.* **4**, 1–13 (2014).
[47] Doi, T., Iriyama, Y., Abe, T. & Ogumi, Z. Pulse voltammetric and ac impedance spectroscopic studies on lithium ion transfer at an electrolyte/$Li_{4/3}Ti_{5/3}O_4$ electrode. *Anal. Chem.* **77**, 1696–1700 (2005).
[48] Yamada, I., Abe, T., Iriyama, Y. & Ogumi, Z. Lithium-ion transfer at $LiMn_2O_4$ thin film electrode prepared by pulsed laser deposition. *Electrochem. commun.* **5**, 502–505 (2003).
[49] Yamada, I., Iriyama, Y., Abe, T. & Ogumi, Z. Lithium-ion transfer on a Li_xCoO_2 thin film electrode prepared by pulsed laser deposition-Effect of orientation-. *J. Power Sources* **172**, 933–937 (2007).
[50] Xu, J., Chou, S. L., Gu, Q. F., Liu, H. K. & Dou, S. X. The effect of different binders on electrochemical properties of $LiNi_{1/3}Mn_{1/3}Co_{1/3}O_2$ cathode material in lithium ion batteries. *J. Power Sources* **225**, 172–178 (2013).
[51] Huang, J. *et al.* An analytical three-scale impedance model for porous electrode with agglomerates in lithium-ion batteries. *J. Electrochem. Soc.* **162**, A585–A595 (2015).
[52] C. Heubner, A. Nickol, J. Seeba, S. Reuber, N. Junker, M. Wolter, M. Schneider, A. Michaelis. Understanding thickness and porosity effects on the electrochemical performance of $LiNi_{0.6}Co_{0.2}Mn_{0.2}O_2$ -based cathodes for high energy Li-ion batteries. *J. Power Sources* **419,** 119–126 (2019).
[53] Zheng, H., Li, J., Song, X., Liu, G. Battaglia, V. S. A comprehensive understanding of electrode thickness effects on the electrochemical performances of Li-ion battery cathodes. *Electrochim. Acta* **71,** 258–265 (2012).
[54] Jow, T. R., Marx, M. & Allen, J. L. Distinguishing Li^+ charge transfer kinetics at 1. NCA/electrolyte and graphite/electrolyte interfaces, and 2. NCA/electrolyte and LFP/electrolyte interfaces in Li-ion cells. in *ECS Transactions* **33**, 1–13 (2011).

[55] Seid, K. A. *et al.* An in situ multiscale study of ion and electron motion in a lithium-ion battery composite electrode. *Adv. Energy Mater.* **5**, 1–10 (2015).
[56] Qiu, X. Y. *et al.* Reprint of 'investigation of layered $LiNi_{1/3}Co_{1/3}Mn_{1/3}O_2$ cathode of lithium ion battery by electrochemical impedance spectroscopy'. *J. Electroanal. Chem.* **688**, 393–402 (2013).
[57] Amin, R. & Chiang, Y. M. Characterization of electronic and ionic transport in $Li_{1-x}Ni_{0.33}Mn_{0.33}Co_{0.33}O_2$ (NMC333) and $Li_{1-x}Ni_{0.50}Mn_{0.20}Co_{0.30}O_2$ (NMC523) as a function of Li content. *J. Electrochem. Soc.* **163**, A1512–A1517 (2016).
[58] Ligneel, E., Lestriez, B., Hudhomme, A. & Guyomard, D. Effects of the solvent concentration (solid loading) on the processing and properties of the composite electrode. *J. Electrochem. Soc.* **154**, 235–241 (2007).
[59] D. Guy, B. Lestriez, R. Bouchet, D. Guyomard, "Critical role of polymeric binders on the electronic transport properties of composites electrode", *J. Electrochem. Soc.*, 2006, **153**, A679-A688
[60] Saunier, J., Gorecki, W., Alloin, F. & Sanchez, J. Y. NMR study of cation, anion, and solvent mobilities in macroporous poly(vinylidene fluoride). *J. Phys. Chem. B* **109**, 2487–2492 (2005).
[61] Krachkovskiy, S. A., Pauric, A. D., Halalay, I. C. & Goward, G. R. Slice-selective NMR diffusion measurements: A robust and reliable tool for in situ characterization of ion-transport properties in Lithium-ion battery electrolytes. *J. Phys. Chem. Lett.* **4**, 3940–3944 (2013).
[62] Ligneel, E., Lestriez, B., Hudhomme, A. & Guyomard, D. Effects of the solvent concentration (solid loading) on the processing and properties of the composite electrode. *J. Electrochem. Soc.* **154**, 235–241 (2007).
[63] Saunier, J., Alloin, F., Sanchez, J. Y. & Barrière, B. Plasticized Microporous Poly(vinylidene fluoride) Separators for Lithium-Ion Batteries. I. Swelling Behavior of Dense Membranes with Respect to a Liquid Electrolyte - Characterization of the Swelling Equilibrium. *J. Polym. Sci. Part B Polym. Phys.* **42**, 532–543 (2004).
[64] Kataoka, H., Saito, Y., Sakai, T., Quartarone, E. & Mustarelli, P. Conduction mechanisms of PVDF-type gel polymer electrolytes of lithium prepared by a phase inversion process. *J. Phys. Chem. B* **104**, 11460–11464 (2000).
[65] Park, Y. S., Oh, E. S. & Lee, S. M. Effect of polymeric binder type on the thermal stability and tolerance to roll-pressing of spherical natural graphite anodes for Li-ion batteries. *J. Power Sources* **248**, 1191–1196 (2014).

CHAPTER 6: SUMMARY, DISCUSSION AND GENERAL CONCLUSION

Results from the NMR part have revealed that, in addition to the geometric tortuosity, any existing interactions between the electrolyte species and composite component surfaces will greatly slow down diffusion. Swelling of the binder through electrolyte interaction/absorption increases viscosity in the bulk through concentration gradients. The increased Li^+ viscosity in the bulk and the trapping of DMC in the polymer reduces the T_2 and in combination with the restrictive pore environment reduces the T_2 values of both species. The observed plateau and the greatly decreased T_2 values highlight the heavy interactions that the restricted species are experiencing in contrast with the electrolyte bulk. The greatly reduced T_2 values also impede our ability to detect the diffusion values of heavily restricted components in the attenuation curve. These were greatly seen in the case of DMC in the pellets and of Li^+ in the pure polymer film where the faster components were clearly observed but the slower components were obscured. Nevertheless, the experienced tortuosity of any species diffusing in a pore matrix will be greater if there any existing interactions between the pore wall surface (in the case of an electrode: AM and additive-binder surfaces) and the electrolyte species. This is vital when ionic transport limitations are considered in an environment or system that relies on ionic diffusion to optimally operate.

The electrochemical performance evaluation of positive electrodes designed for electric vehicle applications in both charge and discharge were done at different current regimes and temperatures. Analyses were centered on linking the influence of loading, porosity and additive content with capacity delivery. To an extent, reproducibility was generally hampered due the use of the coin cell system. This was greatly amplified by wetting problems encountered with the additive rich NAxb series. Extra capacities at high rates during charge were possibly attributed to parasitic reactions shifting our analyses by using the capacities of the succeeding discharge.

The observed increased specific capacity delivery at very low current densities in combination with decreased porosity, reduced mass loading at higher current densities and in general at increased temperatures are in accordance with existing literatures. Remarkably, electrodes of the

NAx series, even at decreased electronic percolation; exhibited adequate to superior performance than the NAxb series.

Cell resistance analyses at varying temperatures showed two distinct resistance signatures between charge and discharge. Thermal activation energy during discharge is similar to activation energies associated with the electronic conductivity of the NMC material. This draws the conclusion that the cell's conductivity rests with the electronic conductivity of the electrodes. Interestingly, the electronic conductivity of the active material is enough to compensate against the lack of electronic percolation and thus allow proper functioning. The lower conductivity of the active material in the lithiated state greatly increases the cell resistance at the beginning of charge.

Higher nominal capacities during charge in combination with higher temperatures demonstrate the better intrinsic kinetics of the material in the delithiated state (174.5 vs.170 mAh/g). Interestingly, at plateau is reached at temperatures exceeding 22°C.

PD fitting was successfully done at current densities or C-rates exceeding the critical regime C*. It was surprisingly easy to handle and takes into account accessible parameters such as: the properties of the electrolyte (C_0, D_0 and t_+), the microstructure of the electrode (L and ε), electrochemical properties of the active material (Q_0), and finally cycling conditions (I). Assessing the validity of this model was worthwhile as it could be a practical tool for researchers and engineers for diagnosing and optimizing the efficiency of the composition and the microstructure of an electrode.

We were also able to get adequate matching of both C* and capacity decay behavior using the three parameters: D, T and ε. In depth analyses show:

- D_{eff} values are several times higher than bulk D_0 when tortuosity that only considers Fick's law is used.
- Adjusting T_{eff} values at diffusion coefficients similar to the bulk electrolyte reveal that the electrode tortuosity is an average of the tortuosity of both macro- and meso-

porosities and also to an extent the nano-porosity confined in both CB-PVdF and fragmented NMC clusters.

- By taking the diffusion coefficient equal to that of the bulk electrolyte and considering the tortuosity equal to that of the macroporosity, the values of ε_{eff} obtained are equal to or less than the macroporosity of the electrodes.

Focused analysis of the ε_{eff} values affirm that low tortuosity macropores primarily homogenizes the salt concentrations in the electrolyte. These values of ε_{eff}, lower than that of the macroporosity is then seen as proof of defects points existing in the microstructure of the electrode which alters the efficiency of this macroporosity. These defect points are areas of mesoporosity that break the percolation of the macroporosity. This could have been better observed if we had been able to enlarge the FIB/SEM voxel volume. A larger FIB-SEM voxel volume would allow us to obtain better average tortuosity values of the microstructure of our electrodes. Higher amounts of CB/PVdF in the electrodes also seems to induce a higher concentration these defect points, presumably due to the interactions of lithium with CB and the solvent of the electrolyte with PVdF. Since the PVdF swelling by the solvent increases with temperature, the PVdF rich electrodes result in a collapse of the effective porosity and power performance with temperature.

To better visualize this ion transport phenomena, we would like to introduce the “traffic concept”. Porous and less tortuous electrodes represent a city having a high percentage of straight, less curved, and multi-lane roads. Denser electrodes represent a city that has more curved and intricately connected roads with less number of lanes. Effectively, the denser electrodes have increased ion traffic congestion and therefore already experiences heavy traffic at a microporous level form its higher level of tortuosity. In contrast, less dense electrodes enjoy free ion traffic at a macroporous level due to less tortuosity. The aforementioned defect points are road chokepoints of reduced road size requiring the ions to merge and congest at these specific chokepoints as they pass through. The increased congestion generates bottlenecks further hampering ion traffic even at increased bulk diffusion coefficient (increased temperature and concentration gradient from one pore section to another): i.e. like a high-speed car required to reduce to a halt as it approaches these choke points. The end result is a “traffic butterfly

effect” wherein ion traffic accumulates similar to the depletion phenomena stated heavily in literatures. Furthermore, increased additive content increases chokepoint sites and therefore increases overall traffic. In summary, power performance; as limited by ion diffusion, is highly dictated to how one can minimally generate these chokepoints in order to minimize ion depletion in the pore reservoirs. From a binder perspective, one must choose a binder that neither heavily interacts with the electrolyte nor one that weakly disperses and forms chokepoints at small pore sized areas. From a pore microstructure perspective, particle sizes and calendaring should be optimized to best reduce chokepoint paths.

UNIVERSITE MATIERE BRETAGNE MOLECULES LOIRE ET MATERIAUX

UNIVERSITÉ DE NANTES

Titre : Évaluation des performances électrochimiques de batteries lithium-ion et mesures de leurs propriétés de transport par RMN haut champ

Mots clés : Batteries Li-Ion, matériaux de cathode NMC, performances électrochimiques, propriétés de transport

Résumé : Les applications automobiles des batteries lithium-ion exigent deux caractéristiques principales : le kilométrage (énergie) et le couple (puissance). La demande en énergie peut être facilement obtenue en augmentant le grammage des électrodes. Cependant, la puissance souffre du fait que l'épaisseur accrue des électrodes augmente la longueur du trajet pour le transport des ions, ce qui constitue le principal facteur limitant pour un fonctionnement correct à des densités de courant élevées. Cette étude traite de l'influence des paramètres d'électrode sur les performances électrochimiques, en particulier à des densités de courant élevées. Des cyclages électrochimiques en conjonction avec la RMN PFG-SE ont été réalisés pour identifier les limitations de performances et pour étudier la diffusion des ions dans la porosité de l'électrode.

Les mesures électrochimiques révèlent que la conductivité intrinsèque du matériau actif détermine les performances à faibles densités de courant et au début de la charge grâce via la résistance de polarisation. Aux fortes densités de courant, un grammage élevé et l'obstruction du réseau CB-PVdF entravent le transport des ions. Ceci est bien illustré par notre modèle analytique qui relie les différents paramètres de l'électrode à la densité de courant critique. Les mesures de RMN confortent l'hypothèse selon laquelle une teneur accrue en CB-PVdF augmente la tortuosité en raison de toutes les interactions de ces additifs avec les espèces de l'électrolyte.

Title: Evaluation of electrochemical performance of lithium-ion batteries and measurements of their transport properties by high-field NMR

Keywords: Li-ion batteries, NMC cathode material, electrochemical performance, transport properties

Abstract: Automotive applications of Lithium ion batteries demand two key characteristics: mileage (energy) and torque (power). Energy demand can be simple achieved by increasing electrode mass loadings. However, power suffers due to that increased electrode thickness increases the path length for ion transport, which is the key limiting factor for proper functioning at high current densities. This study deals with how the different electrode parameters affect electrochemical performance especially at high current densities. Electrochemical cycling in conjunction PFG-SE NMR were done to pinpoint performance limitations and to study ion diffusion within the electrode porosity.

Electrochemical measurements reveal that at low rates the intrinsic conductivity of the active material dicates performance through the polarization resistance. At high current densities, increased mass loading and obstruction from the CB-PVdF network hampers ion transport. This is best illustrated by our analytical model which relates the various electrode parameters with the maximum working rate. NMR measurements support the hypothesis that increased CB-PVdF content increases tortuosity due to any existing interactions between the electrolyte species and these additives.